Computer simulations of liquid crystals

Alastair Dewar, M.Chem.

A thesis submitted in fulfilment of requirements for the degree of
Doctor of Philosophy

to
School of Chemistry
University of Edinburgh

2005

Declaration

I hereby declare that this thesis is of my own composition, and that it contains no material previously submitted for the award of any other degree. The work reported in this thesis has been executed by myself, except where due acknowledgement is made in the text.

Alastair Dewar

Abstract

To develop a theoretical understanding of the liquid crystalline behaviour of bent-core liquid crystals, we have performed isothermal-isobaric (NPT) Monte Carlo simulations of a simple molecular model. The molecular model consists of 7 soft spheres constrained to form a rigid 'v' shape, with external bond angle, γ. Neighbouring sites on a given molecule are separated by one unit sphere diameter, σ.

We have investigated the phase behaviour of these model molecules, with $\gamma = 0°$, $\gamma = 20°$ and $\gamma = 40°$. In this system the intermolecular interactions were described by the full Lennard-Jones (LJ) potential. With $\gamma = 0°$, the model exhibits isotropic, uniaxial nematic, untilted Smectic A and crystalline phases. In the system with $\gamma = 20°$, no untilted Smectic A phase is found, albeit with a enhanced range over which the uniaxial nematic is stable. For the $\gamma = 40°$, the system exhibits racemic smectic and crystalline phases, but no nematic or untilted smectic phases.

The phase behaviour of polar model molecules have also been studied. Dipolar interactions were calculated via the Ewald summation method. With $\gamma = 0°$ with $\mu^* = 0$ we find isotropic, uniaxial nematic, untilted smectic A and herringbone phases. With $\mu^* = 1$ we find, isotropic, uniaxial nematic, untilted smectic A and crystalline phases. With $\mu^* = 2$ we find isotropic, tilted smectic B and tilted crystalline phases. With $\gamma = 20°$ and $\mu^* = 0$ we observe isotropic, uniaxial nematic and herringbone phases. With $\mu^* = 1$ we find isotropic and nematic phases and with $\mu^* = 2$ we observe an antiferroelectric crystal. With $\gamma = 40°$ and $\mu^* = 0$ we find isotropic and tilted smectic B phases, with $\mu^* = 1$, we observe similar phase behaviour. With $\mu^* = 2$ we find an antiferroelectric crystal.

We have also investigated the phase behaviour of model molecules constructed from 5 spheres with and without flexible tails. The effect of flexible tails was investigated utilising configurational-bias Monte Carlo. With γ in the range $0° - 40°$ and without tails we observe isotropic and herringbone phases. With $\gamma = 0°$ with flexible tails we observe isotropic and tilted smectic phases. With $\gamma > 0°$ we observe isotropic and tilted ferroelectric smectic phases. We also observe large smectic-layer fluctuations within the layers.

We have also calculated and compared splay and bend flexoelectric coefficients for model molecules with γ in the range $0° - 40°$. We have found a critical angle, below which both coefficients are negligible. Above this critical angle the molecules can behave as wide aspect wedges and as banana-shaped molecules, giving rise to non-zero coefficients. Systems without attractive interactions generally give rise to smaller flexoelectric coefficients compared to the corresponding systems with attractive interactions.

The removal of attractive interactions destabilises the low temperature solid phases, increasing the observed molecular tilt. Inclusion of dipolar interactions stabilises the layered phases, with a decrease in molecular tilt. This tilt is reduced at increased dipole moment magnitudes. In none of the systems did we observe any chiral phases, whether they be synclinic ferroelectric or anticlinic antiferroelectric.

Acknowledgements

I would like to thank my supervisor Dr. Philip Camp for his never ending patience and advice over the last few years. I would also like to thank Rob, Steven, Peter, and my family for their support during the last three and a half years. I would also like to thank the Engineering and Physical Science Research Council (EPSRC) for funding.

The ultimate banana simulation...

Contents

List of Tables

List of Figures

CHAPTER 1

Introduction

We are taught from a early age that matter exists in three phases, solid, liquid and gas. The simplest of the states of matter is the gas phase. Experiments performed by Boyle in the 17^{th} century form the basis of ideal gas behaviour and Maxwell's kinetic gas theory. In the solid phase, the particles may be highly ordered on a lattice. The only allowed motion of the particles is vibration about their lattice positions. As such, the solid phase is characterised by long range order in all three-dimensions. The liquid phase is the most challenging of the states of matter to describe theoretically. Using current levels of theory it is not possible to provide a complete molecular level description of even the simplest fluid phases.

Mean field theory can be utilised to describe phase behaviour of complex liquids, albeit with approximations and assumptions that may give rise to spurious predictions. We can also use computational techniques to systematically study the molecular properties of liquids. At the molecular level, we have to use quantum mechanics to describe the motion of particles and calculate the molecular properties of fluids. At present, cutting-edge quantum mechanical techniques can only deal with isolated molecules or periodic materials. Rather than use quantum mechanics to describe atomic motion and restrict ourselves to the solid or gas phases, we can resort to classical mechanics. This is known as molecular modelling or classical atomistic simulation. In molecular modelling, the internal energy of a molecule is the sum of all the bond energies, torsions, non-bonded interactions, electrostatic interactions and hydrogen bonding. It must be noted

that we would be restricted to specific materials if we were to use quantum mechanical or classical atomistic simulations. Another approach to enlighten theoretical understanding of fluids is to adopt a coarse grained model to mimic the key features of the material under study.

1.1 An introduction to Liquid Crystals

Liquid crystals were discovered by Reinitzer in 1888, whilst he was conducting light scattering experiments of systems close to undergoing a phase transition. These new phases possess physical properties intermediate between those of solid and liquid phases. The liquid crystalline phases can be classified in terms of their translational (positional) and orientational ordering [1, 2]. At high temperature the isotropic (random) phase (I) is found, in which the positions and orientations of the molecules are randomly distributed. Cooling from the isotropic phase, the nematic (N) phase is formed. In the nematic phase the molecular positions are randomly distributed, yet the long axes of the molecules are aligned with director vector, $\vec{n}(\vec{r})$, which is defined as the average orientation of all the molecules. Cooling further, the smectic phases are formed. In the smectic phases the system has periodicity in one dimension, with distinct layers formed and the molecules orientationally aligned. In the smectic A (SmA) phase, each layer behaves like a two-dimensional fluid. In the smectic B (SmB) or hexatic phase, the molecules have adopted translational ordering on a triangular lattice. The smectic C (SmC) phase is similar to the smectic A phase, albeit with the director tilted with respect to the layer normal. A diagrammatic representation of the liquid crystalline phases is shown in Fig. 1.1

There are two general classes of liquid crystalline materials; *thermotropic* liquid crystals or *lyotropic* liquid crystals. The phase behaviour of *thermotropic* liquid crystals is governed by temperature. This is a result of sterically anisotropic interactions. *Thermotropic* liquid crystals are typically found in the displays of digital watches and pocket calculators. *Lyotropic* liquid crystals are typically formed by a dispersion of non-spherical particles and the phase behaviour is governed by the concentration of the particles. *Lyotropic* liquid crystals are important in foodstuffs, cleansers and biological systems. It must also be noted that orientationally ordered phases can be formed by spherical molecules with anisotropic interactions, such as the formation of a ferroelectric nematic phase formed by dipolar hard spheres [3].

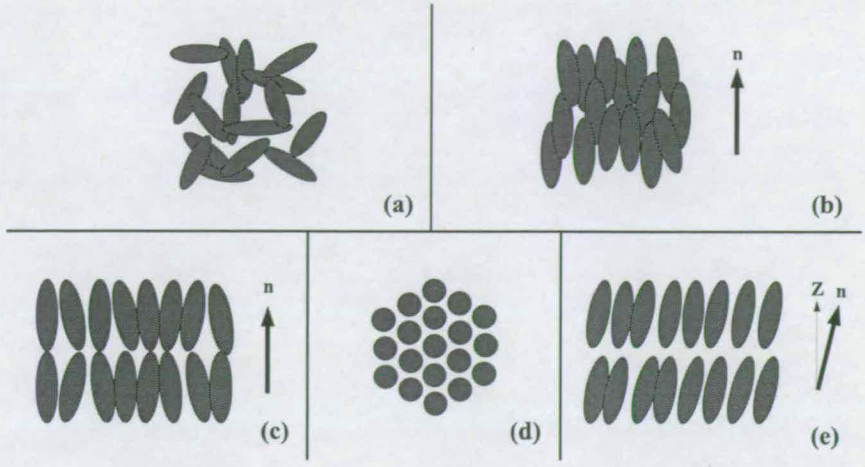

Figure 1.1: Diagrammatic representation of some liquid crystalline phases: (a) the isotropic phase, where there is no orientational or translational ordering, (b) the nematic phase, where there is orientational order, the director **n**, yet no translational order, (c) the smectic A phase, where there is translational ordering in one direction only, the layers acting as a 2-*D* fluid, (d) the smectic B ('hexatic') phase, where the molecules within each layer adopt a small degree of translational ordering, and (e) the smectic C phase, where the director is tilted away from the layer normal (**Z**)

The steric anistropic interactions found in *thermotropic* liquid crystals can take many forms. Some examples of *thermotropic* liquid crystals are: *p*-azoxyanisole (PAA) [1] and 4-pentyl-4′-cyanobiphenyl (5CB) [2], which are both rod-shaped and give rise to liquid crystalline phases. Another example with an alternative form of steric anisotropy is Nonyloxybow (NOBOW) as shown in Fig. 1.2 [4], which is banana-shaped. A useful review of the mesomorphic phase behaviour as a function of molecular geometry is presented in Ref. [5].

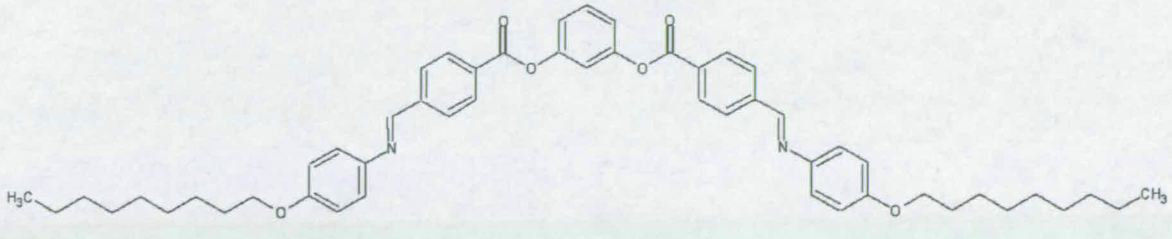

Figure 1.2: The structure of Nonyloxybow (NOBOW) [4].

Since the late 1960's, *thermotropic* liquid crystals have been mainly used in optical displays, such as the common digital watch, pocket calculator, and more recently flat-screen computer screens and mobile phone displays. Other new applications of these materials could include optical shutters in photographic equipment, electronic curtains or optical switches in telecommunication applications. Many generations of liquid crystal displays were based on twisted nematic cells as shown in Fig. 1.3. In these cells unpolarised light passes through a polariser and either passes through the liquid crystal when the cell is switched off [Fig. 1.3(A)] or is blocked when the cell is switched on [Fig. 1.3(B)]. When an electric field is applied the molecules align and a polarisation is induced [6] due to field coupling to the dielectric anisotropy. Ref. [7] describes the requirements for materials used and recent developments in material used in twisted nematic displays.

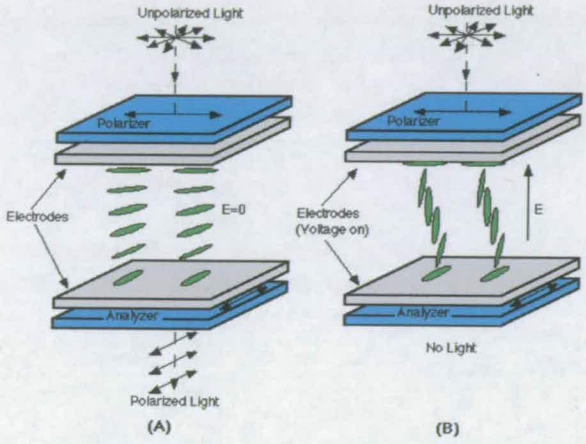

Figure 1.3: A twisted nematic cell.

The response time of such devices is poor (approximately $\sim 30\text{ms}$) and as a consequence research is being directed to developing surface stabilised ferroelectric display devices for future generations of liquid crystal displays and optical switches. These are based upon spontaneously polarised ferroelectric smectic phases which allows for faster switching. In order to form ferroelectric phases, linear molecules have to be chiral [8], which are expensive to manufacture and require stereoselective synthesis on a large scale. To ease the manufacturing process and reduce costs of surface stabilised ferroelectric displays, other materials are being investigated. One such class of materials is bent-core, 'banana-shaped' liquid crystals, which shall be discussed in the next section.

1.1.1 Bent-core molecules

Bent-core molecules were first synthesised by Niori *et al.* [9] in 1996. These molecules possess steric anisotropy and can form a tilted smectic phase, raising the possibility of forming ferroelectric and antiferroelectric phases. The generic structure of this class of compounds is shown in Fig. 1.4. In this case the R groups are alkyl [4, 9] or alkoxy [4, 10, 11, 12, 13] with carboxy and amide linking groups. Materials have also been synthesised with different combinations of linking groups; such as carboxy and thiocarboxyllic linking groups [14] and carboxy groups only [15]. Pelzl *et al.* [15] report the formation of a nematic phase constituted by bent-core molecules. Another variation upon the generic structure is the increase in the number of aromatic rings from 5 to 7 [16]. These materials possess bend angles between $110° - 138°$ [17].

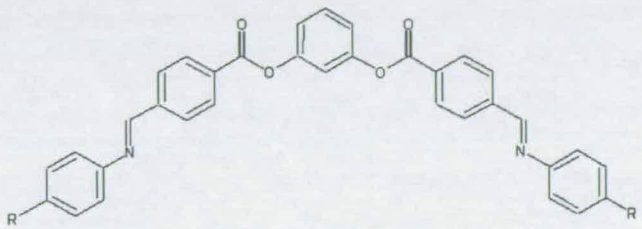

Figure 1.4: Generic bent-core liquid crystal structure.

Although the molecules are achiral, with C_{2v} symmetry, individual smectic layers are chiral, as shown in Fig. 1.5. This surprising chirality can be ascribed to the homogeneous molecular tilt, with respect to the layer polarisation, within a smectic layer. This molecular tilt results in a non-superimposible mirror image. As a result of this new phases can be proposed; these depend upon the nature of the smectic layers in a given system. The first of these new phases is the chiral ferroelectric, shown in Fig. 1.6(a), where the layer polarisations are parallel and thus there is a net polarisation. The layers are tilted the same with respect to the layer polarisation [the $(-)$ form], this is referred to as synclinic. The next phase is the racemic ferroelectric as shown in Fig. 1.6(b), has alternating layers tilted in alternating directions (anticlinic), thus the layers have alternating chirality and are hence are racemic. The chiral antiferroelectric phase, shown in Fig. 1.6(c), has zero net polarisation as the layer polarisations are anti-parallel. The layers are tilted in the same sense with respect to the layer polarisation, giving rise to a zig-zag arrangement when viewing from one end and all layers posses the same chirality. In the racemic antiferroelectric phase [Fig. 1.6(d)] alternating layers possess opposing tilt with respect to the layer polarisation and hence opposing

chirality. It must be noted that the majority of systems are racemic [4, 10, 11] although some chiral systems are found [18]. It is also possible to form paraelectric phases, whereby the layer polarisations are randomly distributed within a plane or randomly oriented.

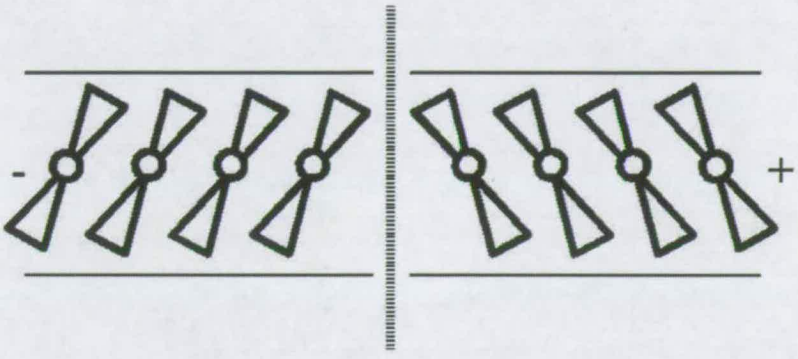

Figure 1.5: End-on view of a smectic layer, the molecular tilt induces chirality as the mirror (right) image is non-superimposible upon the original system (left).

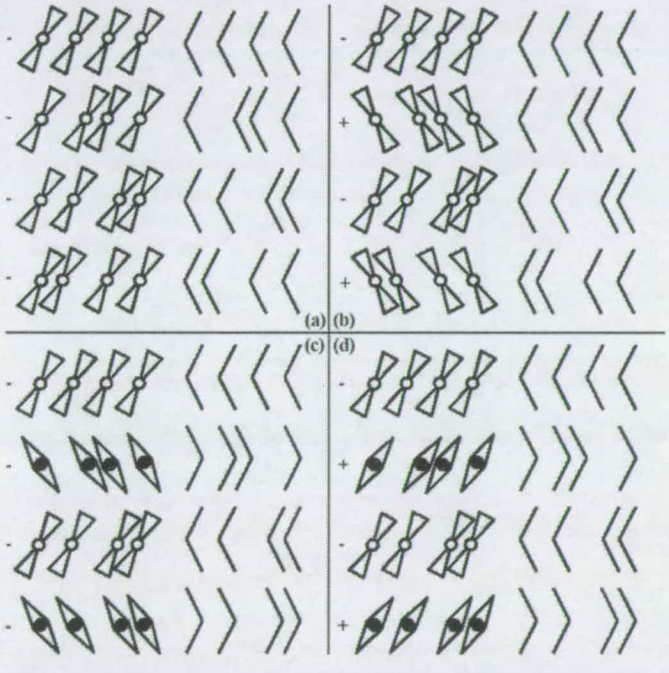

Figure 1.6: Diagrammatic representations of: (a) the chiral ferroelectric, (b) the racemic ferroelectric, (c) the chiral antiferroelectric and (d) the racemic antiferroelectric.

1.1.2 Flexoelectric effect

With bent-core molecules it is also possible to induce the flexoelectric effect, which is the liquid crystal analogue of piezoelectricity. In the flexoelectric effect a net polarisation is induced by deformation of the director field $[\vec{n}(\vec{r})]$ in the

nematic phase of molecules that possess steric anisotropy. There are two types of deformation that give rise to the flexoelectric effect in liquid crystals, these are; splay of wedge-shaped molecules, which is shown in Fig. 1.7(a) and bending of bent-core molecules [Fig. 1.7(b)]. As such there will be two contributions to the flexoelectric polarisation, $\vec{p^f}$ and can be calculated via the function in Eqn. 1.1. By calculation of both the flexoelectric coefficients, e_1 and e_3 for a series of bend angles (in the range $0° \rightarrow 40°$), this work shall suggest optimal molecular parameters for desired optical properties.

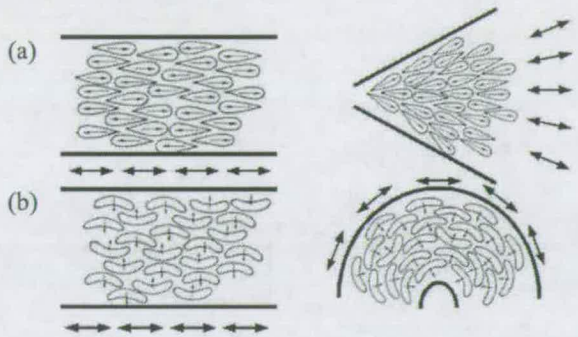

Figure 1.7: The effects of applying; (a) splay and (b) bend deformations to the director field of a nematic liquid crystal formed of wedge-shaped and banana-shaped molecules, respectively. The black arrows denote the local director field at the indicated locations.

$$\vec{p^f} = e_{11}(\nabla \cdot \vec{n})\vec{n} + e_{33}(\nabla \times \vec{n}) \times \vec{n} \tag{1.1}$$

1.2 Molecular models of liquid crystals

The focus of this work is to investigate the phase behaviour and bulk properties of bent-core ("banana-shaped") liquid crystals. With current computer algorithms it is only possible to study isolated molecules at the atomistic level including quantum mechanical effects, which would only yield structural information of the molecules. It is possible to perform complex dynamical calculations using density functional theory coupled with molecular dynamics [19]. It must be noted that the largest current simulation utilising this technique is of 64 water molecules (192 atoms). A typical banana-shaped molecule is composed of > 100 atoms and this would restrict this type of calculation to a single molecule. DFT-MD is therefore unsuitable for determining the phase behaviour of banana-shaped molecules as the calculations would not yield the true bulk properties. In

any case, we can neglect quantum mechanical effects as the thermal wavelength [$\Lambda = \sqrt{(h^2/2\pi mkT)}$] is much less than the molecular length-scale.

We can employ classical atomic simulations, whereby we use a parametrised force field technique coupled with molecular dynamics [20, 21, 22]. As this work is concerned with developing generic key-structure property relationships, using a force field coupled with molecular dynamics is unsuitable as it would restrict us to a specific system. In order to find these generic relationships a simple, yet structurally relevant model has been used.

There are several types of model that are amenable to model bent-core systems, including dimers of Gay-Berne ellipsoids [23, 24, 25] which represents the geometry of the molecules coupled with attractive interactions, albeit non-uniformly, hard spherocylinder dimers [26, 27] which describe the packing of liquid crystals and a multi-site model typically constructed from several soft-spheres [28, 29, 30] in which the geometry and interaction potential can be easily controlled and mimics the aromatic ring structure of the bent-core molecules.

This work shall utilise a composite of soft spheres. The spheres are arranged in a rigid 'v' shape as shown in Fig. 1.8, where we can control the molecular geometry, by varying γ and the interaction potential. Neighbouring spheres on a given molecule are separated by a distance equal to 1 unit sphere diameter and the arms of the molecule are given by two unit vectors $\vec{e_1}$ and $\vec{e_2}$, with $\vec{e_1} \cdot \vec{e_2} = -\cos\gamma$. The molecular frame of the molecule is defined with three orthonormal vectors given by,

$$\vec{a} = \frac{\vec{e_1} - \vec{e_2}}{|\vec{e_1} - \vec{e_2}|} \tag{1.2}$$

$$\vec{b} = \frac{\vec{e_1} + \vec{e_2}}{|\vec{e_1} + \vec{e_2}|} \tag{1.3}$$

$$\vec{c} = \vec{a} \times \vec{b} \tag{1.4}$$

The total configurational energy is given by a sum of pair interactions between the pairs of spheres on different molecules,

$$U = \sum_{i=1}^{N_m - 1} \sum_{i>J}^{N_m} \sum_{k=1}^{N_s} \sum_{l=1}^{N_s} u(|r_{ik} - r_{jl}|), \tag{1.5}$$

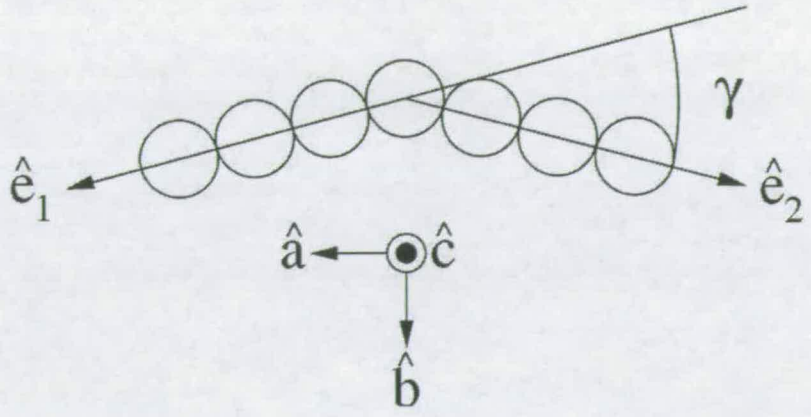

Figure 1.8: The composite of soft spheres model.

where N_m is the total number of molecules, N_s the number of spheres per molecule, r_{ik} the position vector of the k^{th} sphere on the i^{th} molecule, and $u(r)$ is the sphere-sphere interaction potential.

To gain a key understanding of bent-core liquid crystals, we shall investigate the phase behaviour of model molecules with various degrees of complexity. The first step of this investigation shall ascertain the phase behaviour of apolar model molecules with attractive dispersion interactions, as presented in Chapter 3. We shall then probe the phase behaviour of model molecules with long range dipolar interactions and short range purely repulsive sphere-sphere interaction, the results of which are presented in Chapter 4. The third stage shall examine the effect of the number of spheres that are used to construct the core of the molecule with and without attractive interactions as described in Chapter 5. We shall add further complexity to the model, by grafting flexible side chains on to the both ends of each molecule, the results of which are presented in Chapter 6. Finally, the splay and bend flexoelectric coefficients will be calculated for a series of molecules with γ in the range $0° \rightarrow 40°$, as presented in Chapter 7. All of these studies shall be performed using Monte Carlo (MC) computer simulations, as described in Chapter 2. Chapter 8 concludes this thesis.

CHAPTER 2

Statistical mechanics and computer simulations of liquid crystals

In this chapter, we shall summarise some of the key results of classical statistical mechanics and describe the Metropolis Monte Carlo method. We shall also identify the quantities that can be calculated during the course of a simulation.

2.1 Classical statistical mechanics

A simple fluid composed of N_m sterically anisotropic molecules that each have position vectors, $\vec{r}_i$ and orientation vectors, $\vec{\Omega}_i$ for each molecule. Each molecule interacts via a simple pair potential, $u(r)$. Utilising the composite of soft spheres model, as described in section 1.2, the total energy, U, is the sum of the pair interactions over all N_s spheres on all N_m molecules as shown in Equation 2.1,

$$U = \sum_{i=1}^{N_m-1} \sum_{i>J}^{N_m} \sum_{k=1}^{N_s} \sum_{l=1}^{N_s} u(|\vec{r}_{ik} - \vec{r}_{jl}|), \tag{2.1}$$

where the vector $\vec{r}_{ik}$ denotes the position vector of the k^{th} sphere on the i^{th} molecule and $\vec{r}_{jl}$ the position vector of the l^{th} sphere on the j^{th} molecule. To fully define the position and orientation in 'phase space' of N_m molecules, the vectors $\vec{r}_i$ and $\vec{\Omega}_i$ both require $3N_m$ pieces of information; the x, y and z coordinates of the molecules and (θ, ϕ, ψ) the Euler angles to describe the orientation. For a complete description, the linear ($\mathbf{p_i}$) and angular momenta ($\mathbf{J_i}$) are required.

In order to calculate thermodynamic properties of the system, it is necessary to calculate the partition function. This can, in principle be achieved by integrating

the system Hamiltonian, H, over all positions, $\mathbf{r^N} = \{\mathbf{r_1}, \mathbf{r_2}....\mathbf{r_{N_m}}\}$, orientations, $\mathbf{\Omega^N} = \{\mathbf{\Omega_1}, \mathbf{\Omega_2}....\mathbf{\Omega_{N_m}}\}$ and linear and angular momenta $\mathbf{p^N} = \{\mathbf{p_1}, \mathbf{p_2}....\mathbf{p_{N_m}}\}$ and $\mathbf{J^N} = \{\mathbf{J_1}, \mathbf{J_2}....\mathbf{J_{N_m}}\}$ respectively [31].

$$Q = \frac{1}{\delta \mathbf{r}^N \delta \mathbf{p}^N} \int \exp(-\beta H) d\mathbf{r^N} d\mathbf{\Omega^N} d\mathbf{p^N} d\mathbf{J^N}, \tag{2.2}$$

where $\delta \mathbf{r}^N \delta \mathbf{p}^N$ are the uncertainties in $\mathbf{r}^N$ and $\mathbf{p}^N$ respectively and $\beta = 1/k_B T$: As we cannot distinguish individual particles ('Gibbs paradox') due to the coarse grained nature of 'phase space', we have to replace the $\delta \mathbf{r}^N \delta \mathbf{p}^N$ term with $N_m! h^{3N_m}$. The system Hamiltonian is the sum of the kinetic (linear and angular) and potential energies as shown in Eqn. 2.3. Here the potential energy is dependent upon the positions and orientations of the particles.

$$H = \sum_{molecules} \left(\frac{p_i^2}{2m} + \sum_{k=1,2,3} \frac{J_i^2}{2I_k} \right) + U\left(\mathbf{r^N}, \mathbf{\Omega^N}\right), \tag{2.3}$$

when $U(\mathbf{r^N}, \mathbf{\Omega^N}) = 0$ the kinetic terms are the basis for the ideal gas.

It can be shown that the constant volume partition function factorises into kinetic and potential terms,

$$Q_{NVT} = \frac{1}{N! \mathcal{V}^{3N}} \int d\mathbf{r^N} d\mathbf{\Omega^N} \exp[-\beta U], \tag{2.4}$$

where $\int d\mathbf{r}^N d\mathbf{\Omega}^N \exp[-\beta U]$ is the configurational integral, Z_{NVT}, U is the total configurational energy, and $\mathcal{V}$ is the de Broglie thermal volume.

For systems at constant pressure and temperature, i.e. in the isothermal-isobaric ensemble, the enthalpy needs to be considered, $H = U + PV$. The partition function then becomes,

$$Q_{NPT} = \frac{1}{N! \Lambda^{3N}} \int dV \int d\mathbf{r^N} \int d\mathbf{\Omega^N} \exp[-\beta(U + PV)], \tag{2.5}$$

As our pair potential, shown in Equation 2.1, is dependent upon the pair separation as such, we can neglect the orientational dependent terms for the partition function. However, it must be noted that the actual interaction of a pair of molecules is orientationally dependent.

2.2 Computer simulation

With the exponential growth in computational power available to researchers, it is now possible to perform essentially 'exact' calculations of finite temperature thermodynamics with increasingly complex models of classical systems. This has led to the use of computer simulations in new areas of soft condensed matter research, such as liquid crystals, colloids, hydrodynamics, ionic media and critical phenomena. From simulation it is possible to access thermodynamic, dynamical and structural information that is complementary to experimental data. Molecular computer simulations fall in to two general categories; Molecular Dynamics (MD) and Monte Carlo methods (MC).

In molecular dynamics, N-particle trajectories are calculated from the classical solution of Newton's equations of motion utilising pairwise additive interactions such as the Yukawa or Lennard-Jones potentials or more complex potentials. A recent development has seen the use of quantum mechanical calculations to supplement the classical force data for solving the equations of motion [19]. With molecular dynamics the phase space trajectory evolves as a function of time and as such it is possible to measure static and dynamical properties of the model system. In molecular dynamics the 'time average' is the classical limit of the 'ensemble average' computed in Monte Carlo. The work contained in this thesis shall be concerned with purely static quantities and will utilise the Monte Carlo technique outlined below.

In Monte Carlo simulations, the different microstates of an ensemble are sampled, where an ensemble is a collection of microstates that share common thermodynamic properties. Each ensemble is defined by three thermodynamic variables, which are quoted in conjugate pairs of intensive and extensive variables, which are energy (U) and temperature (T), volume (V) and pressure (P) and the number of particles (N) and the chemical potential (μ).

Considering a system in the canonical ensemble, the number of particles, volume and temperature are fixed and U is purely the configurational energy of the model system. In the isothermal-isobaric ensemble N, P and T are held fixed, in this case the appropriate energy function is $H = U + PV$, i.e. the enthalpy. From section 2.1, it can be seen that the kinetic and configurational components of both the canonical and isothermal-isobaric partition functions can be resolved, with the former being evaluated analytically (equations 2.4 and 2.5) leading to

equipartition of energy. As a consequence the MC method samples configurational space only. For the canonical ensemble the average of a physical quantity, A, which is solely dependent upon the particle coordinates, is given by,

$$\langle A \rangle_{NVT} = \frac{\int d\mathbf{r}^N A(\mathbf{r}^N) \exp -\beta U(\mathbf{r}^N)}{\int d\mathbf{r}^N \exp -\beta U(\mathbf{r}^N)} \tag{2.6}$$

$$= \frac{1}{Z_{NVT}} \int d\mathbf{r}^N A(\mathbf{r}^N) \exp -\beta U(\mathbf{r}^N) \tag{2.7}$$

Utilising a modern desktop computer, one might try to generate a large number of random configurational states and then average $A(\mathbf{r}^N)$ over these generated states. The ensemble average then becomes,

$$\langle A \rangle_{NVT} = \lim_{N \to \infty} \frac{\sum_N \langle A(\mathbf{r}_s^N) \rangle \exp -\beta U(\mathbf{r}_s^N)}{\sum_N \exp -\beta U(\mathbf{r}_s^N)}. \tag{2.8}$$

However, even with a small system, the number of configurations $(\mathbf{r}_s^N)$ that can be sampled is orders of magnitude smaller than the total number of configurations possible, which will result in poor averages. In the majority of configurations $U(\mathbf{r}_s^N)$ is large, due to the high probability of at least two molecules overlapping. This produces a low Boltzmann factor for that configuration. For a statistical system in equilibrium, configurations occur with a probability given by the Boltzmann distribution,

$$P_B(C_i) = \frac{1}{Z_{NVT}} \exp\left(-\beta E(C_i)\right), \tag{2.9}$$

where C_i is the i^{th} configuration. Instead of randomly generating configurations, they could be generated with the probability of the Boltzmann distribution (equation 2.9). This would ensure that only statistically important configurations are sampled and hence averages would converge more rapidly. This is an example of importance sampling. The ensemble average over states, s, then becomes,

$$\langle A \rangle_{NVT} = \frac{1}{N} \sum_s A(\mathbf{r}_s^N). \tag{2.10}$$

However, as the partition function, Q is unknown, we have to generate a Markov chain of states, which depends only on the current state and has no memory of past states. At equilibrium, the average number of trial moves accepted that results in a system leaving the old state to any new state must be equal to the

number of trial moves that result from all other new states to the old state, giving rise to detailed balance. This implies,

$$\Pi(o \rightarrow n)P(o) = \Pi(n \rightarrow o)P(n), \tag{2.11}$$

where $\Pi(o \rightarrow n)$ and $\Pi(n \rightarrow o)$ are the transition probabilities for the system going from the old state to the new and visa versa respectively. $P(o)$ and $P(n)$ are the probabilities of the old and new states as given by equation 2.9. Thus,

$$\frac{\Pi(o \rightarrow n)}{\Pi(n \rightarrow o)} = \frac{P(n)}{P(o)} = \frac{\exp(-\beta U_n)}{\exp(-\beta U_o)} \tag{2.12}$$

$$= \exp(-\beta(U_n - U_o)) \tag{2.13}$$

To utilise this result, a suitable MC simulation technique framework is required. One such technique is the algorithm developed by Metropolis *et al.* [32]. The acceptance of a trial move is given by,

$$\Pi(o \rightarrow n) = \min[1, \exp(-\beta(U_n - U_o))]. \tag{2.14}$$

The Metropolis algorithm does not stipulate how one configuration is allowed to evolve to the next. This evolution can arise as a result of perturbing the system with respect to a system or configurational degree of freedom. In the canonical ensemble, these perturbations can act upon the particle positions or orientations or a change the shape of the simulation cell. In the isothermal-isobaric ensemble there is an additional degree of freedom with the volume fluctuations.

In the isothermal-isobaric ensemble, the acceptance condition has to be modified to take account of the enthalpy, H. As a consequence the Boltzmann distribution now becomes,

$$P_B(V) = \frac{1}{Z_{NPT}} \exp -\beta[U(\mathbf{r}^N, V) + PV - N\beta^{-1} \ln V], \tag{2.15}$$

where P is the pressure, $U(r^N, V)$ the configurational energy at volume V and $Z_{NPT} = \int dV \int d\mathbf{r}^{\mathbf{N}} \exp[-\beta(U + PV)]$. Detailed balance is now written,

$$\frac{\Pi(o \rightarrow n)}{\Pi(n \rightarrow o)} = = \frac{\exp -\beta\left[U(\mathbf{r}^N, V_n) + PV_n - N\beta^{-1} \ln V_n\right]}{\exp -\beta\left[U(\mathbf{r}^N, V_o) + PV_o - N\beta^{-1} \ln V_o\right]} \tag{2.16}$$

$$= \exp\left[(-\beta(U_n - U_o) - \beta P(V_n - V_o) + N \ln\left(\frac{V_n}{V_o}\right)\right], \quad (2.17)$$

where V_o and V_n are the volumes of the old and new states respectively. In this ensemble trial translations and rotations of molecules are attempted as well as fluctuations in system volume.

The algorithm for Metropolis Monte Carlo is [32]:

1. Select a particle (or the entire system) at random.
2. Perform a simple translation, rotation or volume fluctutation.
3. Calculate the change in the appropriate energy function of the entire system.
4. Accept or reject the given perturbation according to Eqn. 2.17.

A simple translation is achieved by moving the apical (central) sphere in a random direction and random distance. The rotations are performed using the Barker-Watts method [33]. This method rotates the molecule about one of the x, y or z axes which is selected at random. The volume fluctutates anisotropically in a cuboidal simulation cell, with $L_x = L_y \neq L_z$ and isotropically in a cubic cell with $L_x = L_y = L_z$. The cell dimensions are sampled in $\ln V$ for computational convenience [33, 34]. The maximum displacement parameters were adjusted to yield respective acceptance ratios of 50%.

Comprehensive treatments of both Molecular Dynamics and Monte Carlo methods can be found in the textbooks by Allen and Tildesley [33] and Frenkel and Smit [34].

2.2.1 *Periodic boundary conditions*

Even with the exponential growth in computational power and memory it is currently impractical to perform simulations of bulk systems, even with the simplest of potentials. On a typical desktop workstation it is only possible to simulate $10^2 - 10^4$ mutually interacting particles in a cubic or cuboidal simulation cell, even with the most powerful parallel supercomputers only $\sim 10^7 - 10^8$ particles can be routinely simulated. Unfortunately, a significant fraction of those particles are in the vicinity of the simulation cell walls, interactions with which will perturb the system from its true equilibrium state. To minimise these so-called finite-size effects, periodic boundary conditions are applied. This involves the replication of the original simulation cell in all spatial dimensions, as shown in

Fig. 2.1. If a particle were to undergo a simple translation or rotation, then the corresponding particles in the replicated cells undergo the same process. This negates the loss of any particles in the system as one particle leaving the central cell would be replaced by its periodic image from the neighbouring cell at the opposite face. The end result is that the particles are allowed to 'move through' the walls of the simulation cell. In addition to the boundary conditions, the minimum image convention is used. The separation of two particle is taken as the lowest of the real-real, real-image and image-real distances.

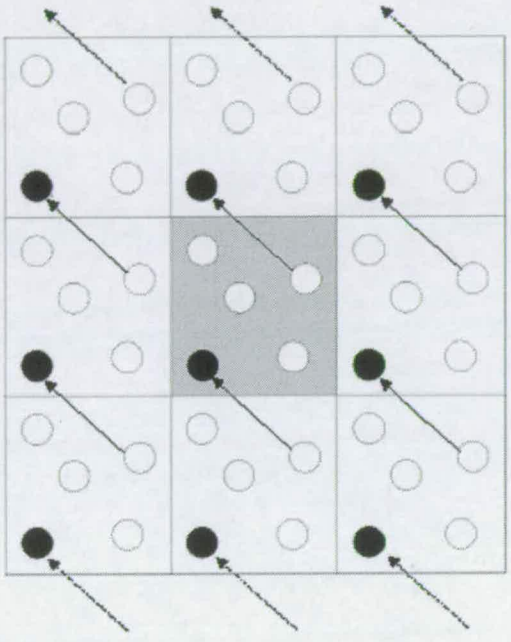

Figure 2.1: Representation of periodic boundary conditions, the central, shaded cell is the original simulation cell.

2.2.2 *Reduced units*

When considering the properties of the system being simulated it is usual to define dimensionless reduced units in terms of the Lennard-Jones parameters. Equations for defining the reduced quantities used in this thesis are given in equations 2.18 - 2.21 [33].

$$U^* = \frac{U}{\epsilon}, \tag{2.18}$$

$$\rho^* = \rho\sigma^3 = \frac{N\sigma^3}{V}, \tag{2.19}$$

$$T^* = \frac{k_B T}{\epsilon}, \tag{2.20}$$

$$P^* = \frac{P\sigma^3}{\epsilon}, \tag{2.21}$$

where σ and ϵ are the Lennard-Jones sphere diameter and the Lennard-Jones well-depth parameter respectively.

2.3 Characterising fluid structure

In addition to the thermodynamic properties of the system calculated routinely, simulations can provide detailed structural and molecular orientational information.

2.3.1 *Structural information*

In all cases, the full radial distribution function, $g(r)$ was calculated. A fourier transform of the radial distrubution data yields the structure factor, which can be accessed via scattering experiments [31].

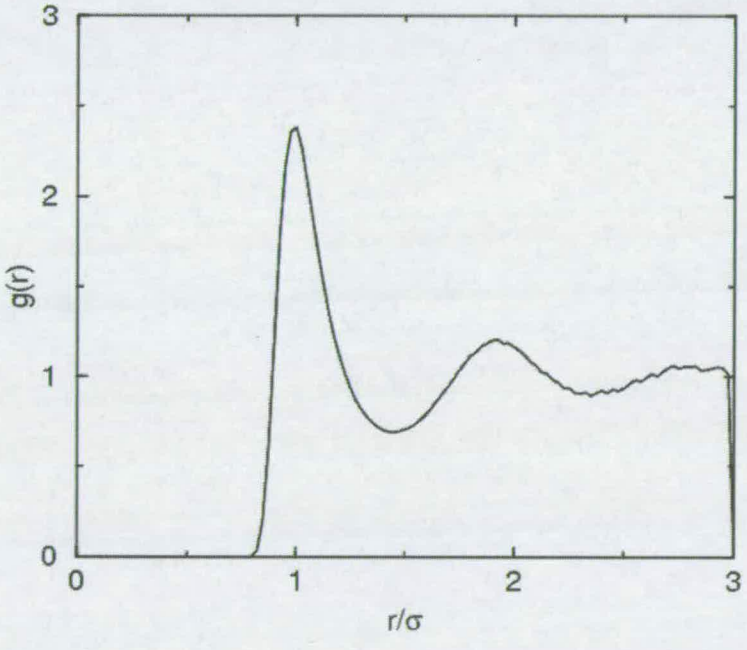

Figure 2.2: A sample radial distribution plot for a simple Lennard-Jones fluid.

To aid charactisation of smectic phases, the correlations between molecules within the same smectic layer were quantified by calculating the in-layer (two-dimensional)

radial distribution function, $g_{xy}(r)$. This latter function is defined by;

$$g_{xy}(r) = \langle \frac{L_{xy}^2}{2\pi N_l^2 r} \sum_{i=1}^{N_l} \sum_{j \neq i}^{N_l} \delta(|\vec{r_i} - \vec{r_j}| - r) \rangle, \tag{2.22}$$

where N_l is the number of molecules within the specified layer and $\vec{r_i}$ is the position vector of the central pivot sphere on the i^{th} molecule. A complementary structural quantity for correlations normal to the smectic layers are calculated via the single particle density, $\rho_z(r)$, which is defined by,

$$\rho_z(r) = \frac{1}{V} \langle \sum_{i=1}^{N_m} \delta(\vec{Z} - \vec{z_i}) \rangle \tag{2.23}$$

To further identify which layered phase has been adopted, it is worthwhile to calculate the mean squared displacement that a molecule migrates as a function of simulation 'time' from the molecule's initial starting position to its latest position in the simulation as shown in Eqn. 2.24

$$\langle R^2 \rangle = \frac{1}{N_m} \sum_{i=1}^{N_m} \left[\vec{r_i}(t) - \vec{r_i}(0) \right]^2, \tag{2.24}$$

where $\vec{r_i}(0)$ and $\vec{r_i}(t)$ are the postion vectors of the i^{th} molecule at $t = 0$ and time, t respectively. In dynamics, $\langle R^2 \rangle = 6Dt$, where D is the diffusion constant. We do not calculate dynamics, as a result $\langle R^2 \rangle$ will depend on Monte Carlo time, τ, thus,

$$\langle R^2 \rangle \propto D'\tau, \tag{2.25}$$

where D' is some measure of mobility.

2.3.2 *Orientational order parameters*

When investigating the phase behaviour of any liquid crystalline material it is useful to define orientational order parameters which identify the distinct phases. The values of these parameters change upon a phase transition and thus can be used to identify these transitions [35, 36]. The ordering of the molecules was assumed to involve the preferential ordering of a set of molecular axes, $\vec{a}$, $\vec{b}$ and $\vec{c}$ defined in section 1.2. Two order parameters are required to differentiate between uniaxial and biaxial ordering [26], which are described by Q_{00}^2 and Q_{22}^2 as

defined in equations 2.26 and 2.27.

$$Q_{00}^2 = \frac{1}{2}(3\cos^2\theta - 1) \tag{2.26}$$

$$Q_{22}^2 = \frac{1}{2}(1+\cos^2\theta)\cos 2\phi\cos 2\psi - \cos\theta\sin 2\phi\sin 2\psi, \tag{2.27}$$

where (θ, ϕ, ψ) are the Euler angles in the laboratory frame. The orientation vectors $\vec{a}$, $\vec{b}$ and $\vec{c}$ are used to define the laboratory frame axes. The director of the most aligned orientation vector is taken as to define the laboratory Z-axis, the second most the Y-axis. The X-axis is orthogonal to both the Y-axis and Z-axis. When the values $Q_{00}^2 = 1$ and $Q_{22}^2 = 0$, indicates a perfect uniaxial ordering, whilst $Q_{00}^2 = 1$ and $Q_{22}^2 = 1$, indicates perfect biaxial orientational order. For the isotropic phase both Q_{00}^2 and Q_{22}^2 are zero. In order to calculate the orientational order parameters it is necessary to evaluate the laboratory frame axes by diagonalisation of the order tensor $\mathbf{Q}_{\alpha\alpha}$, for each orientation vector $\vec{\alpha} = \vec{a}, \vec{b}$ or $\vec{c}$ [35, 36].

$$\mathbf{Q}_{\alpha\alpha} = \frac{1}{2N_m}\sum_{i=1}^{N_m}(3\vec{\alpha}_i\vec{\alpha}_i - \mathbf{I}), \tag{2.28}$$

where $\mathbf{I}$ is the second-rank unit tensor, N_m the number of molecules and $\alpha_i = \vec{a_i}, \vec{b_i}, \vec{c_i}$. Diagonalisation of each tensor yields the eigenvalues, $\lambda^+ \geq \lambda^\circ \geq \lambda^-$ and the corresponding orthonormal eigenvectors, $\vec{n^+}, \vec{n^\circ}, \vec{n^-}$. The molecular axis with the largest λ^+ is identified as the Z-axis of the molecular frame and the corresponding eigenvector (director) defines the laboratory Z-axis $(\vec{Z})$. The molecular axis with the second largest λ^+ is the Y-axis $(\vec{Y})$ of the molecular frame and the corresponding eigenvector (director) defines the laboratory Y-axis. The molecular axis with the lowest λ^+ is taken to be the X-axis of the molecular frame and the X-axis $(\vec{X})$ is orthogonal to the Y and Z-axes. Given these assignments, the order parameters defined in equations 2.26 and 2.27 are equal to;

$$Q_{00}^2 = \vec{Z}.\mathbf{Q}_{zz}.\vec{Z} \tag{2.29}$$

$$Q_{22}^2 = \frac{1}{3}(\vec{X}.\mathbf{Q}_{xx}.\vec{X} + \vec{Y}.\mathbf{Q}_{yy}.\vec{Y} - \vec{X}.\mathbf{Q}_{yy}.\vec{X} - \vec{Y}.\mathbf{Q}_{xx}.\vec{Y}) \tag{2.30}$$

It must be noted that a finite sample size will impact upon the order parameters calculated via the diagonalisation of $Q_{\alpha\alpha}$. In the isotropic phase the errors are $\mathcal{O}(1/\sqrt{N_m})$, while in the orientationally ordered phases, the errors are $\mathcal{O}(1/N_m)$

[37]. The net polarisation (P) of the system is also calculated via,

$$P = \frac{1}{N_m} \sum_{i=1}^{N_m} \vec{b_i} \cdot \vec{n_b^+} \tag{2.31}$$

The average molecular tilt angle, ϕ, between the molecular $\vec{a}$ axes and smectic layer normal was computed using,

$$\cos\phi = \frac{1}{N_m} \sum_{i=1}^{N_m} |\vec{a_i} \cdot \vec{I}|, \tag{2.32}$$

where $\vec{I}$ is the layer normal. The layer normal is assumed to lie parallel to the Z-axis of the simulation cell, the local layer normal can be calculated as per the method outlined by Withers *et al.* [38]. To investigate the chirality of smectic or crystalline phases the chiral ordering parameter χ is calculated. This can be related to the angle of tilt (ϕ) and calculated as per equation 2.34.

$$\chi = \frac{1}{N_m} \sum_{i=1}^{N_m} \vec{a_i^z} \cdot \vec{c_i^z} \tag{2.33}$$

$$= \frac{1}{2} \sin 2\phi, \tag{2.34}$$

where $\vec{a_i^z}$ is the z-component of $\vec{a_i}$ and $\vec{c_i^z}$ is the z-component of $\vec{c_i}$.

Statistical errors upon the orientational order parameters and thermodynamic properties were calculated using block averaging as described in Appendix D.2 in Ref. [34] and in Refs. [33, 39].

CHAPTER 3

Apolar bent-core liquid crystals with attractive interactions[1]

In this chapter we shall investigate the effect of attractive interactions upon a system of composite soft sphere (CSS) molecules as shown in Fig. 3.1. The molecules interact via the full Lennard-Jones potential, which mimics attractive dispersion interactions. This approach may answer some of the key questions posed by these bent-core systems, such as the surprising chirality observed experimentally [18], and help identify useful structure-property relationships.

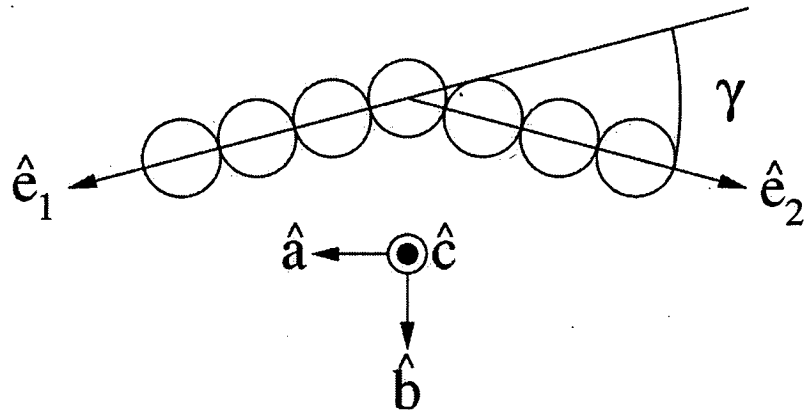

Figure 3.1: The composite of soft spheres model.

Hard particles, such as hard spherocylinders, are useful for studying liquid crystalline materials. It has been established that the structure of liquids is dominated by the packing of molecules (entropy). Hard particles provide a useful reference fluid for atomic systems and can be related to soft potentials via peturbatation

[1]This chapter is based upon 'Computer simulations of bent-core liquid crystals', A. Dewar and P.J. Camp, Phys. Rev. E, **70**, 011704, (2004)[40]

theory [31]. The phase behaviour of hard-spherocylinder dimers was studied in preliminary work by Camp *et al.* [26] and in greater depth by Lansac *et al.* [27]. In this latter work, isotropic, uniaxial nematic, paraelectric smectic-A, antiferroelectric smectic-A, paraelectric crystalline and antiferroelectric crystalline phases were found. In neither of these studies were tilted phases found.

Williamson and Jackson have studied the phase behaviour of linear hard sphere chains, composed of seven hard spheres. In this study the equation of state was obtained by compressing the isotropic fluid and expanding the crystalline phase. As well as the isotropic and crystal phases, nematic and smectic A liquid crystalline phases were observed. To alleviate the problem of molecules locking together, reptation moves were introduced, whereby the centre of mass is shifted by one diameter along the molecular axis [41].

Various continuous potentials have been studied to date, including Gay-Berne dimers [23, 24] and site-site models [29]. Memmer performed constant pressure Monte Carlo (NpT-MC) of Gay-Berne ellipsoid dimers with an external bond angle of $\gamma = 40°$ in a cuboidal simulation cell [23], which showed nematic and untilted antiferroelectric smectic phases. Neal *et al.* [24] performed NpT-MD simulations of a similar Gay-Berne model with varying bond angle in the range $0° \leq \gamma \leq 70°$. These simulations were performed in a cuboidal simulation cell with fixed aspect ratio . With $\gamma = 0°$ (linear dimers), isotropic, nematic, smectic-A and a smectic-B phases were found. With $\gamma = 10°$, the nematic phase is lost. At a bond angle of $\gamma = 20°$, the nematic phase is reinstated and smectic-B phase found. At $\gamma = 40°$ an interesting twisted grain boundary (TGB) phase was observed.

A simple site-site model composed of seven soft spheres interacting via a Weeks-Chandler-Anderson repulsive potential was studied by Xu *et al.* [29]. Xu *et al.* performed Monte Carlo simulations in the canonical (NVT) ensemble , utilising a cuboidal simulation cell of variable shape containing four smectic layers. Molecules were constructed with an external bond angle of $\gamma = 40°$. At such a bond angle Xu *et al.* observed tilted paraelectric crystalline and paraelectric smectic-A phases [29].

In this chapter we shall present simulation results of bent-core liquid crystals using the CSS model, shown in Fig. 3.1. The bent-core molecules as shown in Fig. 1.4 possess an external bond angle of $\gamma = 60°$. It must be noted that the real

molecules are not rigid, and that there are intramolecular rotations. These intramolecular rotations can affect the external bond angle significantly and in condensed phases, particular conformations may be thermodynamically favoured if they result in enhanced packing or interaction stability. The alkyl or alkoxy chains can influence the overall molecular elongation and hence the effective bend angle. Experimental measurements indicate that γ is usually in the range $20° - 40°$. With this in mind, we present simulation results of a family of model bent-core molecules.

3.1 Simulation techniques

We performed constant pressure, constant temperature Monte Carlo (NpT-MC) of N_m molecules in a cuboidial or cubic simulation cell with periodic boundary conditions applied [33, 34]. The sphere-sphere interatction potental is described by the $(12, 6)$ Lennard-Jones potential,

$$U_{ij}(r_{ij}) = \begin{cases} 4\epsilon \left[\left(\frac{\sigma}{r_{ij}}\right)^{12} - \left(\frac{\sigma}{r_{ij}}\right)^{6} \right] & r_{ij} \leq r_c \\ 0 & r_{ij} \geq r_c \end{cases}, \tag{3.1}$$

where r_{ij} is the pair separation, ϵ the potential well depth, σ the Lennard-Jones sphere diameter and r_c is the potential cut-off distance (2.5σ). In this study each molecule consists of seven Lennard-Jones spheres arranged in a rigid 'v' shape with the sphere-sphere distance set to a unit sphere diameter (1σ). This 7-sphere core of the model would represent the rigid bent-core of real molecules (c.f. Figure 1.4); for brevity we refer to these molecules as composite Lennard-Jones molecules (CLJMs).

In the simulations, one MC sweep consisted of one trial translation or one trial rotation per molecule and a single volume fluctuation. The rotation moves were performed using the Barker-Watts method as described in Sec. 2.2. Volume moves were carried out by sampling in $\ln V$ [33]. In the cuboidal simulations the dimension to be scaled (L_{xy} or L_z) was selected at random. Typically the CPU time for 400 MC sweeps (one simulation block) is approximately 600 seconds. For simulations investigating a possible phase transition between the ferroelectric and antiferroelectric phases one molecular 'flip' was attempted per molecule in addition to the standard translation, rotation and volume moves. This molecular 'flip' takes the mirror image of the vectors $\vec{e}_1$ and $\vec{e}_2$ in the plane of the

molecule, and repositions the apical sphere to the mid-point of the vector connecting ends of the arms of the molecule. All maximum displacement parameters for translation, rotations and volume fluctuations were adjusted to give respective acceptance ratios of 50%.

3.1.1 Starting configurations

For a typical starting configuration each layer was based upon a simple square lattice and then replicated in the z direction. The layer spacing was governed by the vectors $\vec{e}_1$ and $\vec{e}_2$. Molecules were aligned with the long axis ($\vec{a}_i$), as calculated via Eqn. 1.2, of the molecules parallel to the layer normal (Z-axis) and all the $\vec{b}_i$ axes (Eqn. 1.3), parallel to the Y-axis to maximise the uniaxial and biaxial order parameters.

To investigate the stability of a chiral ferroelectic phase, simulations were performed with molecules pre-tilted to the same degree (with given value of χ) and allowed to equilibrate from that point.

Upon generation of the initial configurations, these were allowed to equilibrate under constant volume (NVT) Monte Carlo simulations at $\rho^* = 0.14$, which corresponds to a sphere density of $\simeq 1.0$.

For each system, we performed sequences of simulations starting at high density ($\rho^* = 0.14$) at constant pressure, to ensure that the molecules tilted spontaneously, for bond angles $\gamma = 0°, 20°$ and $40°$. Once equilibrated, the temperature was raised until a transition to a homogeneous fluid phase (isotropic or nematic) was observed. We then switched over to a cubic simulation cell. Along with these heating runs, we also performed some cooling runs to verify the existence of a phase transition. At $\gamma = 40°$ simulations were also performed to investigate the relative mechanical stabilities of the ferroelectric and antiferroelectric phases and a chiral ferroelectric phase.

To ensure that the cuboidal simulations with bond angles $\gamma = 0°, 20°$ and $40°$, did not artificially stabilise the untilted solid or smectic phases, the pressure tensor, Π,was computed via,

$$\Pi = \left(\frac{N_m k_b T}{V}\right) I + \frac{1}{V} \sum_{i=1}^{N_m-1} \sum_{j>i}^{N_m} \sum_{k=1}^{N_s} \sum_{l=1}^{N_s} (\vec{r}_{ik} - \vec{r}_{jl}) f_{ijkl}, \tag{3.2}$$

where I is the second-rank unit tensor, f_{ijkl} is the force between the k^{th} sphere of the i^{th} molecule and the l^{th} sphere on the j^{th} molecule and $(\vec{r}_{ik} - \vec{r}_{jl})$ the corresponding sphere-sphere separation vector. In this case the force is given by,

$$f_{ijkl} = -\nabla_{r_{ij}} U(r_{ijkl}). \tag{3.3}$$

3.2 Simulation Results

3.2.1 Linear molecules, $\gamma = 0°$

The equation of state of linear ($\gamma = 0°$) CLJM's along an isobar with $p^* = 4.0$ is shown in Fig. 3.2. Snapshots of a final simulation configuration at a temperature of $T^* = 2.0$ (which correspond to the lowest branch of the equation of state) are shown in Figs. 3.3(a) and (b) These snapshots clearly show the crystalline ordering within each layer and that the layers are tilted with respect to the layer normal. This tilt ($\sim 14°$) has also been observed in calculations by Paolini *et al.* [30] of a soft-sphere model consisting of a linear chain of eleven spheres at low temperature. This molecular tilt was found to depend on the applied pressure [30]. This molecular tilt is also observed in the simulations of 3– and 5–Lennard-Jones sphere linear molecules by Galindo *et al.* [42].

In the calculations presented here, the average tilt angle, ϕ_f, is $\phi_f \simeq 35°$, which is indicative of the close-packing of the sphere within each layer as shown in Fig. 3.4. This tilt angle is comparable to the range of angles observed experimentally by x-ray diffraction methods, which lie in the range $24° - 26°$ [43], however in these simulations there is no overall global tilt direction. Rather the tilt directions alternate between layers giving rise to a racemic phase. At low temperatures, the diagonal elements of the pressure tensor, Π_{xx}, Π_{yy} and Π_{zz} which can be related to the pressure of the system. The root-mean-square fluctuations about p^* were found to be as high as $0.5\epsilon/\sigma^3$. This is thought to arise from the use of only four tilted layers, which results in large statistical fluctuations. It would be interesting to allow the simulation cell to tilt for low temperature simulation results as per the Parrinello-Rahman method [44, 45].

The low temperature phase is stable up to a temperature of $T^* = 3.0$, at which point a transition occurs to a state that persists over the range $3.5 \leq T^* \leq 5.0$, as shown by a distinct branch along the equation of state shown in Fig. 3.2. Snapshot representations of a simulation configuration at a temperature of $T^* = 4.0$

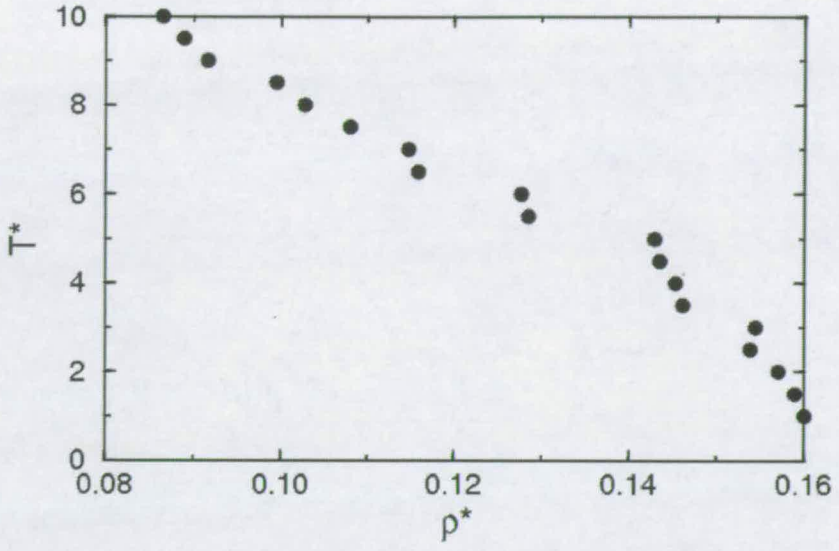

Figure 3.2: Equation of state for $\gamma = 0°$ with $p^* = 4.0$. The error bars are smaller than the symbol size.

are shown in Figs. 3.3(c) and (d), as obtained from heating from the low temperature phase. In order to evaluate whether this phase is a metastable state, a simulation cooling from a untilted smectic A phase ($T^* = 6.0, \rho^* = 0.128$) was performed in a cubic simulation cell, snapshots of which are shown in Figs. 3.3(e) and (f). After cooling the final equilibrium density was $\rho^* = 0.147$, which lies upon the same branch of the equation of state as obtained via heating simulations. Snapshots of the final configuration are shown in Figs. 3.3(g) and (h). It must be noted that the molecular tilt has reformed spontaneously and that the short-range ordering with a layer [Fig. 3.3(h)] is hexagonal, albeit with no long range ordering apparent, it must be noted that anomalous tilt is observed when cooling in cubic simulation cells [46]. This can also been seen by examination of a radial distribution plot, shown in Fig. 3.5. The split peak at $r/\sigma \simeq 2$ for $T^* = 4.0$ is indicative of hexagonal packing. Thus this phase has been assigned as a tilted smectic B phase, on account of this hexagonal ordering. The mean squared displacement ($\langle R^2 \rangle$) as calculated by Eqn. 2.24 is shown in Fig. 3.7 at $T^* = 4.0$ clearly shows an increase in the 'diffusion' constant as compared to the low temperature crystalline phase. With the low mean squared displacement at this temperature, we could also assign this as a solid phase as opposed to a tilted smectic B.

Heating further along this isobar, an untilted paraelectric smectic phase is found at temperatures of $T^* = 5.5$ and $T^* = 6.0$. Snapshot representations at a temperature of $T^* = 6.0$ are shown in Figs. 3.3(e) and (f). The in-layer structure of this

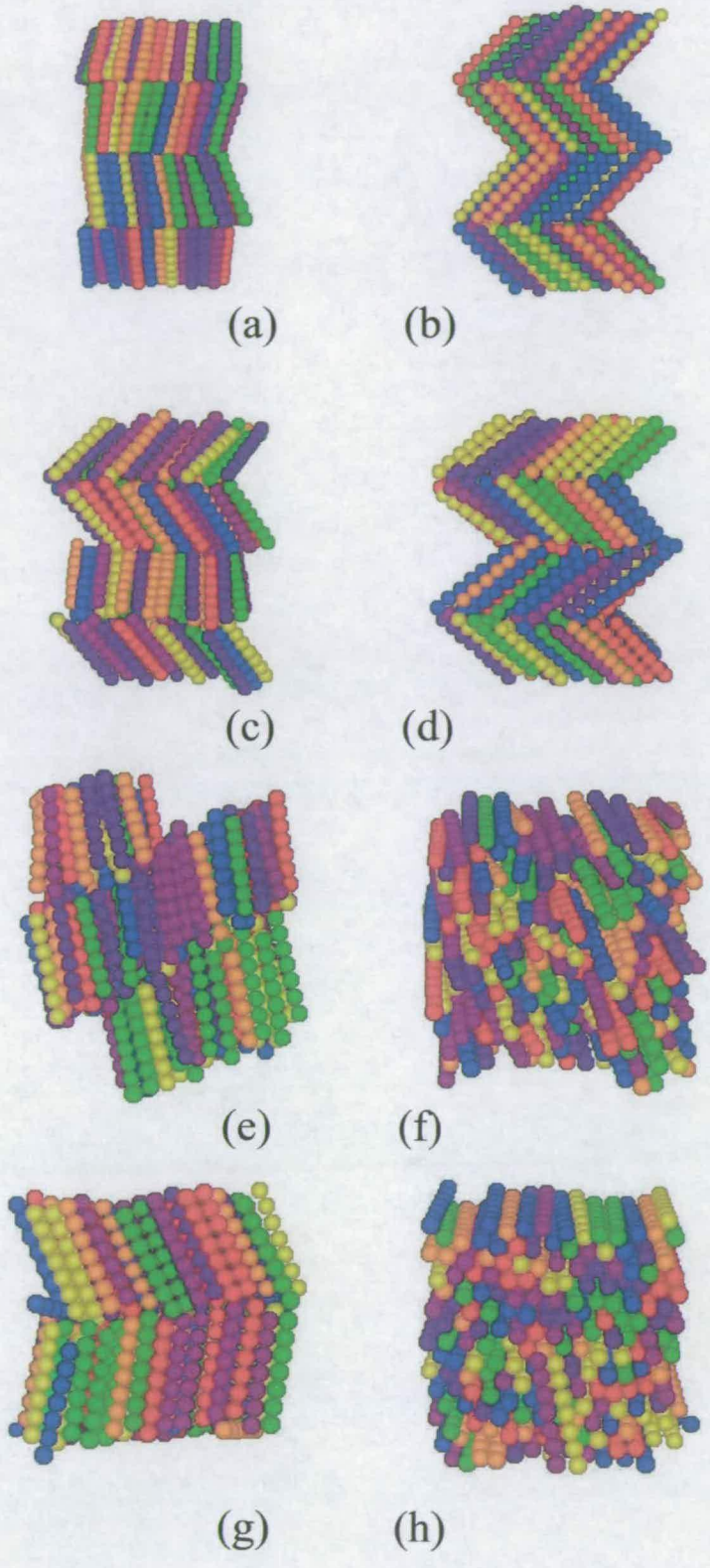

Figure 3.3: Snapshot representations of CLJM's with $\gamma = 0°$ along an isobar with $p^* = 4.0$: (a) and (b) crystalline phase at $T^* = 2.0$ (cuboidal cell); (c) and (d) tilted smectic B at $T^* = 4.0$ (cuboidal cell); (e) and (f) untilted smectic A at $T^* = 6.0$ (cubic cell); (g) and (h) tilted smectic B phase at $T^* = 4.0$ (cubic cell). Colours are assigned at random.

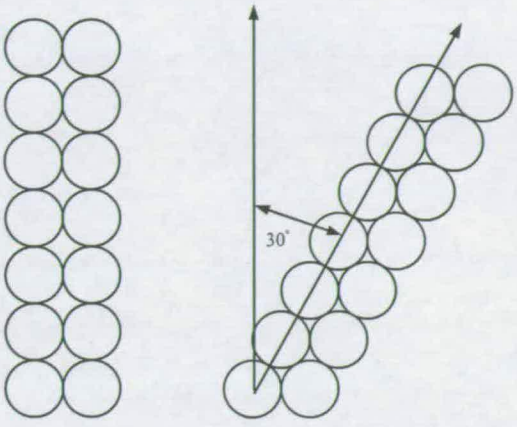

Figure 3.4: Diagramatic representation of the hexagonal close packing possible when molecules are tilted to $\sim 30°$.

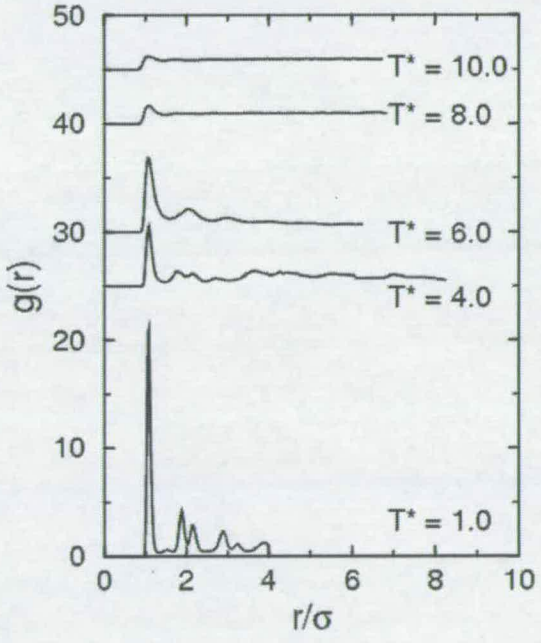

Figure 3.5: Radial distribution data of CLJM's with $\gamma = 0°$ along an isobar $p^* = 4.0$ for $T^* = 1.0, 4.0, 6.0, 8.0$ and 10.0. Plots have been displaced for clarity.

phases, as shown in Figs. 3.3(f) only displays short-range ordering, and hence this is a smectic A phase.

Above a temperature of $T^* = 6.5$, we find a uniaxial nematic phase over the range $6.5 \leq T^* \leq 8.5$, snapshots of which are shown in Figs. 3.6(a) and (b). Above a temperature of $T^* = 9.0$ the isotropic phase is found and a snapshots are shown in Figs. 3.6(c) and (d). A plot of $\langle R^2 \rangle$ as a function of MC cycles is shown in Fig. 3.7. The smectic-nematic phase transition is signified by an order of magnitude increase in the slope, hence 'diffusion' coefficient observed upon entering the nematic phase.

A useful method of evaluating the liquid crystalline phases found is to plot the nematic order parameter as a function of temperature along this isobar [35, 36], as shown in Fig. 3.8. The crossover from the tilted smectic and crystalline phases to the untilted phases can be clearly seen at $T^* \leq 5.0$. The values of Q^2_{00} are lower for the tilted phases than the nematic phase as the layers are not uniformly tilted. The nematic-isotropic phase transition is signalled by the drop in Q^2_{00} between $T^* = 8.5$ and $T^* = 9.0$

3.2.2 $\gamma = 20°$

With the introduction of the bend into the model molecules, we raise the possibility of forming chiral phases as discussed in section 1.1.1. The extent of the resultant chirality can be calculated via equation 2.34. Additional parameters, Q^2_{22}, the biaxial order parameter and P, the bulk polarisation, can be evaluated using Eqns. 2.30 and 2.31.

The equation of state for CLJM's with $\gamma = 20°$ heating along an isobar $p^* = 4.0$ is shown in Fig. 3.9. The simulation at $T^* = 3.5$ did not converge onto any of the branches of the equation of state. The snapshots are shown in Figs. 3.10(a) and (b). In these snapshots it can be seen that the molecules have adopted a herringbone type structure. This is likely to represent a metastable state. Free energy calculations would be necessary to support this assertion.

Snapshots of the final simulation configuration at a temperature of $T^* = 2.0$ are shown in Figs. 3.10(c) and (d). It can be clearly seen that the layers are tilted with respect to the layer normal, with $\phi_f \simeq 35°$ and the tilt direction alternating between adjacent layers. The polarisations within layers remain intact. The biaxial order parameter, Q^2_{22}, shown in Fig. 3.11(a) and the bulk polarisation, shown in

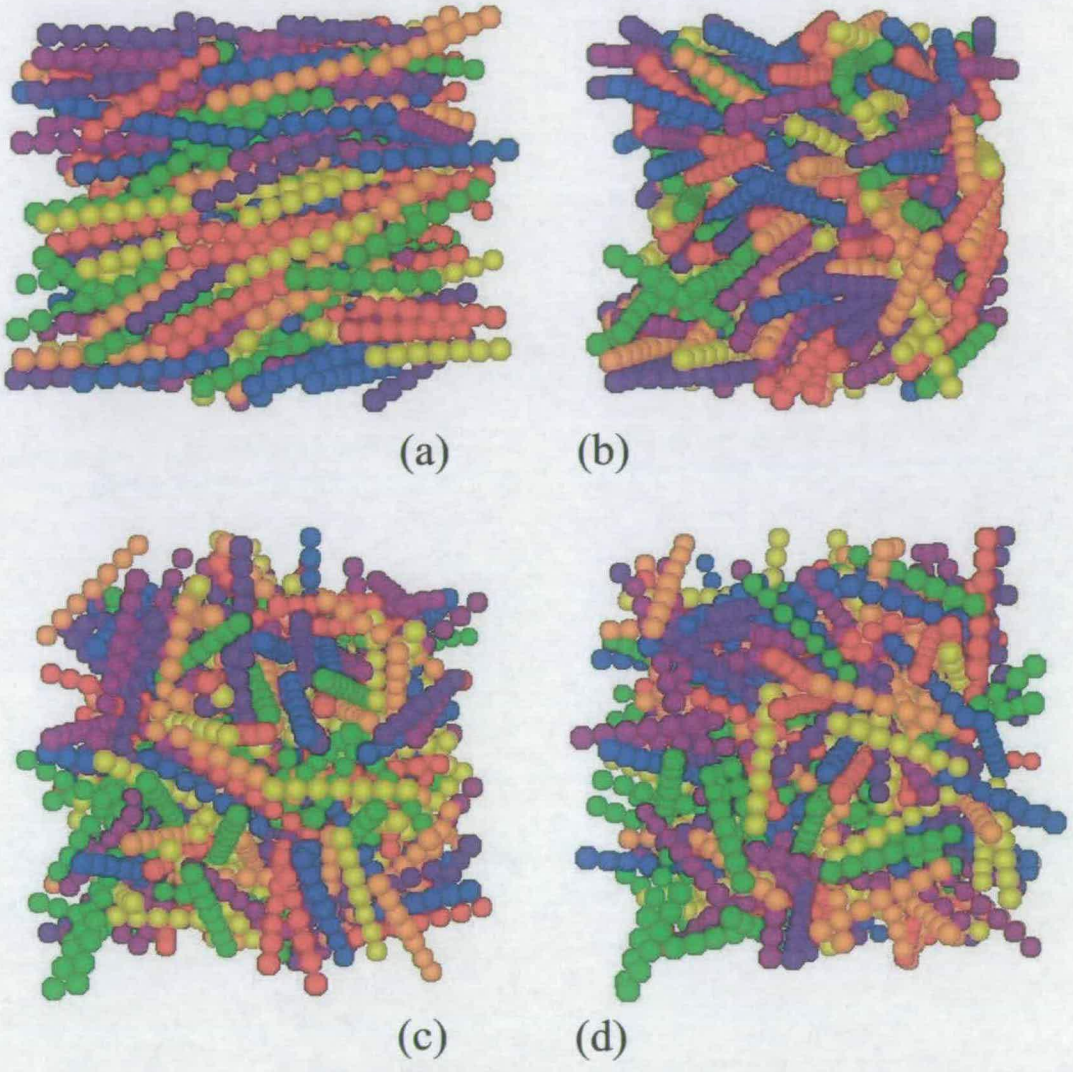

Figure 3.6: Snapshot representations of CLJM's with $\gamma = 0°$ along an isobar with $p^* = 4.0$: (a) and (b) uniaxial nematic phase at $T^* = 8.0$ (cubic cell); (c) and (d) isotropic phase at $T^* = 10.0$ (cuboidal cell).

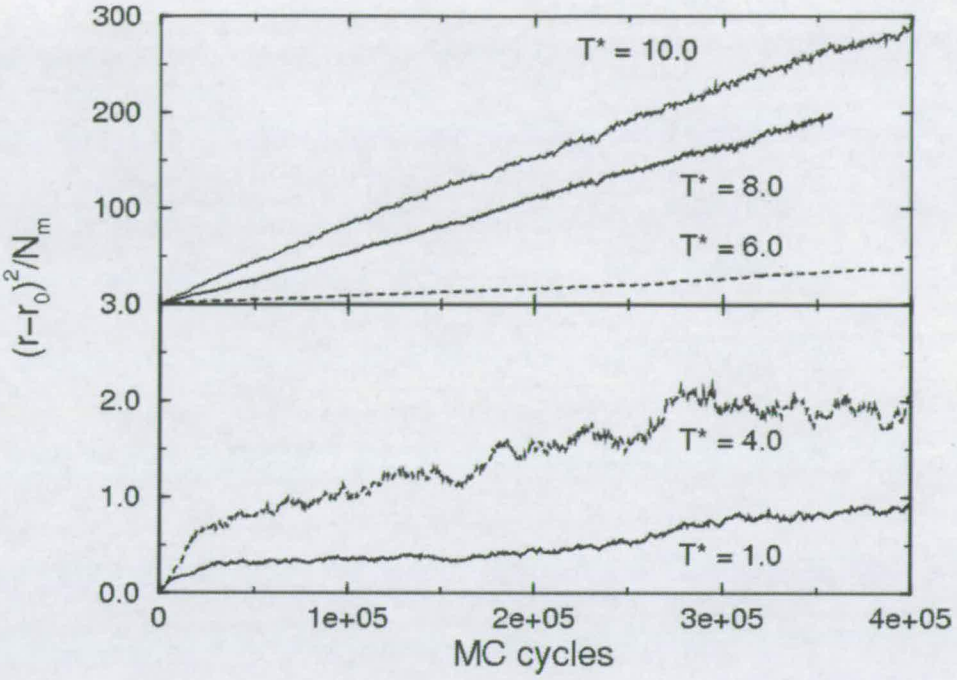

Figure 3.7: $\langle R^2 \rangle$ data for $\gamma = 0°$ with $p^* = 4.0$ and $T^* = 1.0$ (solid line), 4.0 (dashed line) and $T^* = 6.0$ (dashed line), 8.0 (solid line), 10.0 (dotted line).

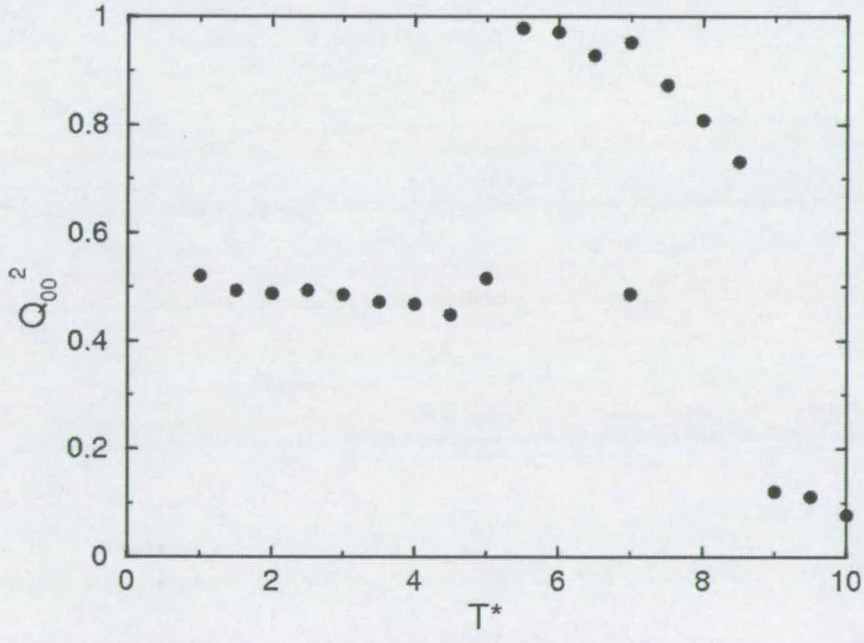

Figure 3.8: Uniaxial order parameter, Q_{00}^2, of CLJM's with $\gamma = 0°$ along an isobar with $p^* = 4.0$ plotted as a function of temperature. The error bars are smaller than the symbol size.

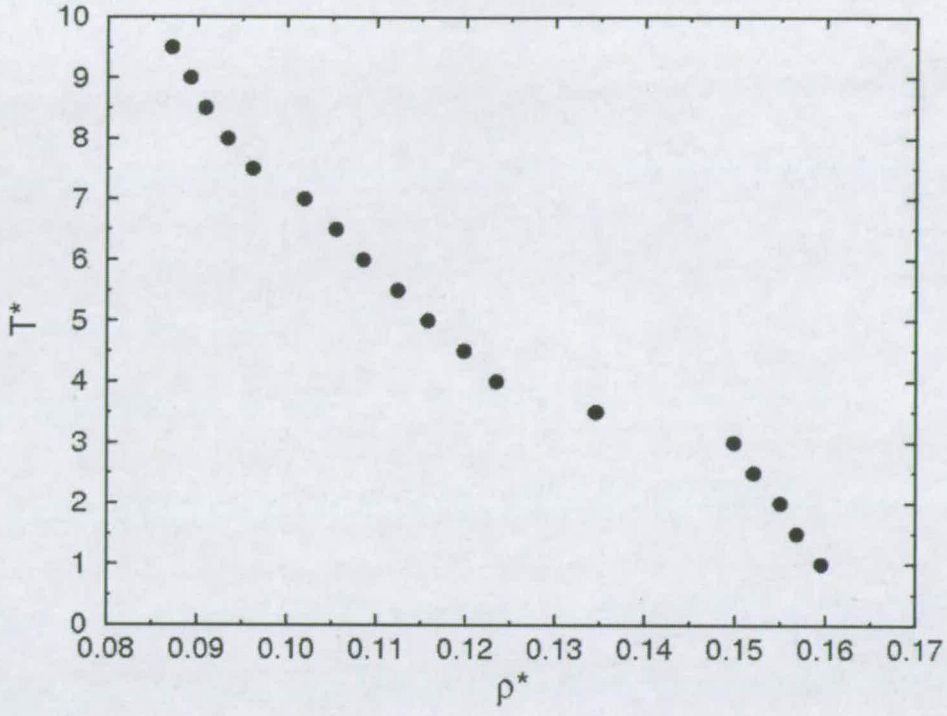

Figure 3.9: Equation of state for $\gamma = 20°$ with $p^* = 4.0$. The error bars are smaller than the symbol size.

Fig. 3.11(b) are both low, even at low temperature. This would indicate a low degree of correspondence between adjacent layers. As the layer polarisations are disordered, as shown by low bulk polarisation values and that the molecules themselves remain ordered within layers, we assign this as a superparaelectric phase. We do not find any ferroelectric or antiferroelectric phases. The values of the chiral ordering parameter [Fig.3.11(c)] are non-zero at low temperature suggesting a chiral phase, it remains to be seen if this is an artefact of the simulation as the layers appear to posses varying degrees of opposing molecular tilts. Figure 3.12 shows the in-layer radial distribution function, $g_{xy}(r)$, at $T^* = 2.0$. The second peak at $r/\sigma \simeq 2.0$ is split, which is indicative of short-range hexagonal ordering and is characteristic of a smectic B phase.

To investigate the smectic-nematic phase transition, a simulation cooling from a equilibrated nematic phase to a temperature of $T^* = 3.0$ was performed. Snapshot representations of a simulation configuration are shown in Figs. 3.10(e) and (f). The final equilibrium density was $\rho^* = 0.1325$, which does not lie on any of the branches already found on the equation of state upon heating. From the snapshot is is apparent that molecules have aligned in two domains, supported by

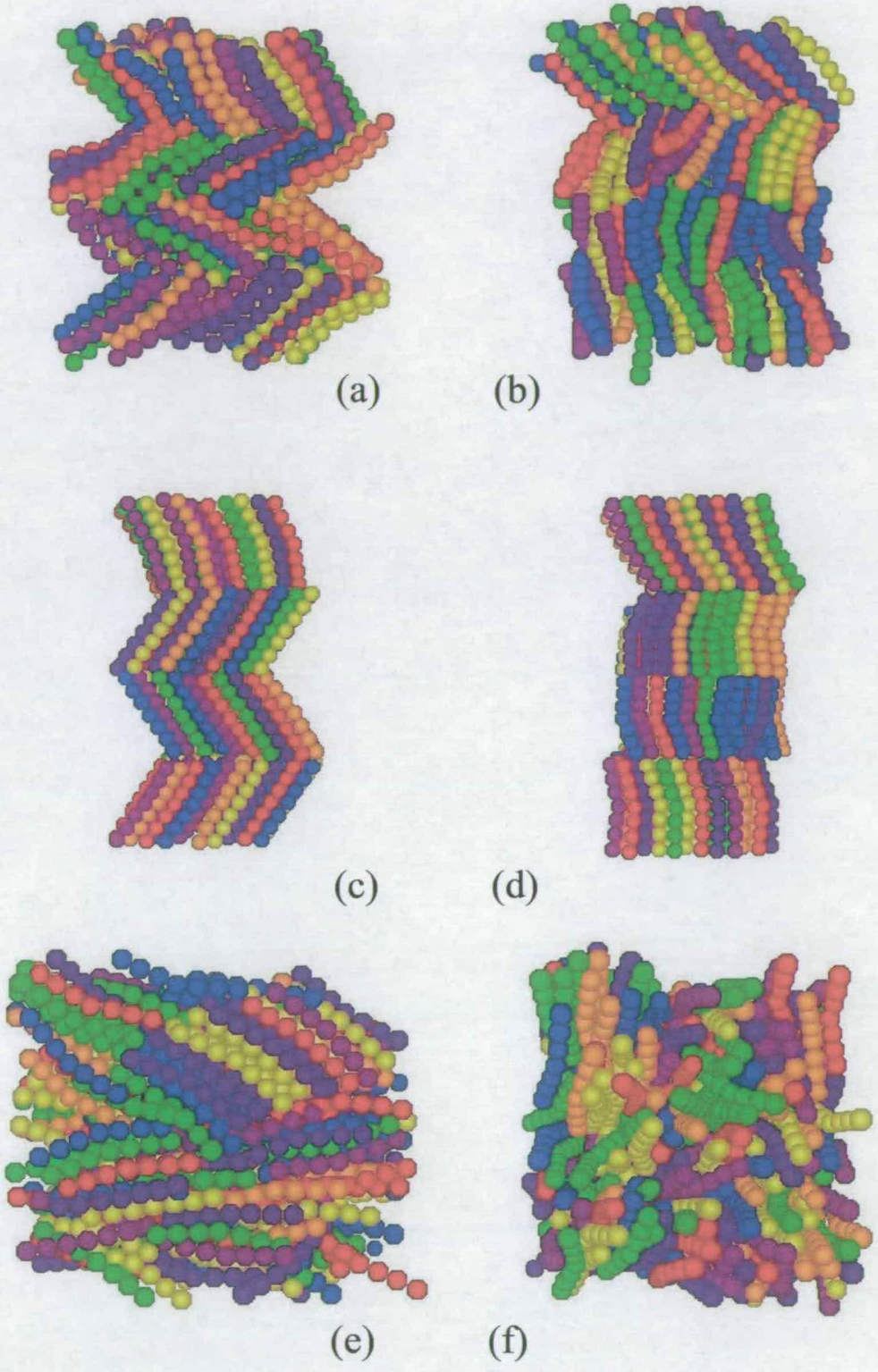

Figure 3.10: Snapshot representations of CLJM's with $\gamma = 20°$ along an isobar with $p^* = 4.0$: (a) and (b) 'herringbone' phase at $T^* = 3.5$ (cuboidal cell); (c) and (d) tilted smectic B at $T^* = 2.0$ (cuboidal cell); (e) and (f) glassy state at $T^* = 3.0$ (cubic cell).

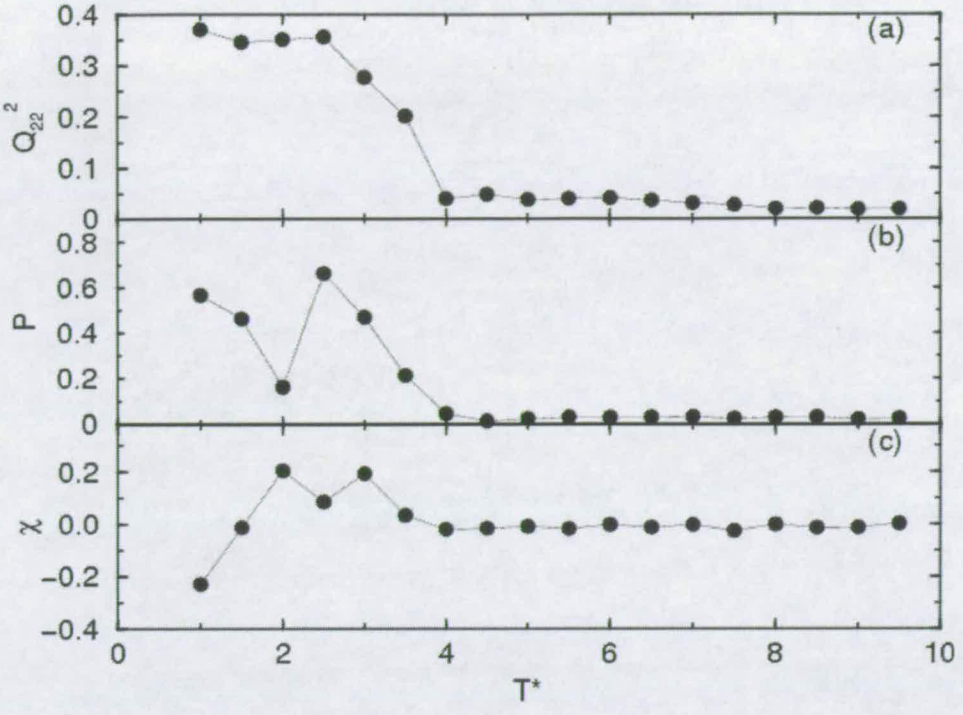

Figure 3.11: (a) Biaxial order parameter, Q_{22}^2, (b) bulk polarisation, P, and (c) chiral ordering parameter, χ, of CLJM's with $\gamma = 20°$ along an isobar with $p^* = 4.0$ plotted as a function of temperature. The error bars are smaller than the symbol size.

$Q_{00}^2 \simeq 0.8$, albeit with no layers present. As such this is likely to be a metastable, glassy state.

Heating further along the isobar yields a uniaxial nematic phase, and snapshots at a temperature of $T^* = 5.0$ are shown in Figs. 3.13(a) and (b). This nematic phase is stable over a wider range as that seen for $\gamma = 0°$, with $4.0 \leq T^* \leq 7.0$. Further heating along the isobar yield the isotropic phase, snapshots at $T^* = 8.0$ are shown in Figs. 3.13(c) and (d).

In Fig. 3.14, the uniaxial order parameter is plotted as a function of temperature along an isobar with $p^* = 4.0$. The nematic-isotropic phase transition is signalled by a drop in Q_{00}^2, over the range $7.0 \leq T^* \leq 7.5$. The smectic phases at $T^* < 3.0$, exhibit smaller values of Q_{00}^2, due to the random tilt directions of the layers [see Figs. 3.10(c) and (d)].

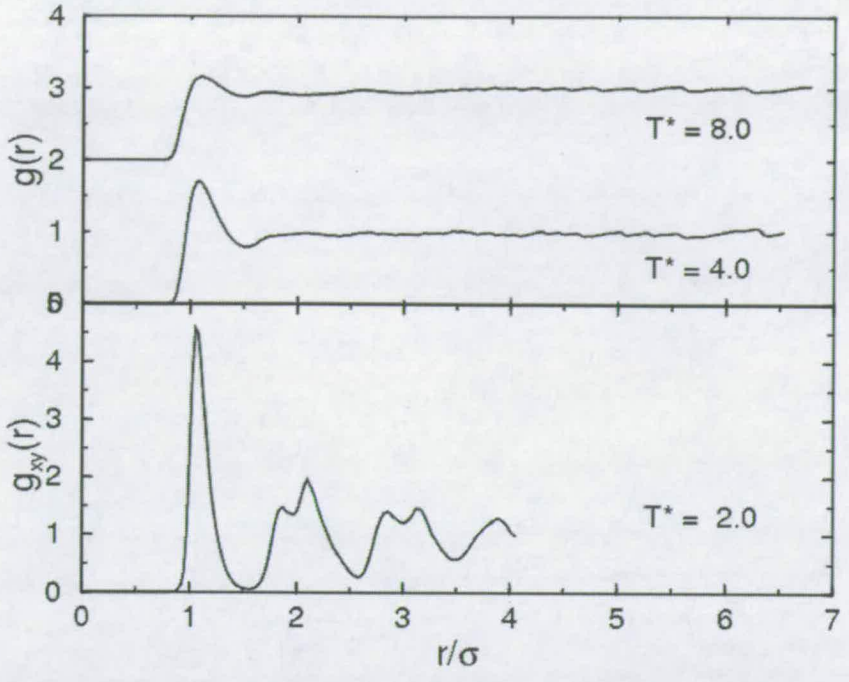

Figure 3.12: In-layer radial distribution data, $g_{xy}(r)$, of CLJM's with $\gamma = 20°$ along an isobar with $p^* = 4.0$ for $T^* = 2.0$ (lower plot) and radial distribution data $[g(r)]$ of CLJM's with $\gamma = 20°$ along an isobar with $p^* = 4.0$ for $T^* = 4.0, 8.0$ (upper plot). Plots have been displaced by two units for clarity.

3.2.3 $\gamma = 40°$

Equations of state for CLJM's with $\gamma = 40°$ along isobars $p^* = 0.5, 1.0, 2.0, 4.0$ are shown in Fig. 3.15. For the high density, low-temperature branch of the $p^* = 4.0$ isobar, two sets of results are presented; one sequence started from an untilted ferroelectric configuration (filled circles) and the other from a corresponding antiferroelectric configuration (unfilled circles). The equation of state does not give a clear indication as to which of the polarisation states is the more mechanically stable. The biaxial order parameter and the bulk polarisation [Figures 3.16(a) and 3.16(b) respectively] were seen to decay as the layers become uncorrelated. As such, we suggest that a superparaelectric phase is found, and that there is no thermodynamic driving force for the formation of a ferroelectric or antiferroelectric phases. As with previous isobars for $\gamma = 0°$ and $20°$, we observe a significant molecular tilt along all isobars, with $\phi_f \simeq 27°$. Which is comparable to experimental values as found by Zennyoij *et al.* [47].

Unlike Memmer [23] we find no evidence of any nematic phases along any of the isobars with such an extreme bond angle, nor do we find a twisted grain

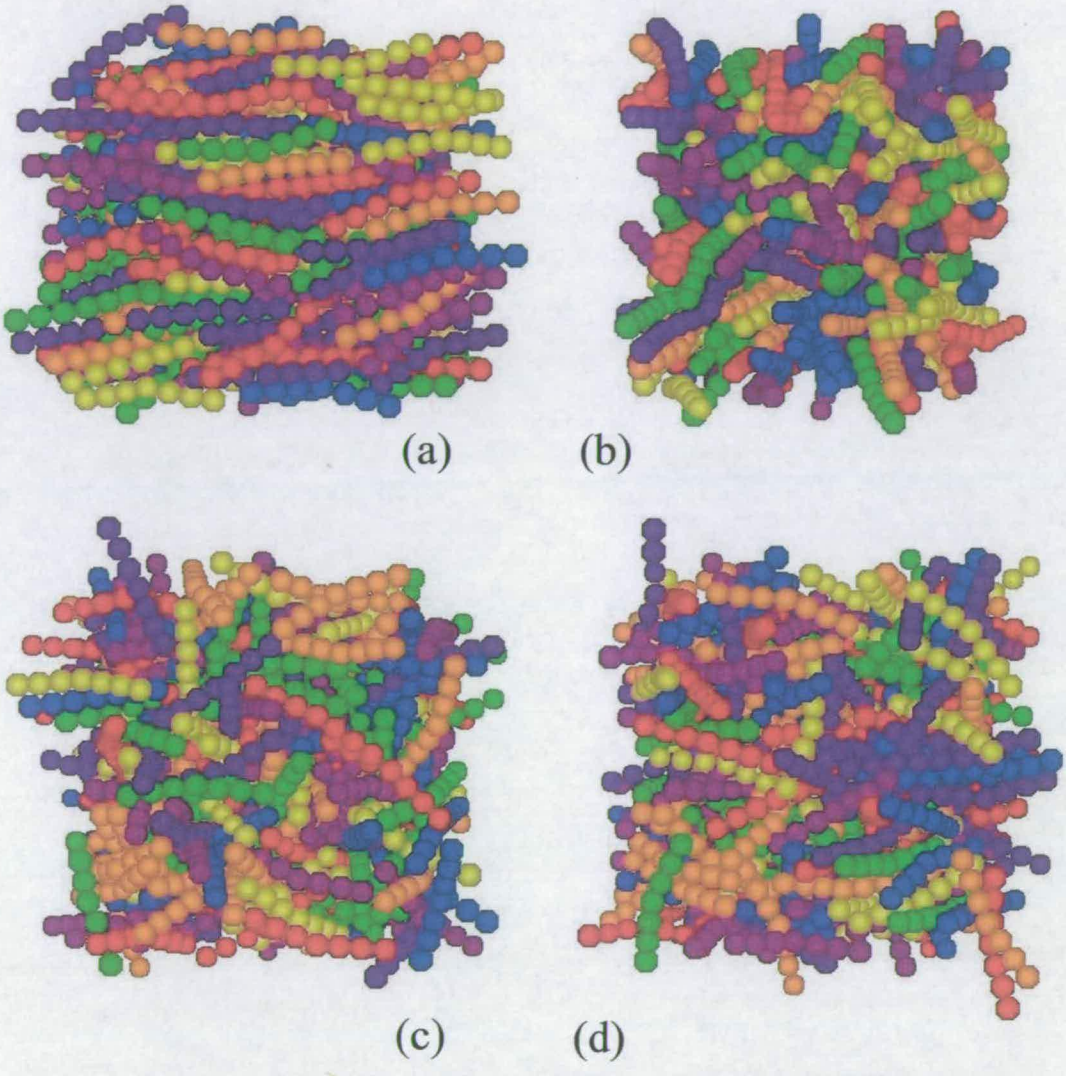

Figure 3.13: Snapshot representations of CLJM's with $\gamma = 20°$ along an isobar with $p^* = 4.0$: (a) and (b) uniaxial nematic phase at $T^* = 3.5$ (cubic cell); (c) and (d) isotropic phase at $T^* = 8.0$ (cubic cell).

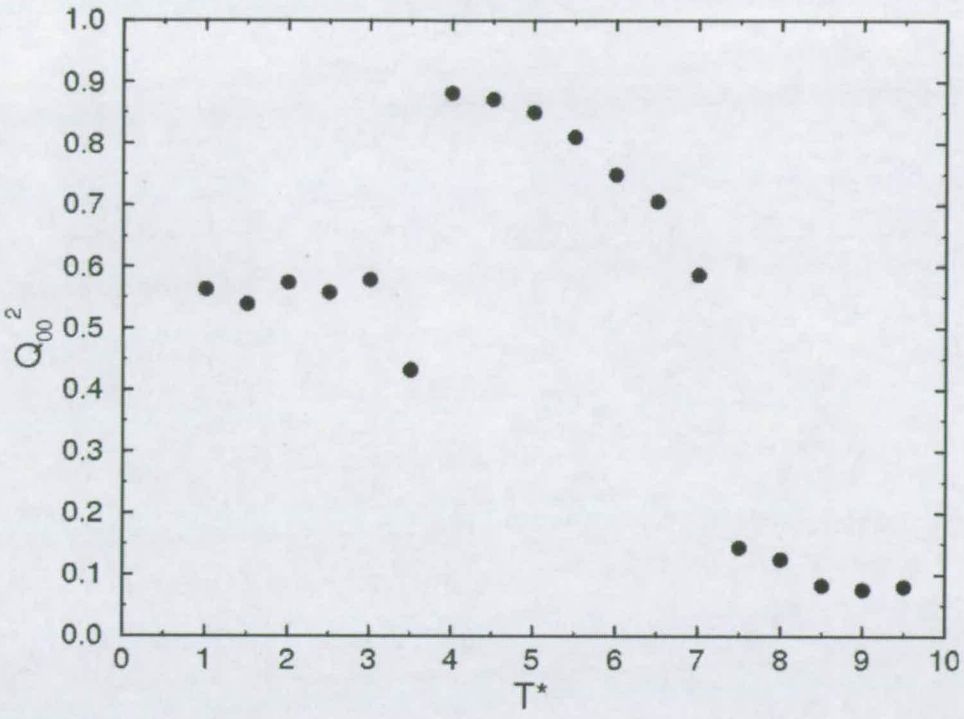

Figure 3.14: Uniaxial order parameter, Q_{00}^2, of CLJM's with $\gamma = 20°$ along an isobar with $p^* = 4.0$ plotted as a function of temperature. The error bars are smaller than the symbol size.

boundary phase as reported by Neal *et al.* [24] for this system. However, we do find subtle changes in the structural features of the tilted smectic phases, as shown by the in-layer radial distribution function, $g_{xy}(r)$, before finally "melting" to the isotropic phase. These are shown in Figs. 3.17(a)-(d) for the isobars $p^* = 0.5, 1.0, 2.0$ and 4.0, respectively. At low pressures, $p^* < 2.0$ the in-layer radial distribution at low temperatures all retain a split second peak, which is characteristic of a smectic B phase, which persists to the transition to the isotropic phase. However, at higher pressures ($p^* = 4.0$) a subtle change in the in-layer radial distribution is observed. At low temperature the in-layer distribution function is similar to those of smectic B phase already observed at lower pressures. At an intermediate temperature, $T^* = 4.5$ smectic A ordering is apparent and snapshot representations at this temperature are shown in Figs. 3.18(a) and (b). Hexatic smectic phases are a variant of the smectic B phase, where translational ordering persists over a longer length scale than in the smectic B phase.

Figure 3.19 shows the variation of the uniaxial order parameter as a function of temperature along isobars $p^* = 0.5, 1.0, 2.0$ and 4.0. The smectic-isotropic phase transition is clearly identifiable by a drop in Q_{00}^2 at; $T^* = 3.0 - 3.5$ for $p^* = 0.5$, $T^* = 3.5 - 4.0$ for $p^* = 1.0$ and $p^* = 2.0$, and $T^* = 4.5 - 5.0$ for $p^* = 4.0$.

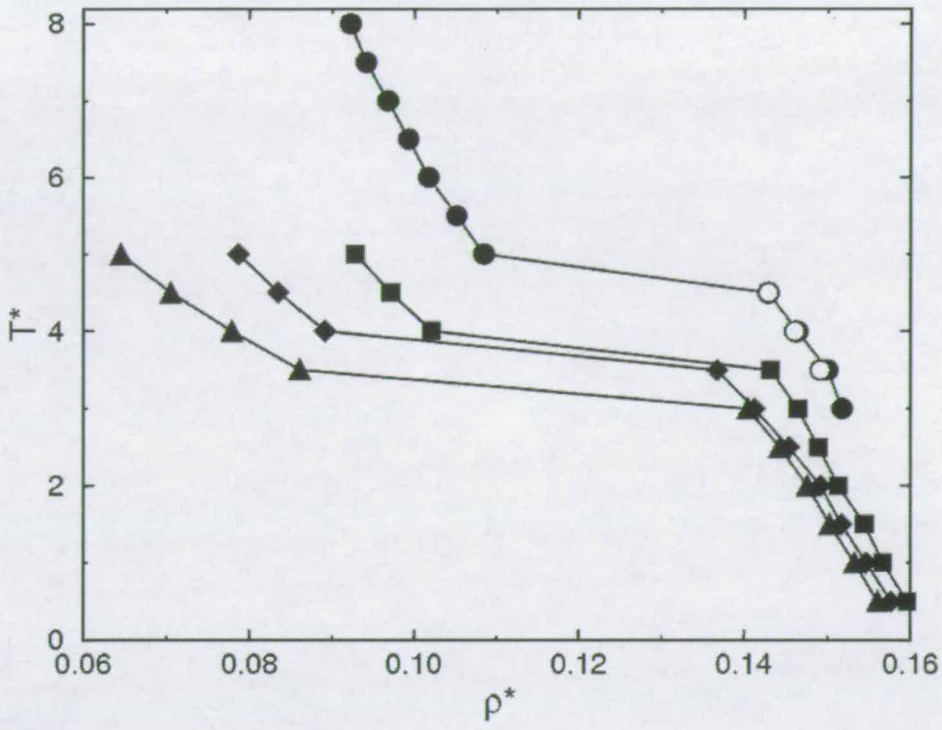

Figure 3.15: Equation of state for $\gamma = 40°$ with $p^* = 0.5$ (filled triangles), 1.0 (filled diamonds), 2.0 (filled squares) and 4.0 (filled circles). Unfilled circles denote results from from simulations starting from an antiferrolectric starting configuration. The error bars are smaller than the symbol size.

Cooling simulations

In order to investigate the smectic-isotropic phase transition further, we performed a series of cooling runs for isobars at $p^* = 1.0$ and $p^* = 2.0$. The equation of state for these simulations compared with the corresponding heating data is shown in Fig. 3.20. State points below $T^* = 4.0$ form a low temperature extension to the isotropic branch. The uniaxial order parameter for these state points are all below $Q_{00}^2 \simeq 0.1$, which is indicative of the isotropic phase, thus indicating that a metastable phase has been formed. Snapshots for the lowest temperature state points on both isobars $p^* = 1.0$ and $p^* = 2.0$ are shown in Figs. 3.21(a) and (b) and 3.21(c) and (d) respectively. This metastable state may arise as a result of interlocking dimers that form as a consequence of the "bumpy" nature of the molecular model used in this work [26].

Chiral simulations

Simulations started from a untilted configuration developed random molecular tilts. To investigate the relative mechanical stabilities of a uniformly tilted phase

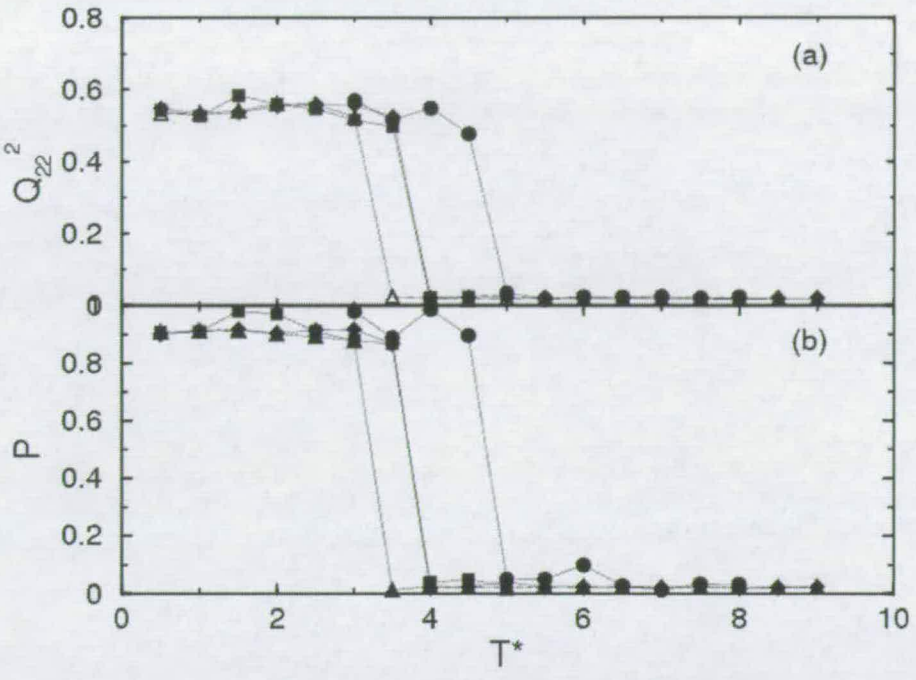

Figure 3.16: (a) Biaxial order parameter, Q_{22}^2, and (b) bulk polarisation, P, of CLJM's with $\gamma = 40°$ along isobars with $p^* = 0.5$ (filled triangles), 1.0 (filled diamonds), 2.0 (filled squares) and 4.0 (filled circles) plotted as a function of temperature. The error bars are smaller than the symbol size.

and a randomly tilted phase, we performed simulations from a uniformly tilted configuration with $\phi_i = 25°$. The equation of state for $\gamma = 40°$ with $p^* = 2.0$ is shown in Fig. 3.22 for both the untilted and tilted starting configurations. From this it can be seen that the smectic-isotropic phase transition for the pre-tilted simulations is at higher temperature than the randomly tilted system. This extra mechanical stability may be a result of the increased interdigitation possible between neighbouring layers in the uniformly tilted phase. Although this uniformly tilted phase appears to be more mechanically stable, free energy calculations for these systems are necessary to assess the true thermodynamically stable state. As with the randomly tilted phases, there is a significant molecular tilt, with the final molecular tilt, $\phi_f = 32°$. To ensure that simulations were unbiased by the choice of the starting tilt angle, simulations were performed with a alternate starting tilt of 40° and yielded a final molecular tilt of $\phi_f = 33°$. Figure 3.23, shows the chiral order parameter, χ as a function of temperature, clearly showing the racemic (randomly tilted) and a chiral (uniformly tilted) phases. A typical chiral phase can be seen in Figs. 3.24(a) and (b).

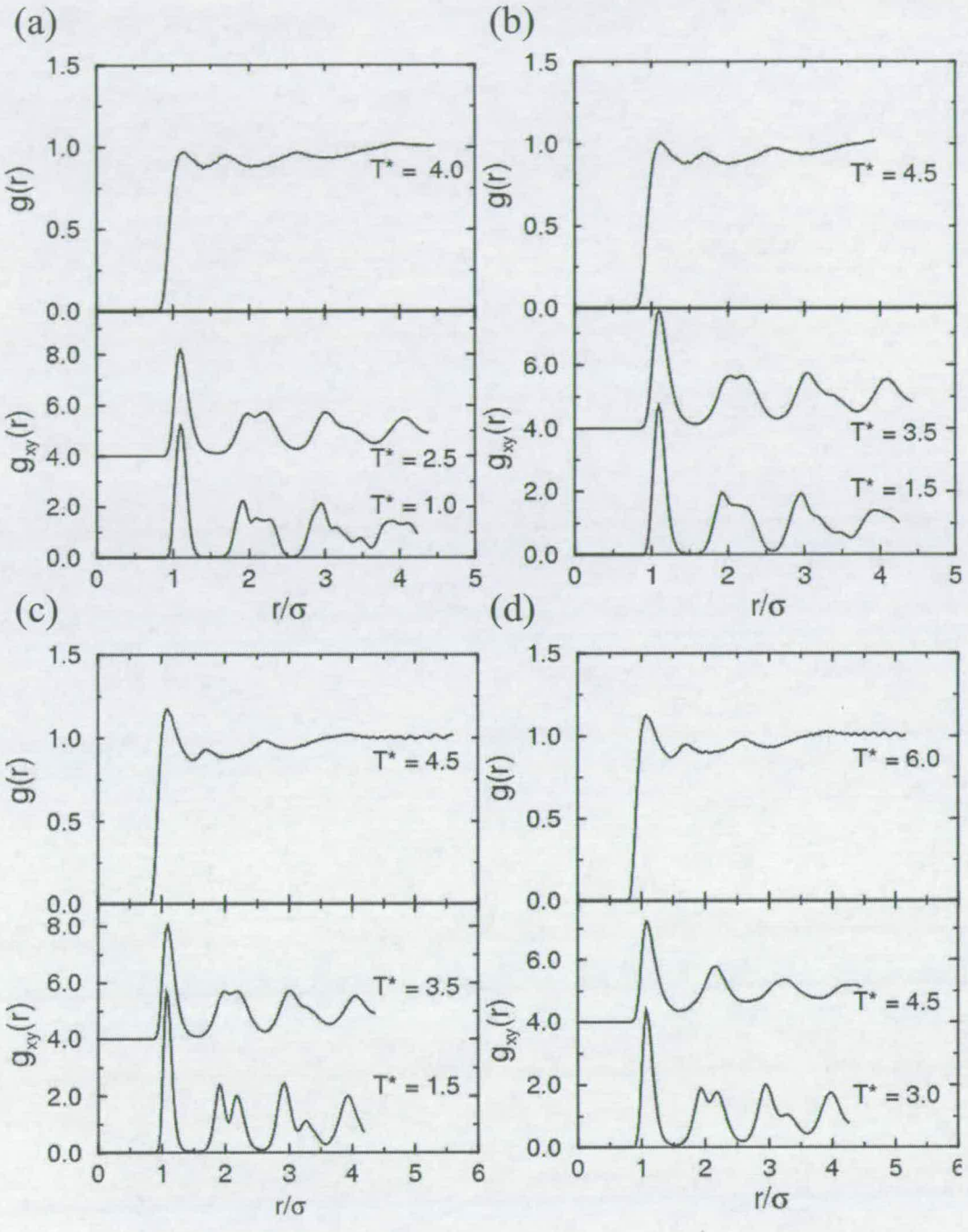

Figure 3.17: In layer and normal radial distribution data of CLJM's with $\gamma = 40°$: (a) along an isobar with $p^* = 0.5$ for $T^* = 1.0, 2.5$ (lower plot) and $T^* = 4.0$ (upper plot); (b) along an isobar with $p^* = 1.0$ for $T^* = 1.0, 3.5$ (lower plot) and $T^* = 4.5$ (upper plot); (c) along an isobar with $p^* = 2.0$ for $T^* = 1.5, 3.5$ (lower plot) and $T^* = 4.5$ (upper plot); (d) along an isobar with $p^* = 4.0$ for $T^* = 3.0, 4.5$ (lower plot) and $T^* = 6.0$ (upper plot). Plots have been displaced four units for clarity.

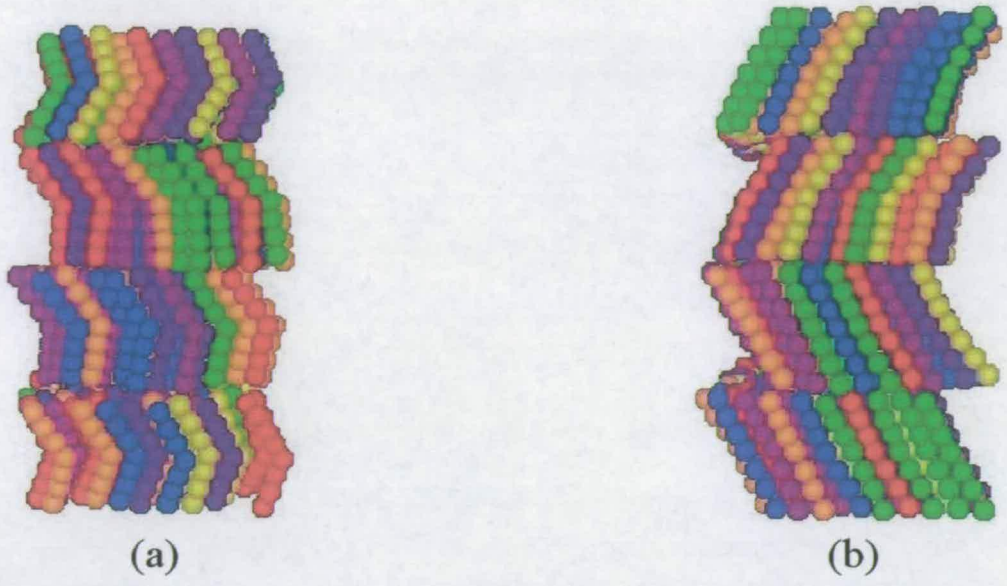

Figure 3.18: Snapshot representations of CLJM's with $\gamma = 40°$ along an isobar with $p^* = 4.0$: (a) and (b) racemic smectic A at $T^* = 4.5$ (cuboidal cell).

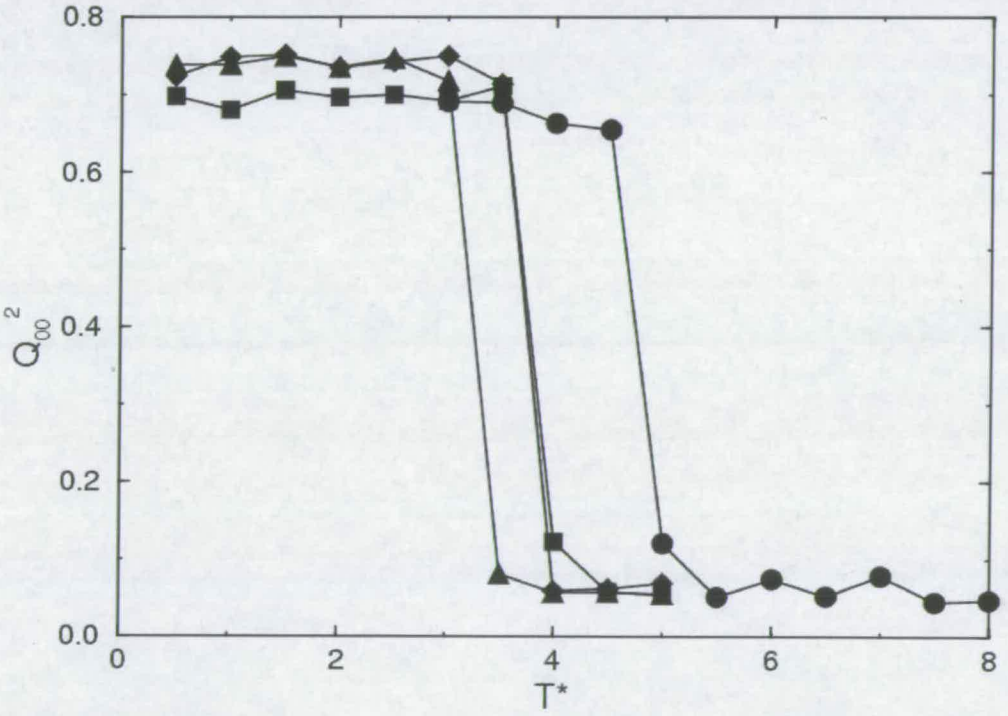

Figure 3.19: Uniaxial order parameter, Q_{00}^2, of CLJM's with $\gamma = 40°$ along isobars with $p^* = 0.5$ (filled triangles), 1.0 (filled diamonds), 2.0 (filled squares) and 4.0 (filled circles) plotted as a function of temperature. The error bars are smaller than the symbol size.

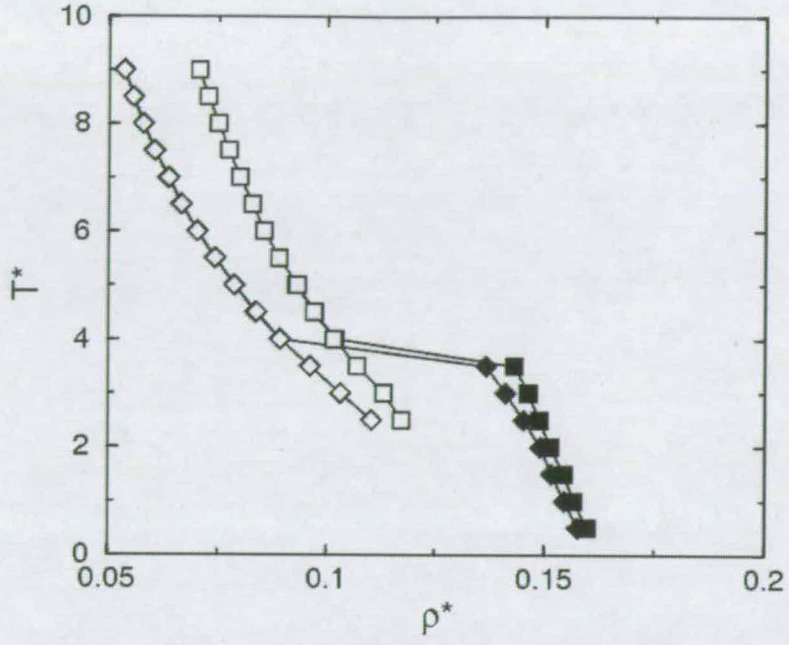

Figure 3.20: Equation of state for $\gamma = 40°$ with $p^* = 1.0, 2.0$. Filled symbols arise from heating simulations and unfilled from cooling simulations. The error bars are smaller than the symbol size.

3.2.4 $\gamma = 60°$

This bond angle represents the rigid bond-angle of the bent-core molecules. Equations of state for CLJM's with $\gamma = 60°$ along isobars $p^* = 2.0$ and 4.0 are shown in Fig. 3.25. The equation of state displays two distinct branches for both isobars. Values of the uniaxial order parameter, Q_{00}^2 are close to a value of 1, which would suggest a crystalline phase at low temperatures. Examination of appropriate snapshots at $T^* = 5.0$ and $p^* = 4.0$, shown in Figs. 3.26(a) and (b) also reveal a highly ordered phase. The molecules are tilted, but interestingly, this tilt is non-uniform within each layer, which may be a result of packing within the layers. Above $T^* = 4.0$ and $T^* = 6.0$ for $p^* = 2.0$ and 4.0 respectively, the solid melts to an isotropic fluid. With $\gamma = 60°$, Lansac *et al.* [27] found a polarised smectic A phase, which is not found in this work. We suggest that the attractive tail of the Lennard-Jones potential coupled with the shortened effective elongation of the model molecules below some critical length precludes the formation of liquid crystalline phases.

Although not directly relevant to the focus of this work, some interesting phase behaviour was observed at low pressure and temperature. A snapshot of this

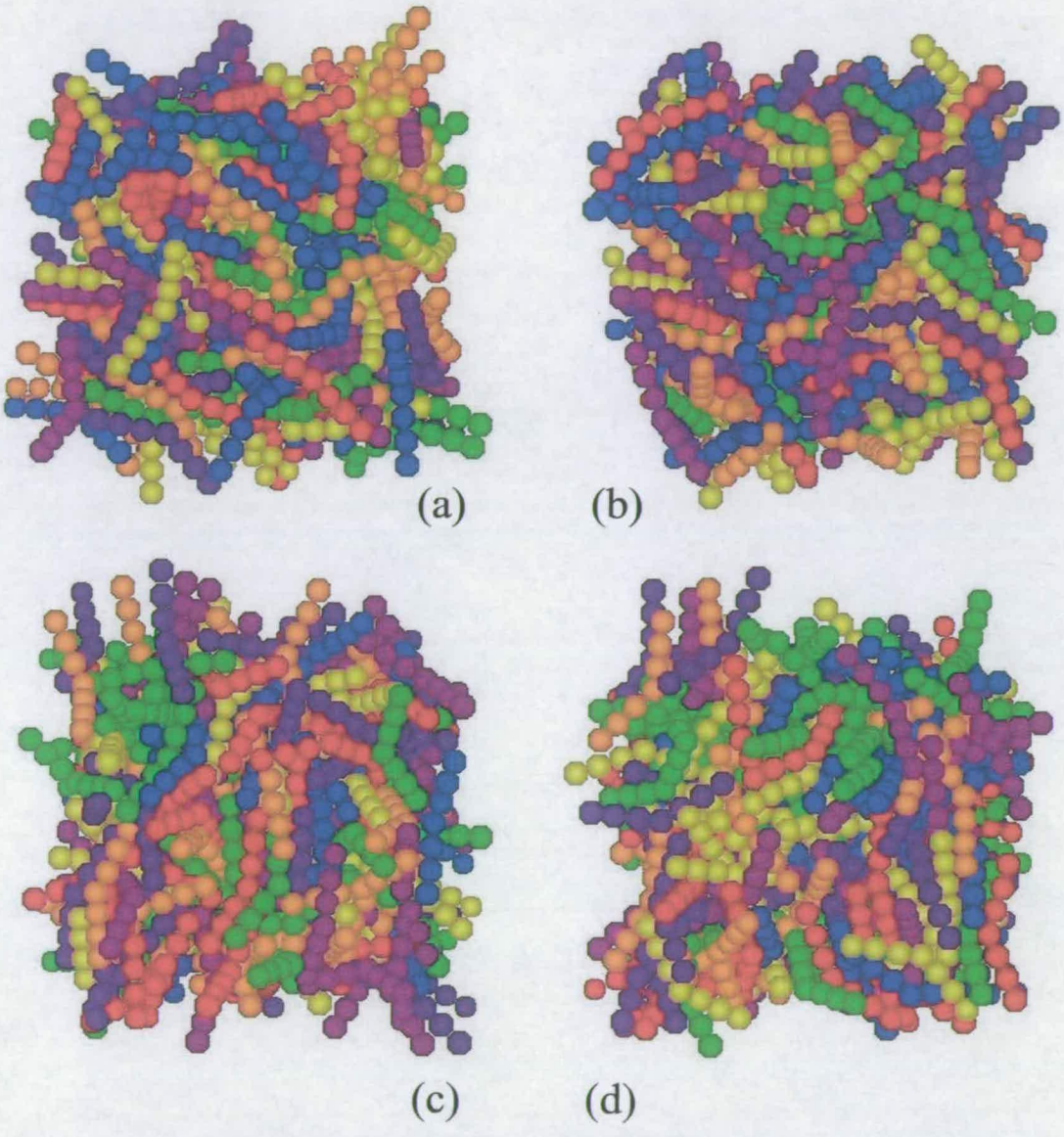

Figure 3.21: Snapshot representations of CLJM's with $\gamma = 40°$: (a) and (b) cooling from an equilibriated isotropic phase with $p^* = 1.0$ (cubic cell); (c) and (d) cooling from an equilibriated isotropic phase with $p^* = 2.0$ (cubic cell).

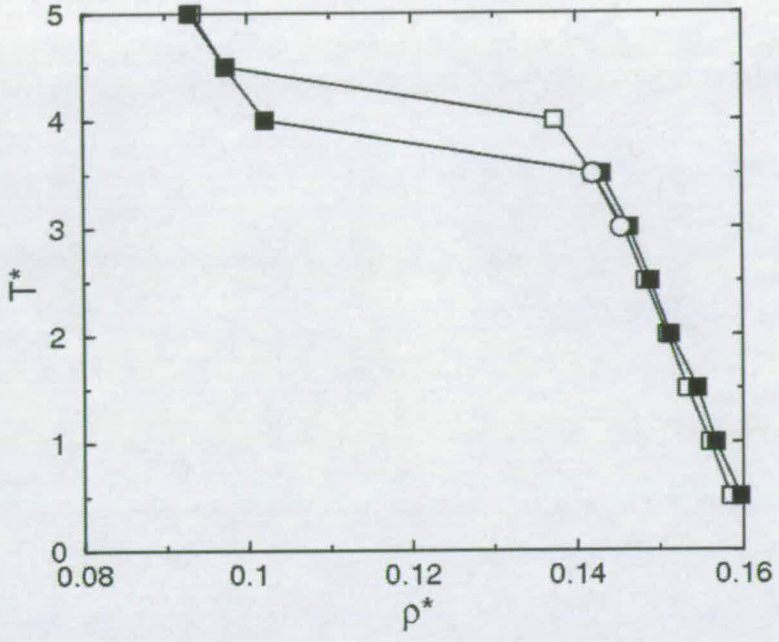

Figure 3.22: Equation of state for $\gamma = 40°$ with $p^* = 2.0$. Filled symbols arise from heating simulations and unfilled from simulations with uniform tilt. The error bars are smaller than the symbol size.

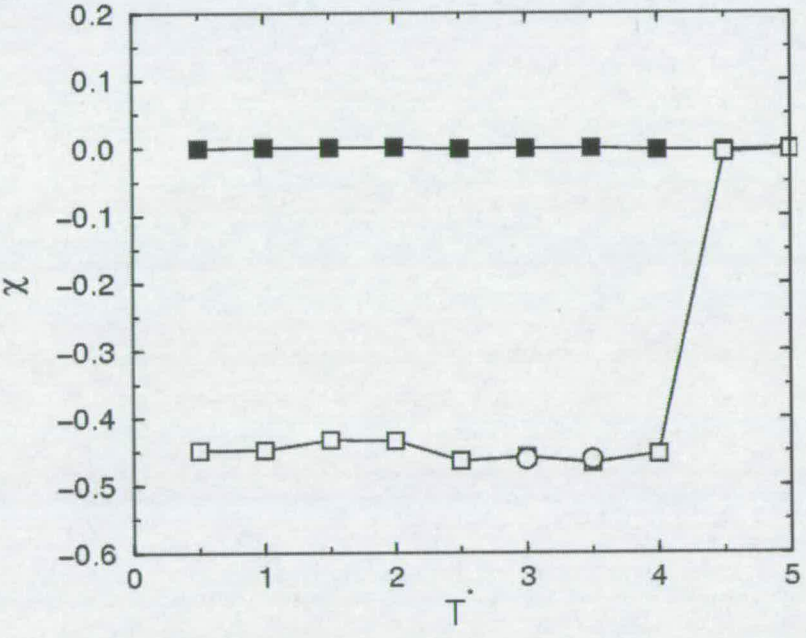

Figure 3.23: Chiral order parameter, χ, of CLJM's with $\gamma = 40.°$ along an isobar with $p^* = 2.0$ plotted as a function of temperature for randomly tilted molecules (filled squares) and pre-tilted molecules with $\phi = 25°$ (open squares) and $\phi = 40°$ (open circles). The error bars are smaller than the symbol size.

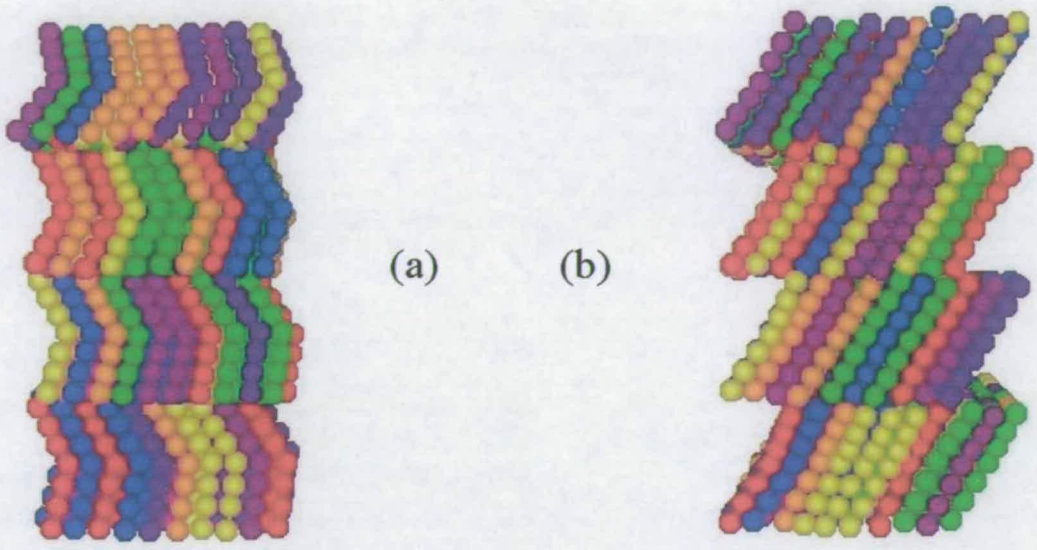

Figure 3.24: Snapshot representations of CLJM's with $\gamma = 40°$ along an isobar with $p^* = 2.0$: (a) and (b) chiral (uniformly tilted) phase at $T^* = 1.5$ (cuboidal cell).

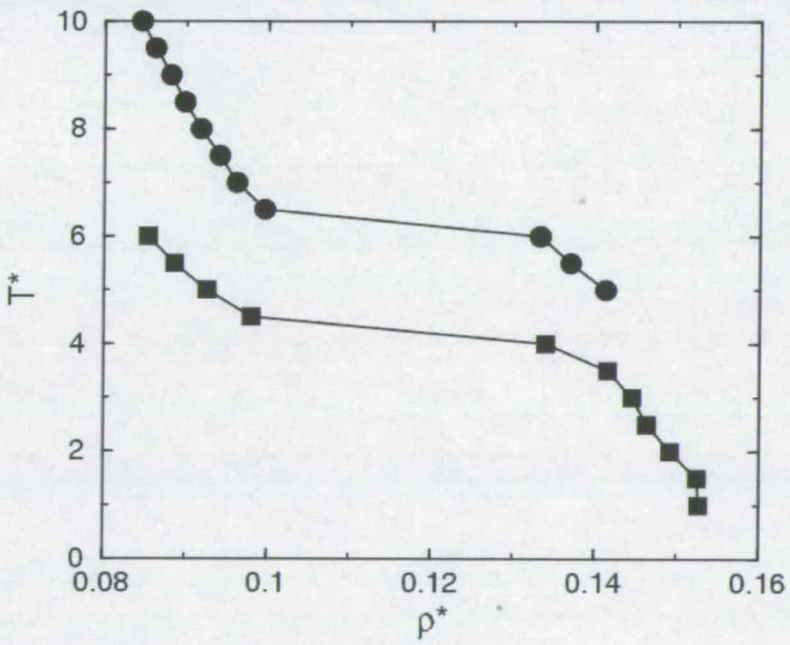

Figure 3.25: Equation of state for $\gamma = 60°$ with $p^* = 2.0$ (filled squares) and $p^* = 4.0$ (filled circles). The error bars are smaller than the symbol size.

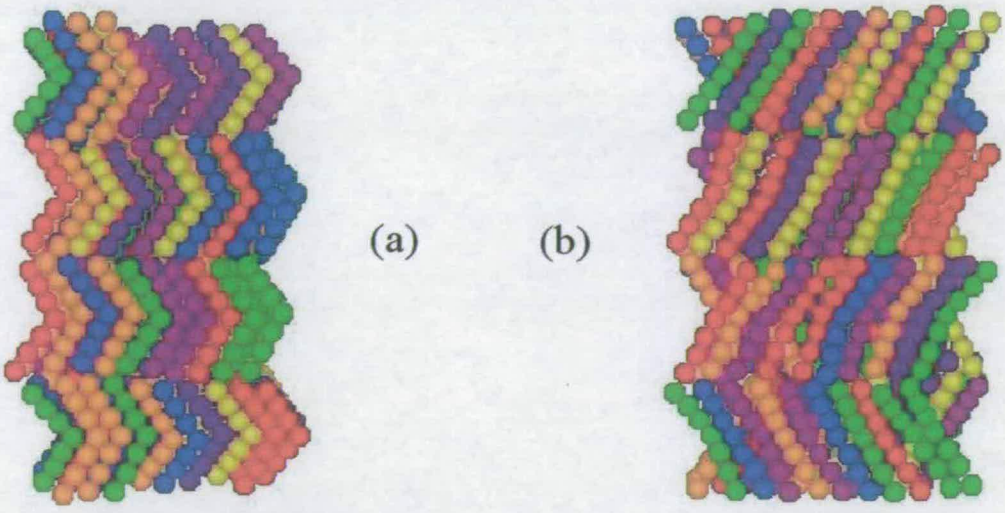

Figure 3.26: Snapshot representations of CLJM's with $\gamma = 60°$ along an isobar with $p^* = 4.0$: (a) and (b) at $T^* = 5.0$ (cuboidal cell).

phase at $T^* = 1.0$ and $p^* = 0.02$ is shown in Fig. 3.27. Molecules have clustered together under these conditions, where a low density gas would be anticipated. Under these conditions the average molecule-molecule attractive energy is $-27.92(8)k_bT$, which is sufficient for formation of clusters.

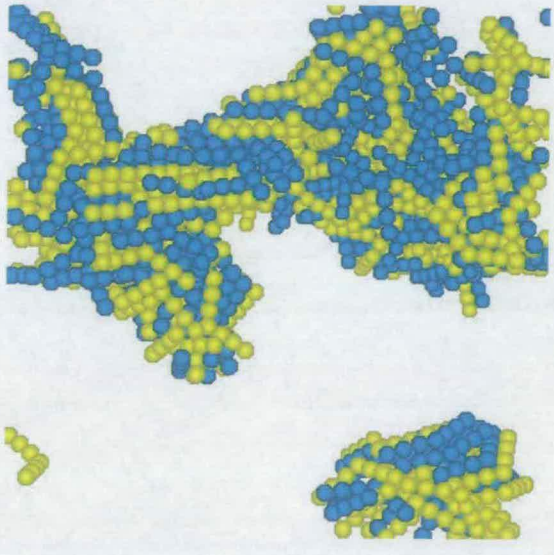

Figure 3.27: Snapshot representation of CLJM's with $\gamma = 60°$ with $p^* = 0.02$ and $T^* = 1.0$.

3.3 Conclusions

In this chapter we have presented results from constant-pressure Monte Carlo simulations of model bent-core molecules (CLJM's) composed of seven Lennard-

Jones spheres arranged in a rigid 'v' shaped molecule with given external bond angle, γ. The phase behaviour of CLJM's has been studied as a function of γ.

With $\gamma = 0°$ (linear molecules), this work has found isotropic, uniaxial nematic, untilted smectic A, tilted smectic B and crystalline phases. These tilted phases possess a molecular tilt of around 35° with respect to the layer normal, which supports the assertion by Xu *et al.* [29] that tilted smectic layers are stabilised for this simple site-site model. The phase behaviour is also consistent with previous work with linear molecules composed of eleven soft spheres (with purely repulsive interactions only) [30] with the exception of the smectic B phase. This tilted smectic B phase merits further investigation, perhaps with the use of free-energy calculations to assess the thermodynamic stability of such a phase.

For the system with $\gamma = 20°$, we find isotropic, nematic and tilted smectic B phases. The range over which the nematic phase is found is enhanced with respect to that found for $\gamma = 0°$, albeit with the loss of the untilted smectic A phase. Again the molecular tilt found in the smectic B phase was found to be about 35° with respect to the layer normal.

With $\gamma = 40°$, the nematic phase is no longer present, with only the isotropic and tilted smectic phases present. At high pressure, the tilted smectic phase exhibited smectic A ordering at high temperature and smectic B at low temperature, with a molecular tilt of 27° with respect to the layer normal.

Cooling of a fully equilibriated isotropic phase to a temperature below the smectic-isotropic phase transition yielded a metastable state with low uniaxial order parameter, Q^2_{00}. This phase may be a result of the "bumpy" nature of our model molecules, with spheres on neighbouring molecules taking advantage of favourable interactions thus forming an interlocking dimer unit.

For $\gamma = 60°$, we only find isotropic and crystalline phases. With the large external bond angle in this case, the effective molecular elongation is about 1σ less than when $\gamma = 0°$. This reduction in elongation is likely to be a major factor in the loss of orientationally ordered phases.

In none of the systems did we find any truly chiral phases, whether they be synclinic ferroelectric or anticlinic antiferroelectric. In simulations with $\gamma = 40°$, starting from ferroelectric and antiferroelectric configurations, the molecular tilt formed spontaneously, however the overall biaxiality did not persist for the duration of the simulation runs. Simulations starting from a chiral configuration

exhibited a molecular tilt similar to the racemic systems with the equation of state suggesting that the uniformly tilted (chiral) phase is more mechanically stable than the randomly tilted (racemic) phase, possibly due to the increased interdigitation possible between adjacent layers. Free-energy calculations, perhaps utilising umbrella sampling, would be required to investigate whether this is the case. The range of values for the molecular tilt observed in simulations ($\phi_f = 27° - 35°$) compares favourably with experimental observations ($\phi = 24° - 34°$) [43, 47]. A molecular tilt within the range specified may be ascribed to the increase in favourable attractive interactions on neighbouring molecules when the molecules tilt to $\sim 30°$. A tilt $> 30°$ may increase these favourable interactions, with the layers interdigitating which would reduce the configurational entropy of the system. The tilt angle observed is likely to represent the optimal balance of energy and entropy [48, 49]. To further clarify this issue, absolute free-energy calculations for system with varying degrees of tilt could be performed.

The bent-core molecules themselves are not rigid and can possess a series of of external bond angles, γ. Ideally a series of simulations with γ in the range $0° - 60°$ would need to be performed to provide a fuller understanding of these molecule, perhaps with inclusion of some degree of flexibility within the CLJM model.

CHAPTER 4

Polar bent-core molecules without attractive interactions

As we have utilised a 'building block' approach we have thus far neglected the transverse electric dipoles of bent-core molecules. It is unclear what effects the dipolar interactions will have on the phase behaviour of these systems, and whether or not they are crucial to the formation of chiral phases. We shall investigate the effect of removing the attractive interactions and compare the results to those presented in Chapter 3. As a result we can obtain key insights on the influence of attractive (dispersion) interactions and dipolar interactions upon phase behaviour.

The effects of longitudinal dipole moments (dipoles aligned parallel to the long axes of the spherocylinders) on the phase behaviour of hard spherocylinders have been studied by McGrother *et al.* [50, 51]. They found that the smectic phases were stabilised with respect to the nematic phase as a consequence of strong dipolar interactions possible within a single smectic layer. In some systems, especially at low temperatures, the nematic phase was lost completely, with a smectic A - isotropic phase transition observed. Gil-Villegas *et al.* [52] investigated the effects of transverse dipole moments (dipoles perpendicular to the long axes of the spherocylinders) on the phase behaviour of hard spherocylinders. In the Gil-Villegas [52] study the dipolar interactions stabilised the smectic A phase relative to the nematic phase, and at low temperatures ring-like and elongated chain-like domains were reported within smectic layers. Levesque *et al.* [53] investigated the effect of dipole location (with respect to the long axis of the spherocylinder), dipole orientation, and dipole magnitude upon phase

behaviour. With a longitudinal dipole the smectic layers were found to be unpolarised and with a transverse dipole a net polarisation parallel to the smectic planes was observed, suggesting a ferroelectric phase.

The effect of longitudinal dipoles on the phase behaviour of Gay-Berne ellipsoids has been throughly investigated [54, 55, 56, 57, 58]. As with the hard spherocylinder system, the inclusion of dipolar interactions stabilises the smectic phases and it is suggested that the pressure and temperature at which the isotropic phase is formed is insensitive to the strength of the dipole [57]. Gwozsz *et al.* [59] used molecular dynamics to investigate the phase behaviour of Gay-Berne model molecules with a transverse dipole moment. Systems with and without dipolar interactions both reached a smectic phase under the same conditions. At low densities partial orientational order is observed [59]. Within a smectic layer the positional ordering of the molecules is enhanced [59]. Berardi *et al.* report the formation of chains and ring structures within smectic layers for a system composed of Gay-Berne ellipsoids [60].

Johnston *et al.* [25] studied polar bent-core molecules using Gay-Berne dimers that possess transverse dipole moments. As with longitudinal and transverse dipole moments [51, 57], the addition of the dipole stabilised the smectic phases as compared to a corresponding apolar system [24]. Interestingly, the addition of the dipole increased the angle of the tilted phases observed compared to the apolar system [24]. With a molecular bend angle of $\gamma = 10°$, smectic A, tilted smectic B and a spontaneously polarised smectic B phases were observed. With $\gamma = 20°$, smectic A and tilted antiferroelectric smectic B phases were found and the nematic phase was destabilised with respect to the apolar case. The model with $\gamma = 40°$ exhibited a biaxial smectic and antiferroelectric biaxial smectic phases, whereby the long axes of the molecules align as well as the dipole vectors.

In this chapter we present simulation results of a simple site-site model (Fig. 4.1) coupled with dipolar interactions with γ in the range $0° - 40°$. In this system we utilise a simple, repulsive sphere-sphere potential for comparison with the bent-core molecules with attractive dispersions modelled in Chapter 3.

4.1 Simulation techniques

We performed constant pressure, constant temperature Monte Carlo (NpT-MC) simulations of N_m molecules in a cuboidal or cubic simulation cell with periodic

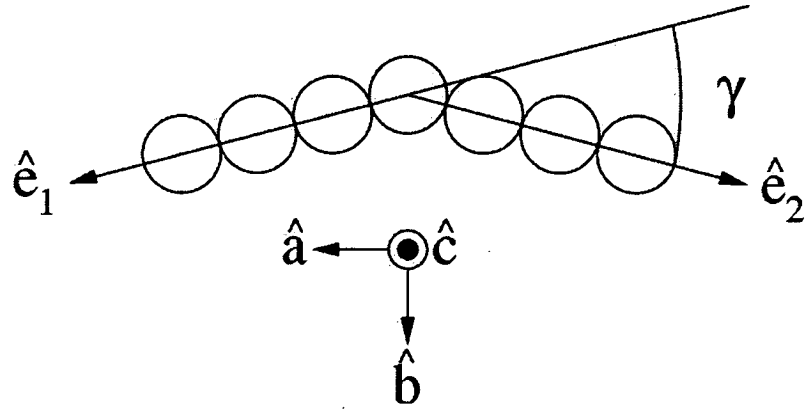

Figure 4.1: The composite of soft spheres model.

boundary conditions applied [33, 34]. The total configurational energy, U, is given by;

$$U = \sum_{i=1}^{N_m-1}\sum_{j>i}^{N_m}\sum_{k=1}^{N_s}\sum_{l=1}^{N_s} 4\epsilon\left(\frac{\sigma}{r_{ij}}\right)^{12} + \sum_{i=1}^{N_m-1}\sum_{j>i}^{N_m} U^{\mu\mu} \tag{4.1}$$

$$U^{\mu\mu} = \left(\frac{\vec{\mu_i}\cdot\vec{\mu_j}}{r_{ij}^3}\right) - \frac{3(\vec{\mu_i}\cdot\vec{r_i})(\vec{\mu_j}\cdot\vec{r_j})}{r_{ij}^5}, \tag{4.2}$$

where ϵ is the potential well depth, σ is the Lennard-Jones sphere diameter, r_{ij} is the pair separation, $\vec{\mu_i}$ is the dipole vector on the i^{th} molecule, and $\vec{r_i}$ is the corresponding position vector. As with the apolar system (chapter 3) a model molecule is constructed from seven soft-spheres arranged in a rigid 'v' shape with the sphere-sphere distance set to 1σ. The dipole is constrained to lie parallel to the $\vec{b}$ vector of the molecules and is located on the apical sphere, i.e. the steric and electrostatic dipoles are parallel. For brevity we refer to these molecules as composite polar molecules (CPMs).

The dipolar potential (equation 4.2) is unsuitable for use in its current form as the long-ranged tail of the dipole-dipole interaction is not amenable for sphere truncation as used with short-ranged potentials. In order to calculate the dipolar energy two techniques can be used. These are the reaction field [33, 51] and the Ewald summation technique [33, 34]. The Ewald summation method involves computationally demanding lattice sums in reciprocal space and is generally accepted to be the more accurate of the two methods. The reaction field method assumes a cut-off distance and a dielectric continuum outside this cut-off dis-

tance. With these Ewald sums the dipolar interaction energy is given by;

$$
\begin{aligned}
U^{\mu\mu} &= \frac{1}{2}\sum_{i=1}^{N_m}\sum_{j=1}^{N_m}\left[\sum_{|n|}^{\infty}\left(\vec{\mu_i}\cdot\vec{\mu_j}\right)B\left(r\right)\left(\vec{r_{ij}}+\vec{n}\right)\right. \\
&- \left(\vec{\mu_i}\cdot\vec{r_{ij}}\right)\left(\vec{\mu_j}\cdot\vec{r_{ij}}\right)C\left(r\right)\left(\vec{r_{ij}}+\vec{n}\right) \qquad (4.3) \\
&+ \left.\sum_{\vec{k}\neq 0}\left(\frac{1}{\pi L^3}\right)\left(\vec{\mu_i}\cdot\vec{k}\right)\left(\vec{\mu_j}\cdot\vec{k}\right)\left(\frac{4\pi^2}{\kappa^2}\right)\exp\left(-\frac{\vec{k}^2}{4\kappa^2}\right)\cos\left(\vec{k}\cdot\vec{r_{ij}}\right)\right] \qquad (4.4) \\
&- \sum_{i=1}^{N}\frac{2\kappa^3\mu_i^2}{3\pi^{\frac{1}{2}}} \qquad (4.5) \\
B\left(r\right) &= \operatorname{erfc}\left(\kappa r\right)\frac{1}{r^3}+\left(\frac{2\kappa}{\pi^{\frac{1}{2}}}\right)\frac{\exp\left(-\kappa r^2\right)}{r^2} \qquad (4.6) \\
C\left(r\right) &= 3\operatorname{erfc}\left(\kappa r\right)\frac{1}{r^5}+\left(\frac{2\kappa}{\pi^{\frac{1}{2}}}\right)\left(2\kappa^2+\frac{3}{r^2}\right)\exp\frac{\left(-\kappa^2 r^2\right)}{r^2} \qquad (4.7)
\end{aligned}
$$

For these simulations we use conducting 'tin-foil' boundary conditions, where $\epsilon_s = \infty$.

The equations shown in Eqns. 4.3-4.5 represent the dipole-dipole interaction energy. This can be resolved into three components, the real space sum (Eqn. 4.3), k (reciprocal)-space sum (Eqn. 4.4), and a self-potential term (Eqn. 4.5), respectively. A description of the simplified equations used can be found in Appendix A.

In the simulations one MC sweep consisted of one trial translation or one trial rotation per molecule and a single volume fluctuation. The rotation moves were performed using the Barker-Watts method [33] and volume fluctuations performed by sampling in $\ln V$ [33] as described in Chapter 2. In the cuboidal simulations the dimension to be scaled (L_{xy} or L_z) was selected at random. Typically the CPU time for a simulation block of 400 MC sweeps was in excess of 900 seconds. All maximum displacement parameters were adjusted to give respective acceptance ratios of 50%.

Starting configurations

For a typical starting configuration each layer was based upon a simple square lattice and then replicated in the z direction. The layer spacing was governed by the vectors $\vec{e_1}$ and $\vec{e_2}$. Molecules were aligned with the long axes ($\vec{a_i}$) of the molecules parallel to the layer normal (Z-axis) and all the $\vec{b_i}$ vectors parallel to the Y-axis to maximise the uniaxial and biaxial order parameters. It is well known

that the preferred alignment for two adjacent dipoles is nose to tail, giving rise to chains of dipoles or antiparallel dipoles. As a consequence of this, molecules in adjacent layers are orientated in opposite directions, giving rise to zero net polarisation, i.e. an antiferroelectric phase.

Upon generation of the initial configurations, these were allowed to equilibrate at constant volume (NVT) Monte Carlo simulations at $\rho^* = 0.14$, which is comparable to the starting density used in Chapter 3.

For each system, we performed sequences of simulations starting at high density ($\rho^* = 0.14$), to ensure that the molecules tilted spontaneously, for bond angles $\gamma = 0°, 20°$ and $40°$. The temperature was raised until a transition to a homogeneous fluid phase (isotropic or nematic) was observed. We then switched over to a cubic simulation cell. Along with these heating runs, we also performed some cooling runs to verify the existence of a phase transition. Equations for defining the reduced units of dipole strength and temperature are shown in Eqns. 4.8 and 4.9, respectively.

$$\mu^* = \sqrt{\frac{\mu^2}{\sigma^3 \epsilon}} \tag{4.8}$$

$$T^* = \frac{k_b T}{\epsilon} \tag{4.9}$$

We calculated the structural properties, $g(r), g_{xy}(r), \rho_z(r)$ and $\langle R^2 \rangle$ and orientational order parameters of the fluid phases as described in Section 2.3.

4.2 Simulation Results

4.2.1 *Linear molecules, $\gamma = 0°$*

In this section we describe the results of simulations performed to investigate the effect of dipole strength on linear CPMs.

$\mu^* = 0.0$

The equation of state of linear ($\gamma = 0°$) CPMs along an isobar with $p^* = 4.0$ and $\mu^* = 0.0$ is shown in Fig. 4.2. The equation of state exhibits four distinct branches; herringbone, untilted smectic A, uniaxial nematic and isotropic phases. Snapshots of a simulation configuration at a temperature of $T^* = 2.0$ are shown in Figs. 4.3(a) and (b). These snapshots clearly show the highly tilted nature of the

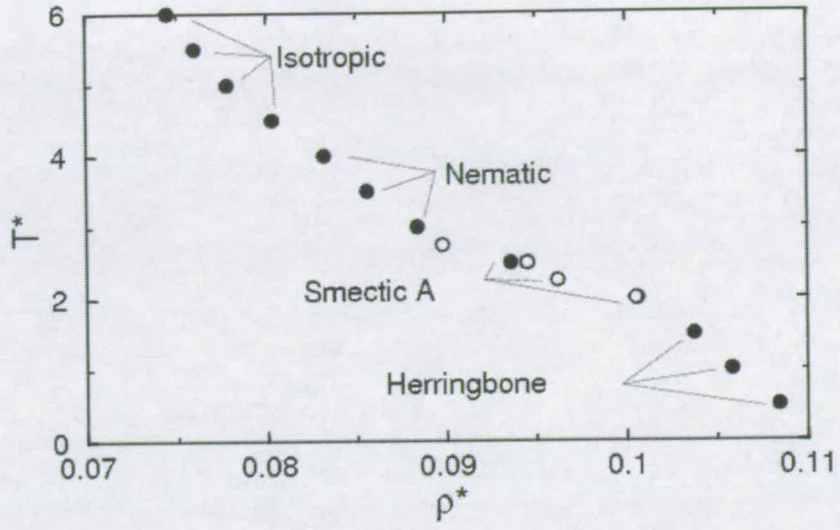

Figure 4.2: Equation of state for $\gamma = 0°$ with $p^* = 4.0$ and $\mu^* = 0.0$. Filled circles represent the results of heating simulations and open circles from cooling simulations. Error bars are smaller than the symbol size.

phase formed at this state point, with $\phi \simeq 60°$. As a result of this high tilt angle values of Q_{00}^2 are low. This phase is similar to the herring-bone structure reported in Section 3.2.1 and by Paolini *et al.* [30], albeit with drastically increased molecular tilt in our system. The in-layer radial distribution plot, shown in Fig. 4.4, is not indicative of hexagonal close packing. This is reinforced by the near zero slope of $\langle R^2 \rangle$, shown in Fig. 4.5. Examination of a series of in-layer snapshots at a temperature of $T^* = 2.0$ (Fig. 4.6) we can clearly see the random translational order within each layer.

Raising the temperature to $T^* = 2.5$, yields a highly defective smectic A phase, shown in Figs. 4.3(c) and (d). This phase exhibits two aligned domains that are perpendicular to one another, which will give rise to unusual textures. To investigate the stability of this phase, a simulation cooling from a fully equilibrated nematic phase was performed. After cooling the final equilibrium density was $\rho^* = 0.0945$, which lies upon the same branch of the equation of state for the heating runs. Snapshots of the final configuration are shown in Figs. 4.3(e) and (f). Examination of the in-layer radial distribution plot, shown in Fig. 4.4, exhibits short-range ordering as found in smectic A phases and has been classified as such a phase.

Above a temperature of $T^* = 3.0$, we find a uniaxial nematic phase, shown in Figs. 4.7(a) and (b). Above $T^* = 4.5$ we find the isotropic phase, as shown

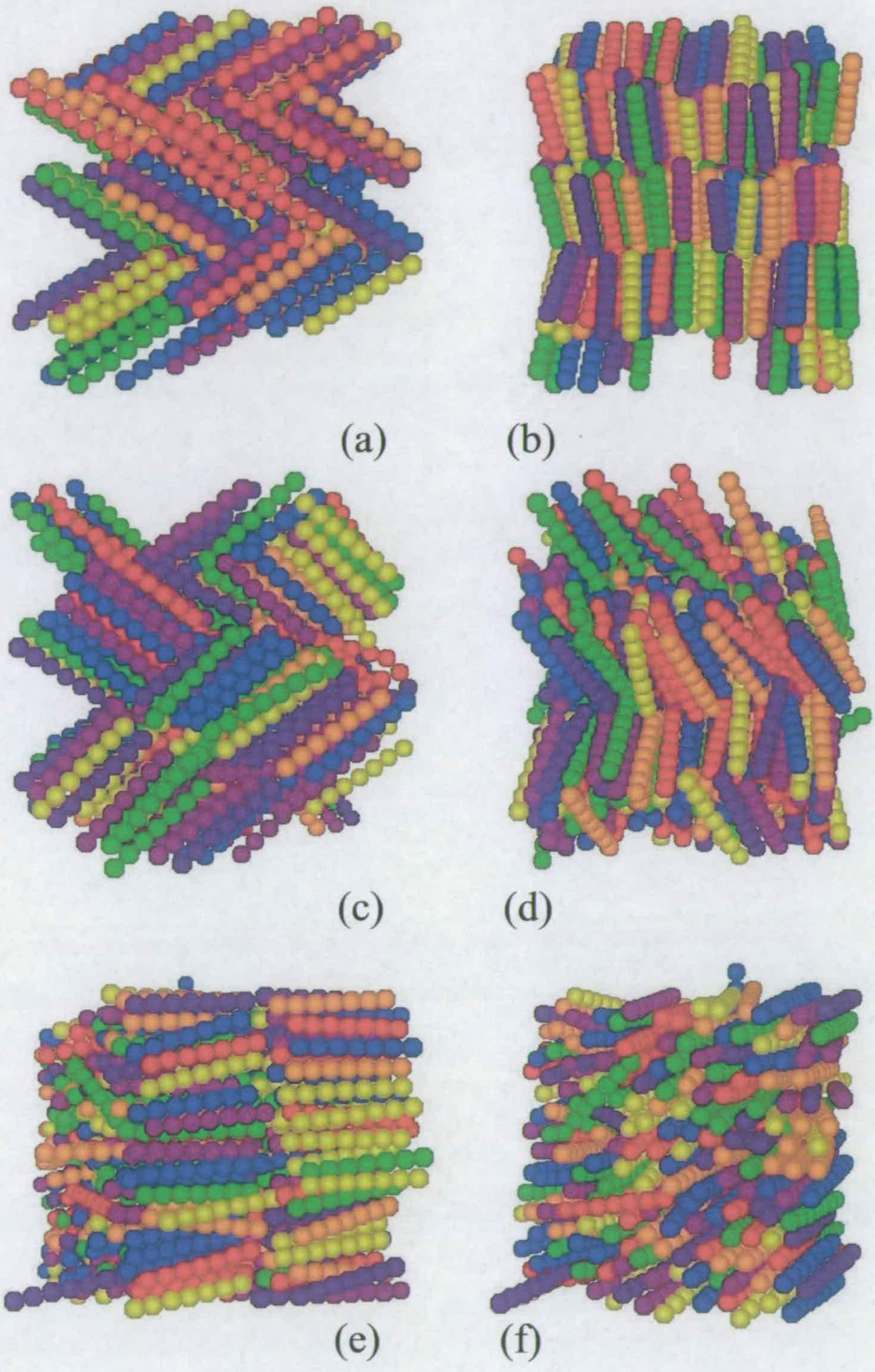

Figure 4.3: Snapshot representations for $\gamma = 0°$ with $p^* = 4.0$; (a) and (b) $\mu^* = 0.0$ and $T^* = 2.0$, (c) and (d) $\mu^* = 0.0$ and $T^* = 2.5$ and (e) and (f) $\mu^* = 0.0$ and $T^* = 2.5$ cooled from a fully equilibrated nematic phase.

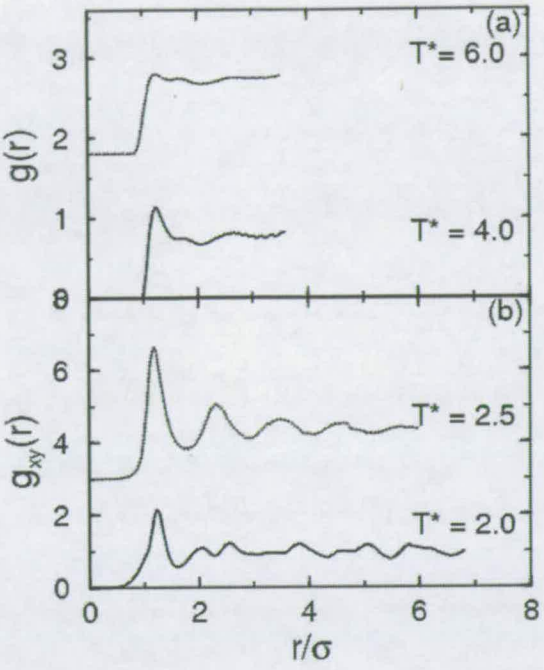

Figure 4.4: (a) Radial distribution data for $T^* = 4.0$ (solid line), 6.0 (dotted line) and (b) in-layer radial distribution data for $T^* = 2.0$ (solid line), 2.5 (dotted line) for $\gamma = 0°$ with $p^* = 4.0$ and $\mu^* = 0.0$. Plots have been displaced for clarity.

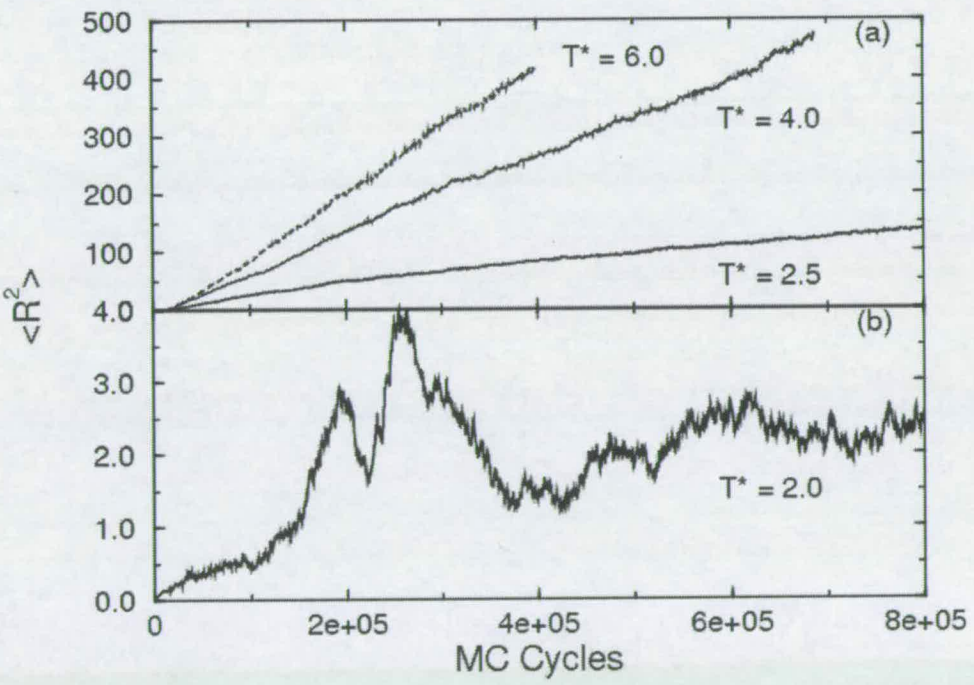

Figure 4.5: $\langle R^2 \rangle$ for $\gamma = 0°$ with $p^* = 4.0$ and $\mu^* = 0.0$ with (a) $T^* = 2.5$ (solid line), 4.0 (dotted line), 6.0 (dashed line) and (b) $T^* = 2.0$ (solid line).

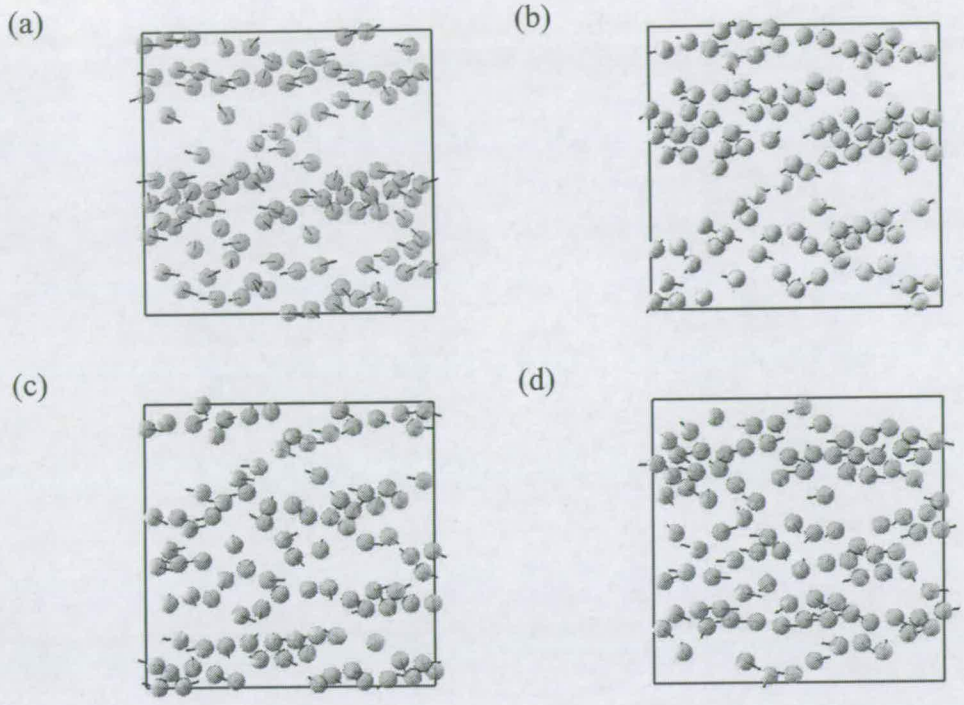

Figure 4.6: In-layer snapshot representations for $\gamma = 0°$ with $p^* = 4.0$, $\mu^* = 0.0$ and $T^* = 2.0$: (a) molecules $1 - 100$; (b) molecules $101 - 200$; (c) molecules $201 - 300$; (d) molecules $301 - 400$. The black line indicates the direction of the dipole vector for each molecule (in this system $\mu^* = 0.0$) and layers are perpendicular to the Z-axis.

in Figs. 4.7(c) and (d). The radial distribution plots (Fig. 4.4) exhibit no positional/translational ordering, which is indicative of both the nematic and isotropic phases. Examination of the $\langle R^2 \rangle$ plot, shown in Fig. 4.5 clearly shows the solid-nematic phase transition with a large increase in the slope of $\langle R^2 \rangle$ upon entering the nematic phase.

A plot of Q_{00}^2, as a function of temperature, is shown in Fig. 4.8. The crossover from the highly tilted solid phase to the untilted phases can be seen over the range $1.5 \leq T^* \leq 2.0$. The values of Q_{00}^2 are lower for the tilted phases than the untilted smectic A and nematic phases on account of the random tilt directions. The nematic-isotropic phase transition is signalled by the drop in Q_{00}^2 between $T^* = 4.0$ and $T^* = 4.5$

$\mu^* = 1.0$

The equation of state of linear CPMs along an isobar with $p^* = 4.0$ and $\mu^* = 1.0$ is shown in Fig. 4.9. Snapshot representations of a simulation configuration at a

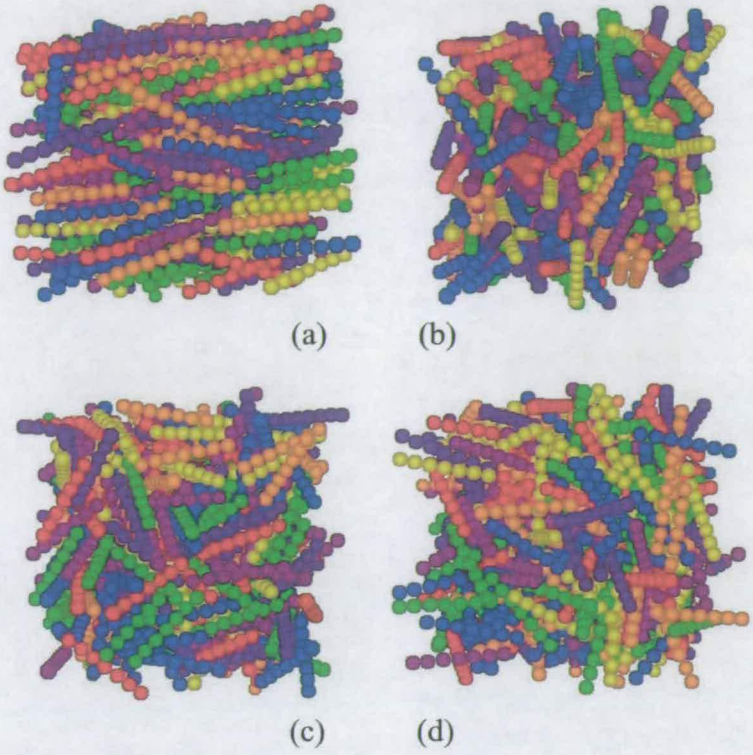

Figure 4.7: Snapshot representation for $\gamma = 0°$ with $p^* = 4.0$, (a) and (b) $\mu^* = 0.0$ and $T^* = 4.0$ and (c) and (d) $\mu^* = 0.0$ and $T^* = 6.0$.

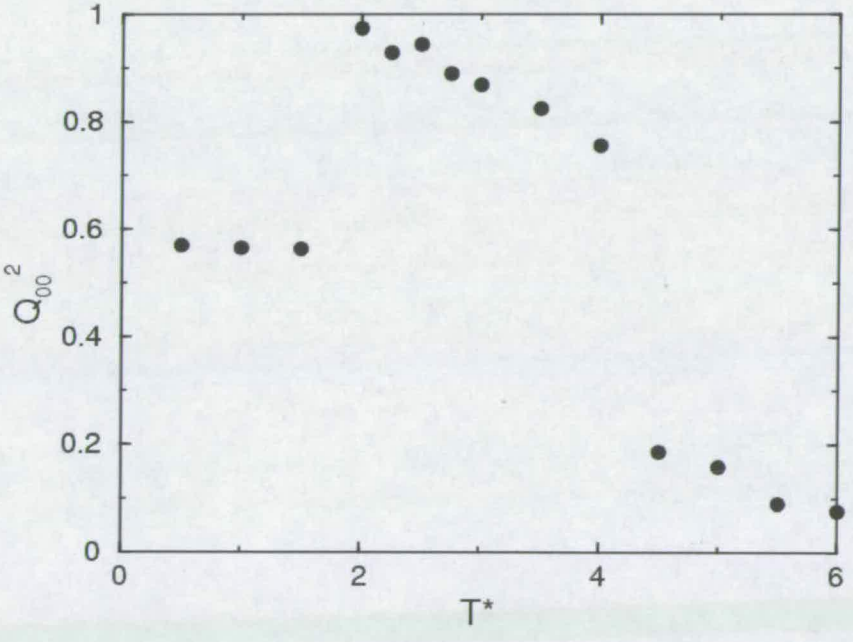

Figure 4.8: Nematic order parameter plotted as a function of temperature for $\gamma = 0°$ with $p^* = 4.0$ and $\mu^* = 0.0$. Error bars are smaller than the symbol size.

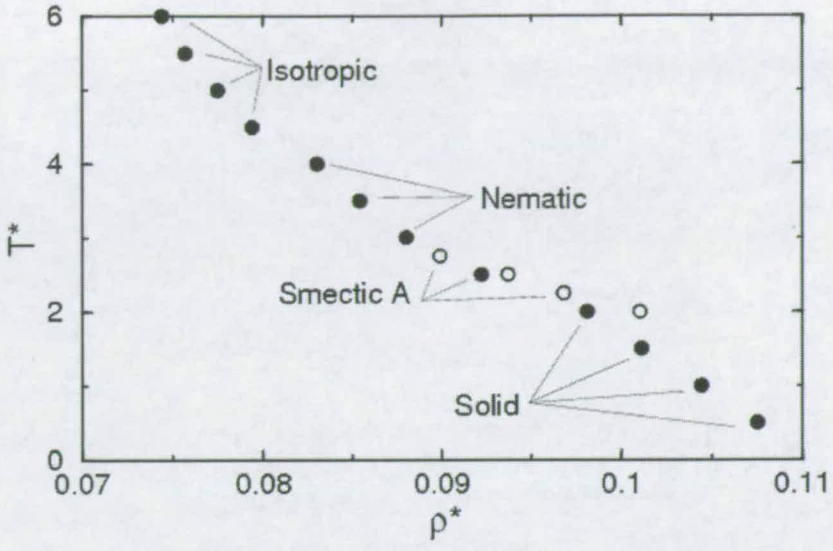

Figure 4.9: Equation of state for $\gamma = 0°$ with $p^* = 4.0$ and $\mu^* = 1.0$. Filled circles represents simulation results obtained from heating and open circles from cooling simulations. Error bars are smaller than the symbol size.

temperature of $T^* = 2.0$ are shown in Figs. 4.10(a) and (b). In contrast to the system with $\mu^* = 0.0$ the tilt angle at the same temperature is significantly less, with $\phi = 20.1°$. This reduction in tilt is likely to arise from increased dipolar nose-tail interactions. When the molecules are untilted the dipoles can aligned nose-tail. If the molecules are tilted this nose-tail alignment is lost as shown in Fig. 4.11. A plot of the in-layer radial distribution, shown in Fig. 4.12, is sharply peaked, thus indicative of a crystalline state. In-layer snapshots, shown in Fig. 4.13, exhibit a more ordered system compared to Fig. 4.6, however the dipole directions are randomly distributed. Phases arising from heating simulations are likely to be metastable states and require cooling simulations to fully elucidate the phase behaviour of this system.

Heating to a temperature of $T^* = 2.5$, shown in Figs. 4.10(c) and (d), yields a highly defective smectic A phase similar to that found at the same temperature with $\mu^* = 0.0$, which is likely to be metastable. Although not as well defined as the $\mu^* = 0.0$ case, two orthogonal domains are forming. To assess the stability of this phase a series of simulations cooling from a fully equilibrated nematic phase were performed (Fig. 4.9 - open circles). Below a temperature of $T^* = 2.75$ an untilted smectic A phase was found, which persisted to $T^* = 2.25$. Snapshots of this phase can be found in Figs. 4.10(e) and (f) and a snapshot of the smectic layers shown in Fig. 4.14, both of which exhibit short-range ordering, although no chains or rings can be distinguished. The radial distribution plot (Fig. 4.12)

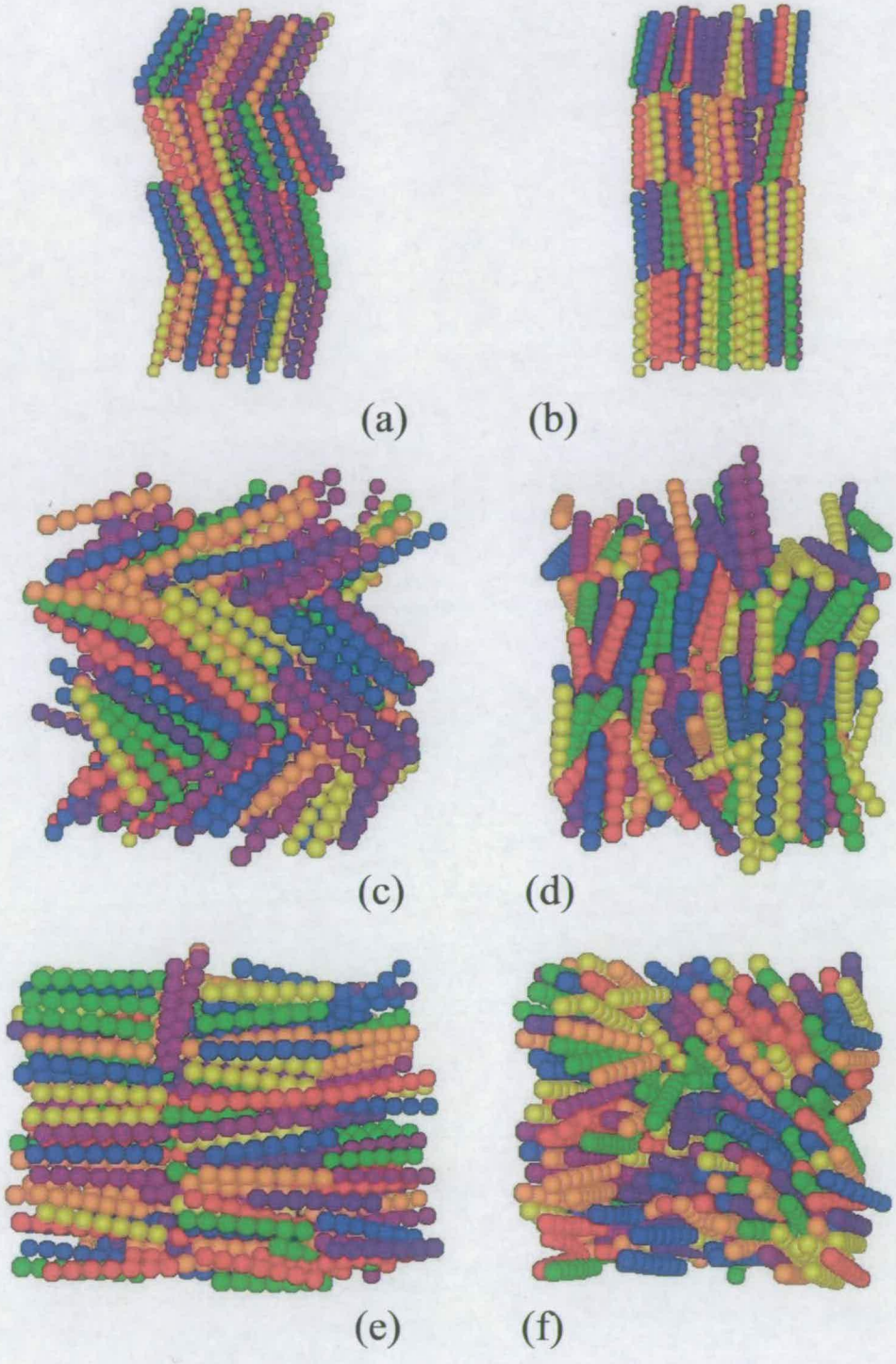

Figure 4.10: Snapshot representation for $\gamma = 0°$ with $p^* = 4.0$; (a) and (b) $\mu^* = 1.0$ and $T^* = 2.0$, (c) and (d) $\mu^* = 1.0$ and $T^* = 2.5$ and (e) and (f) $\mu^* = 1.0$ and $T^* = 2.5$ cooled from a fully equilibrated nematic phase.

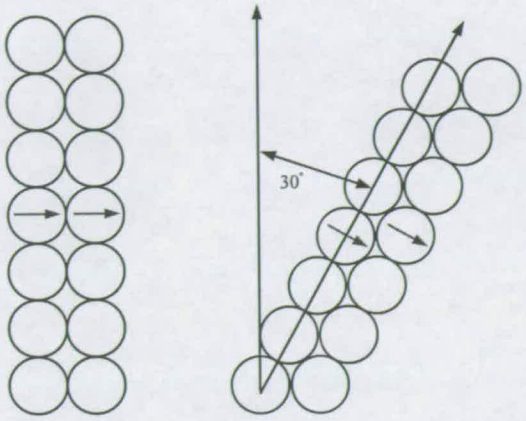

Figure 4.11: Diagramatic representation of the dipole arrangement upon tilting of molecules to $\sim 30°$. The arrow indicates the direction of the dipole moment.

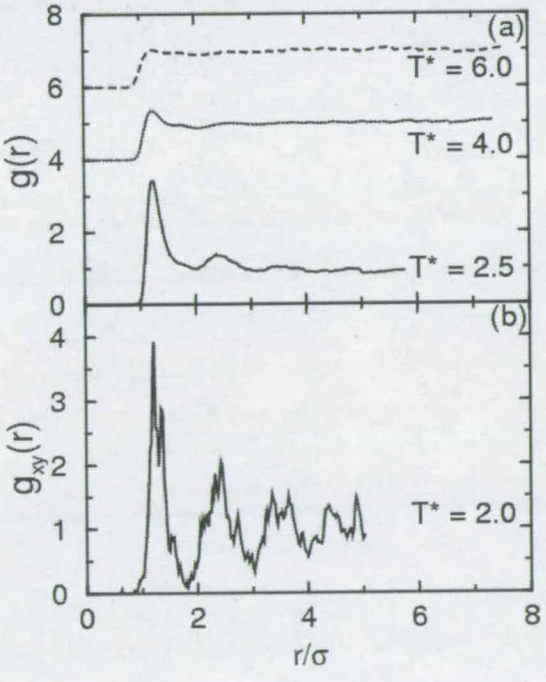

Figure 4.12: (a) Radial distribution data for $T^* = 2.5$ (solid line), 4.0 (dotted line), 6.0 (dashed line) and (b) in-layer radial distribution data for $T^* = 2.0$ (solid line) for $\gamma = 0°$ with $p^* = 4.0$ and $\mu^* = 1.0$. Plots have been displaced for clarity.

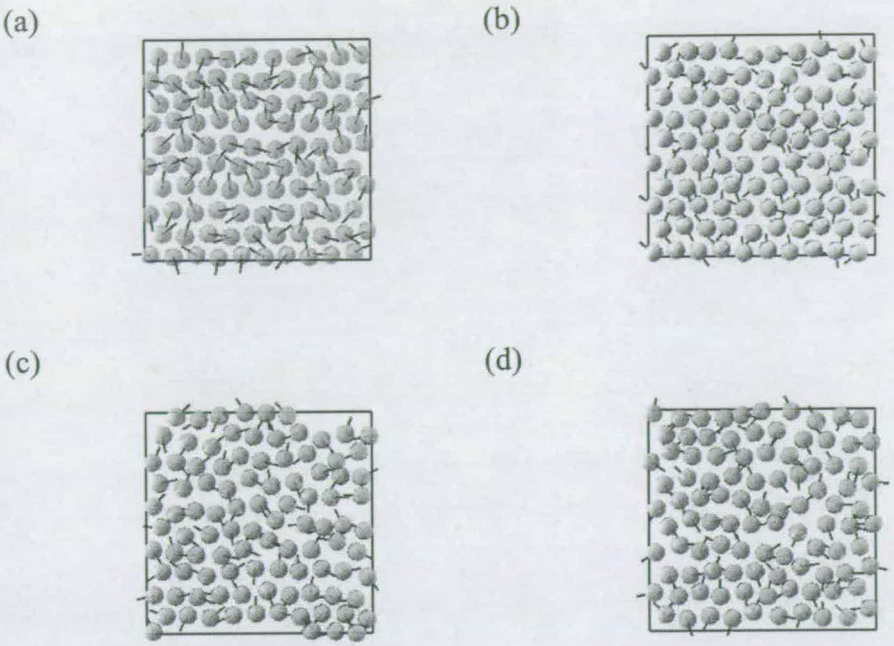

Figure 4.13: In-layer snapshot representations for $\gamma = 0°$ with $p^* = 4.0$, $\mu^* = 1.0$ and $T^* = 2.0$: (a) molecules $1 - 100$; (b) molecules $101 - 200$; (c) molecules $201 - 300$; (d) molecules $301 - 400$. The black line indicates the direction of the dipole vector for each molecule and layers are perpendicular to the Z-axis.

confirms this short-range ordering and has been assigned as an untilted smectic A phase.

Heating above $T^* = 2.75$ yields a uniaxial nematic phase and above $T^* = 4.5$ the isotropic phase. The nematic phase is stable over the range $2.75 \leq T^* \leq 4.0$. Snapshots of both the nematic and isotropic phases can be seen in Figs. 4.15(a) and (b) and 4.15(c) and (d) respectively. The radial distribution functions are shown in Fig. 4.12, clearly showing only short-range ordering . The mean square displacement (Fig. 4.16) clearly shows the order of magnitude increase in the gradients of $\langle R^2 \rangle$ upon entering the nematic and isotropic phases, over the untilted smectic A phase.

A plot of the nematic order parameter as a function of temperature along an isobar with $p^* = 4.0$ and $\mu^* = 1.0$, is shown in Fig. 4.17. We observe a tilted solid phase with $Q_{00}^2 \simeq 0.8 - 0.9$ at low temperature, as with the $\mu^* = 0.0$ system, the layers are randomly tilted, which reduces the nematic order parameter. It must be noted that the inclusion of dipolar interactions decreases the observed tilt.

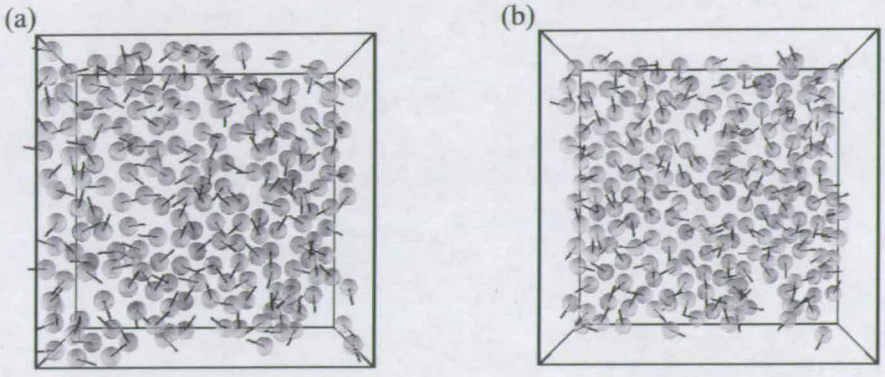

Figure 4.14: In-layer snapshot representations for $\gamma = 0°$ with $p^* = 4.0$, $\mu^* = 1.0$ and $T^* = 2.5$, for both layers. The black line indicates the direction of the dipole vector for each molecule and layer are perpendicular to the Z-axis.

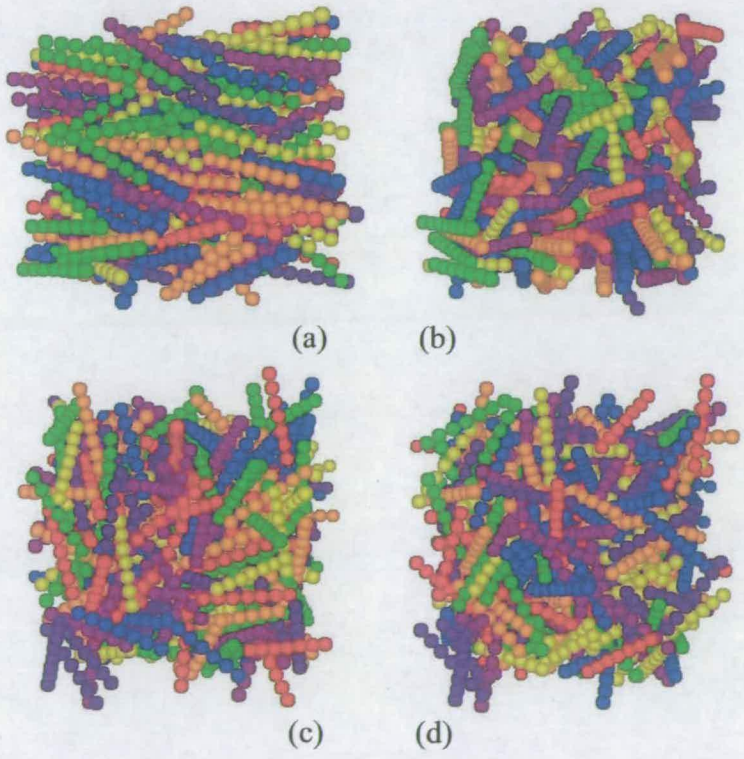

Figure 4.15: Snapshot representation for $\gamma = 0°$ with $p^* = 4.0$, (a) and (b) $\mu^* = 1.0$ and $T^* = 4.0$ and (c) and (d) $\mu^* = 1.0$ and $T^* = 6.0$.

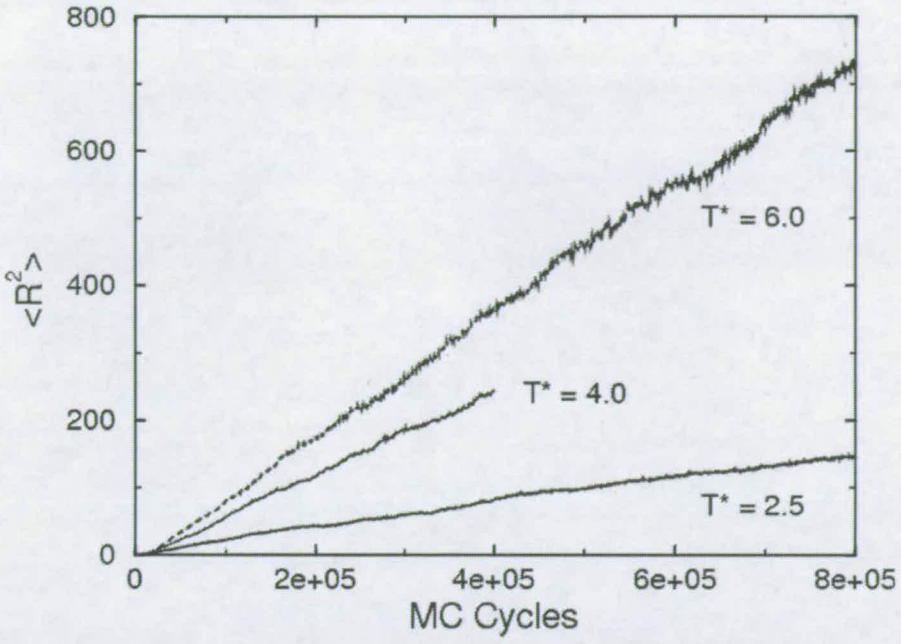

Figure 4.16: Mean squared displacement data for $\gamma = 0°$ with $p^* = 4.0$ and $\mu^* = 1.0$ with $T^* = 2.5$ (solid line), 4.0 (dotted line), 6.0 (dashed line).

This decrease in tilt is a result of the more energetically favourable dipole nose-tail interactions at low tilt angles as shown in Fig. 4.11. A large dipole moment would prefer a zero tilt arrangement. The phase transition from the crystalline phase to the untilted smectic A phase can be seen over the range $2.0 \leq T^* < 2.5$. The nematic-isotropic phase transition is signalled by a drop in Q_{00}^2 between $T^* = 4.0$ and $T^* = 4.5$.

$\mu^* = 2.0$

The equation of state of linear ($\gamma = 0°$) CPMs along an isobar with $p^* = 4.0$ and $\mu^* = 2.0$ is shown in Fig. 4.18. The equation of state exhibits three distinct branches corresponding to, tilted solid, another tilted solid and isotropic. Snapshots of a simulation configuration at a temperature of $T^* = 2.0$ are shown in Figs. 4.19(a) and (b). The tilt angle, $\phi = 14.1°$ with respect to the layer normal is less than that found for the corresponding temperature with $\mu^* = 1.0$. This reduction in tilt is likely to be a result of increased dipole nose-tail interactions. Examination of the in-layer radial distribution, shown in Fig. 4.20 exhibit crystalline ordering on account of the sharply defined peaks. The gradient of $\langle R^2 \rangle$ is almost negligible at this temperature. As such we have a crystalline state. In-layer snapshots of a simulation configuration, reveal a highly ordered structure with small dipole chains having been formed, albeit with no ring structures

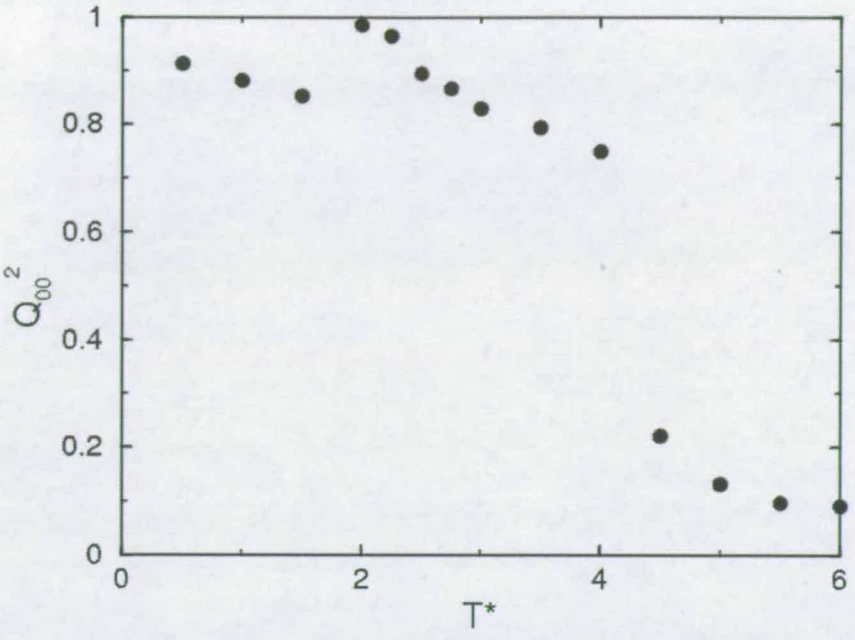

Figure 4.17: Nematic order parameter plotted as a function of temperature for $\gamma = 0°$ with $p^* = 4.0$ and $\mu^* = 1.0$. Error bars are smaller than the symbol size.

apparent. This is surprising as we would have anticipated the dipoles to have formed extended chains and rings as seen with dipolar hard spheres that possess comparable dipole strengths [61].

Heating further yields another tilted crystal phase, which is stable over the temperature range $2.5 \leq T^* \leq 6.0$. Snapshots at a temperature of $T^* = 4.0$ are shown in Figs. 4.19(c) and (d). The tilt angle for this phase is, $\phi = 17.3°$, with respect to the layer normal. The radial distribution plot, shown in Fig. 4.20 is sharply peaked which would suggest a solid phase. The gradient of $(\langle R^2 \rangle)$ as a function of MC cycles (yielding a "diffusion" coefficient) levels off after a few MC cycles. As such this is likely to be a tilted solid phase. In-layer snapshots, shown in Fig. 4.22, possess defects.

Heating above a temperature of $T^* = 6.0$ we find an isotropic phase, snapshots of which are shown in Figs. 4.19(e) and (f). There is an order of magnitude increase in the slope of $\langle R^2 \rangle$ upon entering the isotropic phase.

A plot of Q_{00}^2 as a function of temperature along an isobar is shown in Fig. 4.23. Values of $Q_{00}^2 > 0.8$ persist for $T^* \leq 6.0$. Although solid, a slight drop in Q_{00}^2 between $T^* = 2.0$ and $T^* = 2.5$, would suggest a tilted smectic B phase, with a slightly increase degree of tilt. The angles of tilt within these low temperature systems is decreased by strong dipolar nose-tail interactions. Above $T^* = 6.5$, the

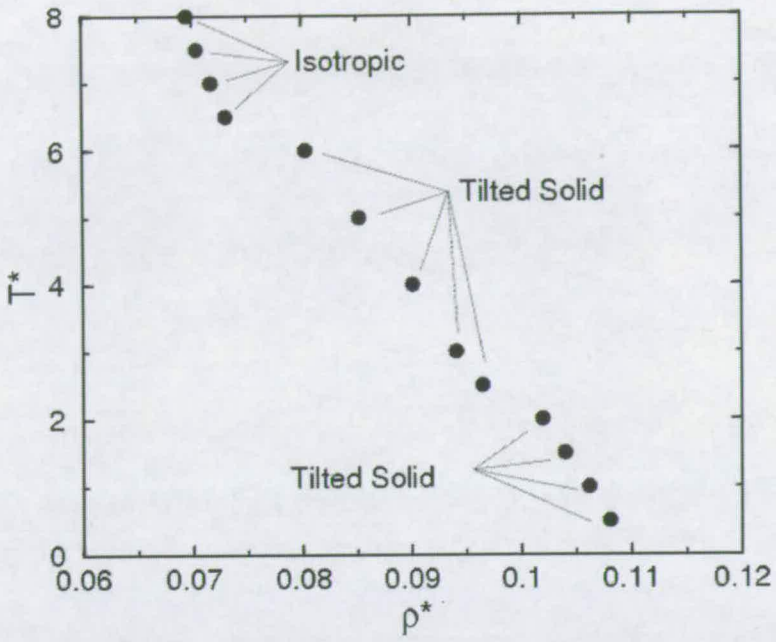

Figure 4.18: Equation of state for $\gamma = 0°$ with $p^* = 4.0$ and $\mu^* = 2.0$. Filled circles denote heating simulations. Error bars are smaller than the symbol size.

drop in the nematic order parameter is indicative of a tilted smectic B to isotropic phase transition.

Chaining simulations

It is well known that dipolar hard spheres with a high dipole moment at low densities and temperatures form super structures (chains and rings) in 3D [61, 62]. In order to investigate the possibility of such structures forming with CPMs a series of simulations were performed at low density, low temperature and high dipole moment values. A snapshot is shown in Fig. 4.24. From this no superstructural motifs are evident. It can be envisaged that the bulky nature of the CPMs would be sufficient to prevent formation of chains.

4.2.2 $\gamma = 20°$

With the introduction of the bend into the model molecules, we raise the possibility of forming chiral ferroelectric and antiferroelectric phases as discussed in Sec. 1.1.1. With the inclusion of dipolar interactions, the antiferroelectric phases are likely to be the more thermodynamically stable of the two polarisation states on account of dipoles in adjacent layers aligning antiparallel to one another. Here we present results for CPMs with μ^* in the range $0.0 - 2.0$ and $\gamma = 20°$.

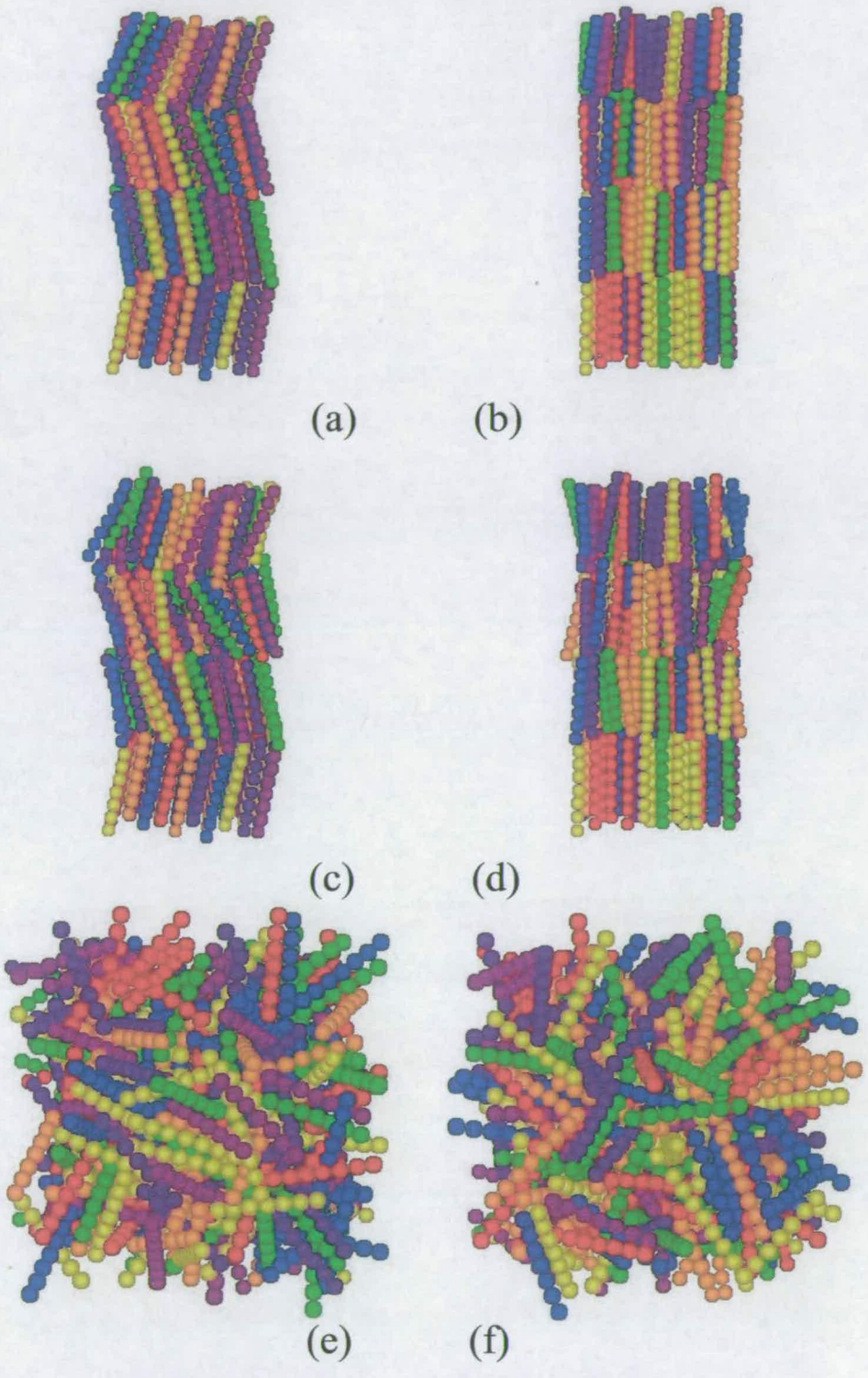

Figure 4.19: Snapshot representation for $\gamma = 0°$ with $p^* = 4.0$; (a) and (b) $\mu^* = 2.0$ and $T^* = 2.0$, (c) and (d) $\mu^* = 2.0$ and $T^* = 4.0$ and (e) and (f) $\mu^* = 2.0$ and $T^* = 8.0$.

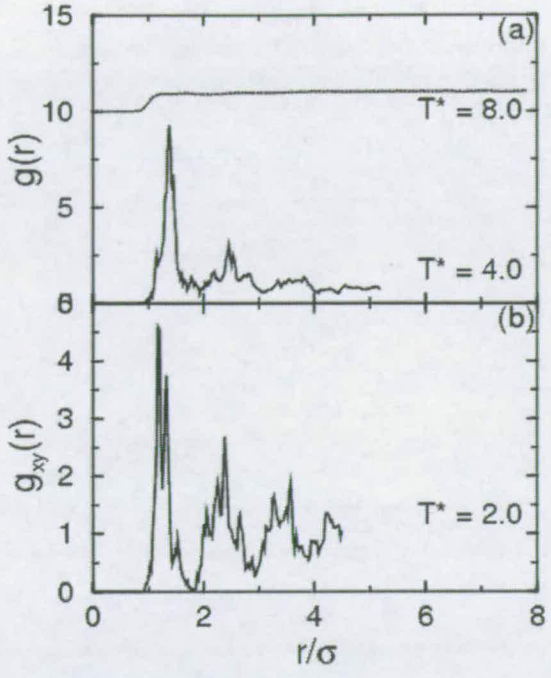

Figure 4.20: (a) Radial distribution data for $T^* = 4.0$ (solid line), 8.0 (dotted line) and (b) in-layer radial distribution data for $T^* = 2.0$ (solid line) with $\gamma = 0°$ with $p^* = 4.0$ and $\mu^* = 2.0$. Plots have been displaced by 10 units for clarity.

$\mu^* = 0.0$

The equation of state of CPMs with $\gamma = 20°$ along an isobar with $p^* = 4.0$ and $\mu^* = 0.0$ is shown in Fig. 4.25. Snapshots at $T^* = 1.0$ are shown in Figs. 4.26(a) and (b). As with CPMs with $\gamma = 0°$ and $\mu^* = 0.0$ (Section 4.2.1), we find a herringbone phase with molecules tilted, with $\phi \simeq 53°$ with respect to the layer normal. The in-layer radial distribution function, shown in Fig. 4.27(b) exhibits short-range ordering character with two peaks in the range $r/\sigma = 2.0-3.0$. A plot of $\langle R^2 \rangle$ as a function of MC cycles is shown in Fig. 4.28. At low temperature, the gradient of $\langle R^2 \rangle$ is small, which is observed with herringbone phases. In-layer snapshots (Fig. 4.29) clearly displays this behaviour. As all layers are highly tilted with respect to the layer normal, it can be suggested that adjacent layer will possess gaps, to allow for the high degree of tilt and interdigitation seen in these systems. The complementary nature of these gaps can be seen clearly in Fig. 4.29.

The biaxial order parameters, Q^2_{22}, for a series of temperatures in the range $T^* = 0.5 - 5.0$ are shown in Table 4.1 decay even at low temperatures. These low Q^2_{22} values would indicate a low degree of correspondence between adjacent layers.

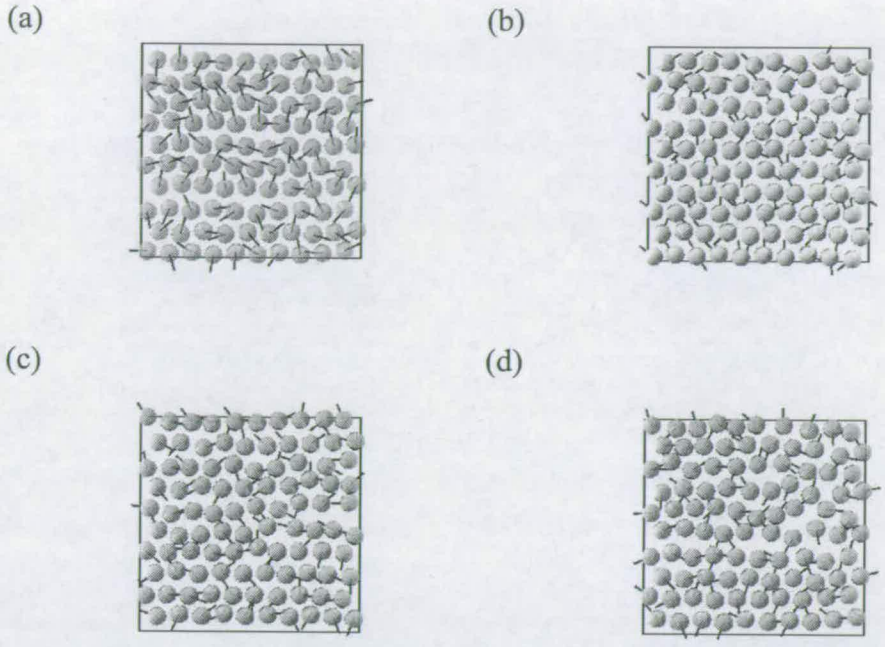

Figure 4.21: In-layer snapshot representations for $\gamma = 0°$ with $p^* = 4.0$, $\mu^* = 2.0$ and $T^* = 2.0$: (a) molecules $1 - 100$; (b) molecules $101 - 200$; (c) molecules $201 - 300$; (d) molecules $301 - 400$. The black line indicates the direction of the dipole vector for each molecule and layers are perpendicular to the Z-axis.

This is likely to be a super paraelectric phase. We do not find any ferroelectric or antiferroelectric phases.

To investigate the solid - nematic phase transition, a simulation from a fully equilibrated nematic phase at $T^* = 2.0$ to a temperature of $T^* = 1.5$ was performed. The final equilibrium density was $\rho^* = 0.0945$, which does not lie on any of the branches of the equation of state. A snapshot of the resultant phase is shown in Fig. 4.26(c) and (d). From the snapshot, it can be seen that the molecules are orientationally ordered with $Q_{00}^2 = 0.8659$. As such this is likely to be a metastable nematic state, with respect to the low temperature herringbone phase.

Heating further along the isobar yields a uniaxial nematic phase, and snapshots at $T^* = 3.0$ are shown in Figs. 4.30(a) and (b). The nematic phase is stable over the range $2.0 \leq T^* \leq 3.0$. Further heating yields the isotropic phase at temperatures over $T^* \geq 3.5$. Snapshots of the isotropic phase is shown in Figs. 4.30(c) and (d).

In Fig. 4.31, the uniaxial order parameter is plotted as a function of temperature along an isobar with $p^* = 4.0$ and $\mu^* = 0.0$. The herringbone phase possesses

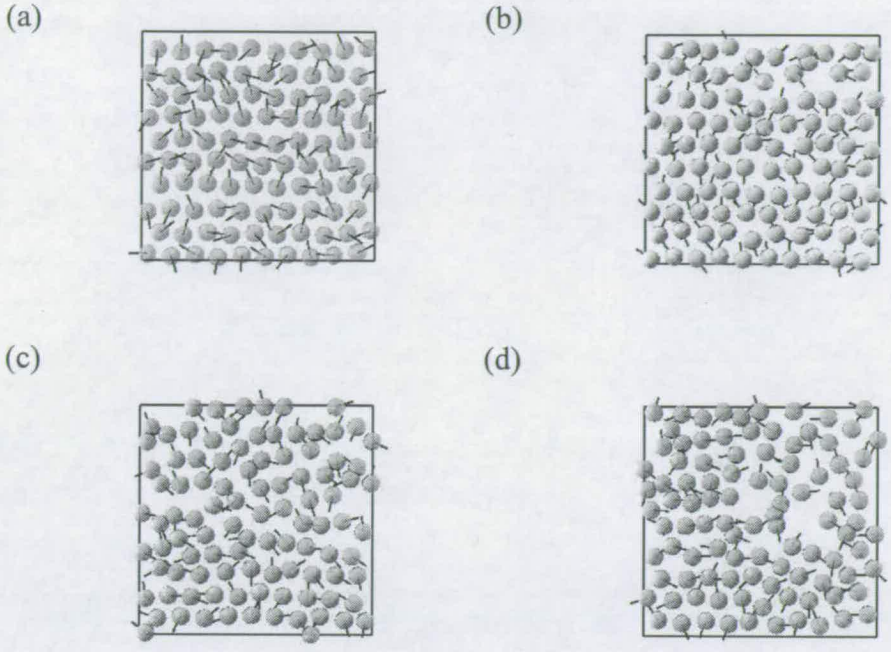

Figure 4.22: In-layer snapshot representations for $\gamma = 0°$ with $p^* = 4.0$, $\mu^* = 2.0$ and $T^* = 4.0$: (a) molecules $1 - 100$; (b) molecules $101 - 200$; (c) molecules $201 - 300$; (d) molecules $301 - 400$. The black line indicates the direction of the dipole vector for each molecule and layers are perpendicular to the Z-axis.

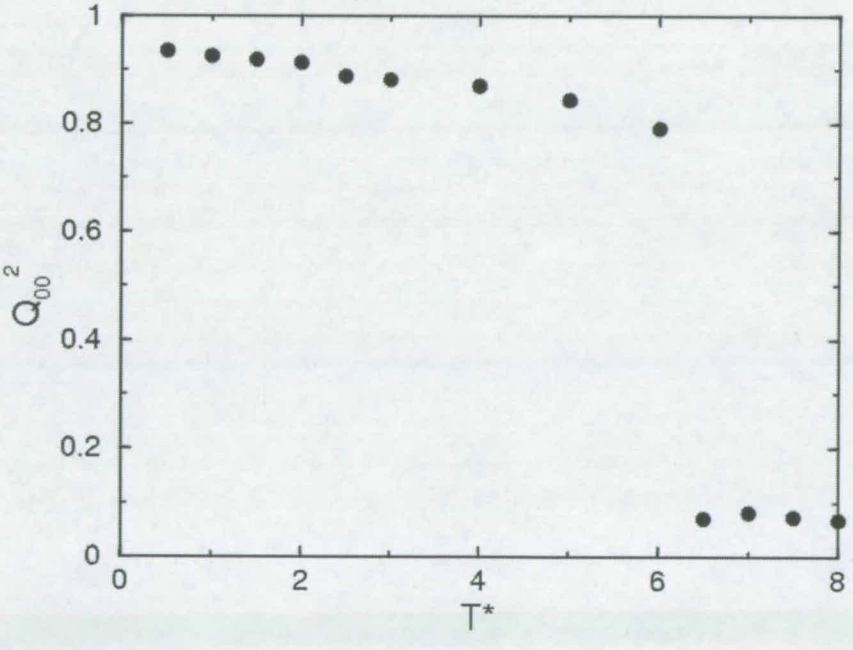

Figure 4.23: Nematic order parameter plotted as a function of temperature for $\gamma = 0°$ with $p^* = 4.0$ and $\mu^* = 2.0$. Error bars are smaller than the symbol size.

Figure 4.24: Snapshot representation for $\gamma = 0°$ with $p^* = 4.0$, $\mu^* = 3.0$ and $T^* = 1.0$ at low density.

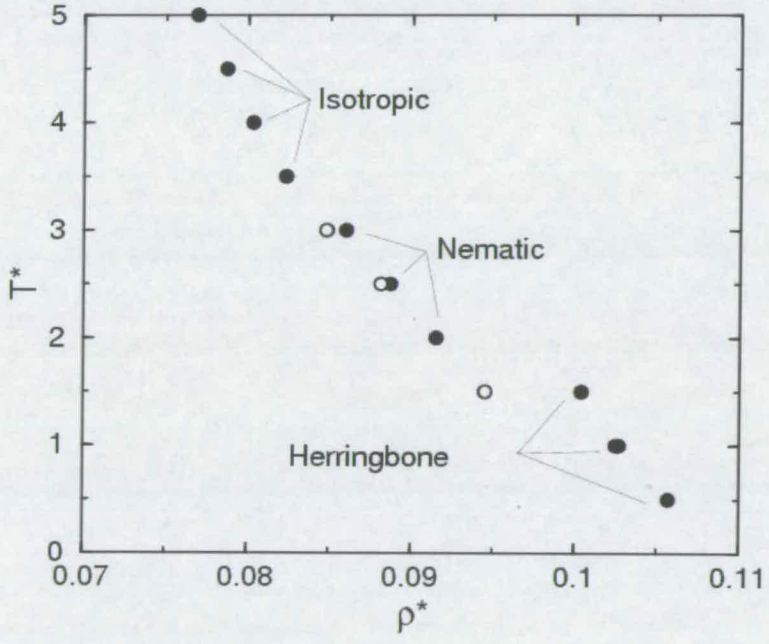

Figure 4.25: Equation of state for $\gamma = 20°$ with $p^* = 4.0$ and $\mu^* = 0.0$. Filled circles denote simulation results obtained via heating and open circles simulation results from cooling. Error bars are smaller than the symbol size.

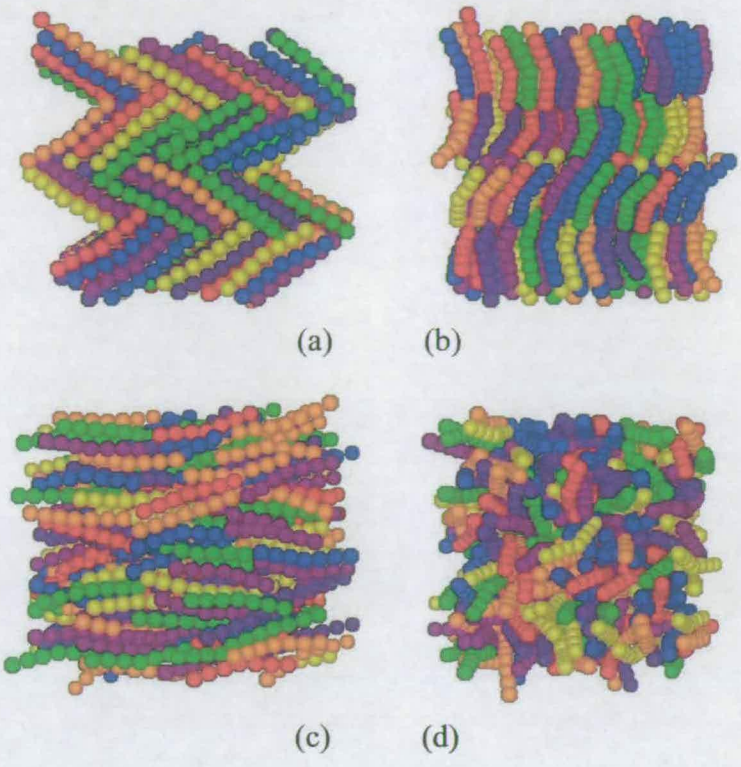

Figure 4.26: Snapshot representation for $\gamma = 20°$ with $p^* = 4.0$, (a) and (b) $\mu^* = 0.0$ and $T^* = 1.0$ and (c) and (d) $\mu^* = 0.0$ and $T^* = 1.5$ cooled from an equilibrated nematic phase.

T^*	Q^2_{22}
0.5	0.080(8)
1.0	0.335(5)
1.5	0.336(6)
2.0	0.04(2)
2.5	0.04(2)
3.0	0.04(2)
3.5	0.04(2)
4.0	0.02(1)
4.5	0.02(1)
5.0	0.02(1)

Table 4.1: Biaxial order parameters for $\gamma = 20°$, $\mu^* = 1.0$ with $p^* = 4.0$. The figure in parentheses represents the uncertainty in the last digit.

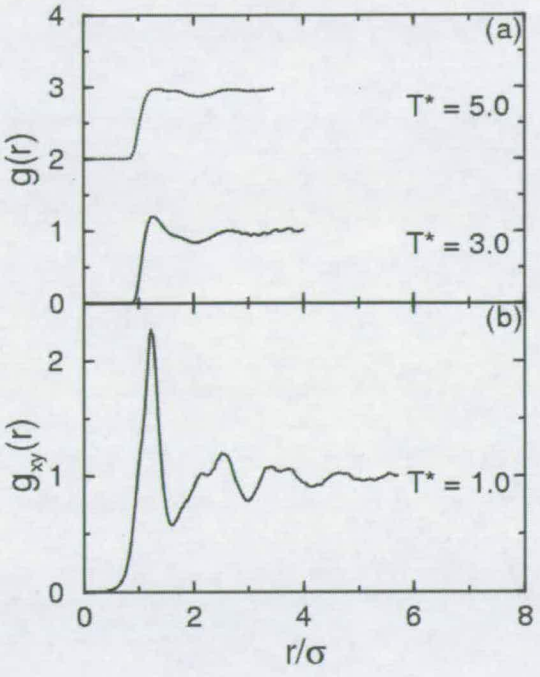

Figure 4.27: (a) Radial distribution data for $T^* = 3.0$ (solid line), 5.0 (dotted line) and (b) in-layer radial distribution data for $T^* = 1.0$ (solid line) with $\gamma = 20°$ with $p^* = 4.0$ and $\mu^* = 0.0$. Plots have been displaced by two units for clarity.

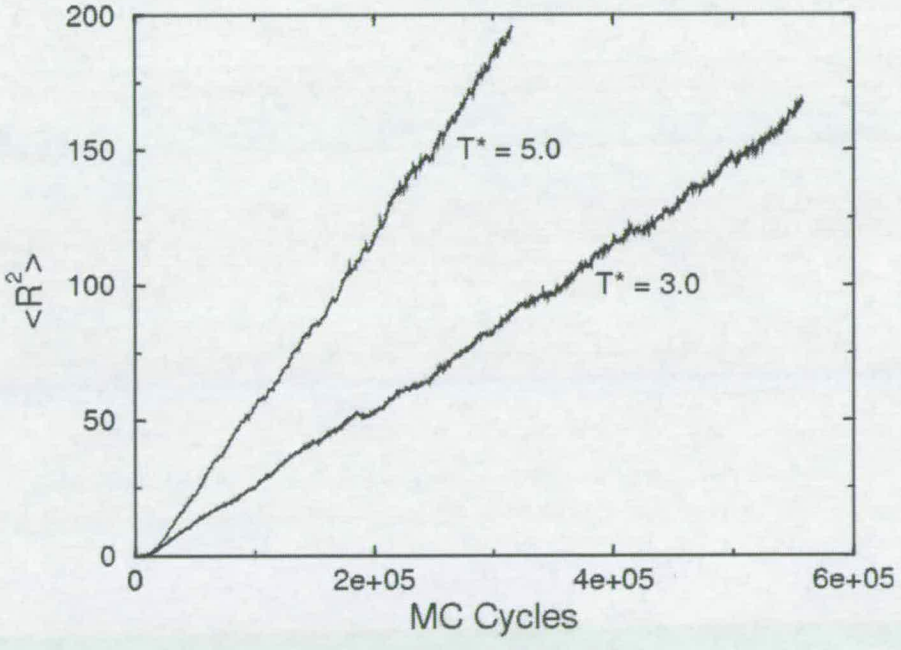

Figure 4.28: Mean squared displacement data for $\gamma = 20°$ with $p^* = 4.0$ and $\mu^* = 0.0$ with $T^* = 3.0$ (solid line) and 5.0 (dotted line).

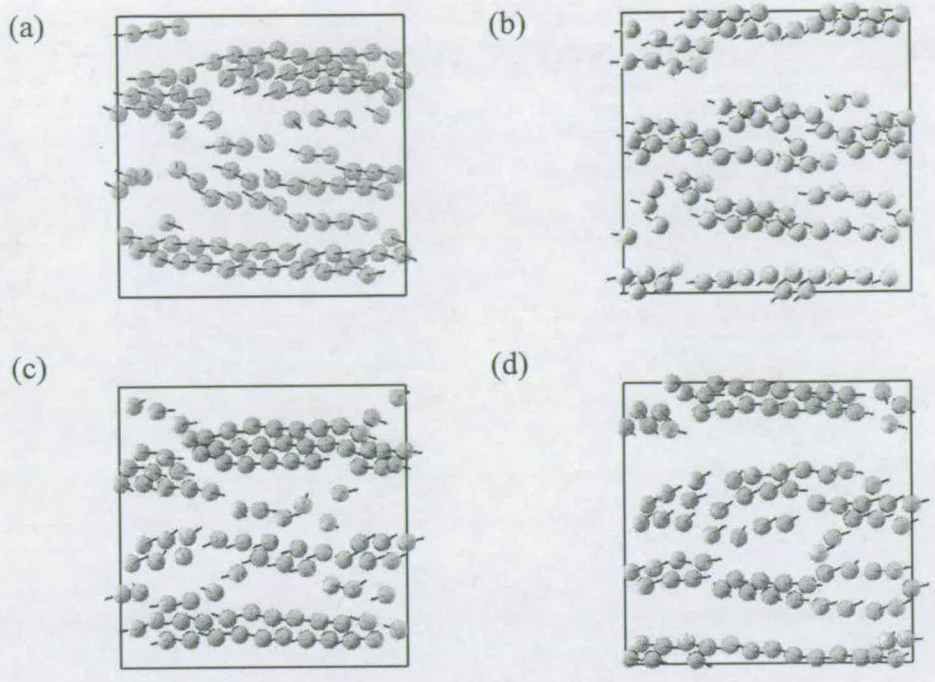

Figure 4.29: In-layer snapshot representations for $\gamma = 20°$ with $p^* = 4.0$, $\mu^* = 0.0$ and $T^* = 1.0$: (a) molecules $1 - 100$; (b) molecules $101 - 200$; (c) molecules $201 - 300$; (d) molecules $301 - 400$. The black line indicates the direction of the dipole vector (in this case $\mu^* = 0.0$) for each molecule and layers are perpendicular to the Z-axis.

$Q_{00}^2 \sim 0.7$ values on account of the random tilt directions of the layers and a transition to the nematic phase marked by a increase in Q_{00}^2 between $T^* = 1.5$ and $T^* = 2.0$. The nematic-isotropic phase transition is signalled by a drop in Q_{00}^2 over the range $3.0 \leq T^* \leq 3.5$.

$\mu^* = 1.0$

At low temperature, $T^* = 1.0$, we found an unusual crystalline phase, shown in Figs. 4.32(a) and (b). From the snapshots it can be seen that there is free volume in-between molecules and that the starting four layer structure has been partially lost and as such will not yield representative bulk phase behaviour. Figure 4.33 shows in-layer snapshots of simulation configurations. In Fig. 4.33(a) the molecules are highly ordered and in subsequent snapshots, molecules along the bottom face are ordered. The dipole orientations and apical sphere positions have been randomised, suggesting partial melting of the perfectly ordered phase. Further melting is prevented as the gradient of $\langle R^2 \rangle$ tends to zero. This would

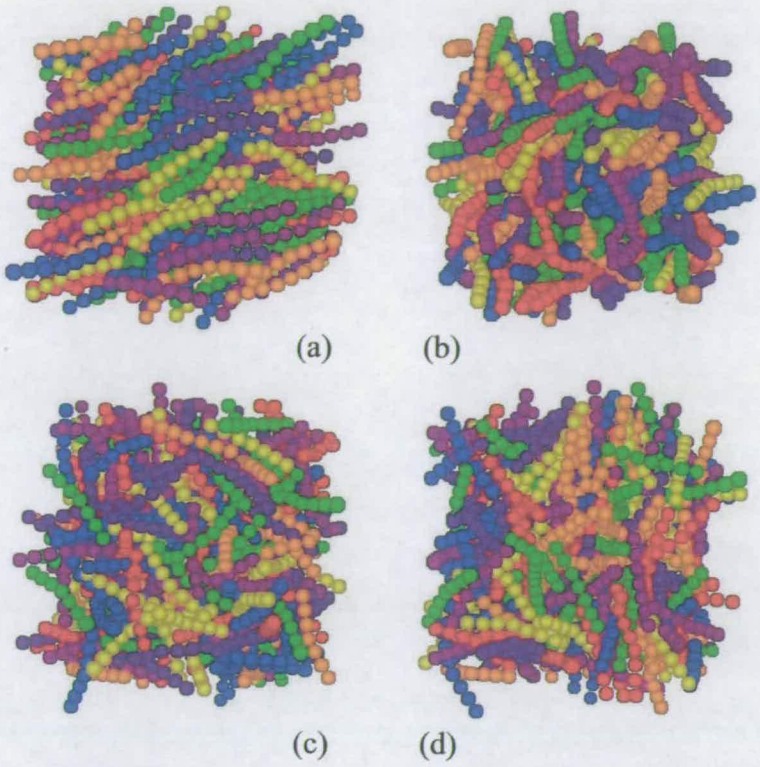

Figure 4.30: Snapshot representation for $\gamma = 20°$ with $p^* = 4.0$, (a) and (b) $\mu^* = 0.0$ and $T^* = 3.0$ and (c) and (d) $\mu^* = 0.0$ and $T^* = 5.0$.

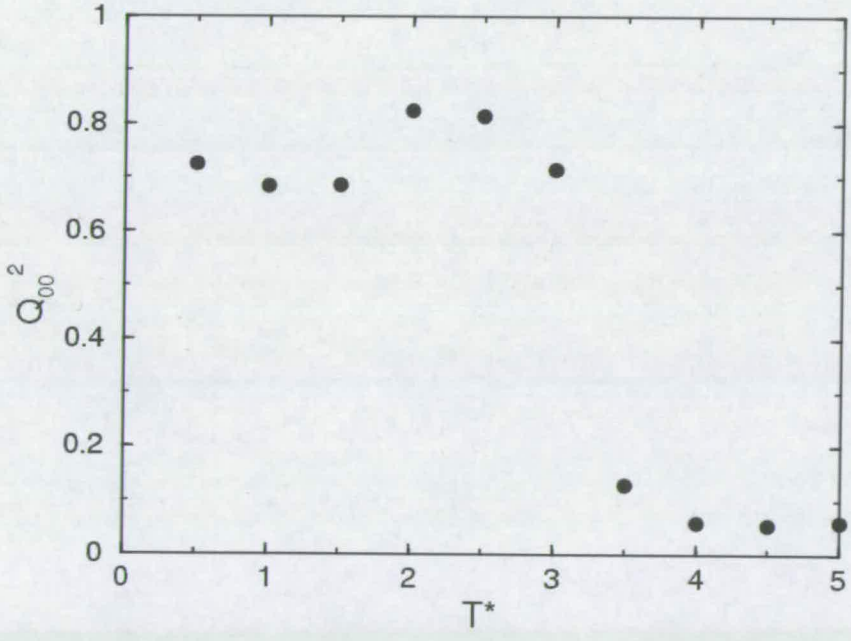

Figure 4.31: Uniaxial order parameter plotted as a function of temperature for $\gamma = 20°$ with $p^* = 4.0$ and $\mu^* = 0.0$. Error bars are smaller than the symbol size.

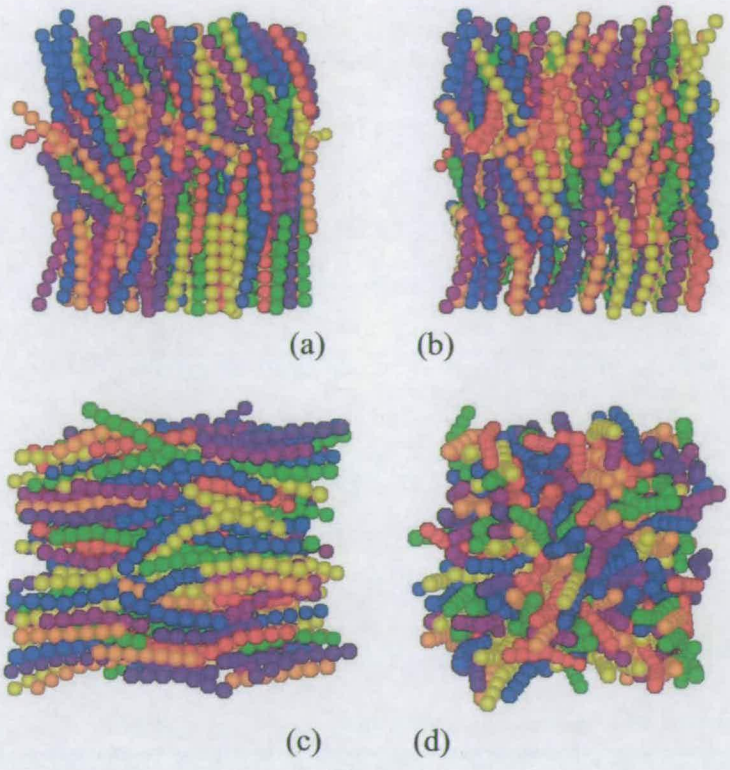

Figure 4.32: Snapshot representation for $\gamma = 20°$ with $p^* = 4.0$, (a) and (b) $\mu^* = 1.0$ and $T^* = 1.0$ and (c) and (d) $\mu^* = 1.0$ and $T^* = 1.0$ cooled from an equilibrated nematic phase.

suggest that an antiferroelectric crystal has been formed. Monte Carlo techniques are inadequate at low temperatures, the mean displacement is vanishingly low and we are unlikely to overcome kinetic barriers. The low displacement will result in 'noisy' radial distribution plots at low temperature.

To investigate the stability of this phase, we cooled a fully equilibrated nematic phase from $T^* = 2.0$ and $\mu^* = 0.0$. After cooling the final equilibrium density was $\rho^* = 0.0992$, which is far greater than the $\rho^* = 0.0736$ obtained via heating. Snapshots of the final simulation configuration are shown in Figs. 4.32(c) and (d). The radial distribution data is shown in Fig. 4.34. For $T^* = 1.0$ the peaks are sharply peaked, which is typical of solid phases. As would be anticipated for such a phase $\langle R^2 \rangle$ remains constant. As such this has been assigned as a glassy nematic phase.

Heating from $T^* = 2.0$, we obtain uniaxial nematic phase over the range $2.5 \leq T^* \leq 3.0$. Snapshots at $T^* = 3.0$ are shown in Figs. 4.35(a) and (b). Above $T^* = 3.5$ we find the isotropic phase as shown in Figs. 4.35(c) and (d). From a

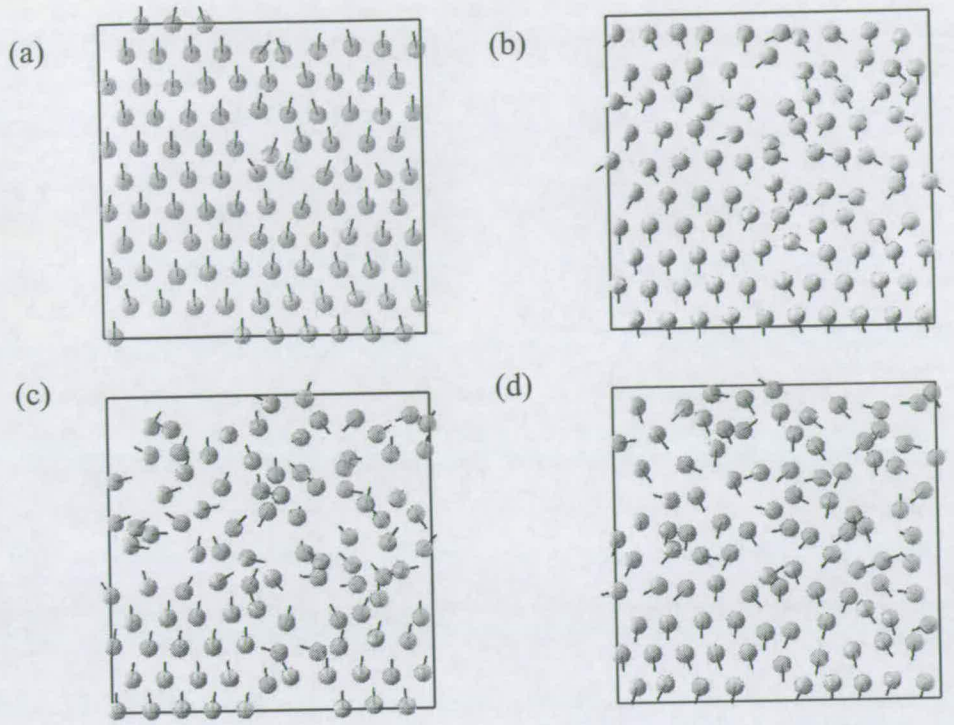

Figure 4.33: In-layer snapshot representations for $\gamma = 20°$ with $p^* = 4.0$, $\mu^* = 1.0$ and $T^* = 1.0$: (a) molecules $1 - 100$; (b) molecules $101 - 200$; (c) molecules $201 - 300$; (d) molecules $301 - 400$. The black line indicates the direction of the dipole vector for each molecule and layers are perpendicular to the Z-axis.

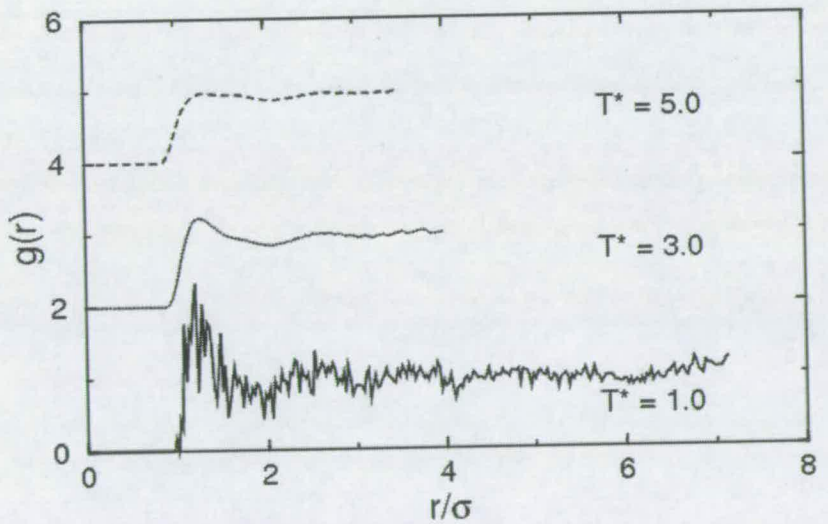

Figure 4.34: Radial distribution data for $T^* = 1.0$ (solid line), 3.0 (dotted line) and 5.0 (dashed line) for $\gamma = 20°$ with $p^* = 4.0$ and $\mu^* = 1.0$. Plots have been displaced by 2 units for clarity.

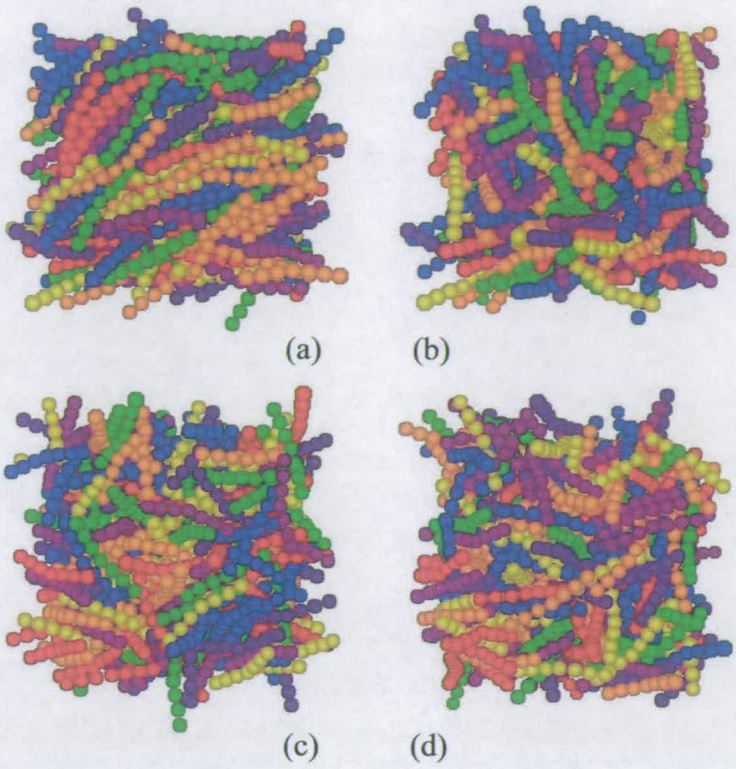

Figure 4.35: Snapshot representation for $\gamma = 20°$ with $p^* = 4.0$, (a) and (b) $\mu^* = 1.0$ and $T^* = 3.0$ and (c) and (d) $\mu^* = 1.0$ and $T^* = 5.0$.

plot of $\langle R^2 \rangle$ (Fig. 4.36), we can clearly see the increase in the gradients of $\langle R^2 \rangle$ in the nematic and isotropic phases.

The equation of state of CPMs with $\gamma = 20°$ along an isobar with $p^* = 4.0$ and $\mu^* = 1.0$ is shown in Fig. 4.37.

A plot of Q_{00}^2 as a function of temperature is shown in Fig. 4.38. Below a $T^* = 2.0$ we find a glassy nematic phase, with $Q_{00}^2 > 0.8$. The nematic-isotropic phase is signalled by the drop in Q_{00}^2 between $T^* = 3.0$ and $T^* = 3.5$.

$\mu^* = 2.0$

Thermodynamic data for CPMs with $\gamma = 20°$ along an isobar with $p^* = 4.0$ and $\mu^* = 2.0$ is shown in Table 4.2. At $T^* = 1.5$ the final equilibrium densities in the cubic and cuboidal cells are vastly different and should have converged to a common density. Snapshots of the final cubic configuration are shown in Figs. 4.39(a) and (b). Visually this appears similar to the phase observed in Figs. 4.32(c) and (d). Again there are significant free spaces in-between molecules. The density

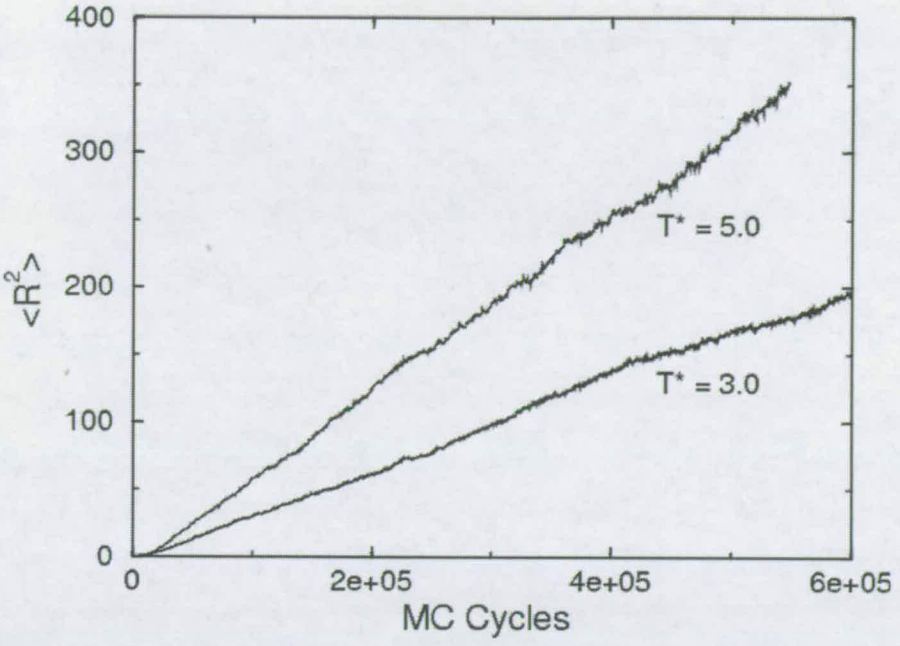

Figure 4.36: Mean squared displacement data for $\gamma = 20°$ with $p^* = 4.0$ and $\mu^* = 1.0$ with $T^* = 3.0$ (solid line) and 5.0 (dotted line).

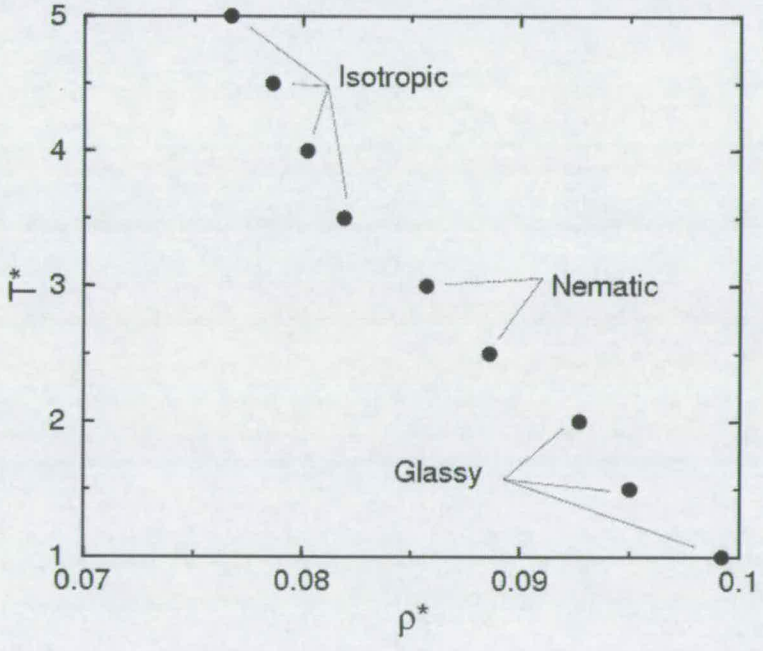

Figure 4.37: Equation of state for $\gamma = 20°$ with $p^* = 4.0$ and $\mu^* = 1.0$. Filled circles denote simulation results obtained via heating. Error bars are smaller than the symbol size.

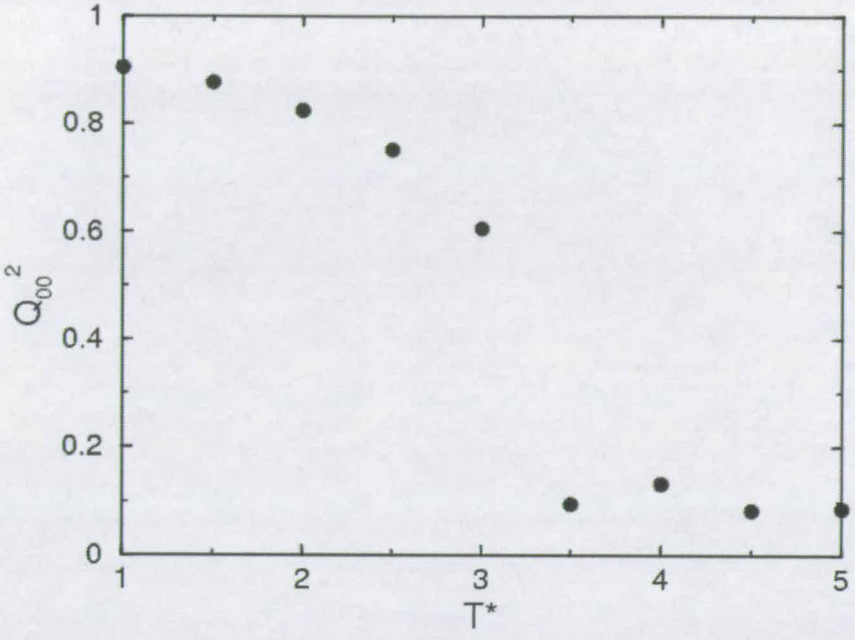

Figure 4.38: Uniaxial order parameter plotted as a function of temperature for $\gamma = 20°$ with $p^* = 4.0$ and $\mu^* = 1.0$. Error bars are smaller than the symbol size.

T^*	ρ^*	Cell
0.5	0.1058(1)	Cuboidal
1.0	0.0987(2)	Cuboidal
1.5	0.0840(1)	Cuboidal
1.5	0.0572(2)	Cubic
2.0	0.0620(1)	Cubic
2.5	0.0640(1)	Cubic

Table 4.2: Thermodynamic data for $\gamma = 20°$, $\mu^* = 2.0$ with $p^* = 4.0$. The figure in parentheses denotes the uncertainty in the last digit.

increases upon heating as shown in Table 4.2. At these higher temperatures the molecules can occupy the free space observed in the lower temperature phases and this is possibly the cause of the increase in density rather than a phenomenological effect. In-layer snapshots, shown in Fig. 4.40 are similar to those presented in Fig. 4.33 and are indicative of an antiferroelectric solid. The results presented here are a result of heating simulations and require cooling simulation to further elucidate the phase behaviour.

4.2.3 $\gamma = 40°$

Here we present results for CPMs with $\gamma = 40°$ and μ^* in the range $0.0 - 2.0$.

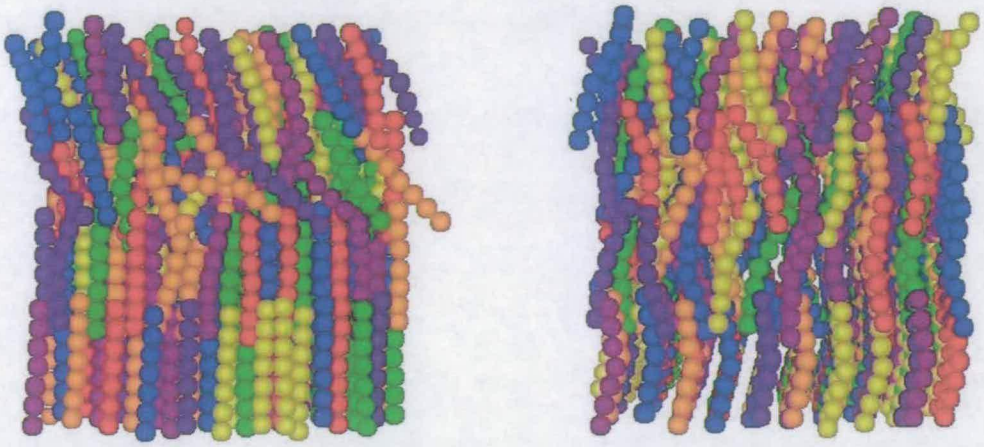

Figure 4.39: Snapshot representation for $\gamma = 20°$ with $p^* = 4.0$, (a) and (b) $\mu^* = 2.0$ and $T^* = 1.5$.

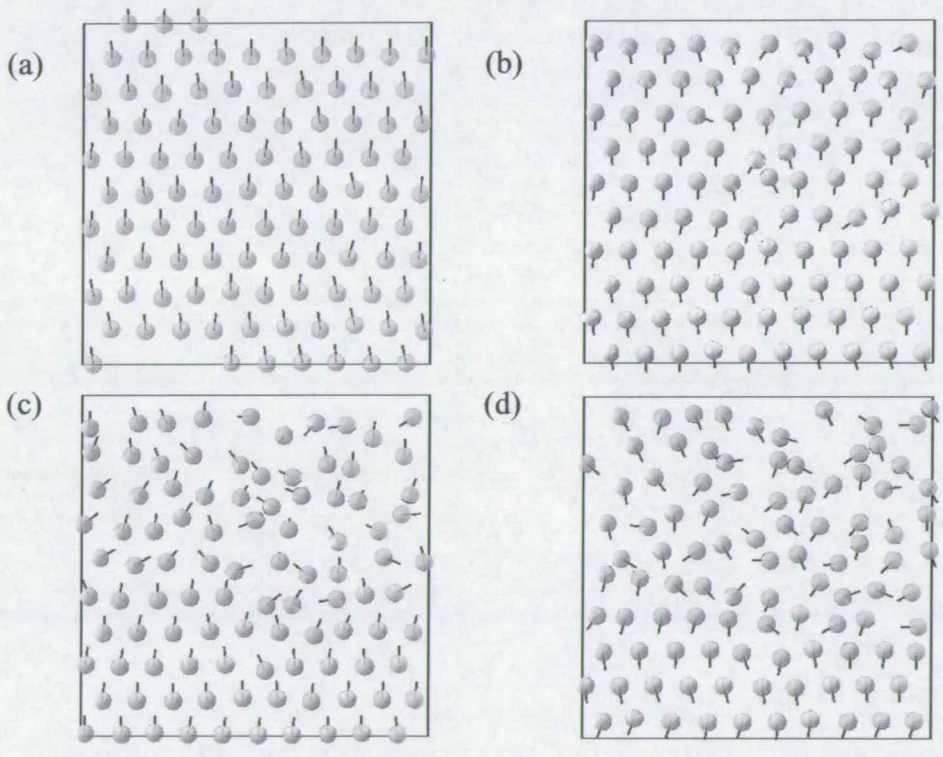

Figure 4.40: In-layer snapshot representations for $\gamma = 20°$ with $p^* = 4.0$, $\mu^* = 2.0$ and $T^* = 1.5$: (a) molecules $1 - 100$; (b) molecules $101 - 200$; (c) molecules $201 - 300$; (d) molecules $301 - 400$. The black line indicates the direction of the dipole vector (in this case $\mu^* = 0.0$) for each molecule and layers are perpendicular to the Z-axis.

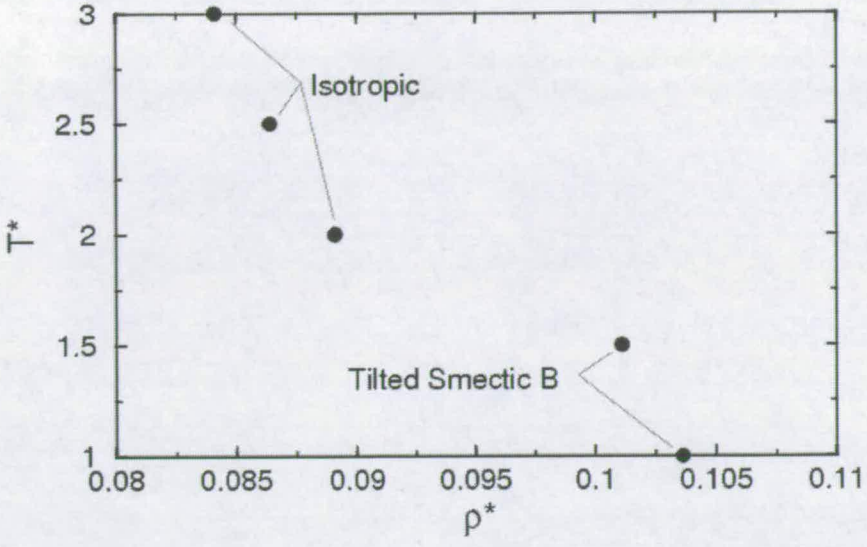

Figure 4.41: Equation of state for $\gamma = 40°$ with $p^* = 4.0$ and $\mu^* = 0.0$. Filled circles denote simulation results obtained via heating. Error bars are smaller than the symbol size.

T^*	Q^2_{00}	Q^2_{22}
1.0	0.355(6)	0.142(8)
1.5	0.39(1)	0.19(2)
2.0	0.05(1)	0.02(1)
2.5	0.093(7)	0.02(1)
3.0	0.061(8)	0.02(1)

Table 4.3: Order parameters for $\gamma = 40°$, $\mu^* = 0.0$ with $p^* = 4.0$. The value in parentheses denotes the uncertainty in the last digit.

$\mu^* = 0.0$

The equation of state for CPMs with $\gamma = 40°$ along an isobar with $p^* = 4.0$ and $\mu^* = 0.0$ is shown in Fig. 4.41. Snapshots at $T^* = 1.5$ are shown in Figs. 4.42(a) and (b). The resultant phase is highly tilted with $\phi = 50.6°$. As with the corresponding CLJM system (Sec. 3.2.3) we find no evidence of any nematic phases along this isobar. Examination of a radial distribution plot, shown in Fig. 4.43, exhibits a split peak at $r/\sigma \simeq 2.0$. This would suggest a smectic B phase. As such we assign this phase as a (highly) tilted smectic B phase. Equal numbers of layers are tilted in opposite directions. The biaxial order parameter, Q^2_{22} (Table 4.3) was seen to decay to < 0.2 as the layers become uncorrelated. As such we suggest that a super paraelectric phase is formed.

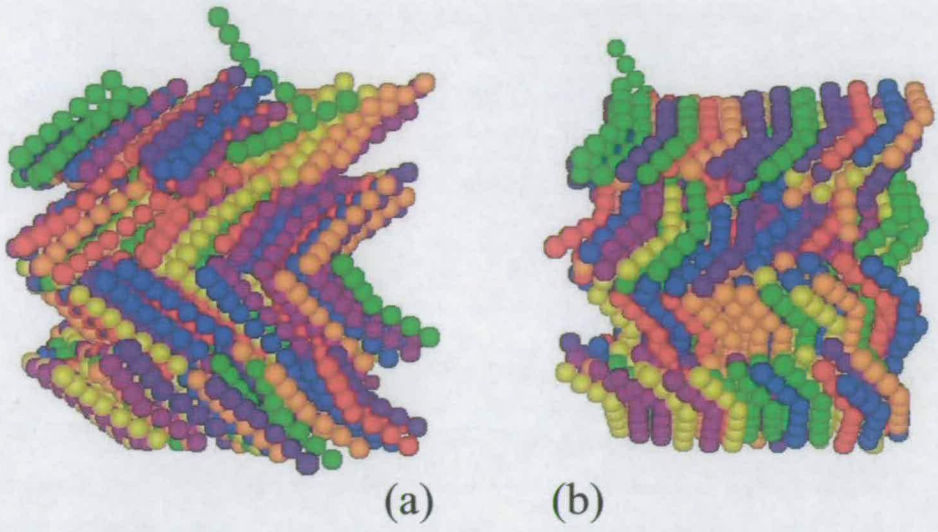

Figure 4.42: Snapshot representations for $\gamma = 40°$ with $p^* = 4.0$, $\mu^* = 0.0$ and $T^* = 1.5$.

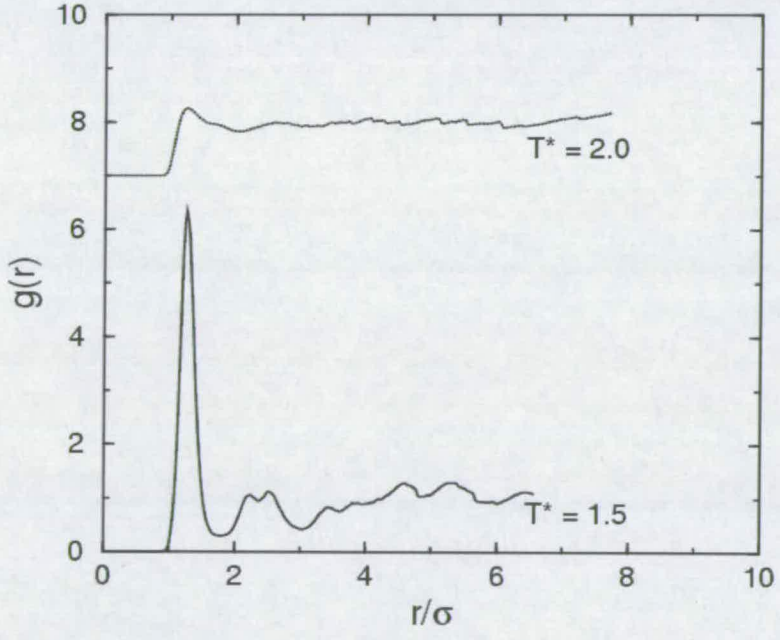

Figure 4.43: Radial distribution data for $T^* = 1.5$ (solid line) and 2.0 (dotted line) for $\gamma = 40°$ with $p^* = 4.0$ and $\mu^* = 0.0$. Plots have been displaced by 7 units for clarity.

T^*	Q_{00}^2
1.0	0.324(7)
1.5	0.321(5)
2.0	0.324(7)
2.5	0.122(6)
3.0	0.08(1)

Table 4.4: Uniaxial order parameter as a function of temperature for $\gamma = 40°$, $\mu^* = 1.0$ along an isobar with $p^* = 4.0$. The figure in parentheses denote the uncertainty in the last digit.

Table 4.3 shows the variation of the uniaxial order parameter as a function of temperature along an isobar with $p^* = 4.0$ and $\mu^* = 0.0$. The smectic-isotropic phase transition is clearly identifiable by a drop in Q_{00}^2 between $T^* = 1.5$ and $T^* = 2.0$.

$\mu^* = 1.0$

As with CPMs with $\gamma = 20°$ and $\mu^* > 1.0$, we again find an unusual solid phase, shown in Figs. 4.44(a) and (b). As we did not find a nematic phase and given the tendency for molcules to interlock upon cooling, we performed a series of simulations heating from a tilted smectic B phase as generated with $\mu^* = 0.0$ at a temperature of $T^* = 1.0$.

The equation of state for CPMs with $\gamma = 40°$ along an isobar with $p^* = 4.0$ and $\mu^* = 1.0$ is shown in Fig. 4.45. Snapshots at $T^* = 2.0$ are shown in Figs. 4.44(c) and (d). This phase is highly tilted, with $\phi \simeq 50°$. This highly tilt angle is likely to be a remnant of the tilted smectic B phase starting configuration. The radial-distribution, $g(r)$, is shown in Fig. 4.46 is not indicative of a smectic B. As such this phase is tentatively assigned tilted smectic.

Upon heating to temperatures greater than $T^* = 2.5$, we find the isotropic phase. These are shown in Figs. 4.44(e) and (f). The inclusion of dipolar interactions have stabilised the low temperature phase, with the smectic-isotropic phase transition occuring at higher temperature compared to CPMs with $\mu^* = 0.0$.

The uniaxial order parameter as a function of temperature is presented in Table 4.4. The tilted smectic-isotropic phase transition is clearly identifiable by the drop in Q_{00}^2 between $T^* = 2.0$ and $T^* = 2.5$.

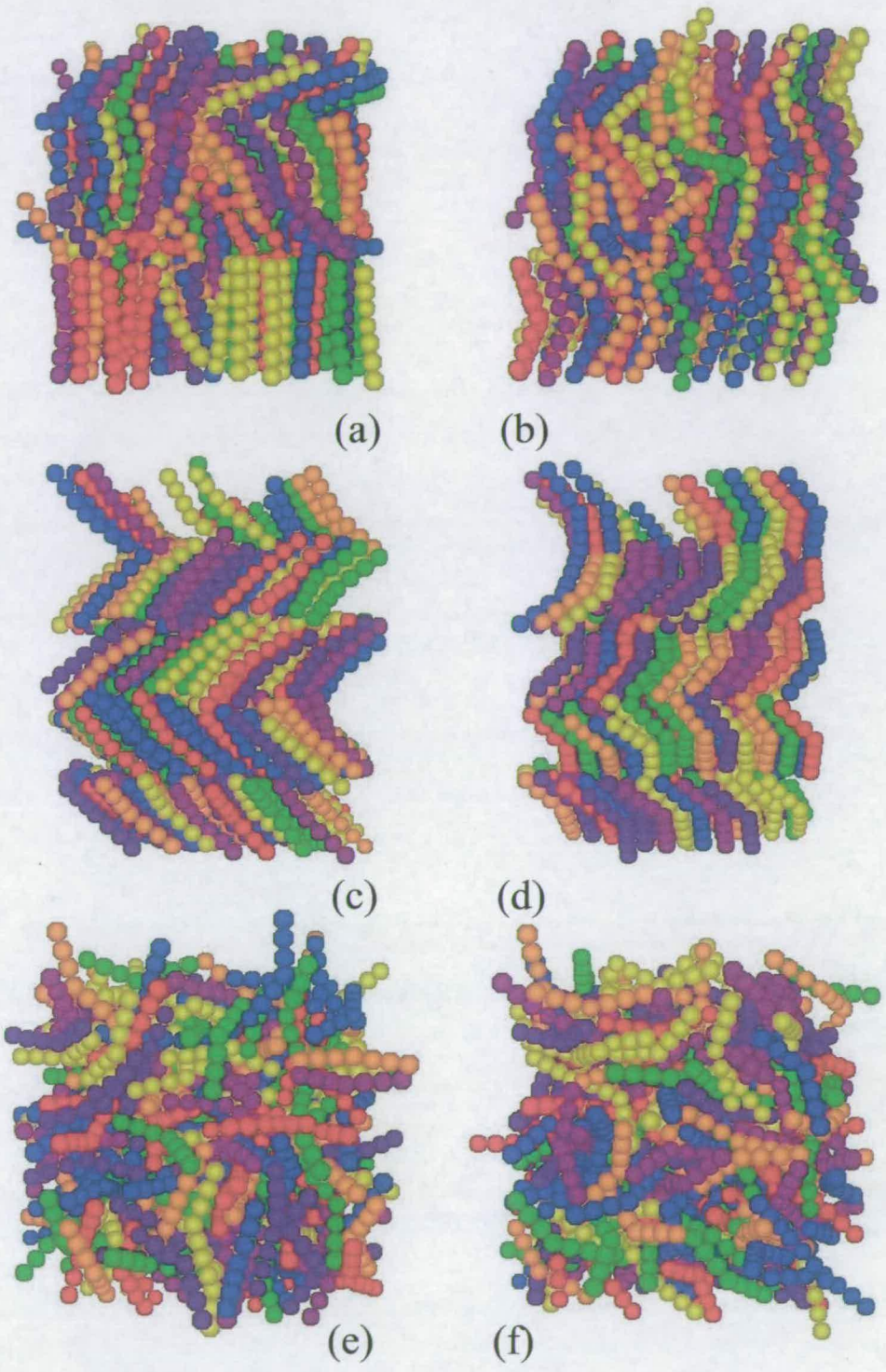

Figure 4.44: Snapshot representation for $\gamma = 40°$ with $p^* = 4.0$, (a) and (b) $\mu^* = 1.0$ and $T^* = 1.0$, (c) and (d) $\mu^* = 1.0$ and $T^* = 2.0$ and (e) and (f) $\mu^* = 1.0$ and $T^* = 2.5$.

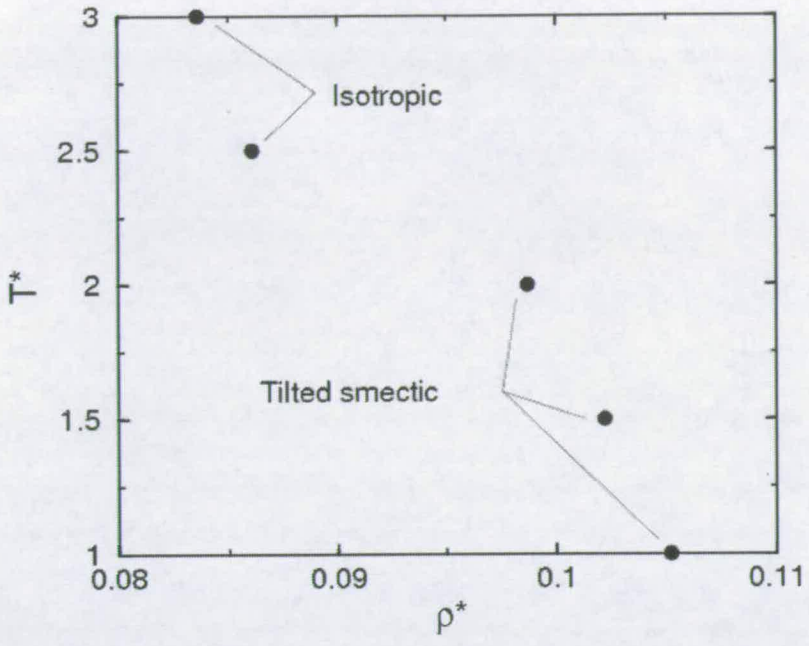

Figure 4.45: Equation of state for $\gamma = 40°$ with $p^* = 4.0$ and $\mu^* = 1.0$. Filled circles denote simulation results obtained via heating. Error bars are smaller than the symbol size.

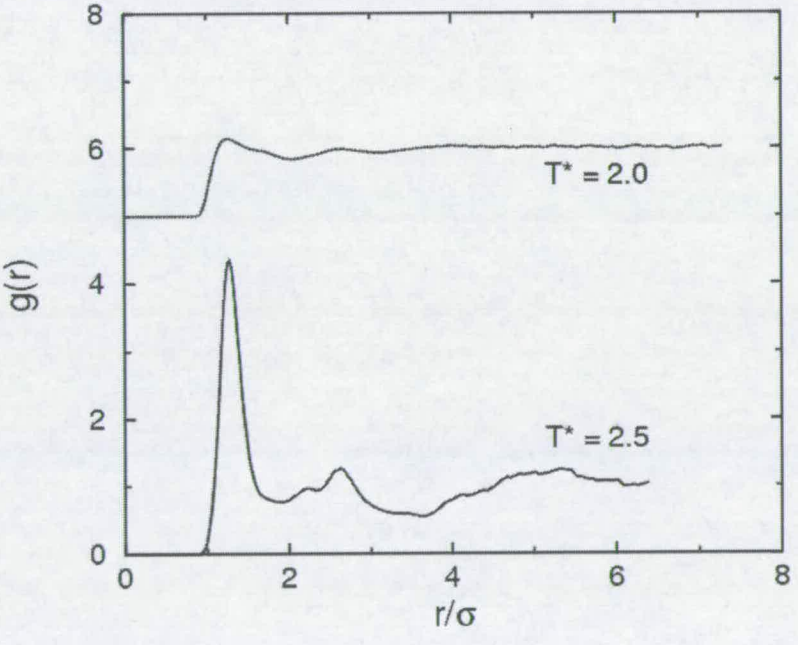

Figure 4.46: Radial distribution data for $T^* = 2.0$ (solid line) and 2.5 (dotted line) for $\gamma = 40°$ with $p^* = 4.0$ and $\mu^* = 1.0$. Plots have been displaced by 5 units for clarity.

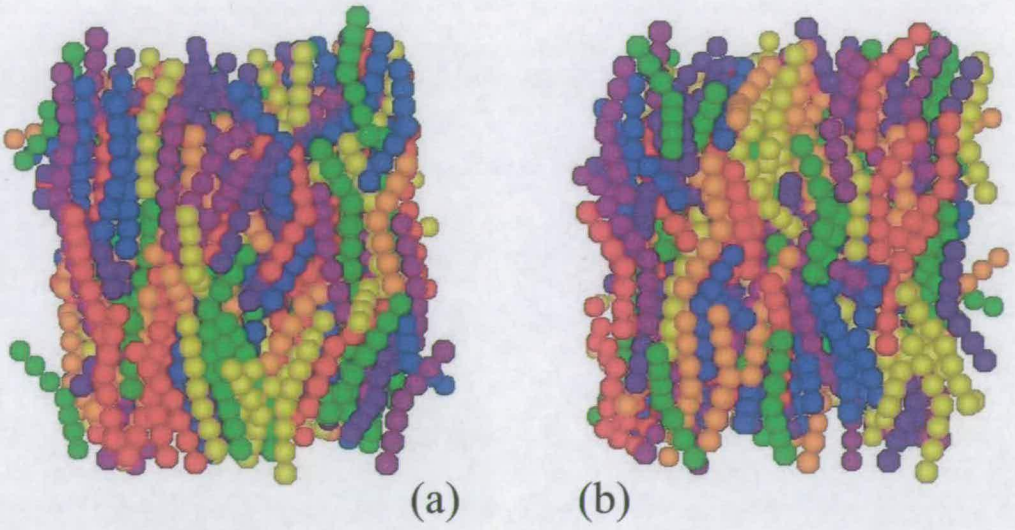

Figure 4.47: Snapshot representations for $\gamma = 40°$ with $p^* = 4.0$, $\mu^* = 2.0$ and $T^* = 1.0$.

$\mu^* = 2.0$

Snapshots of CPMs with $\gamma = 40°$ at $p^* = 4.0$, $T^* = 1.5$ and $\mu^* = 2.0$ are shown in Figs. 4.47(a) and (b). This phase is reminiscent of the crystal phases observed in systems with $\mu^* = 2.0$ and $\gamma = 0°$ and $\gamma = 20°$ and has been characterised therein.

4.3 Conclusions

In this chapter we have presented results from constant-pressure Monte Carlo simulations of model bent-core molecules (CPMs) composed of seven soft-spheres arranged in a rigid 'v' shape, with given external bond angle, γ. Model molecules interact via a simple repulsive sphere-sphere potential coupled with the dipole-dipole interaction. The phase behaviour of CPMs has been studied as a function of γ and μ^*.

With $\gamma = 0°$ (linear molecules) and $\mu^* = 0.0$, we have found isotropic, uniaxial nematic, untilted smectic-A and solid phases. The low temperature solid possesses a herring-bone structure with a molecular tilt of around $60°$ with respect to the layer normal. This tilt is almost twice the tilt found for CLJMs. The phase behaviour is consistent with previous work with linear molecules composed of 11 soft-spheres with a purely repulsive interactions [30], with formation of smectic and nematic liquid crystalline phases. At low temperature, our study and the

Paolini study report a tilted crystalline phase. The phases found here are also consistent with those found for CLJMs in chapter 3. The phase transitions are found at lower temperatures than for the corresponding CLJM case on account of the lack of attractive interactions. At low temperature a herringbone phase is observed as opposed to a pure crystalline phase.

With $\gamma = 0°$ and $\mu^* = 1.0$, we find isotropic, uniaxial nematic, untilted smectic-A and tilted crystalline phases. The inclusion of dipolar interactions clearly stabilises the low temperature layered phases, preventing the formation of the herring-bone phase. The resultant low-temperature phase is a tilted solid phase, with a tilt angle of $\sim 21°$ observed. This increase in mechanical stability of the layered phases arises as a result of the dipolar interactions. The lower tilt angle observed is to maximise the dipole nose-to-tail interaction. The results presented here are consistent with those of hard spherocylinders with a transverse dipole by Levesque *et al.* [53].

With $\gamma = 0°$ and $\mu^* = 2.0$, we find isotropic, tilted smectic B and tilted crystalline phases. Increasing the dipole magnitude further stabilises the layered phases. The low temperature tilted phase is tilted to $\sim 14°$ and the smectic B phase tilted to $\sim 17°$.

With $\gamma = 20$ and $\mu^* = 0.0$, this work has found isotropic, uniaxial nematic and herring-bone solid phases. The molecular tilt in the herringbone phase is $\sim 53°$ with respect to the layer normal. The enhanced stability of the nematic phase found for the CLJM system was not found here. Again phase transitions occur at lower temperature than found for the apolar molecules with attractive interactions.

With $\gamma = 20$ and $\mu^* = 1.0$, we find isotropic and nematic phases. At low temperatures we find a metastable nematic phase (from a cooling simulation) and an unusual crystalline phase arising from heating. Increasing the dipole moment to $\mu^* > 1.0$, gives rise to peculiar phase behaviour. At low temperatures a phase similar to that found at low temperature with heating and $\mu^* = 1.0$ is found. Heating further causes the density to increase, which is unphysical.

With $\gamma = 40°$ and $\mu^* = 0.0$, we find an isotropic phase and a highly tilted smectic B phase, which is tilted to $\sim 50°$ with respect to the layer normal. This is similar to the phase behaviour found for apolar molecules with attractive interactions, albeit with phase transitions at lower temperatures. Heating a low-temperature

phase with $\mu^* = 1.0$ yields similar phases, with the smectic-isotropic phase transition at slightly higher temperature. Simulations with $\mu^* = 1.0$ yielded unusual phase behaviour, similar to that found for $\gamma = 20°$.

As with the apolar system (chapter 3), we do not find any chiral phases, be they ferroelectric or antiferroelectric. In these simulations the molecular tilt developed spontaneously, however the overall biaxiality did not persist for the duration of the simulation results. At low-temperature the molecular tilt is high ($\phi > 50°$). This molecular tilt is likely to represent a balance of enthalpy and entropy. To clarify this issue absolute free energy calculations could be performed. Inclusion of dipolar interactions *decreases* the molecular tilt observed in these systems. As a consequence, dipolar interactions are unlikely to give rise to chiral phases, although the phase behaviour of polar bent-core molecules with attractive interactions remains to be determined. This is supported by Emelyaneko and Osipov [63], who investigated the influence of attractive dispersion interactions. The attractive interactions created background energy and do not perturb the structures formed [31].

With linear molecules, increasing the dipole strength stabilises the layered phases (with a decrease in tilt to $\phi \sim 20°$) and with $\mu^* > 1.0$, the nematic phase is lost as a consequence of this extra stabilisation. The in-layer structures presented here require full characterisation.

For bent-core molecules ($\gamma = 20°, 40°$) dipolar interactions raise unusual phase behaviour. It is unclear at this point whether this unusual phase behaviour is an artefact of the simulations employed. The dipoles are restricted along a given axis and this may preclude the molecules tilting to achieve a balance between enthalpy and entropy. As a consequence the molecules remain perfectly aligned at a given separation, which may explain the free space seen in snapshots of these systems, which allows for contraction of the system at higher temperatures. At low temperature Monte Carlo may be unsuitable as we observe vanishingly small mean displacements and unlikely to overcome any local kinetic barriers.

To ensure that these unusual phases are not a simulation artefact, larger scale simulations would be required, perhaps utilising the Reaction field technique as an alternative to the Ewald summation method used here as it is less computationally demanding than the Ewald summation method and would allow simulation of larger systems. Ideally the influence of dipolar interactions upon

CLJMs with γ in the range $0° - 40°$ and μ^* in the range $0.0 - 2.0$ would need to be investigated.

CHAPTER 5

5 sphere apolar bent-core molecules with and without attractive interactions

In previous chapters we have investigated the phase behaviour of molecules constructed using seven soft spheres, with and without attractive interactions (Chapters 3 and 4 respectively) and with dipoles (Chapter 4). With these systems the external bond angle, γ plays a pivotal role in the phase behaviour. An increase in bond angle, γ, results in a slight reduction of the effective elongation. In this chapter we shall investigate the effect of reducing the molecular elongation by reducing the number of spheres to five.

Hard spherocylinders, which are found to closely mimic the packing of liquid crystalline phases have been studied intensively [64, 65, 66]. Veerman and Frenkel [64] investigated a series of systems with varying the length to diameter (L/D) ratio in the range $0 - 5$. For $L/D < 3.0$ only isotropic, and crystalline phases were observed, whilst with $L/D = 3.0$ a mechanically stable smectic phase is found [64]. For larger ratios of L/D stable smectic and nematic phases were present [64]. McGrother *et al.* [65] re-examined the effect of L/D ratio on phase behaviour. Below $L/D = 3.0$ the spherocylinders approach the hard sphere limit and give rise to crystalline and isotropic phases. Increasing $L/D > 3.0$ increases the stability of the smectic A phase prior to the nematic phase as the spherocylinders are lengthened [65]. Bolhuis and Frenkel [66] mapped the entire phase diagram of spherocylinders as a function of the L/D ratio from $0 \rightarrow \infty$. At low L/D isotropic-smectic A-crystal and isotropic-nematic-smectic A triple points were observed at $L/D = 3.1$ and $L/D = 3.7$, respectively [66]. The nematic phase is increasingly stabilised with respect to the smectic A at higher ratios of L/D. At the close packed limit, two crystal phases are observed. At low L/D the layers

are shifted with respect to another and can intertdigitate slightly. As $L/D \rightarrow \infty$ layers are directly adjoin neighbouring layers, i.e. spherocylinders sit on top of one another [66].

Vega *et al.* [67] investigated the phase behaviour of a series of linear tangent hard sphere models constructed from $3-7$ hard spheres. In a system with three spheres an isotropic fluid and ordered solid were observed. Increasing the number of spheres to five resulted in the formation of a smectic A phase in addition to the isotropic fluid and ordered solid phases. Increasing the number of spheres to > 6, resulted in the formation of isotropic, nematic and smectic A liquid crystalline phases [67].

The phase behaviour of Gay-Berne ellipsoids with fixed length to width ratio has been investigated [68, 69]. Brown *et al.* [70] have investigated the phase behaviour of Gay-Berne ellipsoids as a function of the length to width ratio. As the length to width ratio is increased an 'island' of smectic A stability is formed which extends to lower and higher temperatures above a critical length to width ratio. The isotropic-nematic phase transition is also shifted to lower density (and pressure) at a given temperature as the length to width ratio is increased [70].

Linear Lennard-Jones chains have been studied by Perera and Sokolic [71] and Galindo *et al.* [42]. Perera and Sokolic investigated the phase behaviour of two-, three- and five- site Lennard-Jones chains with the intramolecular sphere-sphere distance $\simeq 0.5\sigma$, where σ is the range parameter in the Lennard-Jones potential (Eqn. 5.2). This system did not yield any orientationally ordered fluid phases. Galindo *et al.* studied the phase behaviour of $3-$ and $5-$sphere linear Lennard-Jones chains with the intramolecular sphere-sphere set equal to σ. As with the Perera and Sokolic study no liquid crystalline phases were observed [42]. Cinacchi *et al.* [72] investigated the phase behaviour of linear chains constructed from nine repulsive spheres and Paolini *et al.* [30] performed simulations with a linear chain of eleven repulsive spheres. As would be anticipated a full range of liquid crystalline phase behaviour was observed [30, 72]. The phase behaviour of flexible Lennard-Jones chains has been investigated, albeit with no liquid crystalline phases reported [73, 74, 75].

In this chapter we shall present simulation results of a simple site-site model constructed with 5 spheres for a series of molecules (Fig. 5.1) with γ in the range $0°-40°$ with and without attractive interactions to investigate the effect of elongation on the phase behaviour of our simple model and by comparison with results

for molecules constructed from 7 spheres (Chapters 3 and 4) and as a precursor for systems with flexible tails.

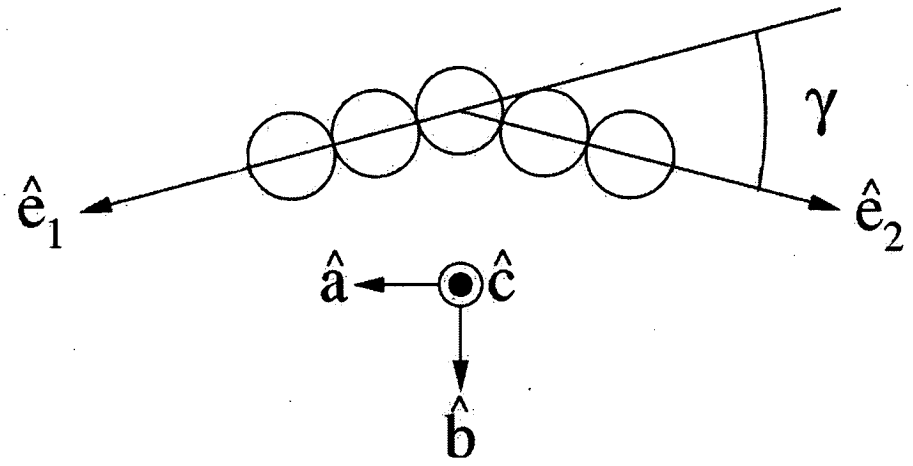

Figure 5.1: The composite of soft spheres model with a 5-sphere core.

5.1 Simulation techniques

We performed constant pressure, constant temperature Monte Carlo (NpT-MC) of N_m molecules in a cuboidial or cubic simulation cell with periodic boundary conditions applied [33, 34]. For systems without attractive interactions the sphere-sphere interaction potential is given by,

$$u = 4\epsilon \left(\frac{\sigma}{r_{ij}}\right)^{12}. \tag{5.1}$$

For the system with attractive interactions, the sphere-sphere interaction potential is,

$$u = 4\epsilon \left[\left(\frac{\sigma}{r_{ij}}\right)^{12} - \left(\frac{\sigma}{r_{ij}}\right)^{6}\right], \tag{5.2}$$

where ϵ is the potential well depth, σ is the Lennard-Jones sphere diameter, and r_{ij} is the pair separation. In this study each molecule consists of 5 soft-spheres arranged in a rigid 'v' shape with sphere-sphere distance set to 1σ. The molecules interact via either equation 5.1 or 5.2: for brevity, we refer to these systems as composite repulsive molecules (CRMs) and composite Lennard-Jones molecules (CLJMs), respectively.

In the simulations one MC sweep consisted of one trial translation or one trial rotation per molecule and a single volume fluctuation. The rotation moves were performed using the Barker-Watts method [33]. Volume moves were carried out by sampling in $\ln V$ [33]. In the cuboidal simulations the dimension to be scaled (L_{xy} or L_z) was selected at random. All maximum displacement parameters were adjusted to give respective acceptance ratios of 50%.

Starting configurations

Starting configurations were prepared as per the route outlined in Chapter 3. Upon generation of the initial configurations, these were allowed to equilibrate under constant volume (NVT) Monte Carlo simulations at $\rho^* = 0.20$. This higher density yields a similar sphere density ($\rho_s \sim 1.0$) to that used for the 7 sphere systems.

For each system, we performed sequences of simulations starting at high density ($\rho^* = 0.20$), to ensure that the molecules tilted spontaneously, for bond angles $\gamma = 0°, 20°$ and $40°$. Once equilibrated, the temperature was raised until a transition to a homogeneous fluid phase (isotropic or nematic) was observed. We then switched over to a cubic simulation cell.

5.2 Simulation Results

5.2.1 5-sphere molecules without attractive interactions

In this section we describe the results of simulations of CRMs with γ in the range $0° - 40°$.

Linear molecules, $\gamma = 0°$

The equation of state of linear ($\gamma = 0°$) CRMs along an isobar with $p^* = 4.0$ is shown in Fig. 5.2. The equation of state has only two distinct branches, suggesting a loss of some or all liquid crystalline phases. Snapshots of a simulation configuration at a temperature of $T^* = 1.5$ are shown in Figs. 5.3(a) and (b). In this system the molecules are tilted to $\phi = 53.37°$ with respect to the layer normal. The radial distribution plot, shown in Fig. 5.4 exhibits short-range ordering, which is consistent with ordering found in herringbone phases discussed in Chapter 4. This is supported by a low gradient of $\langle R^2 \rangle$ as shown in Fig. 5.5.

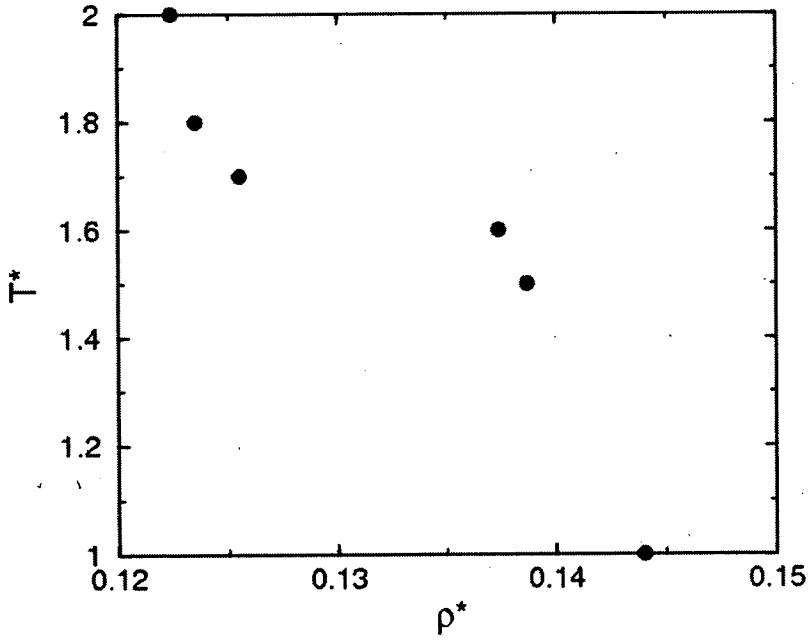

Figure 5.2: Equation of state for $\gamma = 0°$ with $p^* = 4.0$ for CRMs interacting via a simple repulsive potential. Error bars are smaller than the symbol size.

Raising the temperature slightly to $T^* = 2.0$ yields an isotropic phase, as shown in Figs. 5.3(c) and (d). The radial distribution plot (Fig. 5.4) is indicative of such a phase. The $\langle R^2 \rangle$ plot (Fig. 5.5), as calculated using Eqn. 2.24, clearly shows the herringbone-isotropic phase transition with an order of magnitude increase in the gradient of $\langle R^2 \rangle$ upon entering the isotropic phase. We do not find any intermediate liquid crystalline phases. Examination of the nematic order parameter, Q_{00}^2 as a function of temperature, shown in Fig. 5.6 supports this finding. At low temperatures, the values of Q_{00}^2 are low (< 0.5) an account of the random tilt directions found. Any intermediate untilted smectic-A or nematic phases would

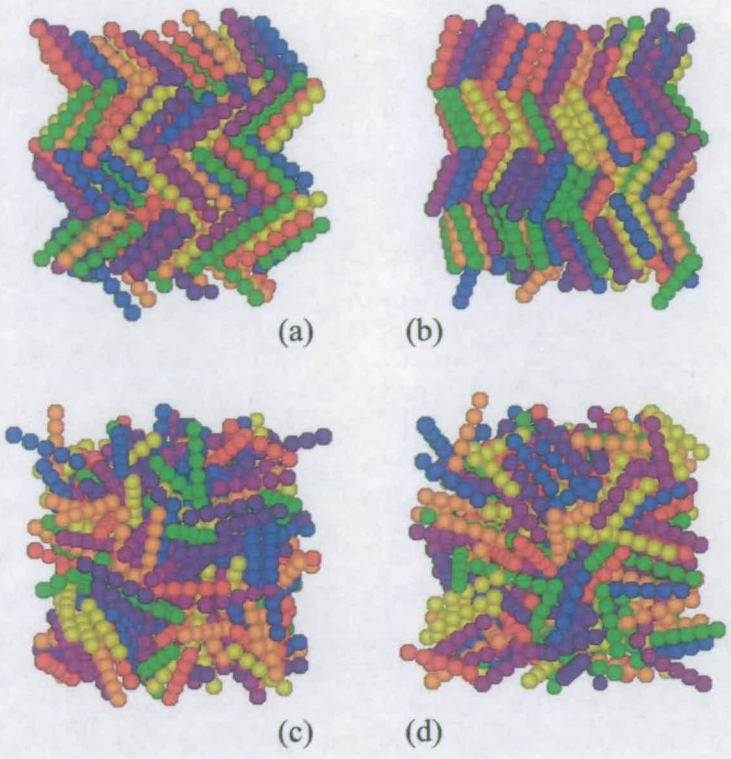

Figure 5.3: Snapshot representations of CRMs with $\gamma = 0°$, $p^* = 4.0$,(a) and (b) $T^* = 1.5$ and (c) and (d) $T^* = 2.0$.

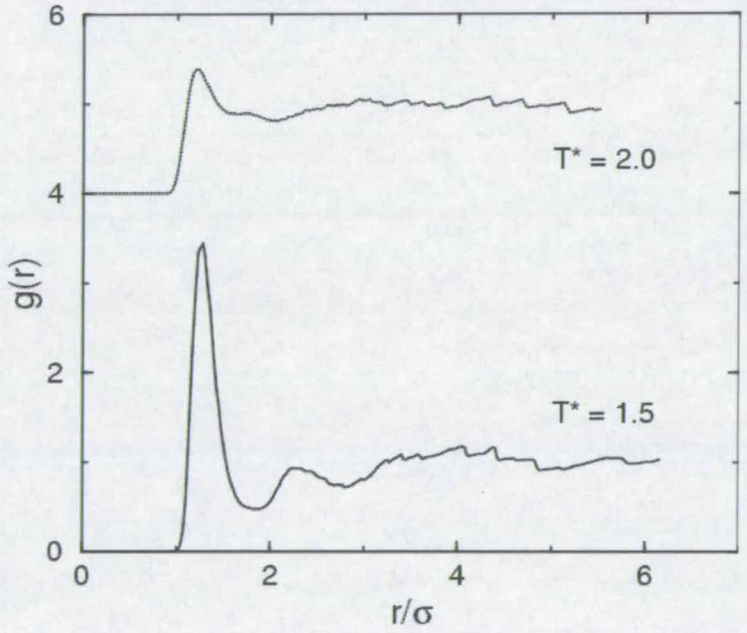

Figure 5.4: Radial distribution data for $T^* = 1.5$ (solid line) and 2.0 (dotted line) for $\gamma = 0°$ with $p^* = 4.0$ interacting via a simple repulsive potential. Plots have been displaced by 4 units for clarity.

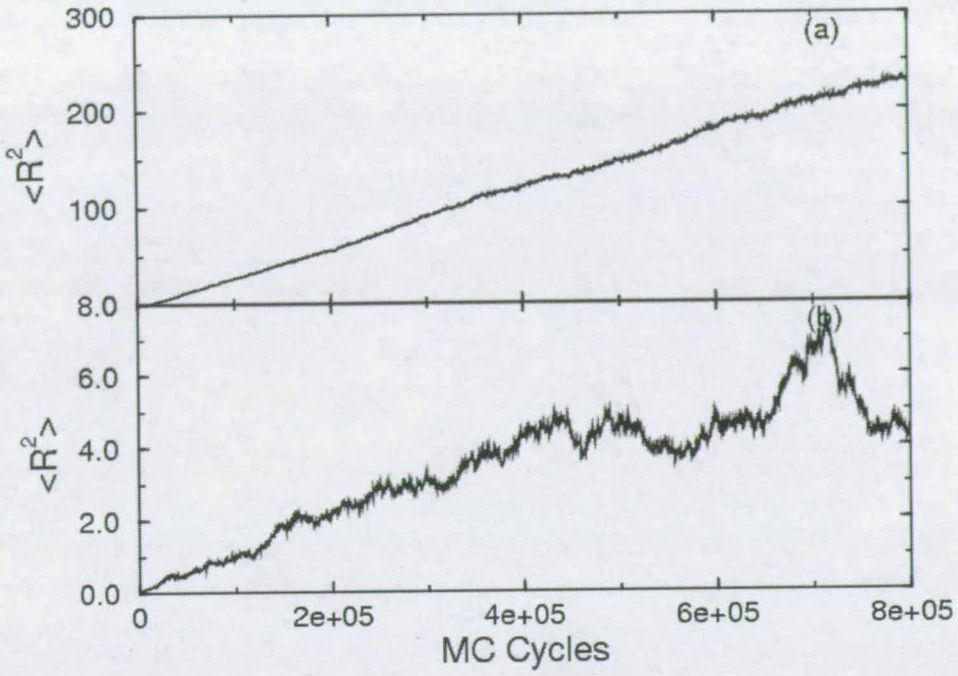

Figure 5.5: Mean squared displacement data for CRMs with $\gamma = 0°$, $p^* = 4.0$ and $T^* = 1.5$ (lower plot) and $T^* = 2.0$ (upper plot).

possess Q^2_{00} values greater than ~ 0.7. The herringbone-isotropic phase transition is signalled by a drop in Q^2_{00} between $T^* = 1.6$ and $T^* = 1.7$, which is supported by the equation of state (Fig. 5.2).

$\gamma = 20°$

Figure 5.7 shows the equation of state diagram for CRMs with $\gamma = 20°$. Snapshots of a simulation configuration at a temperature of $T^* = 0.5$ are shown in Figs. 5.8(a) and (b). From these snapshots we can clearly see that the layers are tilted and ϕ calculated to be $52.42°$. The radial distribution plot, shown in Fig. 5.9 exhibits short-range ordering. As such we suggest this is a herringbone phase. This is supported by a small slope of $\langle R^2 \rangle$, as shown in Fig. 5.10. We also observe Q^2_{00} values (< 0.3) (Table 5.1) as the system is highly tilted with random tilt directions. The biaxial order parameters, Q^2_{22} and the bulk polarisations are shown in Table 5.1. At low temperatures the values for both parameters are low. The low Q^2_{22} values would indicate a low degree of correspondence between adjacent layers. As the layer polarisations are disordered as shown by low bulk polarisation values, we suggest this is a super paraelectric phase.

Heating above a temperature of $T^* = 1.5$ yields the isotropic phase, as shown in Figs. 5.8(c) and (d). The herringbone-isotropic phase transition is signalled by

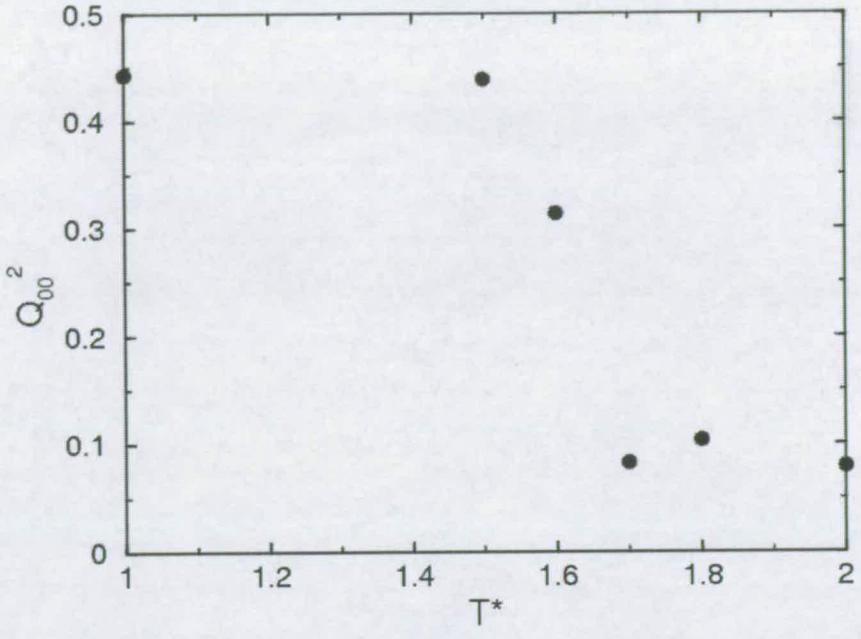

Figure 5.6: Nematic order parameter plotted as a function of temperature for CRMs with $\gamma = 0°$ along an isobar $p^* = 4.0$. Error bars are smaller than the symbol size.

T^*	Q_{00}^2	Q_{22}^2	P
0.5	0.218(4)	0.09(3)	0.07(2)
1.0	0.218(5)	0.03(2)	0.03(2)
1.5	0.12(2)	0.03(2)	0.02(2)

Table 5.1: Uniaxial (Q_{00}^2), biaxial (Q_{22}^2) order parameters and bulk polarisation (P) for CRMs with $\gamma = 20°$ along an isobar with $p^* = 4.0$. The figure in parentheses denotes the uncertainty in the last digit.

an order of magnitude increase in the slope of $\langle R^2 \rangle$ upon entering the isotropic phase, as shown in Fig. 5.10. No intermediate orientationally ordered fluid phases are found.

$\gamma = 40°$

The equation of state of CRMs with $\gamma = 40°$ along an isobar with $p^* = 4.0$ is shown in Fig. 5.11. Snapshots of a simulation configuration at a temperature of $T^* = 0.5$ are shown in Figs. 5.12(a) and (b). This is reminiscent of the herringbone phases reported for $\gamma = 0°, 20°$ systems. Here molecules are tiled to $\phi = 51.27°$ with respect to the layer normal. The radial distribution plot (Fig. 5.13) and a plot of $\langle R^2 \rangle$ as a function of MC cycles (Fig. 5.14) are both indicative of a herringbone

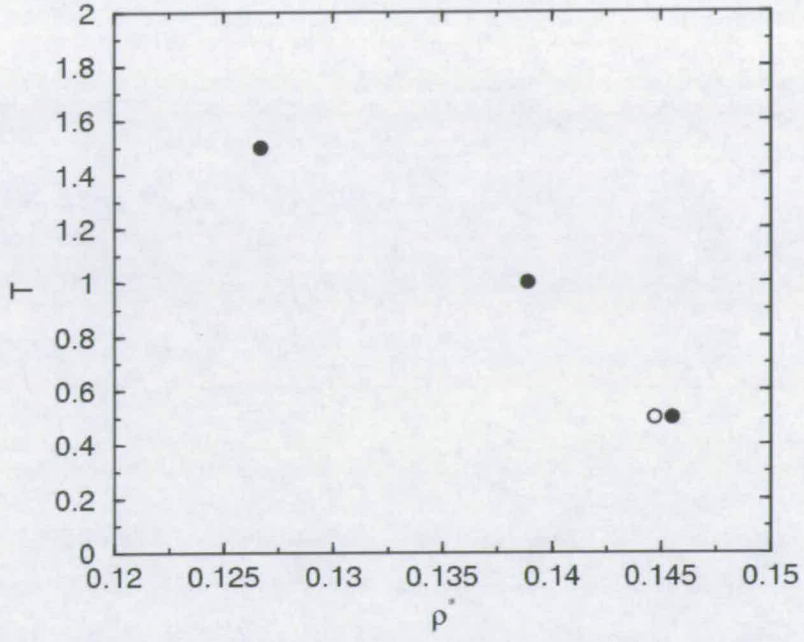

Figure 5.7: Equation of state for CRMs with $\gamma = 20°$ along an isobar with $p^* = 4.0$. Unfilled circles denote simulations in a cuboidal simulation cell, filled circles simulations performed in a cubic simulation cell. Error bars are smaller than the symbol size.

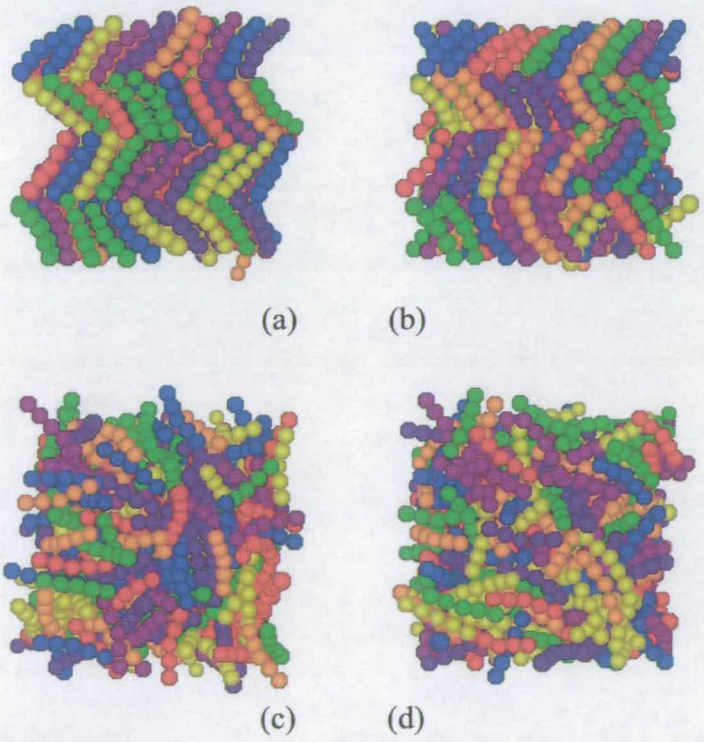

Figure 5.8: Snapshot representations of CRMs with $\gamma = 20°$, $p^* = 4.0$, (a) and (b) $T^* = 0.5$ and (c) and (d) $T^* = 1.5$.

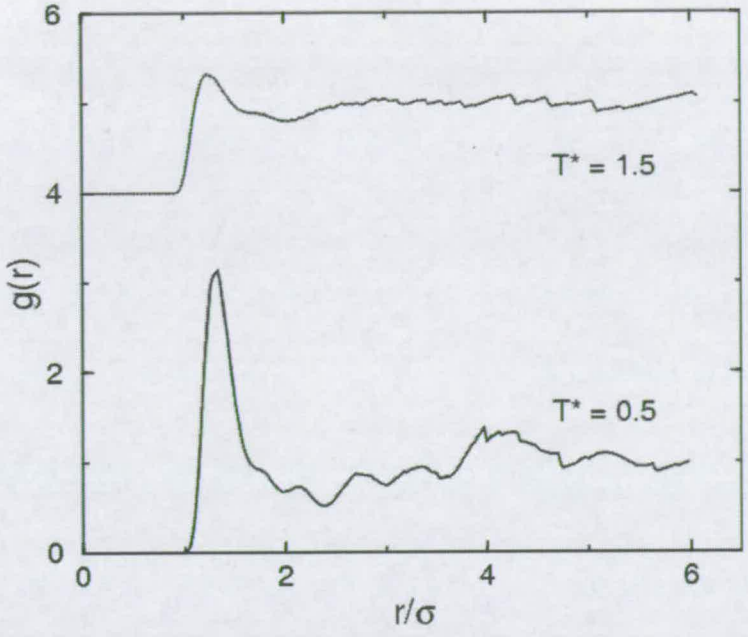

Figure 5.9: Radial distribution data for $T^* = 0.5$ (solid line) and 1.5 (dotted line) for $\gamma = 20°$ with $p^* = 4.0$ interacting via a simple repulsive potential. Plots have been displaced by 4 units for clarity.

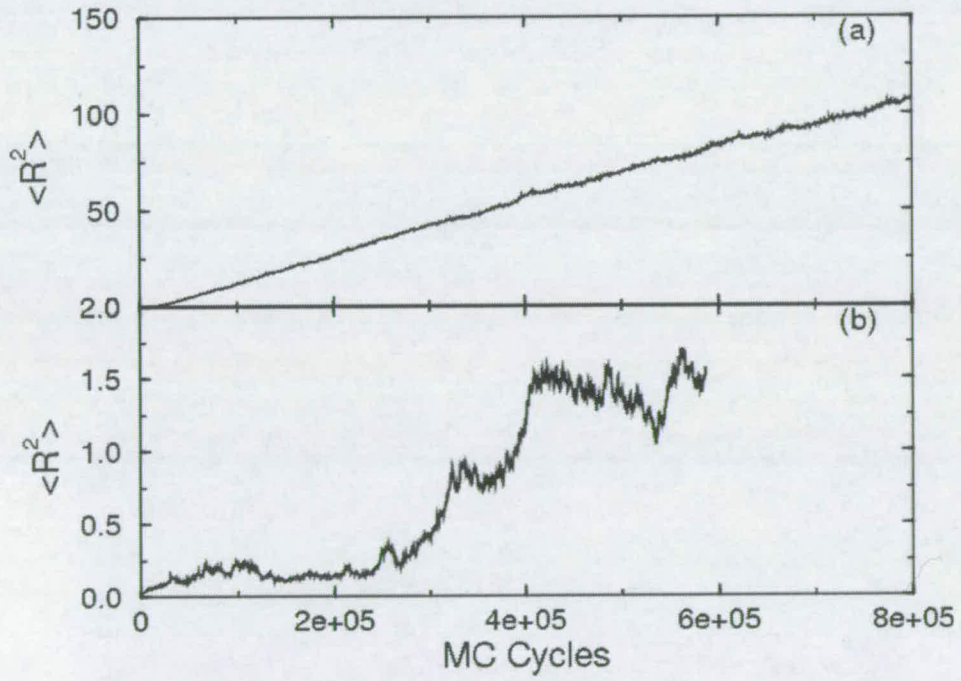

Figure 5.10: $\langle R^2 \rangle$ as a function of MC cycles for CRMs with $\gamma = 20°$, $p^* = 4.0$ and $T^* = 0.5$ (lower plot) and $T^* = 1.5$ (upper plot).

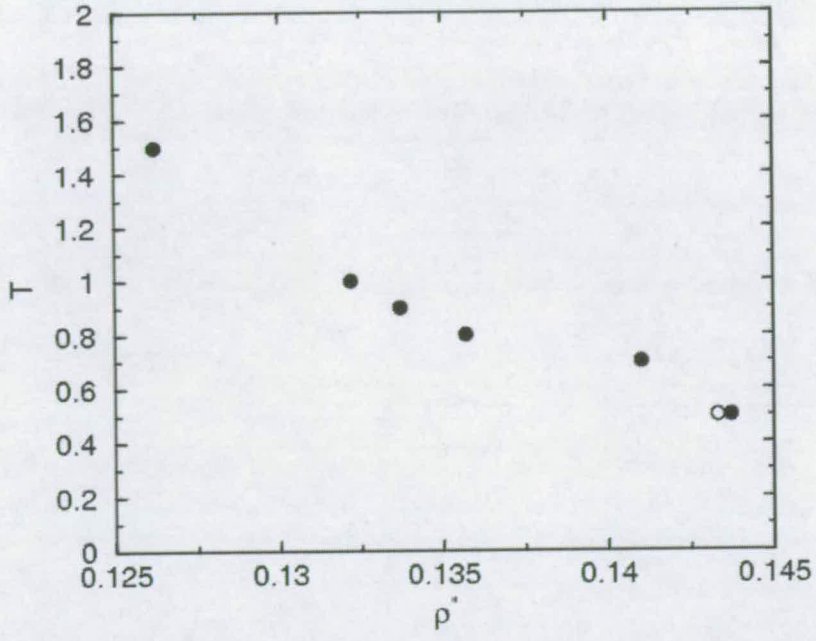

Figure 5.11: Equation of state for $\gamma = 40°$ with $p^* = 4.0$ for CRMs interacting via a simple repulsive potential. Unfilled circles denote simulations in a cuboidal simulation cell, filled circles in a cubic simulation cell. Error bars are smaller than the symbol size.

T^*	Q_{00}^2	Q_{22}^2	P
0.5	0.70(1)	0.080(5)	0.791(6)
0.7	0.64(1)	0.085(6)	0.761(8)
0.8	0.216(7)	0.02(1)	0.03(1)
0.9	0.108(7)	0.02(2)	0.02(2)
1.0	0.08(1)	0.03(2)	0.02(2)
1.5	0.06(2)	0.02(1)	0.03(2)

Table 5.2: Uniaxial (Q_{00}^2), biaxial (Q_{22}^2) order parameters and bulk polarisation (P) for CRMs with $\gamma = 40°$ along an isobar with $p^* = 4.0$. The figure in parentheses denotes the uncertainty in the last digit.

phase. The biaxial order parameters, Q_{22}^2, shown in Table 5.2, were seen to decay as the layers became uncorrelated. Interestingly, the bulk polarisation, also shown in Table 5.2, remain intact. This would suggest a ferroelectric herringbone phase has been formed. It is unclear whether this phase is metastable. Further investigation of this system is required, perhaps with free energy calculations.

Heating above a temperature of $T^* = 0.7$, the isotropic phase is found as shown in Figs. 5.12(c) and (d). The variation of the uniaxial order parameter, Q_{00}^2, as a

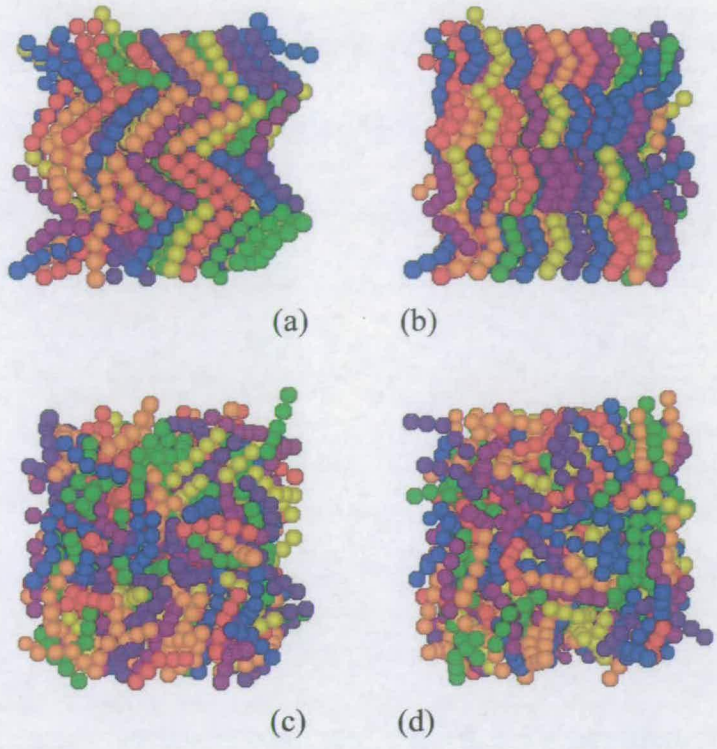

Figure 5.12: Snapshot representations of CRMs with $\gamma = 40°$, $p^* = 4.0$, (a) and (b) $T^* = 0.5$ and (c) and (d) $T^* = 1.0$.

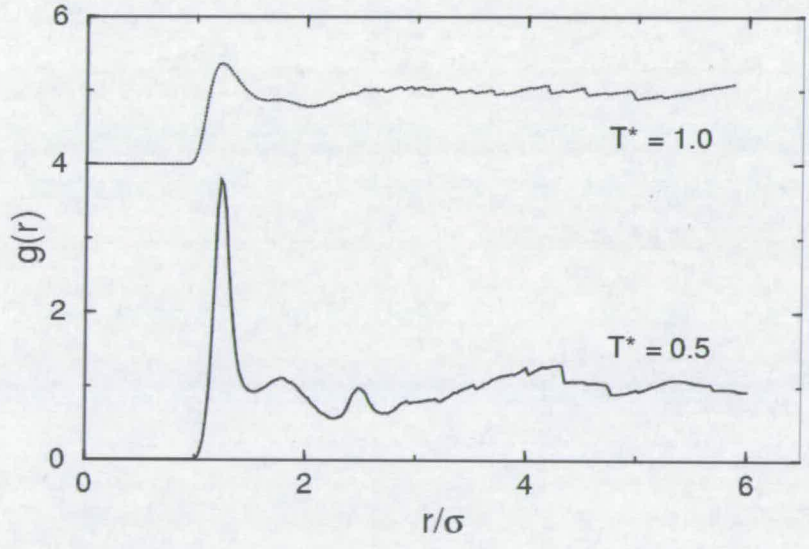

Figure 5.13: Radial distribution data for $T^* = 0.5$ (solid line) and 1.0 (dotted line) for $\gamma = 40°$ with $p^* = 4.0$ interacting via a simple repulsive potential. Plots have been displaced by 4 units for clarity.

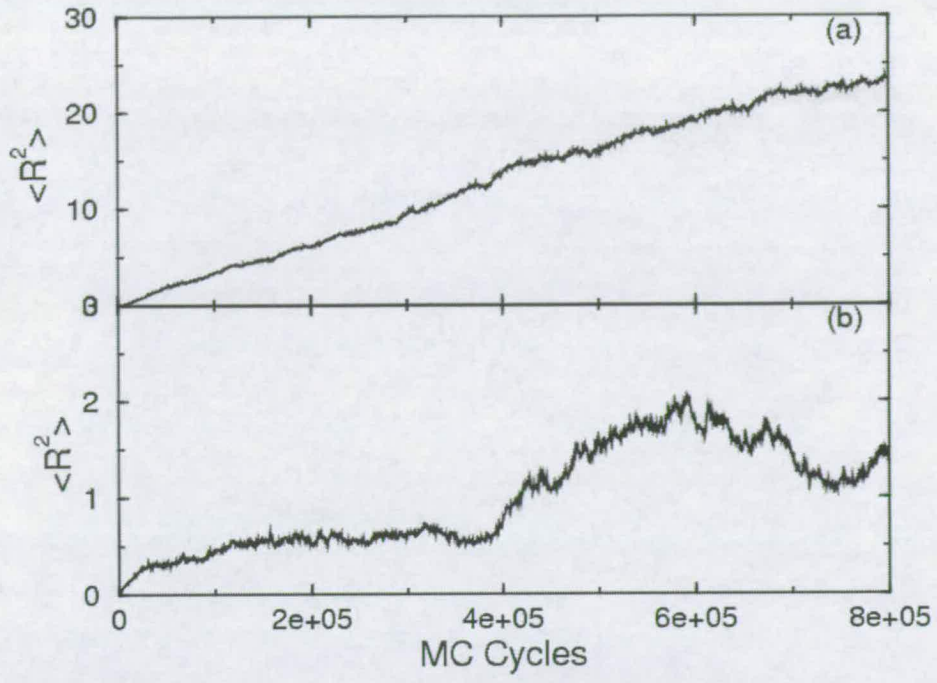

Figure 5.14: Mean squared displacement data for CRMs with $\gamma = 20°$, $p^* = 4.0$ and $T^* = 0.5$ (lower plot) and $T^* = 1.0$ (upper plot).

function of temperature is shown in Table 5.2. The herringbone-isotropic phase transition is signalled by a sharp drop in Q_{00}^2 between $T^* = 0.7$ and $T^* = 0.8$.

5.2.2 5-sphere molecules with attractive interactions

In this section we describe the results of simulations of CLJMs with γ in the range $0° - 40°$.

Linear molecules, $\gamma = 0°$

The equation of state of linear ($\gamma = 0°$) CLJMs along an isobar with $p^* = 4.0$ is shown in Fig. 5.15. The equation of state has only two distinct branches, suggesting a loss of some or all liquid crystalline phases. Snapshots of a simulation configuration at a temperature of $T^* = 1.0$ are shown in Figs. 5.16(a) and (b) and clearly show the crystalline ordering within each layer. The molecules are tilted to $\phi = 30.26°$ with respect to the layer normal. This tilt would suggest that spheres on neighbouring molecules are hexagonally close-packed, however the peak at $r/\sigma \simeq 2.0$ in the radial distribution plot shown, in Fig. 5.17, is not split. This split peak (or lack thereof) would provide a useful diagnostic for the presence of hexagonal packing. On the basis of the molecular tilt, we tentatively

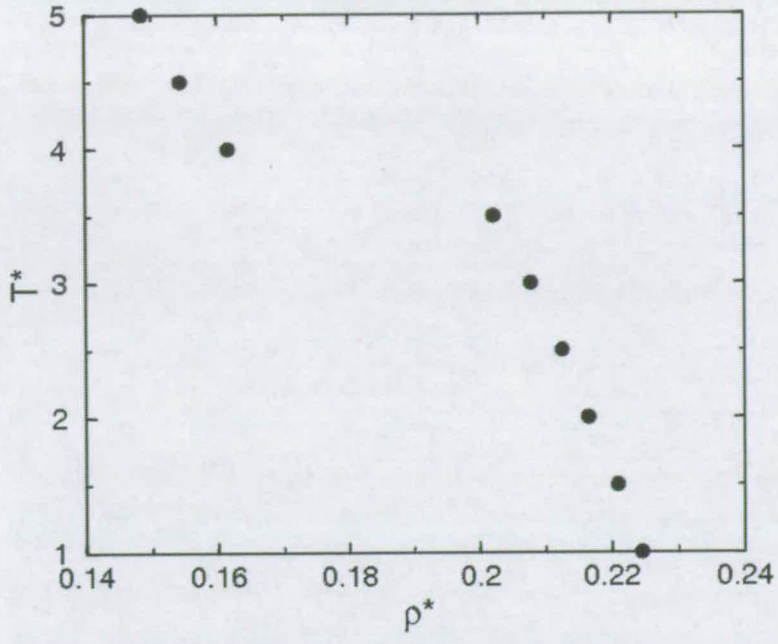

Figure 5.15: Equation of state CLJMs with $\gamma = 0°$ and $p^* = 4.0$. Error bars are smaller than the symbol size.

assign this as a tilted smectic B phase, although it may be a second tilted crystalline state. In these simulations there is no global tilt direction, rather the tilt directions alternate between layers, giving rise to a racemic phase. This is consistent with the work by Galindo *et al.* [42], who do not find any orientationally ordered phases. The Galindo study was primarily focused on the overall phase behaviour of 5 sphere chains, and only reported a single solid phase [42]. This phase persists to a temperature of $T^* = 3.5$, shown in Figs. 5.16(c) and (d). At this temperature the average tilt angle is $\phi = 36.13°$. We find subtle differences in the radial distribution plot of the smectic B phases (Fig. 5.17). At the higher temperature the radial distribution is not a sharply peaked as the low temperature system.

Heating above a temperature of $T^* = 4.0$, we find the isotropic phase. This phase is shown in Figs. 5.16(e) and (f) at a temperature of $T^* = 5.0$. A plot of $\langle R^2 \rangle$ as a function of MC cycles (Fig. 5.18) clearly shows the order of magnitude increase of the slope of $\langle R^2 \rangle$ upon entering the isotropic phase.

A plot of the nematic order parameter, Q^2_{00} is shown in Fig. 5.19. The smectic B phases exhibit lower values of Q^2_{00} due to the random tilt directions of the layers. The tilted smectic B-isotropic phase transition is signalled by a drop in Q^2_{00} between $T^* = 3.5$ and $T^* = 4.0$.

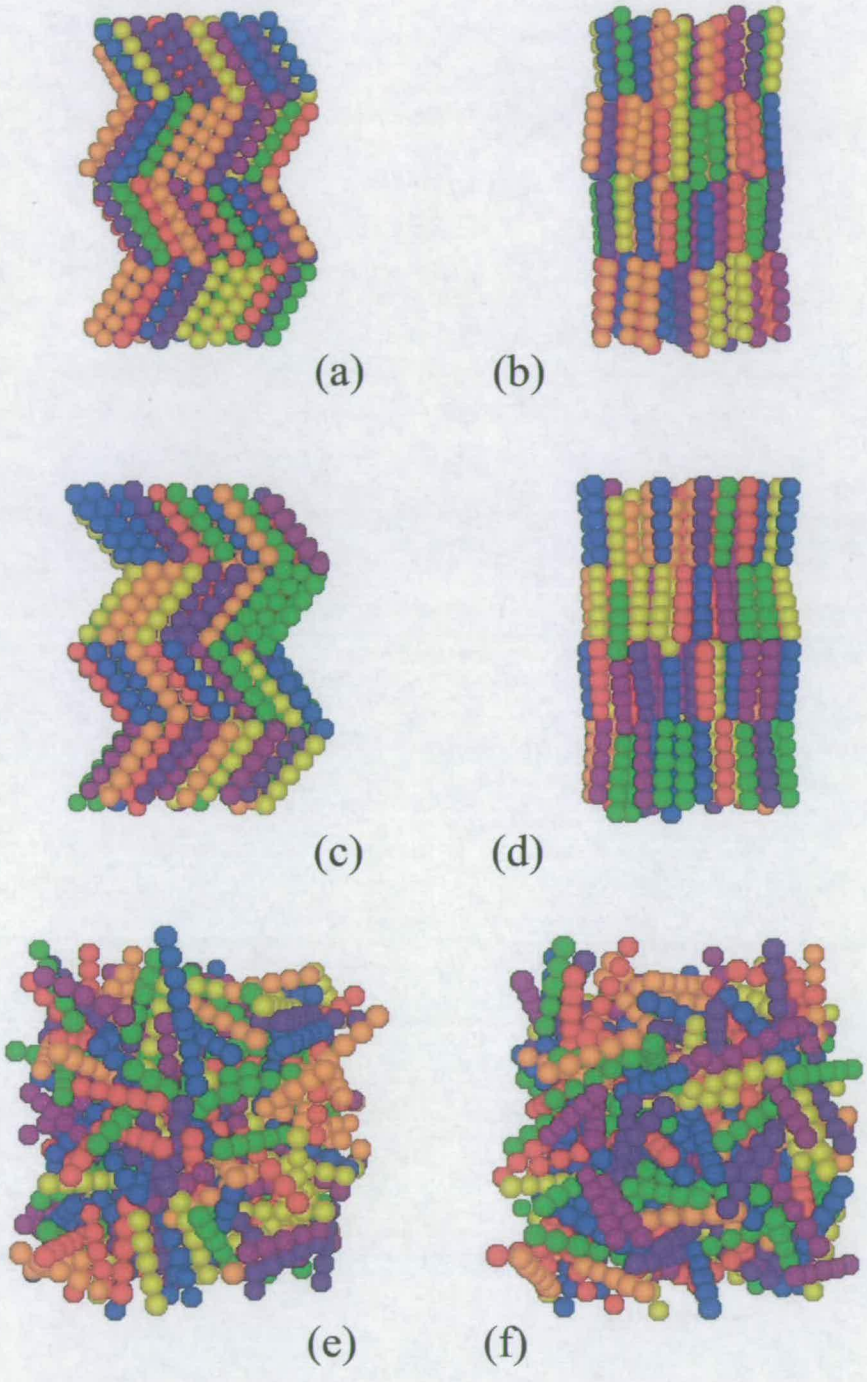

Figure 5.16: Snapshot representations of CLJMs with $\gamma = 0°$, $p^* = 4.0$; (a) and (b) $T^* = 1.0$, (c) and (d) $T^* = 3.0$ and (e) and (f) $T^* = 5.0$.

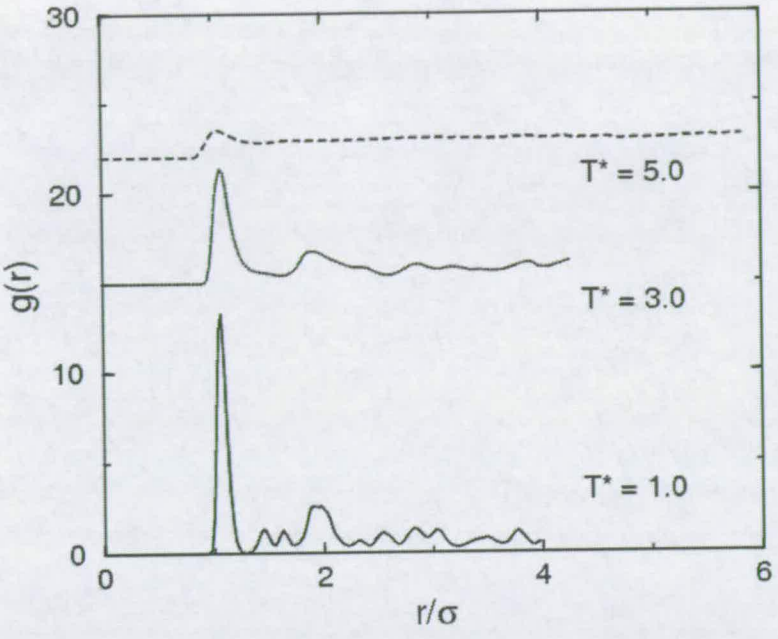

Figure 5.17: Radial distribution data for $T^* = 1.0$ (solid line), 3.0 (dotted line) and 5.0 (dashed line) for $\gamma = 0°$ with $p^* = 4.0$. Plots have been displaced for clarity.

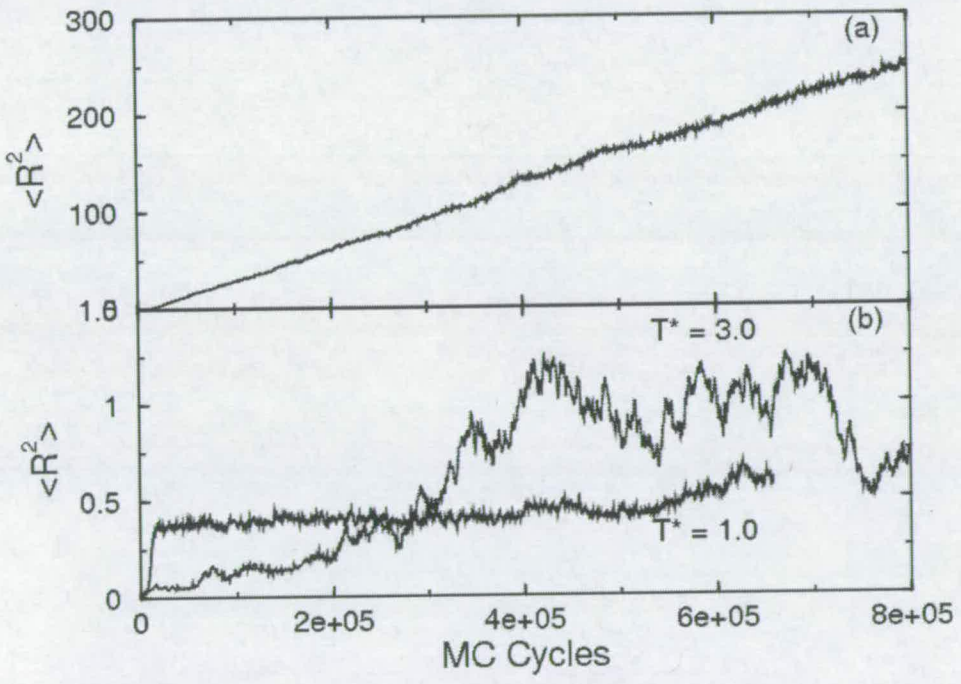

Figure 5.18: Mean squared displacement data for CLJMs with $\gamma = 0°$, $p^* = 4.0$; (a) $T^* = 5.0$ and (b) $T^* = 1.0$ (solid line) and 3.0 (dotted line).

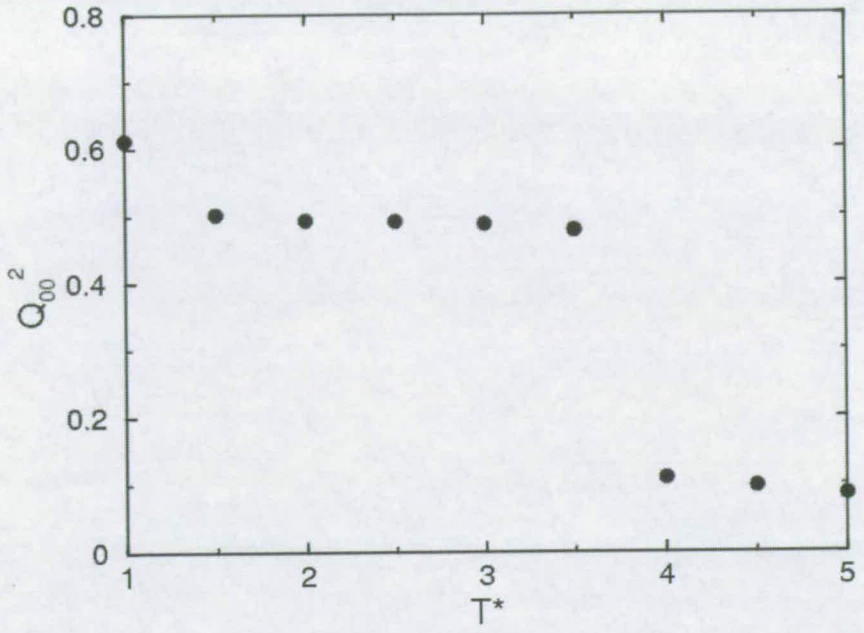

Figure 5.19: Uniaxial order parameter plotted as a function of temperature for CLJMs with $\gamma = 0°$ along an isobar $p^* = 4.0$. Error bars are smaller than the symbol size.

$\gamma = 20°$

Figure 5.20 shows the equation of state of CLJMs with $\gamma = 20°$ along an isobar with $p^* = 4.0$. Snapshots of a simulation configuration are shown in Figs. 5.21(a) and (b). The layers are tilted with $\phi = 36.85$ with respect to the layer normal. The radial distribution plot (Fig. 5.22) exhibits ordering consistent with hexagonal packing within the layers. As such we tentatively assign this as a tilted solid phase. The values of the biaxial order parameter, Q_{22}^2 and the bulk polarisation, shown in Table 5.3, are both small, even at low temperature. This would indicate a low degree of correspondence between adjacent layers. The bulk polarisation is low, thus indicating a super paraelectric phase. This phase persists to a temperature of $T^* = 2.5$. Snapshots of a simulation configuration at this temperature are shown in Figs. 5.21(c) and (d). At this temperature the average tilt of the molecules was found to be $\phi = 37.32°$. The radial distribution (Fig. 5.22) exhibits a broad peak in the range $r/\sigma = 2 - 3$. Figure 5.23 shows a plot of $\langle R^2 \rangle$ as a function of MC cycles. In this case the slope of the $\langle R^2 \rangle$ plot remains low for this phase.

Raising the temperature above $T^* = 3.0$ results in the formation of the isotopic phase, as shown in Figs. 5.21(e) and (f). The variation of the uniaxial order parameter, Q_{00}^2, is shown in Table 5.3. A drop in Q_{00}^2 over the range $2.5 \leq T^* \leq 3.0$

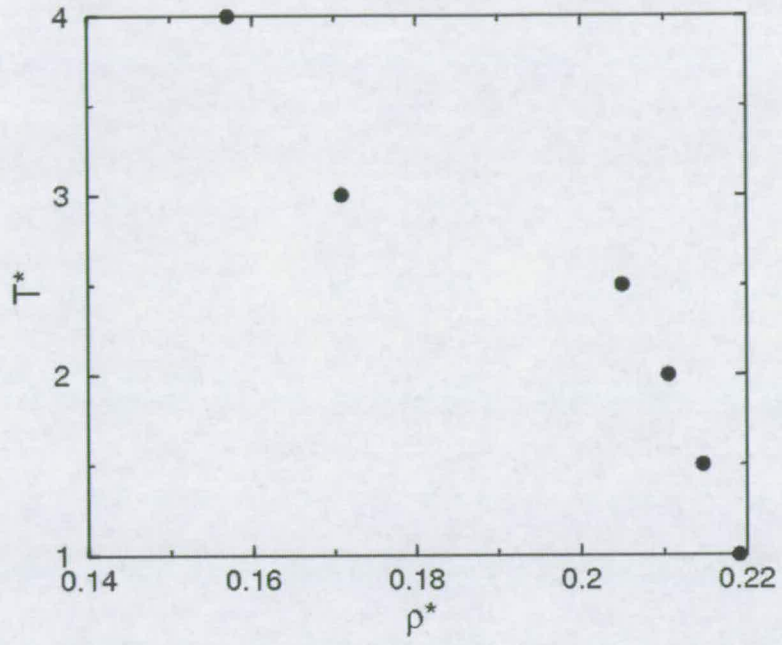

Figure 5.20: Equation of state for CLJMs with $\gamma = 20°$ along an isobar with $p^* = 4.0$. Error bars are smaller than the symbol size.

T^*	Q^2_{00}	Q^2_{22}	P
1.0	0.73(1)	0.271(5)	0.225(5)
1.5	0.70(2)	0.272(8)	0.218(9)
2.0	0.67(2)	0.272(9)	0.24(1)
2.5	0.62(2)	0.27(1)	0.21(2)
3.0	0.13(2)	0.03(2)	0.03(2)
4.0	0.07(2)	0.02(1)	0.02(2)

Table 5.3: Uniaxial (Q^2_{00}), biaxial (Q^2_{22}) order parameters and bulk polarisation (P) for CLJMs with $\gamma = 20°$ along an isobar with $p^* = 4.0$. The value in parentheses denotes the uncertainty in the last digit.

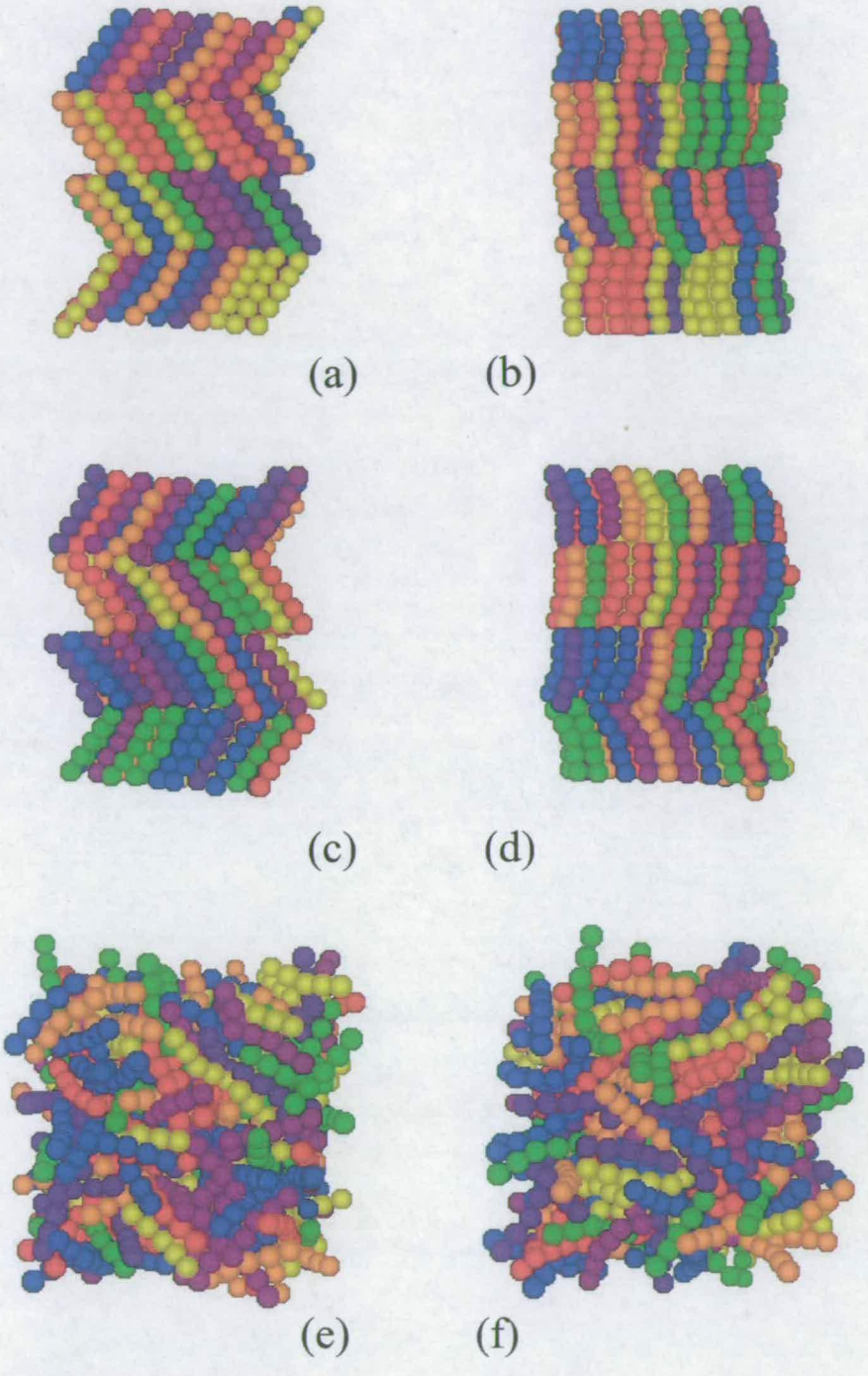

Figure 5.21: Snapshot representations of CLJMs with $\gamma = 20°$, $p^* = 4.0$; (a) and (b) $T^* = 1.0$, (c) and (d) $T^* = 2.5$ and (e) and (f) $T^* = 4.0$.

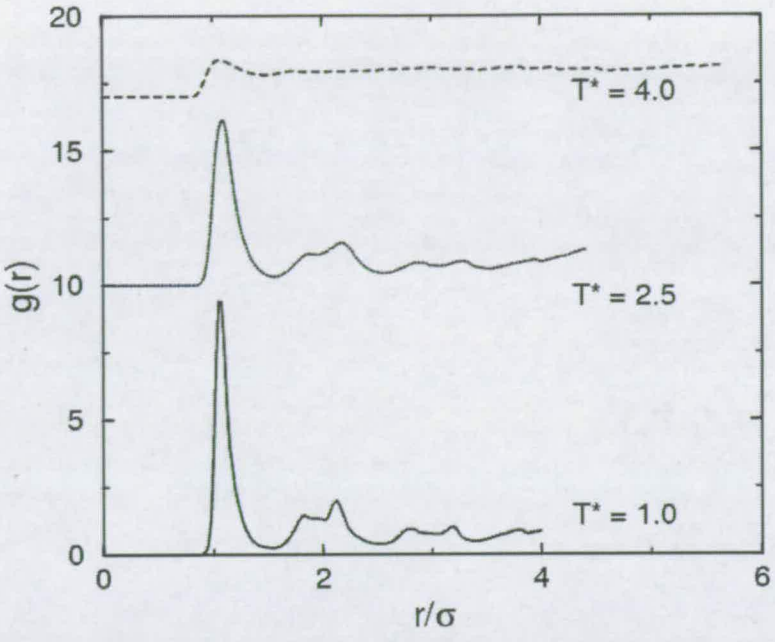

Figure 5.22: Radial distribution data for $T^* = 1.0$ (solid line), 2.5 (dotted line) and 4.0 (dashed line) for $\gamma = 20°$ with $p^* = 4.0$. Plots have been displaced for clarity.

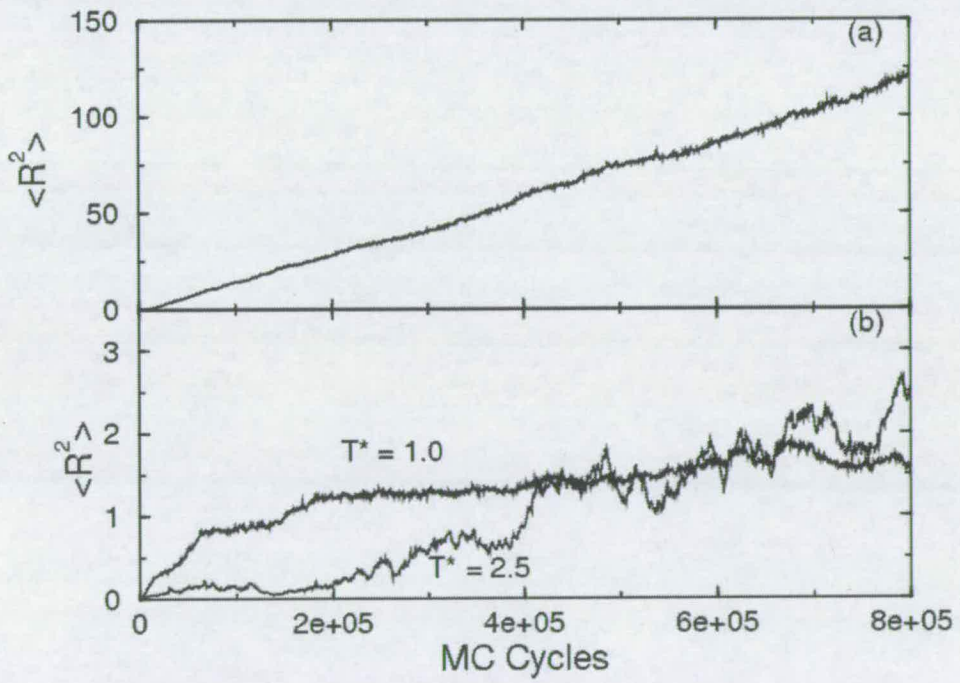

Figure 5.23: Mean squared displacement data for CLJMs with $\gamma = 20°$, $p^* = 4.0$; (a) $T^* = 4.0$ (solid line)and (b) $T^* = 1.0$ (solid line) and 2.5 (dotted line).

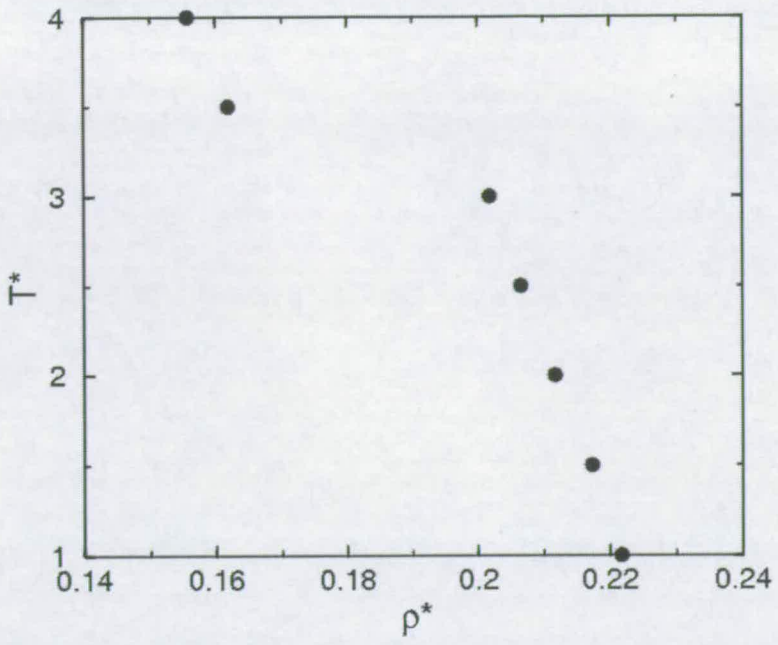

Figure 5.24: Equation of state for $\gamma = 40°$ with $p^* = 4.0$ for CLJMs. Error bars are smaller than the symbol size.

is indicative of a phase transition from tilted smectic B-isotropic phase. No intermediate liquid crystalline phases have been formed.

$\gamma = 40°$

The equation of state of CLJMs is shown in Fig. 5.24 with $\gamma = 40°$ along an isobar $p^* = 4.0$. At low temperature ($T^* = 1.0$), we find a tilted smectic B phase, as shown in Figs. 5.25(a) and (b). The average molecular tilt at this temperature is $\phi = 28.74°$. The radial distribution plot, shown in Fig. 5.26 displays a a double peak at $r/\sigma \simeq 2.0$, which would suggest a degree of hexagonal ordering within each layer. The slope of the mean squared displacement ($\langle R^2 \rangle$) remains low (Fig. 5.27). The corresponding biaxial order parameter at this temperature is $\simeq 0.5$ (Table 5.4), suggesting a low correspondence of tilt between layers. As with the corresponding CRM system (Sec. 5.2.1) the polarisation remains intact (Table 5.4). This is indicative of a ferroelectric polarisation state. This phase is stable up to a temperature of $T^* = 3.0$ [Figs. 5.25(c) and (d)]. The average tilt at this temperature was found to be $\phi = 30.86°$. We find a subtle difference in the radial distribution plot between the low temperature phases. The bulk polarisation (Table 5.4) remains high, and would suggest a ferroelectric polarisation at this state point.

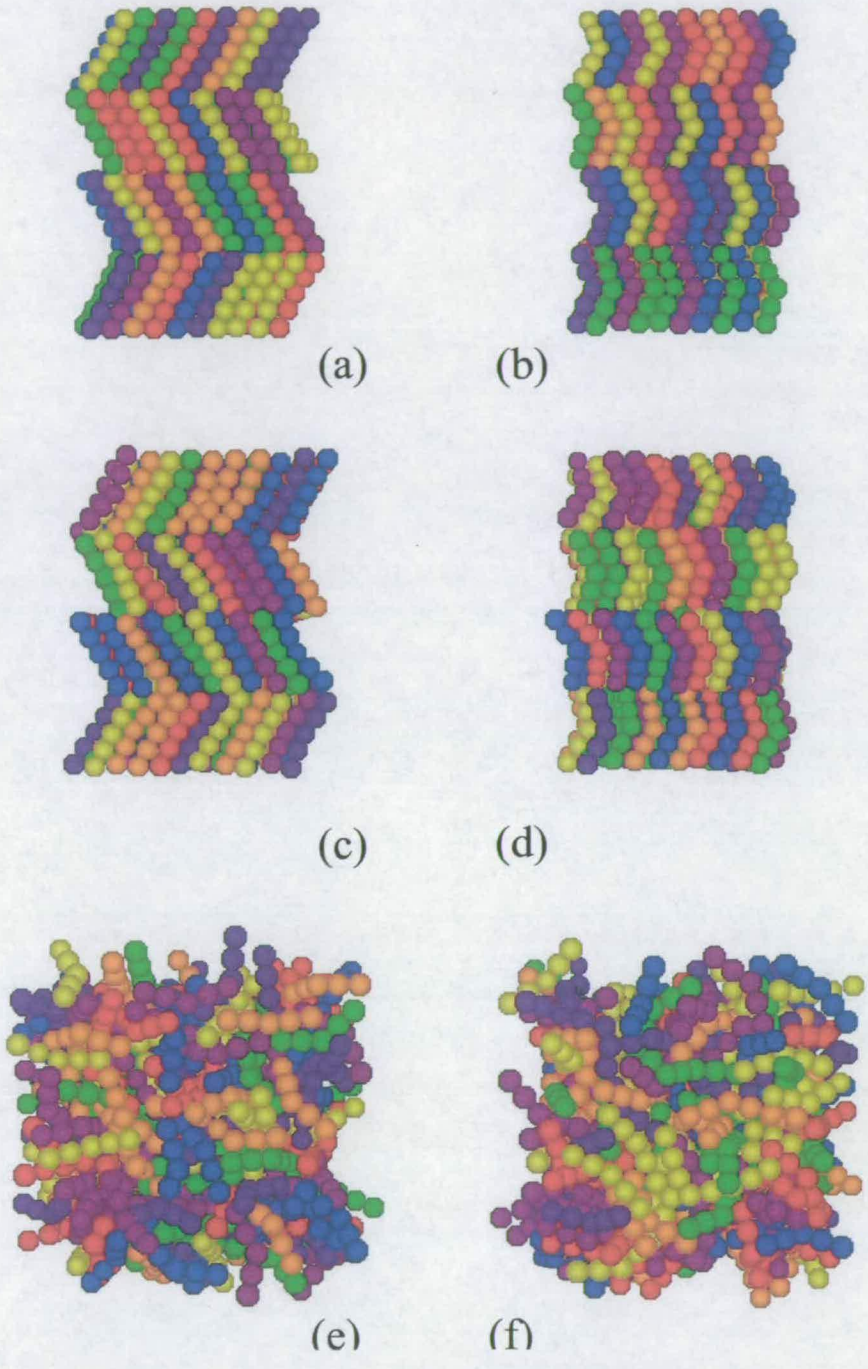

Figure 5.25: Snapshot representations of CLJMs with $\gamma = 40°$, $p^* = 4.0$, (a) and (b) $T^* = 1.0$, (c) and (d) $T^* = 3.0$ and (e) and (f) $T^* = 4.0$.

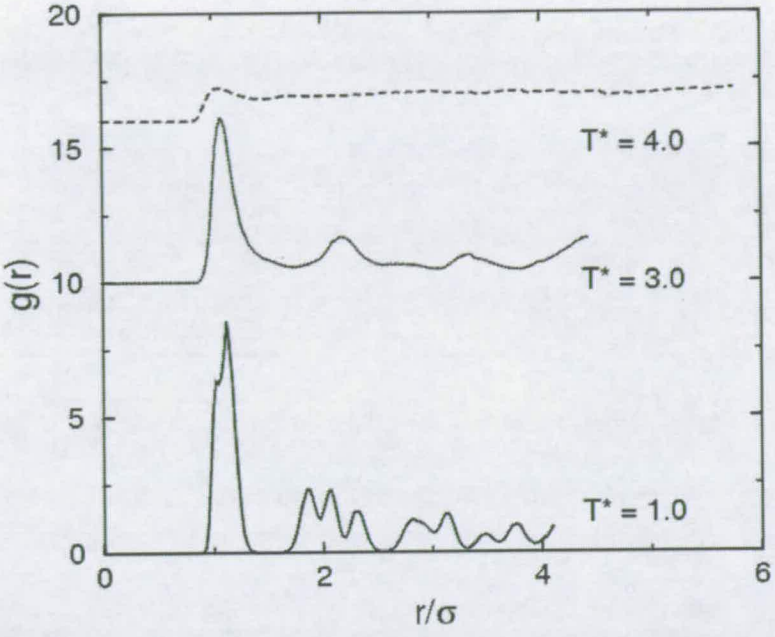

Figure 5.26: Radial distribution data for $T^* = 1.0$ (solid line), 3.0 (dotted line) and 4.0 (dashed line) for $\gamma = 40°$ with $p^* = 4.0$. Plots have been displaced for clarity.

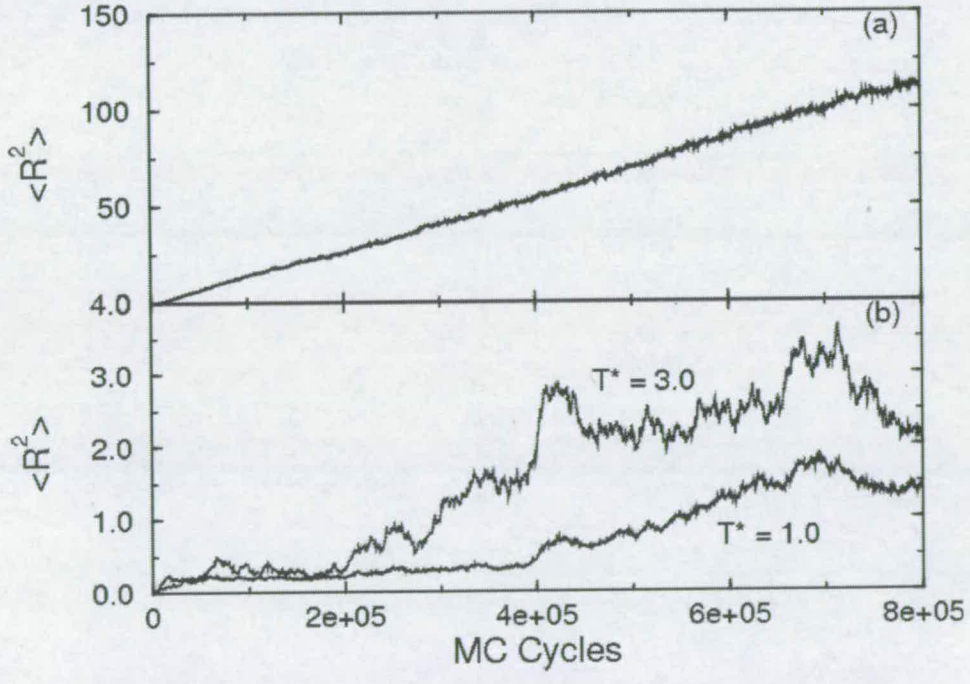

Figure 5.27: Mean squared displacement data for CLJMs with $\gamma = 40°$, $p^* = 4.0$; (a) $T^* = 4.0$ (solid line) and (b) $T^* = 1.0$ (solid line) and 3.0 (dotted line).

T^*	Q^2_{00}	Q^2_{22}	P
1.0	0.988(1)	0.538(6)	0.9960(3)
1.5	0.980(2)	0.545(7)	0.9933(6)
2.0	0.947(4)	0.43(1)	0.982(1)
2.5	0.935(5)	0.44(1)	0.978(2)
3.0	0.902(9)	0.47(1)	0.966(3)
3.5	0.06(2)	0.02(2)	0.02(2)
4.0	0.06(2)	0.02(1)	0.02(2)

Table 5.4: Uniaxial (Q^2_{00}), biaxial (Q^2_{00}) order parameters and bulk polarisation (P) for CLJMs with $\gamma = 40°$ along an isobar with $p^* = 4.0$. The figure in parentheses represents the uncertainty in the last digit.

Above a temperature of $T^* = 3.5$, we find the isotropic phase, as shown in Figs. 5.25(e) and (f). The variation of the uniaxial order parameter, Q^2_{00} as a function of temperature is shown in Table 5.4. A single phase transition from a tilted smectic B phase to the isotropic phase is observed over the range $3.0 \leq T^* \leq 3.5$.

5.3 Conclusions

In this chapter, we have presented results from constant-pressure Monte Carlo simulations of model bent-core molecules constructed from 5 soft-spheres arranged in a rigid 'v' shape, with external bond angle γ. Model molecules interacted via either a simple repulsive potential (CRMs) or the full $(12, 6)$ Lennard-Jones potential (CLJMs). The phase behaviour of these model molecules have been studied as a function of γ and the interaction potential.

With a soft-core repulsive potential we find isotropic and herringbone solid phases for all values of γ studied The herringbone solid phases are tilted to $> 50°$. With $\gamma = 40°$ we find a ferroelectric polarisation state, which is likely to be metastable. This ferroelectric polarisation state requires further clarification by further simulations and free energy calculations with alternative polarisation states. We do not find any intermediate liquid crystalline phases.

With linear molecules ($\gamma = 0°$) with attractive interactions we find isotropic and tilted smectic B phases. The smectic B phase was tilted in the range $30° - 36°$.

With $\gamma = 20°$ with attractive interactions we find isotropic and tilted smectic B phases. The smectic B phases were tilted to $\sim 37°$.

With $\gamma = 40°$ with attractive interactions we find isotropic and tilted smectic B phases. The smectic B phase was tilted in the range $\sim 29° \rightarrow \sim 31°$. The smectic B phase possessed a ferroelectric polarisation state.

We do not find any intermediate orientationally ordered phases with any of the CLJMs systems presented in this chapter.

The addition of attractive interaction clearly reduces low molecular tilt and stabilises the low temperature phases.

By decreasing the effective elongation of the molecule by utilising a 5-soft sphere core, we lose most of the orientationally ordered phases seen with a 7-soft sphere core, irrespective of the interaction potential. We have already identified a lower limit of L/σ as we do not find any orientationally ordered phases with CLJMs with $\gamma = 60°$ constructed of 7 spheres (Sec. 3.2.4). To investigate the effect of elongation and bend of the molecule a series of model systems with a variable number of spheres (to maintain a constant elongation) could be performed.

The ferroelectric phases found in $\gamma = 40°$ CRM and CLJM systems would need to be fully investigated. The pronounced bend of the molecules may prevent the disordering of the layer polarisations from the initial ferroelectric starting configuration. Free energy calculations could be performed on suitable antiferroelectric, ferroelectric and superparaelectric phases to determine the relative mechanical stabilities of each of these phases.

CHAPTER 6

Apolar bent-core molecules with flexible tails

In previous chapters we have investigated the effect of the interaction potential and the molecular elongation upon the phase behaviour of the rigid cores of the bent-core molecules. The bent-core molecules, shown in Fig. 6.1, possess flexible end groups. These terminal end groups are either alkyl [4, 9] or alkoxy [4, 10, 11] chains. The addition of the flexible tails increase the length of the molecules and hence increases the layer spacing observed in x-ray scattering experiments. At this time it is unclear if this increase in layer spacing is in any way connected to the development of chiral phases.

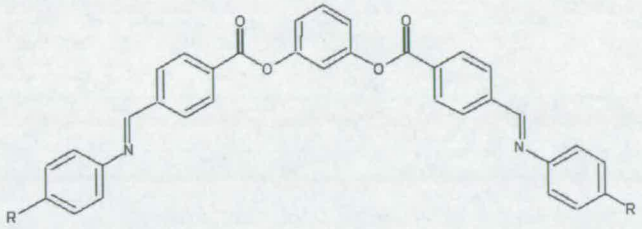

Figure 6.1: Generic bent-core liquid crystal structure.

With the recent growth in computational power and the development of efficient algorithms to model flexibility it is possible to perform simulations of fully flexible molecules. This flexibility can be incorporated into molecular dynamics simulations using the shake and rattle algorithms [33]. In these algorithms the atomic motions are governed by atomic forces and constraints imposed by fixed bond angles and bond lengths. This can lead to a slow evolution of the system and can give rise to difficulties when molecular chains are entangled. Using Monte Carlo techniques we can employ 'unphysical' moves, whereby chains are cut and regrown in a single trial move, thus overcoming local energy barriers.

The tails can be regrown by simple re-insertion of the segments. An example of this method is the insertion of a seven segment hard polymer into a cavity of a lattice of 63 sites, as shown in Fig. 6.2. The probability of generating a chain with a given orientation is given by;

1. Probability of inserting first segment is 1 in 63, as we have 63 lattice sites.
2. Probability of inserting the next 6 segments in the correct positions is $\left(\frac{1}{3}\right)^6$, as we move forward from the start, can move in 1 of 3 directions
3. We could start the insertion from either end of the chain, so multiply by two

The total probability of simply inserting this polymer chain is $P = 2 \times \frac{1}{63} \times \frac{1}{3^6} \simeq 4.4 \times 10^{-5}$. As a consequence we would have to generate a large number of attempts to obtain a trial that satisfies our selection criteria. The rejection of the trial insertion at any point forces the rejection of the entire chain and as such simple insertion of segments is highly inefficient [76]. A recent development has seen the introduction of Configurational Bias Monte Carlo (CB-MC) [34], which is based upon a scheme developed by Rosenbluth [77]. Configurational bias allows us to cut a chain at any point and then regrow the chain, with the application of bias, which is later removed during the acceptance of a trial chain. This allows the system to evolve more efficiently than with molecular dynamics. As the chain grows, it 'feels' its way into suitable voids that will give rise to favourable chain conformations. These calculations are non-trivial and we are approaching the upper computational limit of what we can simulate using in-house computing facilities. It will be necessary to utilise parallel computational facilities for a fully comprehensive study of our model system.

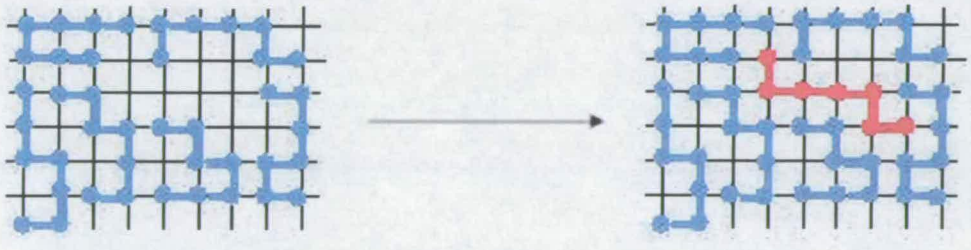

Figure 6.2: Simple insertion of a hard polymer on a lattice. The red chain denotes the inserted polymer [76].

The phase behaviour of hard spherocylinders ($L/D = 4.0$) with flexible tails on both ends has been studied by van Duijneveldt and Allen [78]. In the study the

total length of the spherocylinders is approximately 5σ (which is comparable to the CRM rigid core used previously in Chapter 5) and the tails were regrown utilising CBMC. The flexible tails were constructed of four ideal (zero volume) segments, with only the end segments possessing a hard interaction with the spherocylinder cores. This ensured that the tails did not interact with one another and that the intermediate tail segments could intersect with the spherocylinder cores [78]. The addition of the tails was found to stabilise the smectic A phase at the expense of the nematic phase. In the smectic A and crystal phases the layers were separated further apart upon addition of the tails [78]. Latterly, Van Duijneveldt *et al.* [79], studied the phase behaviour of hard spherocylinders ($L/D = 5$) possessing one flexible tail, with and without a dipole moment at the end of the spherocylinder. In this latter study, each tail was constructed from five ideal segments as per the previous study [78]. The addition of flexible tails was found to destabilise the nematic phase. Combining the effects of dipolar interactions and flexible tails all four phases survive [79].

The phase behaviour of a semi-flexible fused hard sphere model has also been studied by McBride *et al.* [80, 81]. In Ref. [80] the molecule was constructed from 15 hard spheres with a reduced bond length of 0.6, with flexibility introduced at one end of the molecule. The inclusion of a flexible section of six spheres was found to destabilise the nematic phase [80]. In Ref. [81] the effect of altering the number of hard spheres in the flexible section was investigated. Increasing the flexible region to five spheres was found to stabilise the smectic A phase at the expense of the nematic phase [81].

The phase behaviour of Gay-Berne ellipsoids with flexible tails has been studied by McBride and Wilson [82] and Fukunaga *et al.* [83]. Both studies employed molecular dynamics. McBride and Wilson studied the phase behaviour of Gay-Berne ellipsoids with asymmetric flexible chains grafted on to either end of the ellipsoid [82]. In this study, isotropic and smectic B phases were reported at low density over a range of temperatures and isotropic, nematic and solid phases were observed at higher density over a similar range of temperatures. A strong link between the internal molecular structure and the orientational order of the system was observed, at high temperature the *gauche* isomeric form is favoured [82]. A similar change in conformation upon heating has also been reported in simulations of chains constructed from two Gay-Berne ellipsoids connected via a flexible section performed by Wilson [84]. Fukunaga *et al.* [83] employed a single Gay-Berne ellipsoid with a single flexible tail, represented by a chain of united

atoms. The cooperative effect of flexibility and a terminal dipole was found to stabilise the nematic phase along with a head to head association of molecules, which is also observed in x-ray diffraction experiments [83].

Affourard *et al.* [85] investigated the phase behaviour of semiflexible molecules, which possessed flexible end sections of variable length. The molecules were constructed from short multibead chains, where the beads were connected via anharmonic springs. With symmetric molecules and ansiotropic potentials, the smectic A phase is well defined over a wide range of temperatures, whereas the nematic phase is not observed [85]

In this chapter we shall present simulation results of simple model molecules with flexible tails grafted onto both termini. Each molecule shall be constructed from a 5 soft-sphere core coupled with a 3-segment flexible tail at each end, as shown in Fig. 6.3. In effect, we are studying an extended 5-sphere molecule or an 11-sphere molecule with flexible terminal branches. Although no liquid crystalline phases were found with a 5 sphere core (Chapter 5), the inclusion of flexibility is known to stabilise the smectic phases [78]. Here the model shall be studied with γ in the region $0° - 40°$.

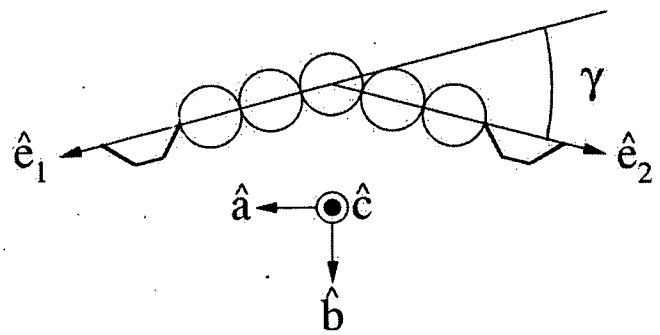

Figure 6.3: The composite model with flexible tails.

6.1 Simulation techniques

6.1.1 *Model construction*

The model, as shown in Fig. 6.3, is constructed from a 5 sphere core and two 3 segment tails. The core sphere-sphere bond length is set to 1σ, with a reduced bond length of 0.6σ for the tail segments (the ratio of the C-C bond length to the

diameter of the aromatic ring is approximately $\simeq 0.6$). The interaction potential between two spheres of types i and j is,

$$U_{ij} = 4\epsilon_{ij}\left(\frac{\sigma_{ij}}{r}\right)^{12}. \tag{6.1}$$

For simplicity we set all the LJ energy parameters equal to ϵ, and the range parameters are given by $\sigma_{cc} = \sigma$ and $\sigma_{tt} = 0$. The core-tail range parameter is determined by the Lorentz-Berthlot mixing rule, i.e., $\sigma_{ct} = \frac{1}{2}(\sigma_{cc} + \sigma_{tt}) = \frac{1}{2}\sigma$. It must be noted that the cores of a molecule do not interact with its tails, allowing the possibility of the 3^{rd} and 4^{th} tail sites overlapping their own cores.

As with the construction of the cores of the molecules, the tail segments are constructed from a set of vectors for both terminal chain groups. For a tail composed of l segments, there are $l + 1$ vectors, as shown in Fig. 6.4. The first vector in the series provides the starting vertex on the terminal core sphere. Each segment is constrained to give,

$$T_i^a \cdot T_{i+1}^a = \cos 109°, \tag{6.2}$$

where T_i^a is the tail vector for the i^{th} segment of tail a. The total starting length of the tail is $\sim 1\sigma$. For brevity, we refer to these systems as composite repulsive molecules with flexible tails (CRM+Ts).

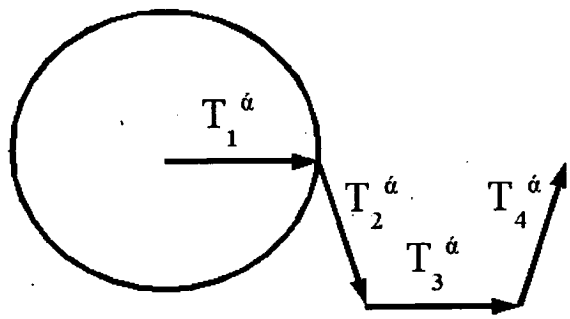

Figure 6.4: The terminal core sphere with the vectors used to construct the tail.

6.1.2 Configurational Bias Monte Carlo

With the Monte Carlo simulation technique we can employ "unphysical" trial moves, whereby the entire chain can be cut and completely regrown as opposed to incremental steps as in conventional Monte Carlo or Molecular Dynamics. A simple method of regrowing the chain is to simply insert subsequent segments, one at a time. Upon complete growth of a tail the normal Metropolis acceptance/rejection criteria are applied. Although a simple technique, this is highly

inefficient as the rejection of any segment, due to overlap, causes the entire move to be rejected as the probability of randomly generating a tail with a favourable configuration is extremely low.

An alternative strategy is to apply bias during the growth of a chain to improve the efficiency by promoting controlled tail growth. This bias is then removed during the acceptance or rejection of the trial chain. This is known as Rosenbluth sampling [77], whereby the bias is applied by accumulating the Rosenbluth weight (W) during tail growth. The Rosenbluth weight is proportional to the Boltzmann factors for all possible trial conformations.

Configurational Bias Monte Carlo [86] is an extension of Rosenbluth sampling. In this technique the contributions to the Rosenbluth weight (w) are used to bias the random choice of the next trial segment. To define the acceptance rules for this system, we have to consider detailed balance, as shown in Eqn. 6.3 (from Chapter 2),

$$P_{\text{old}} \times W_{\text{new}} \times \Pi(\text{old} \rightarrow \text{new}) = P_{\text{new}} \times W_{\text{old}} \times \Pi(\text{new} \rightarrow \text{old}), \tag{6.3}$$

where P_{old} and P_{new} are the probabilities of the old and new states as given by Equation 2.9. $\Pi(\text{old} \rightarrow \text{new})$ and $\Pi(\text{new} \rightarrow \text{old})$ are the transition probabilities of the system going from the old to new states and vice versa. W_{new} represents the *a priori* probability of generating the trial move from the old to the new states and is known as the Rosenbluth weight, which is accumulated during the growth of the chain. Rearranging Eqn. 6.3 yields,

$$\frac{\Pi(\text{old} \rightarrow \text{new})}{\Pi(\text{new} \rightarrow \text{old})} = \exp\left(-\beta \Delta U\right) \frac{W_{\text{new}}}{W_{\text{old}}}. \tag{6.4}$$

Thus the acceptance of a trial move using the Metropolis scheme is,

$$\Pi(\text{old} \rightarrow \text{new}) = \min\left[1, \exp\left(-\beta \Delta U\right) \frac{W_{\text{new}}}{W_{\text{old}}}\right]. \tag{6.5}$$

The probability of generating a particular new chain configuration, with a given Rosenbluth weight (W_{new} and similarly W_{old}) is given by,

$$W_{\text{new}} = \Pi_{i=1}^{l} w_i, \tag{6.6}$$

where $w_i = \sum_{j=1}^{b} \exp(-\beta U_j)$ and is the Rosenbluth weight for the i^{th} segment. The sum indexes l and b represent the number of segments and trial directions,

respectively. The acceptance of a trial chain (A_t) is given by the ratio of new and old Rosenbluth weights as shown in Eqn. 6.7. The probability of selecting a single trial segment from the b trial directions is given by Eqn. 6.8,

$$A_t = \min\left(1, \frac{w_{\text{new}}}{w_{\text{old}}}\right) \tag{6.7}$$

$$P_i = \frac{\exp(-\beta U_i)}{w_i}. \tag{6.8}$$

Mechanics of Configurational Bias Monte Carlo

The procedure for Configurational Bias is outlined below;

1. Disturb the system in some manner, either by translation or rotation of the core of the molecule.
2. For each tail, calculate the old Rosenbluth weights, w_{old}.
   (a) Create $(b-1)$ alternate trial orientations for all l segments and use the original conformation as the b^{th} trial.
   (b) Calculate the interactions of all the $l \times b$ sites with the entire system.
   (c) Calculate the corresponding Boltzmann weights and hence the Rosenbluth weight for each segment, w_i.
   (d) Calculate $w_{\text{old}} = \Pi_{i=1}^{l} w_i$.
3. Generating a new trial conformation.
   (a) Construct a segment at a time.
   (b) Generate b trial orientations.
   (c) Calculate the interaction energy of all b sites with the entire system.
   (d) Calculate the corresponding Boltzmann weights and hence the Rosenbluth weight, w_{seg}.
   (e) Calculate the probability of selecting all b sites using Eqn. 6.8 and generate a random number (R) over the range $[0, 1]$ such that $P_{j-1} < R \leq P_j$, where j denotes the number of the selected trial direction.
   (f) Repeat from (3b) until all l segments grown.
   (g) Calculate $w_{\text{new}} = \Pi_{i=1}^{l} w_i$.
4. This trial chain is accepted/rejected based upon the ratio of the new and old Rosenbluth weights ($w_{\text{new}}/w_{\text{old}}$) as shown in Eqn. 6.7. Repeat for other tail.

5. Now accept/reject the entire trial move utilising the classical Metropolis algorithm, based upon the total energy change, ΔU.

$$\min\left[1, \exp(-\beta \Delta U)\right] \tag{6.9}$$

6.1.3 *Generating alternative trial orientations*

Two methods exist for the generation of trial orientations subject to Eqn. 6.2.

1. Generate a unit vector on a sphere, calculate the scalar product and compare with $\cos 109°$.
2. Generate a unit vector on a sphere, calculate the vector product. Use the resultant vector as a rotation axis and rotate T_i^a by the required angle by the following equation [87],

$$\vec{r'} = \vec{r}\cos(\phi) + \vec{n}(\vec{n} \cdot \vec{r})[1 - \cos(\phi)] + (\vec{r} \times \vec{n})\sin(\phi), \tag{6.10}$$

where $\vec{n}$ is the rotation axis, $\vec{r}$ is the $i-1$ tail segment vector, $\vec{r'}$ the new trial orientation and ϕ the angle of rotation.

Trial orientations were generated using the latter method as it is more efficient.

A useful introduction to Configurational Bias Monte Carlo can be found in Refs. [34] and [76].

6.2 Tail ordering

In addition to the structural and molecular orientation information, described in Section 2.3 we can also calculate complementary functions for the flexible tails.

6.2.1 *Structural properties*

To assess the interdigitation of the tails between layers, we can employ an extended single particle density function as shown in Eqn. 6.11. The single particle density function is calculated for both terminal tail segment vertices in addition

to the apical sphere of the core of the molecules. Each layer has 3 peaks associated with it as shown in Fig. 6.5(top). If the tails are interdigitated the peaks would interweave, as shown in Fig. 6.5(lower).

$$\rho_z(r) = \frac{1}{V}\langle \sum_{i=1}^{N_m} \delta(\vec{Z} - \vec{z}_i)\rangle \tag{6.11}$$

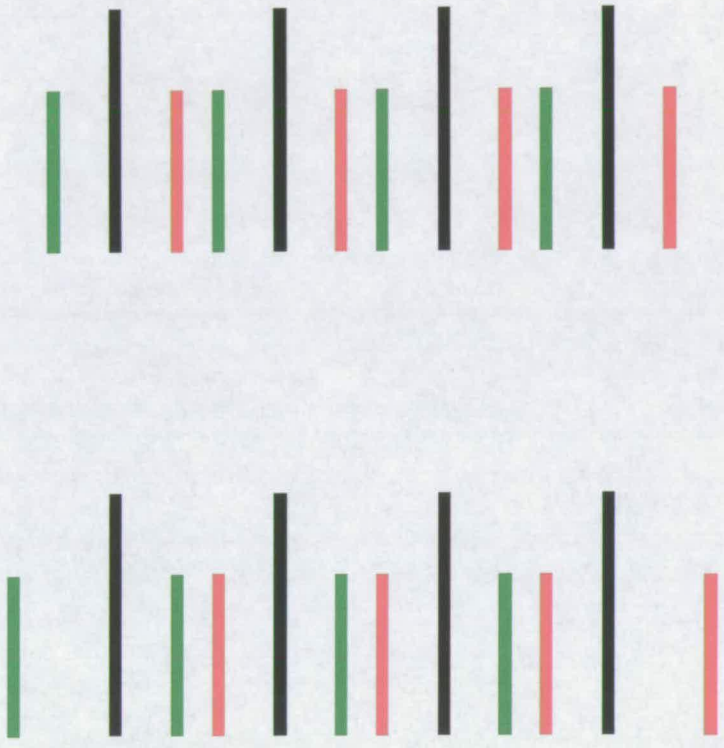

Figure 6.5: Idealised single particle density functions for non-interdigitated (top plot) and interdigitated (lower plot). The red line represents tail one, green line represent tail two and the black line the apical sphere function.

We also calculate probability distribution functions $[P^i(s^i)]$ for the core-end to tail-tip distances, for tail 1 and tail 2 as shown in Eqns. 6.12 and 6.13.

$$P^1(s^1) = \left\langle \frac{V}{N_m^2} \sum_{i=1}^{N_m} \delta(r - \vec{C}_i^1) \right\rangle \tag{6.12}$$

$$P^2(s^2) = \left\langle \frac{V}{N_m^2} \sum_{i=1}^{N_m} \delta(r - \vec{C}_i^2) \right\rangle, \tag{6.13}$$

where $\vec{C}_i^{\alpha}$ is the vector denoting the core-end to tail-tip vector for the α^{th} tail on the i^{th} molecule and N_{seg} is the number of tail segments. The box lengths are used to convert the tail vectors to r/σ.

6.2.2 *Order parameters*

Pseudo-order parameters, T^a and T^b, for the ordering of the tails can be evaluated.

$$T^{\alpha} = \frac{1}{2N_m} \sum_{i=1}^{N_m} \left(3\vec{C}_i^{\alpha}\vec{C}_i^{\alpha} - I \right), \tag{6.14}$$

where $\vec{C}_i^{\alpha}$ is the core-end to tail-tip vector and $\alpha = a, b$ for tail 1 and 2 respectively. Diagonalisation of both tensors yields eigenvalues $\lambda^+ \geq \lambda^\circ \geq \lambda^-$ and corresponding orthonormal eigenvectors, $\vec{n^+}, \vec{n^\circ}, \vec{n^-}$. The eigenvalue, λ^+ gives an indication as to the ordering of the tails. We would not expect large values of T^{α} as the tails do not interact with one another and hence there is no driving force for the tails to spontaneously align. We can also assess the angles that $\vec{C}_i^{\alpha}$ make with the Z-axis of the simulation cell, Ω and Λ for tail 1 and 2, respectively.

$$\cos(\Omega) = \frac{1}{N_m} \sum_{i=1}^{N_m} \vec{C}_{iz}^{1} \tag{6.15}$$

$$\cos(\Lambda) = \frac{1}{N_m} \sum_{i=1}^{N_m} \vec{C}_{iz}^{2} \tag{6.16}$$

A useful indicator of the effect of the tails on the bond angle, γ' can be evaluated from the scalar product of apical sphere - tail-tip vectors, as shown in Eqn. 6.17. Another useful quantity is to calculate the average end-end length of the molecules as shown in Eqn. 6.18.

$$\cos(\gamma') = \frac{1}{N_m} \sum_{i=1}^{N_m} \vec{A}_1 \cdot \vec{A}_2 \tag{6.17}$$

$$\langle L_m \rangle = \frac{1}{N_m} \sum_{i=1}^{N_m} |\vec{r_{tip}^{1}} - \vec{r_{tip}^{2}}|, \tag{6.18}$$

where $\vec{r}_{tip}^{\alpha}$ is the position vector of the terminal tail sphere on the α^{th} tail and $\vec{A}_{\alpha}$ denotes the apical sphere-core tip vector.

In these simulations one MC sweep consists of one trial translation or one trial rotation per molecule and a single volume fluctuation. Configurational Bias was used to re-grow both tails after translation or rotation of the core of the molecule.

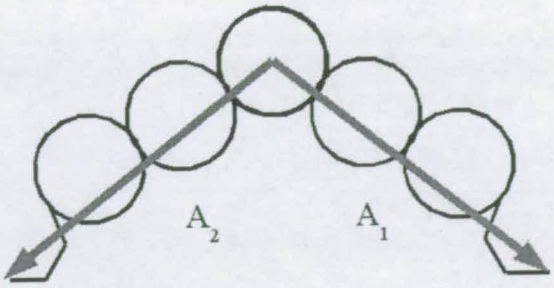

Figure 6.6: The composite model with flexible tails, the grey line denotes the apical sphere - tail-tip vectors ($\vec{A}_i$).

	x	y	z
$\vec{T}_1^1$	$\vec{e}_{1x}$	$\vec{e}_{1y}$	$\vec{e}_{1z}$
$\vec{T}_2^1$	0	$\sin\left(\frac{\gamma}{2}+71\right)$	$\cos\left(\frac{\gamma}{2}+71\right)$
$\vec{T}_3^1$	0	$\sin\left(\frac{\gamma}{2}\right)$	$\cos\left(\frac{\gamma}{2}\right)$
$\vec{T}_4^1$	0	$\sin\left(\frac{\gamma}{2}-71\right)$	$\cos\left(\frac{\gamma}{2}-71\right)$
$\vec{T}_1^2$	$\vec{e}_{2x}$	$\vec{e}_{2y}$	$\vec{e}_{2z}$
$\vec{T}_2^2$	0	$\sin\left(\frac{\gamma}{2}+71\right)$	$-\cos\left(\frac{\gamma}{2}+71\right)$
$\vec{T}_3^2$	0	$\sin\left(\frac{\gamma}{2}\right)$	$-\cos\left(\frac{\gamma}{2}\right)$
$\vec{T}_4^2$	0	$\sin\left(\frac{\gamma}{2}-71\right)$	$-\cos\left(\frac{\gamma}{2}-71\right)$

Table 6.1: Tail vectors for tails one and two

The maximum displacement parameters were adjusted to yield acceptance ratios of 10% and 50% for translations/rotations and volume fluctuations, respectively. Even using CB-MC, these simulations require substantial computational effort. A simulation block of 400 MC sweeps typically requires in the region of 1500 seconds on a 2.2GHz Intel Xeon processor.

6.2.3 *Starting configurations*

In a typical starting configuration, the apical spheres are positioned on a simple square lattice and layers replicated in the Z direction. The layer spacing is governed by the overall length of the molecules (including tails). The tail vectors are dependent upon the constrained geometry and γ. Each layer is a separate entity and tails on neighbouring layers do not interdigitate. Using the vector notation used in Fig. 6.4 the vectors are shown in Table 6.1, where $\vec{e}_1$ and $\vec{e}_2$ denote the vectors utilised to construct the core of the model molecule.

Upon generation of the initial configurations, these were allowed to equilibrate under constant volume (NVT) Monte Carlo simulations at $\rho^* = 0.14$.

For each system, we performed sequences of simulations starting at high density ($\rho^* = 0.14$), to ensure that the molecules tilted spontaneously, for bond angles $\gamma = 0°, 20°$ and $40°$. Once equilibrated, the temperature was raised until a transition to a homogeneous fluid phase occurred. We then switched over to a cubic simulation cell. Along with these heating runs, we also performed some cooling runs to verify the existence of a phase transition.

6.3 Results

6.3.1 *Linear molecules, $\gamma = 0°$*

The equation of state of linear ($\gamma = 0°$) CRM+Ts along an isobar with $p^* = 4.0$ is shown in Fig. 6.7. Snapshots of a simulation configuration at a temperature of $T^* = 1.0$ are shown in Figs. 6.8(a) and (b). This phase is tilted with $\phi = 13.71$. The radial distribution plot, shown in Fig. 6.9 displays short range ordering and is suggestive of a smectic phase. From in-layer snapshots [Figs. 6.10(a)-(d)] it can be seen that the structure within layers is disordered, as such we classify this as a smectic phase. We also performed simulations cooling from $T^* = 2.5$. At equilibrium these systems were found at higher density than the corresponding heating runs (Fig. 6.7 - unfilled circles). As the temperature is increased the density decreases, giving rise to the increased layer spacing. This increase in layer spacing may influence the tail orientations allow greater motion of the tails. The simulations on the heating branch of the equation of state are of metastable states and require simulations for full characterisation of the phase behaviour.

The single particle density plot, shown in Fig. 6.11, shows the interdigitation of the layers. This can also be seen in snapshots of a simulation configuration as shown in Figs. 6.8(a) and (b) at a temperature of $T^* = 1.0$.

At a temperature of $T^* = 3.0$ we find the isotropic phase, as shown in Figs. 6.8(c) and (d). The radial distribution plot at this temperature (Fig. 6.9) is indicative of such a phase. Examination of the $\langle R^2 \rangle$ plot (Fig. 6.12) shows us that the isotropic phase has indeed been formed, on account of the large slope of $\langle R^2 \rangle$. At this high temperature the corresponding single particle density profile, shown in Fig. 6.13, should be flat for a isotropic phase. However, it is not flat and this may be a remnant of the previous layered phase.

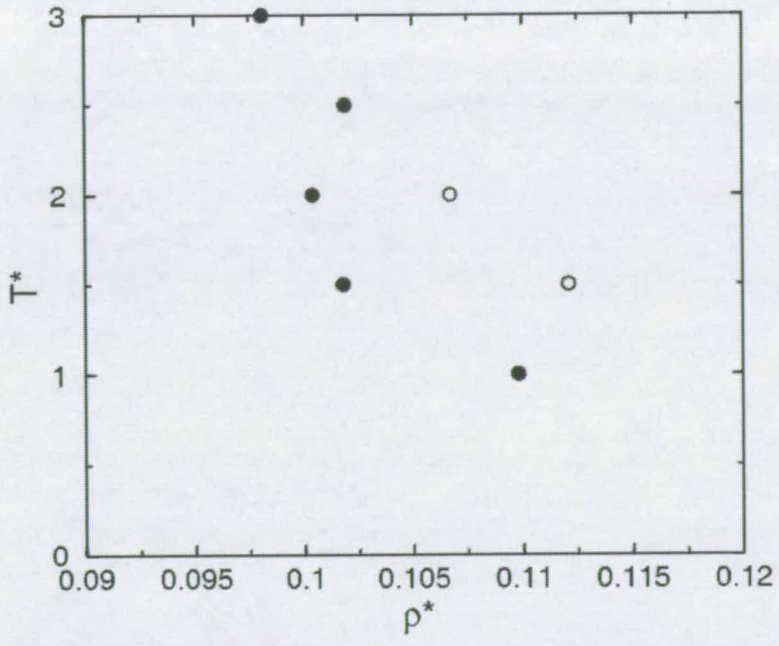

Figure 6.7: Equation of state for $\gamma = 0°$ with $p^* = 4.0$ Filled circles represent simulation results from heating and unfilled circles denote the results of cooling simulations. Error bars are smaller than the symbol size.

A plot of the nematic order parameter, Q^2_{00}, as a function of temperature is shown in Fig. 6.14. This indicates the orientational ordering of the cores of the molecules. The onset of the isotropic phase is marked by a sharp drop in Q^2_{00} between $T^* = 2.0$ and $T^* = 2.5$. There is no intermediate liquid crystal phases. Another indication of the smectic-isotropic phase transition is to examine plots of $\langle \cos \Omega \rangle$ and $\langle \cos \Lambda \rangle$, shown in Fig. 6.15. At low temperature the cores of the molecules lie within a plane perpendicular to the Z-axis. The tails are grown outwards from the molecular cores. Both $\langle \cos \Omega \rangle$ and $\langle \cos \Lambda \rangle$ are non-zero as the cores are aligned parallel to the Z-axis. In the isotropic phase the cores are randomly orientated and although the tails extend outwards from the core, the average of both $\langle \cos \Omega \rangle$ and $\langle \cos \Lambda \rangle$ will be zero within statistical error.

A plot of the probability length functions, as calculated in Eqns. 6.12 and 6.13, for a series of temperatures in the range $1.0 \leq T^* \leq 3.0$ are shown in Fig. 6.16. From this it can be seen that the tail geometry (hence effective length) is independent of temperature. The two peaks represent the *cis* and *trans* geometric forms. The *cis* form is the more favoured geometric form. Identification of the two geometric forms is shown by plotting the effective length as a function of angle between the two groups as shown in Fig. 6.17.

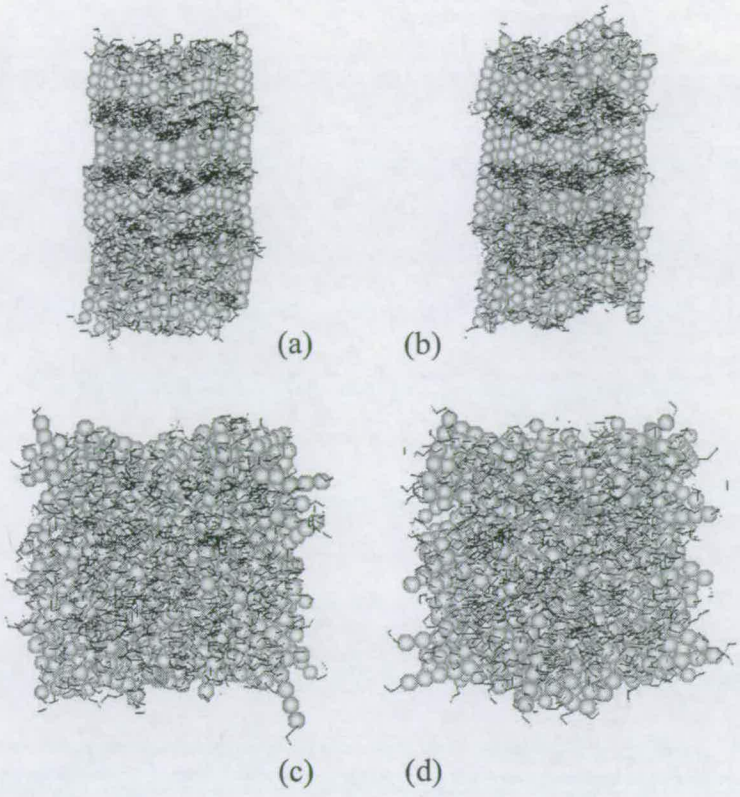

Figure 6.8: Snapshot representations for $\gamma = 0°$ with $p^* = 4.0$, (a) and (b) $T^* = 1.0$ and (c) and (d) $T^* = 3.0$.

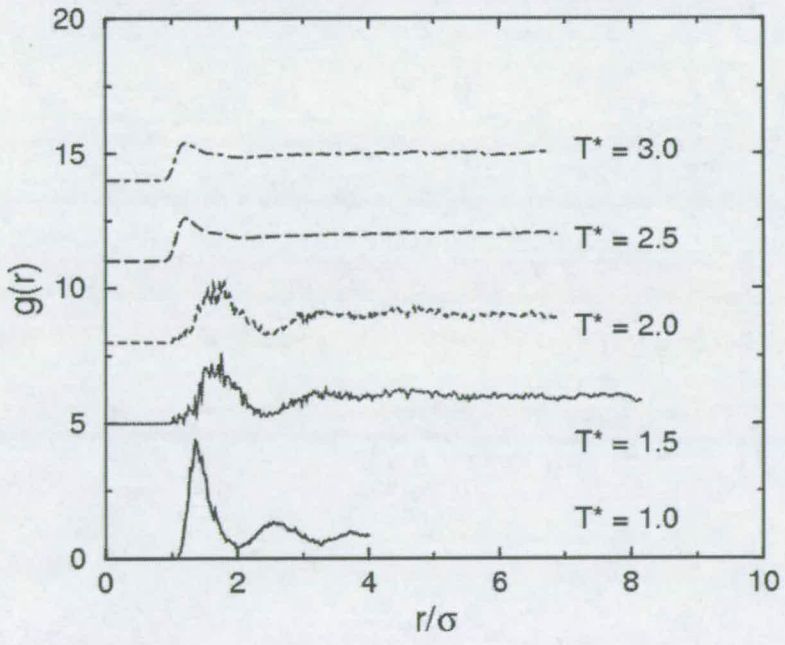

Figure 6.9: Radial distribution data for $T^* = 1.0 - 3.0$ for $\gamma = 0°$ with $p^* = 4.0$. Solid line - $T^* = 1.0$, dotted line - $T^* = 1.5$, dashed line - $T^* = 2.0$, long-dashed line - $T^* = 2.5$ and dot-dashed - $T^* = 3.0$. Plots have been displaced for clarity.

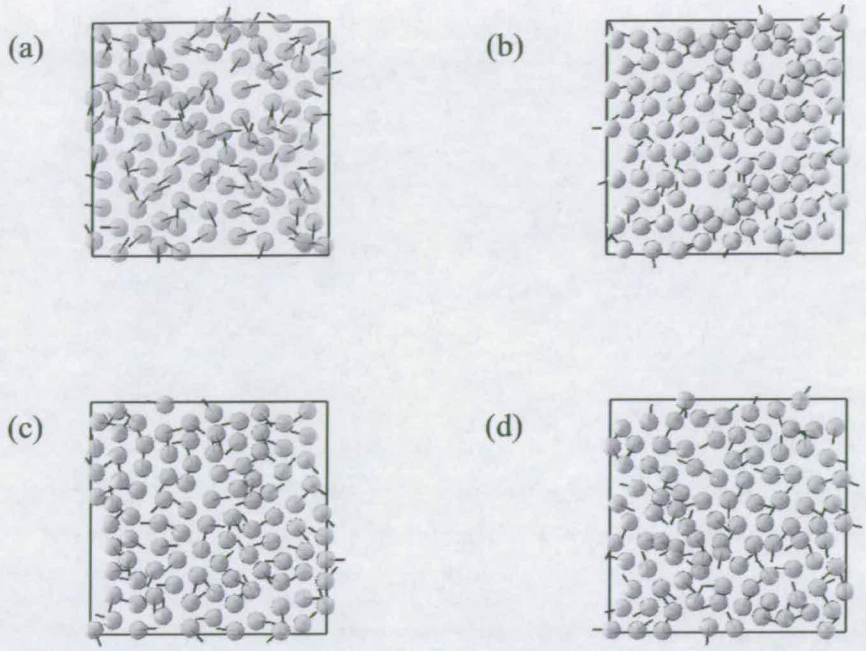

Figure 6.10: In-layer snapshot representations of CRM+Ts with $\gamma = 0°$, $p^* = 4.0$ and $T^* = 1.0$: (a) molecules $1-100$; (b) molecules $101-200$; (c) molecules $201-300$ and (d) molecules $301 - 400$. The black line indicates the direction of the steric dipole vector for each molecule and the layers perpendicular to the Z-axis.

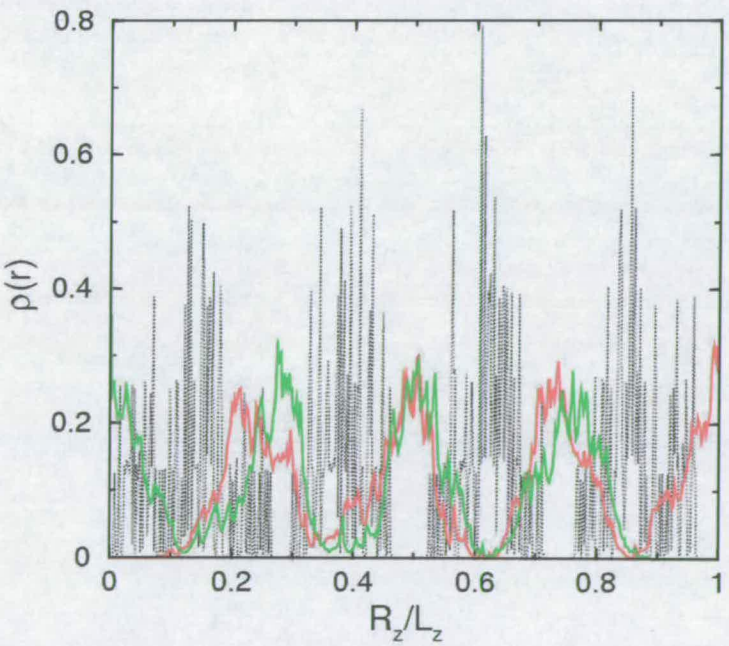

Figure 6.11: Single particle density function for $\gamma = 0°$ and $p^* = 4.0$ with $T^* = 1.0$. The red line corresponds to tail one and the green line tail two. The black dotted line represents the apical sphere single particle function.

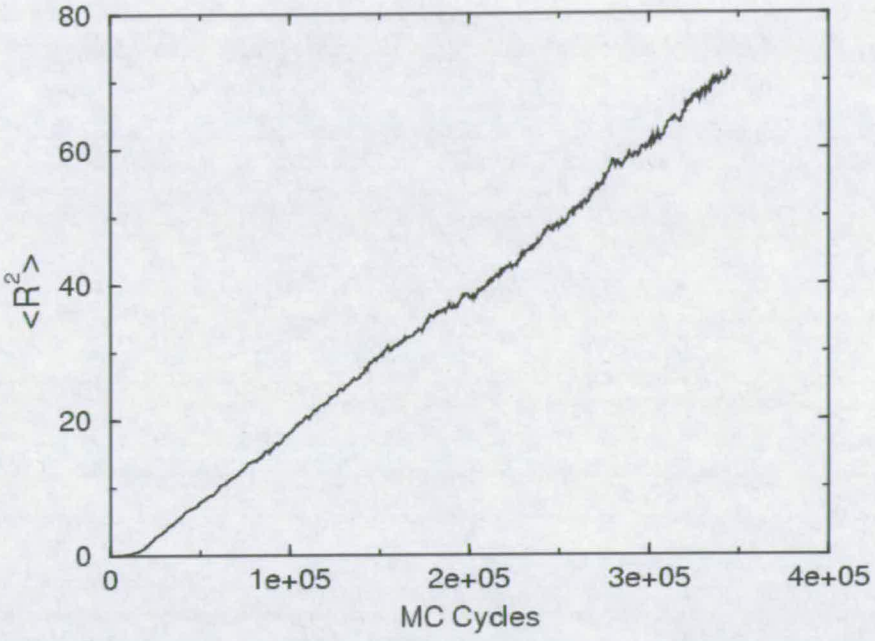

Figure 6.12: $\langle R^2 \rangle$ data for $\gamma = 0°$ and $p^* = 4.0$ with $T^* = 3.0$.

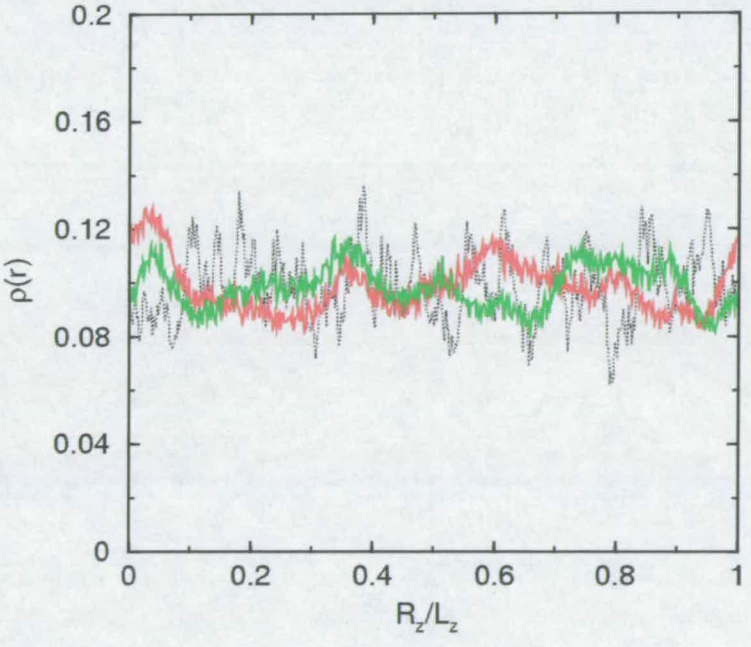

Figure 6.13: Single particle density function for $\gamma = 0°$ and $p^* = 4.0$ with $T^* = 3.0$. The red line corresponds to tail one and the green line tail two. The black dotted line represents the apical sphere single particle function.

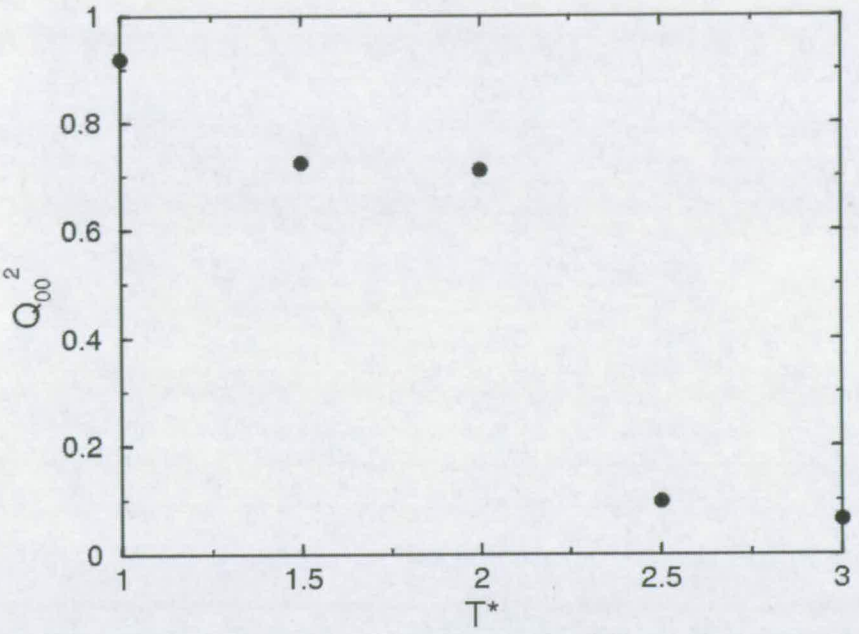

Figure 6.14: Nematic order parameter plotted as a function of temperature for $\gamma = 0°$ and $p^* = 4.0$. Error bars are smaller than the symbol size.

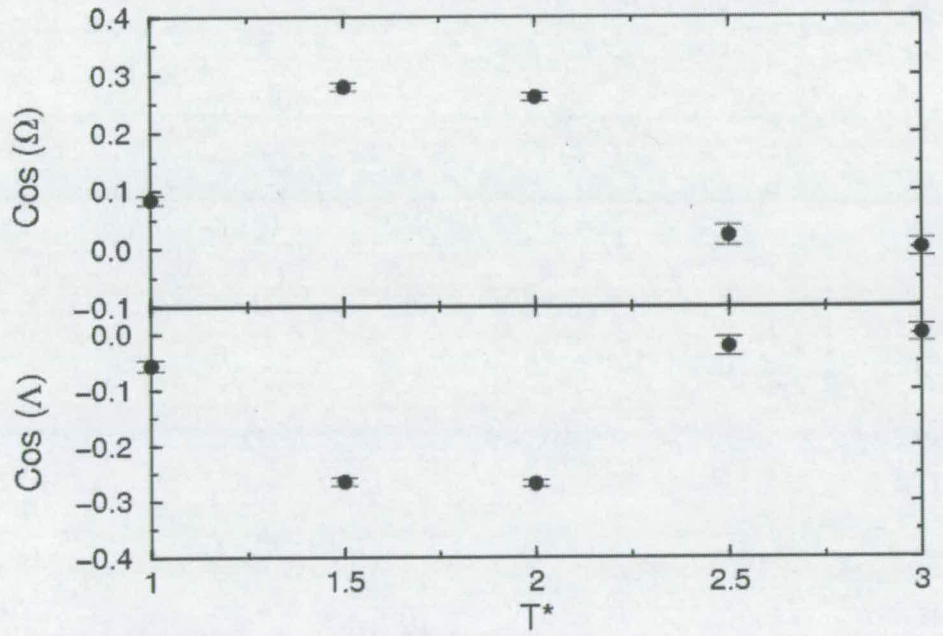

Figure 6.15: $\langle \cos \Omega \rangle$ and $\langle \cos \Lambda \rangle$ plotted as a function of temperature for $\gamma = 0°$ and $p^* = 4.0$. Error bars are smaller than the symbol size.

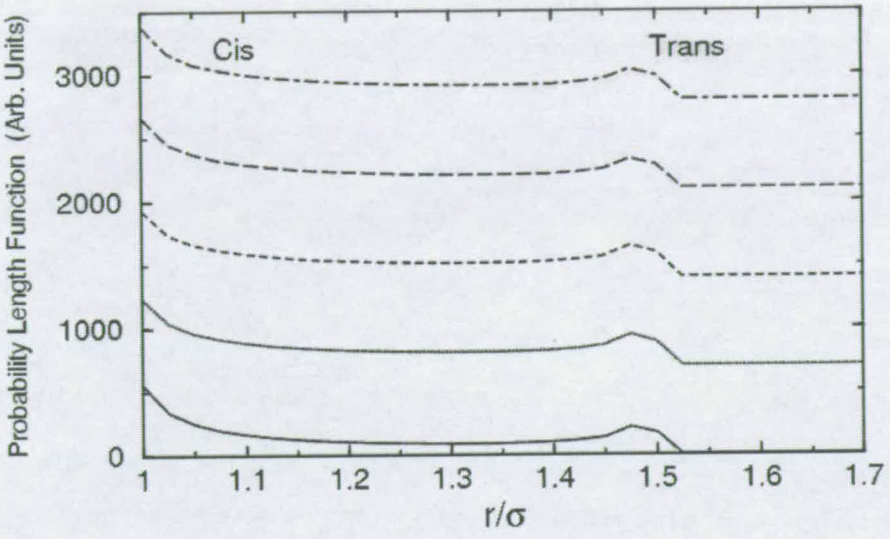

Figure 6.16: Probability length functions for $\gamma = 0°$ and $p^* = 4.0$ plotted as a function of temperature. Solid line, $T^* = 1.0$, dotted line, $T^* = 1.5$, dashed line, $T^* = 2.0$, long-dashed line, $T^* = 2.5$ and dot-dashed line, $T^* = 3.0$. Plots have been displaced for clarity.

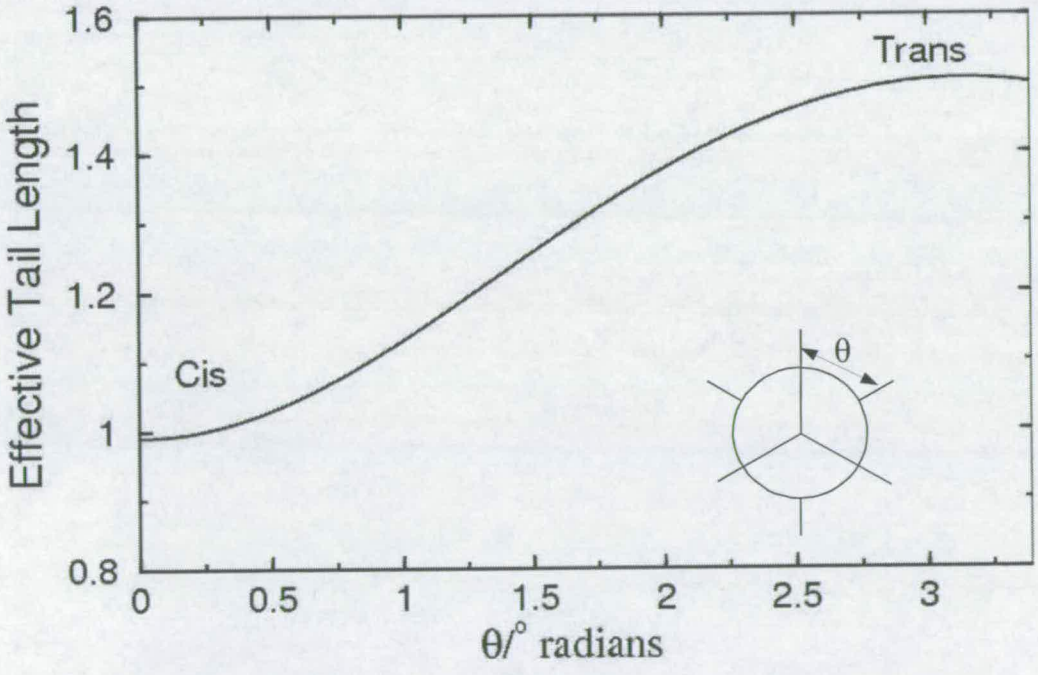

Figure 6.17: The length of the flexible tail as a function of dihedral angle, θ.

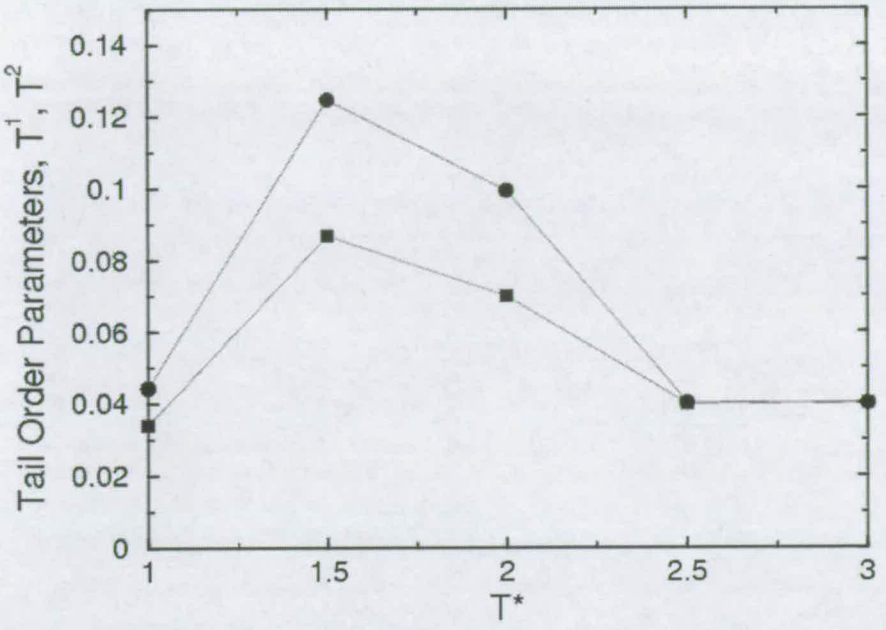

Figure 6.18: Tail order parameters for tail one (filled circles) and tail two (filled squares) for $\gamma = 0°$ and $p^* = 4.0$ plotted as a function of temperature. Error bars are smaller than the symbol size.

The tail order parameters, T^1 and T^2, plotted as functions of temperature along an isobar with $p^* = 4.0$ are shown in Fig. 6.18. Both parameters are low at all temperatures, especially upon entering the isotropic phase. As such, we suggest that the tail order parameters can indicate the formation of a smectic or isotropic phase, it is unclear whether this would be useful for nematic phases. The low values would be anticipated as the tails do not interact with one another and hence there is no driving force for the tails to align with one another.

A more useful quantity to examine is the average tip-tip distance, $\langle L_m \rangle$ as a function of temperature, as shown in Fig. 6.19. Surprisingly at high temperatures, in the isotropic phase, $\langle L_m \rangle$ is lower than at lower temperatures. The cores of the molecules are 5σ in length and the tails themselves are $\sim 1\sigma$ in length. The low values of $\langle L_m \rangle$ would suggest that the tails are contracted towards the core of the molecule as at higher temperatures the influence of repulsive interactions is not as significant as at low temperature.

A plot of $\langle \cos\gamma' \rangle$, as calculated via Eqn. 6.17, as a function of temperature along an isobar with $p^* = 4.0$ is shown in Fig. 6.20. This function should provide a useful indication of the effective bond angle at various temperatures. At low temperature, $T^* = 1.0$, $\gamma' \simeq 45°$. Above a temperature of $T^* = 1.5$, $\gamma' \simeq 30°$. In

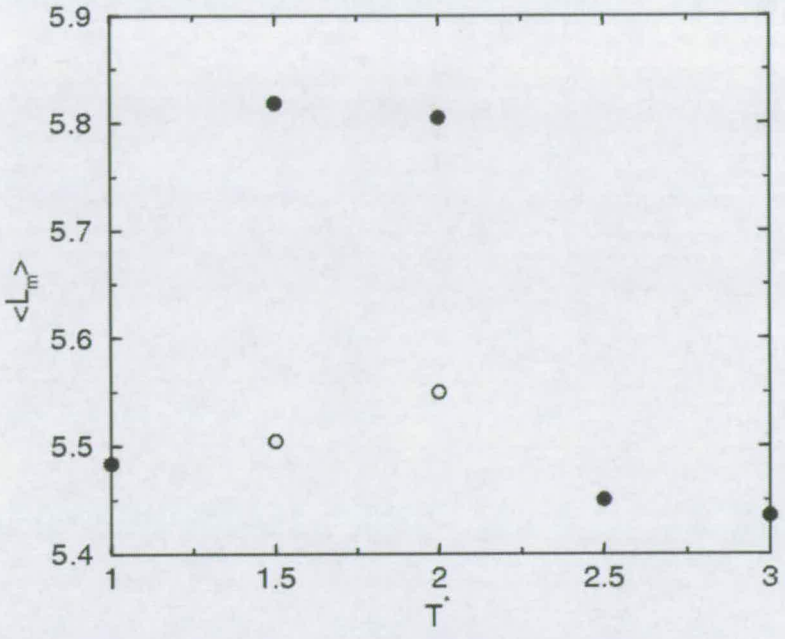

Figure 6.19: ($\langle L_m \rangle$) plotted as a function of temperature for $\gamma = 0°$ and $p^* = 4.0$. Filled circles denote simulation results obtained via heating and unfilled circles result from cooling simulation. Error bars are smaller than the symbol size.

the isotropic phase $\gamma' \simeq 32°$ as the tails have collapsed towards the cores of the molecules.

6.3.2 $\gamma = 20°$

The equation of state of CRM+Ts with $\gamma = 20°$ along an isobar with $p^* = 4.0$ is shown in Fig. 6.21. Figures 6.22(a) and (b), show snapshots of a simulation configuration at a temperature of $T^* = 1.0$. From this it can be seen that the layers are tilted, with ϕ calculated to be $17.83°$ with respect to the layer normal. The radial distribution plot, shown in Fig. 6.23, exhibits some short range ordering, suggestive of a smectic phase. Interestingly at low temperature the biaxial order parameter Q^2_{22} and the bulk polarisation, shown in Table 6.2 remain intact. This would suggest that the layers are correlated, which is surprising due to the increased layer spacing. In-layer snapshots are shown in Figs. 6.24(a)-(d). From these snapshots it can be seen that the molecules are aligned, with defects present within the layers. With the high polarisation this is likely to be a ferroelectric polarisation state. This may be a result of the steric dipole (molecular bend) of the molecules giving rise to enhanced interactions and slow evolution of polarisation. We also performed simulations cooling from $T^* = 2.5$. At equilibrium this

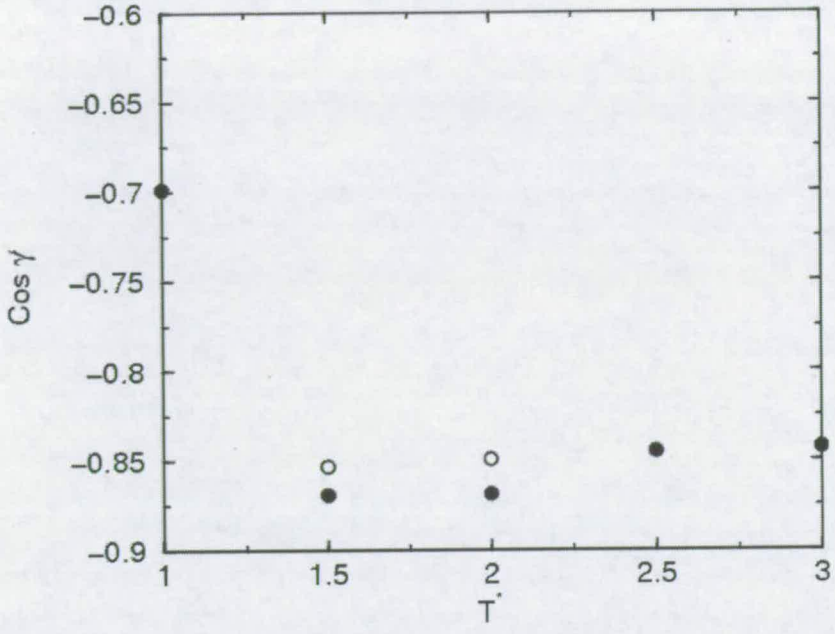

Figure 6.20: $\langle \cos \gamma' \rangle$ plotted as a function of temperature for $\gamma = 0°$ and $p^* = 4.0$. Filled circles denote simulation results obtained via heating and unfilled circles result from cooling simulation. Error bars are smaller than the symbol size.

T^*	Q^2_{00}	Q^2_{22}	P
1.0	0.8653(1)	0.5722(1)	0.8258(2)
1.5	0.7875(1)	0.5350(2)	0.7994(1)
2.0	0.20(2)	0.03(2)	0.03(2)
2.5	0.06(1)	0.02(1)	0.02(2)
3.0	0.06(1)	0.02(1)	0.02(2)

Table 6.2: Uniaxial (Q^2_{00}), biaxial (Q^2_{22}) order parameters and bulk polarisation (P) for CRM+Ts with $\gamma = 20°$ along an isobar with $p^* = 4.0$. Digits in parentheses denote the statistical uncertainty in the last figure based on one standard deviation.

system were found at higher density ($\rho^* \simeq 0.11$) than the corresponding heating run. The states resulting from heating simulations are metastable states and require further simulations for full characterisation of the phase behaviour.

As with CRM+Ts with $\gamma = 0°$ a plot of the single particle density, shown in Fig. 6.25 is indicative of adjoining layers overlapping.

Heating to a temperature of $T^* = 3.0$ yields the isotropic phase, snapshots of which are shown in Figs. 6.22(c) and (d). A plot of $\langle R^2 \rangle$ as a function of MC cycles (Fig. 6.26) clearly a large gradient of $\langle R^2 \rangle$ thus indicative of the isotropic phase. At this high temperature the corresponding single particle density profile, shown

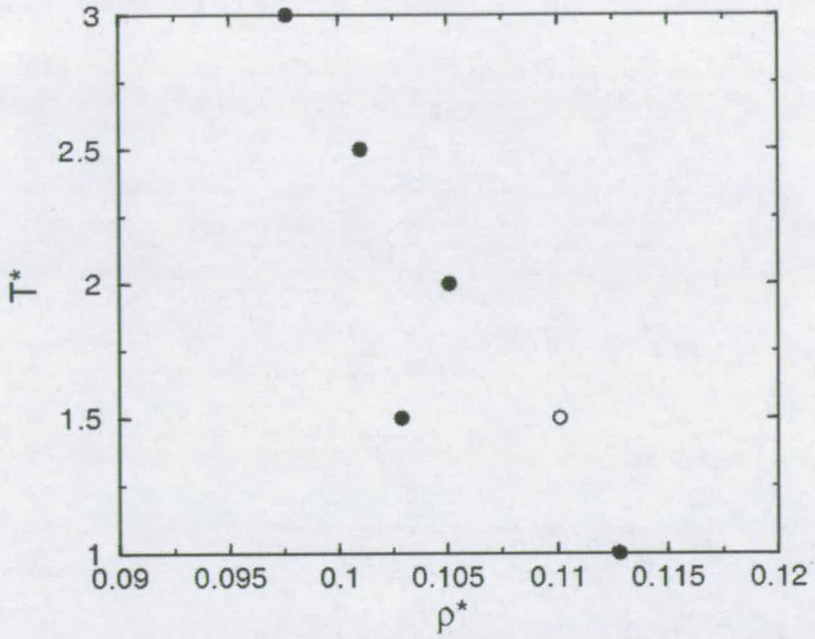

Figure 6.21: Equation of state for $\gamma = 20°$ with $p^* = 4.0$. Filled circles denote simulation results obtained via heating and unfilled circles result from cooling simulation. Error bars are smaller than the symbol size.

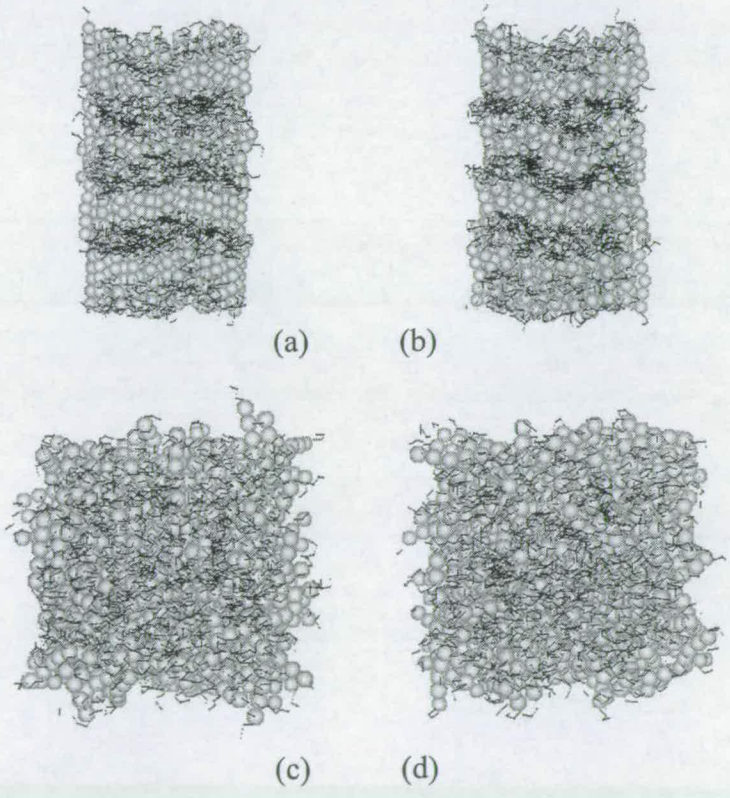

Figure 6.22: Snapshot representation for $\gamma = 20°$ with $p^* = 4.0$ (a) and (b) $T^* = 1.0$ and (c) and (d) $T^* = 3.0$.

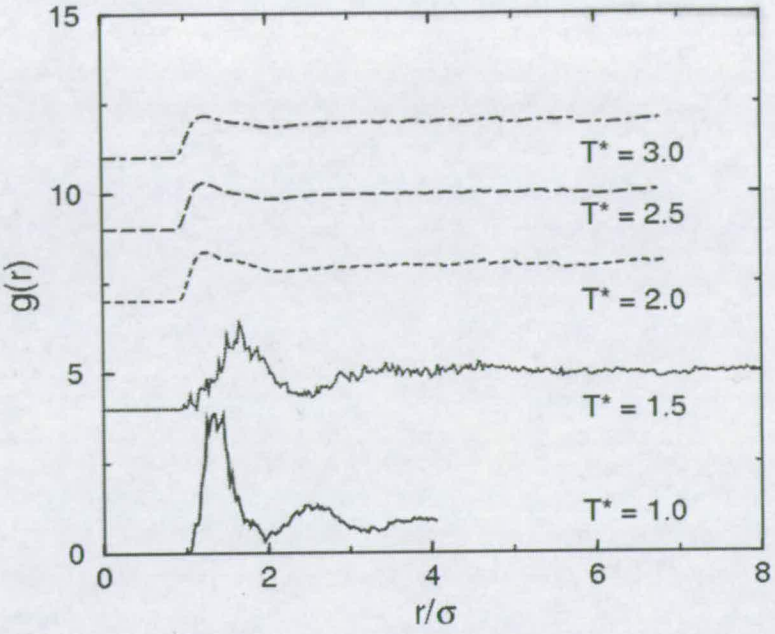

Figure 6.23: Radial distribution data for $T^* = 1.0 - 3.0$ for $\gamma = 20°$ with $p^* = 4.0$. Solid line - $T^* = 1.0$, dotted line - $T^* = 1.5$, dashed line - $T^* = 2.0$, long-dashed line - $T^* = 2.5$ and dot-dashed - $T^* = 3.0$. Plots have been displaced for clarity.

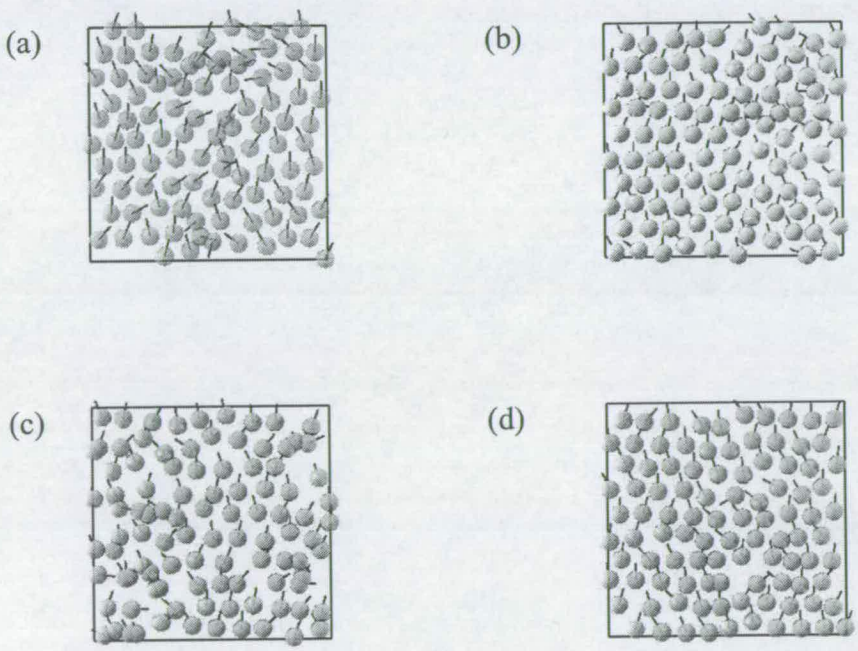

Figure 6.24: In-layer snapshot representations of CRM+Ts with $\gamma = 20°$, $p^* = 4.0$ and $T^* = 1.0$; (a) molecules 1−100, (b) molecules 101−200, (c) molecules 201−300 and (d) molecules 301 − 400. The black line indicates the direction of the steric dipole vector for each molecule and layers are perpendicular to the Z-axis.

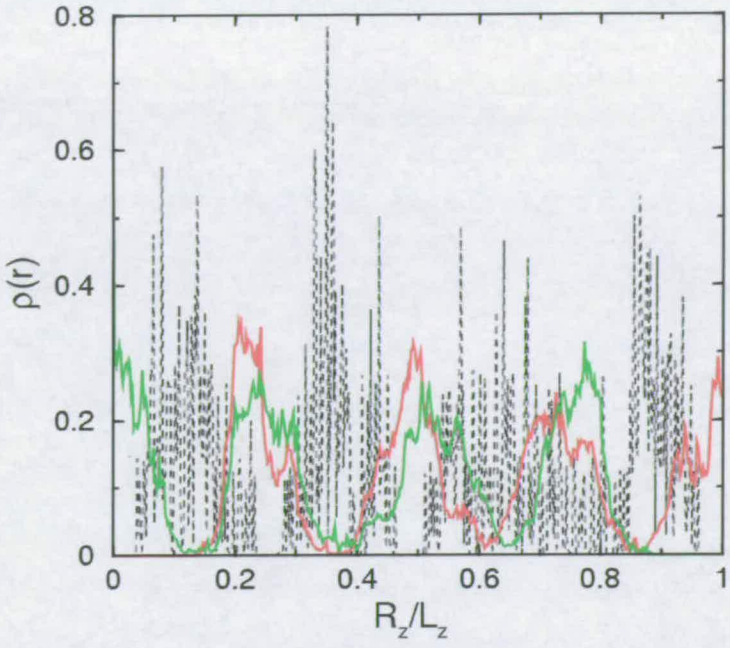

Figure 6.25: Single particle density function for $\gamma = 20°$ and $p^* = 4.0$ with $T^* = 1.0$. The red line corresponds to tail one and the green line tail two. The black dotted line represents the apical sphere single particle function.

in Fig. 6.27, is similar to that presented in Fig. 6.13. Which has been assigned as an isotropic phase.

The variation of the uniaxial order parameter, Q_{00}^2 as a function of temperature is shown in Table 6.2. The smectic-isotropic phase transition is signalled by a sharp drop in Q_{00}^2 between $T^* = 1.5$ and $T^* = 2.0$.

Figure 6.28, shows the probability length functions. As with linear CRM+Ts, the functions are independent of temperature and indicate *cis* and *trans* geometric forms. The tail order parameters are small and hence not ordered (Fig. 6.29).

Figure 6.30, shows the average tip-tip distances as a function of temperature. Upon heating $\langle L_m \rangle$ decreases. This suggests that the tips of the tails are located towards the cores of the molecules as at increased temperature the replusive interactions are not as predominant. Table 6.3 shows the total molecular elongation of the molecules. The effective length of the rigid core at this bond angle is $4.94L/\sigma$. Upon heating γ' decreases from $\gamma' \simeq 51°$ at $T^* = 1.0$ to $\gamma' \simeq 38°$ at $T^* = 3.0$.

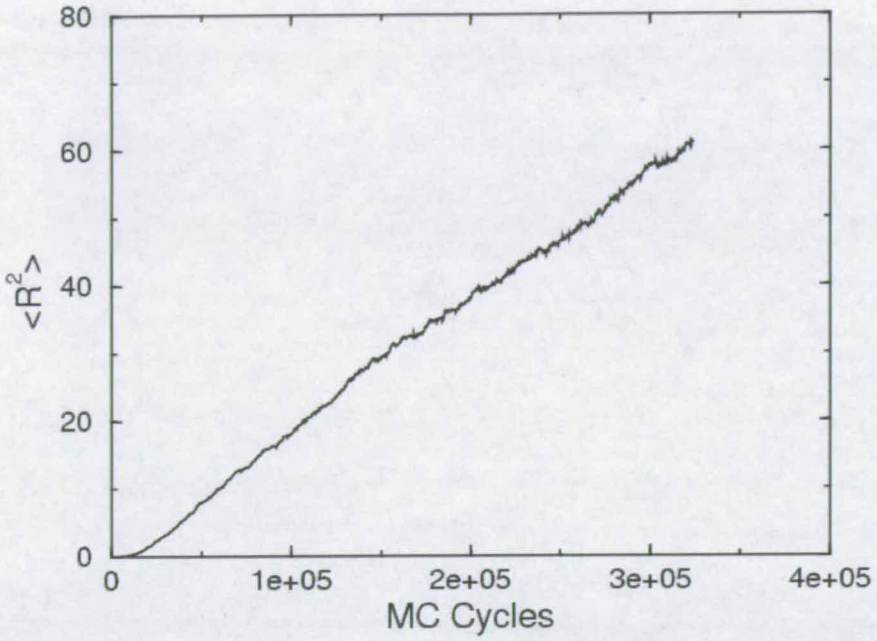

Figure 6.26: $\langle R^2 \rangle$ data for $\gamma = 20°$ and $p^* = 4.0$ with $T^* = 3.0$.

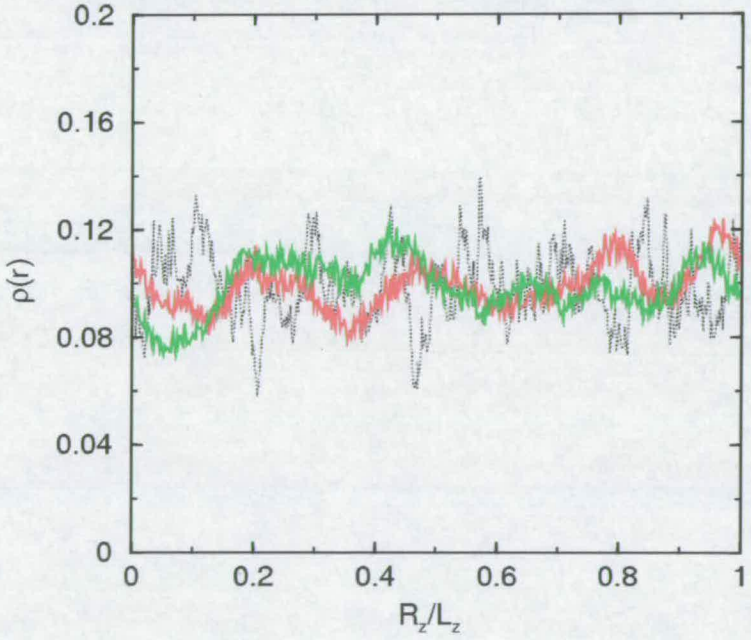

Figure 6.27: Single particle density function for $\gamma = 20°$ and $p^* = 4.0$ with $T^* = 3.0$. The red line corresponds to tail one and the green line tail two. The black dotted line represents the apical sphere single particle function.

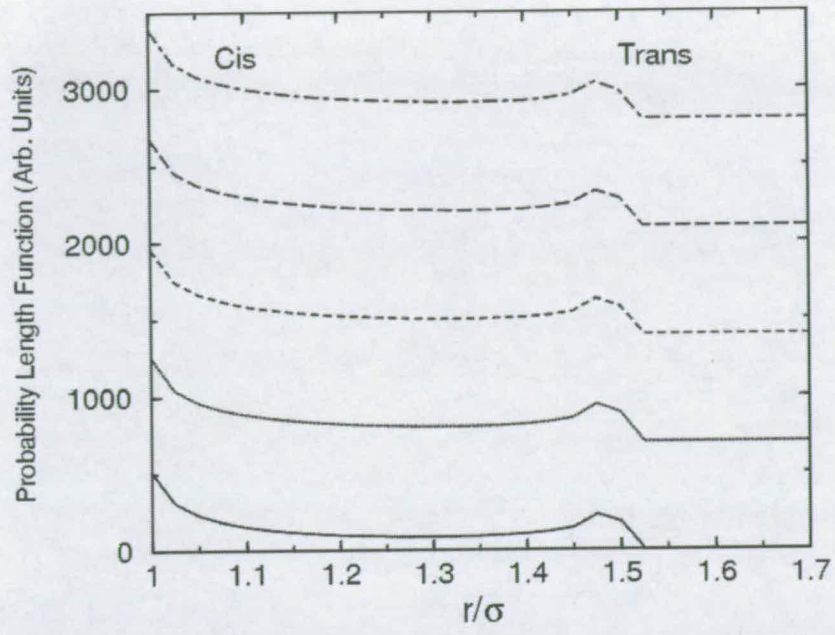

Figure 6.28: Probability length functions for $\gamma = 20°$ and $p^* = 4.0$ plotted as a function of temperature. Solid line, $T^* = 1.0$, dotted line, $T^* = 1.5$, dashed line, $T^* = 2.0$, long-dashed line, $T^* = 2.5$ and dot-dashed line, $T^* = 3.0$. Plots have been displaced for clarity.

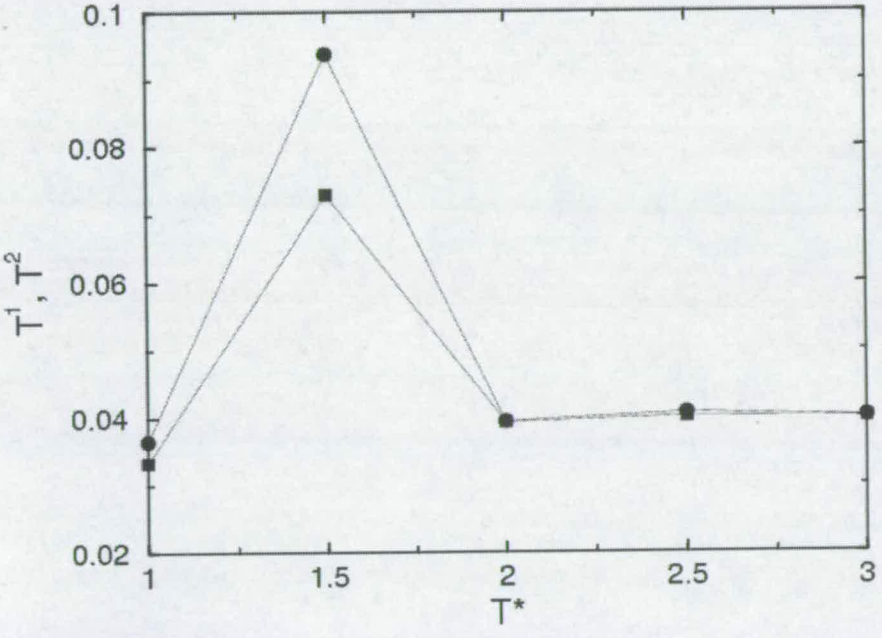

Figure 6.29: Tail order parameters for tail one (circles) and tail two (squares) for $\gamma = 20°$ and $p^* = 4.0$ plotted as a function of temperature. Error bars are smaller than the symbol size.

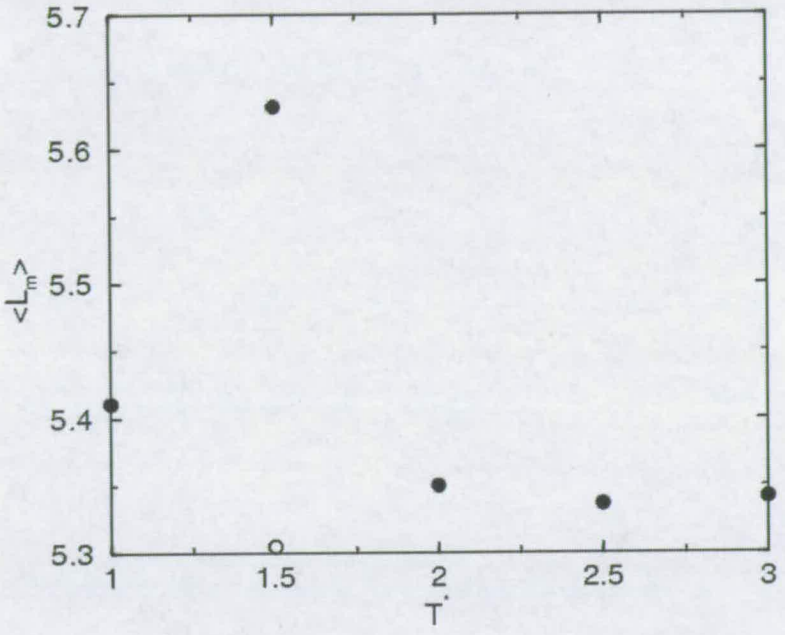

Figure 6.30: ($\langle L_m \rangle$) plotted as a function of temperature for $\gamma = 20°$ and $p^* = 4.0$. Filled circles denote simulation results obtained via heating simulations, unfilled circles denote simulation results obtained via cooling.

T^*	$\langle L_m \rangle$	$\langle \cos\gamma' \rangle$	$\gamma'/°$	Cell type
1.0	5.41(1)	−0.631(5)	50.9(4)	Cuboidal
1.5	5.51(1)	−0.727(2)	43.4(2)	Cuboidal
1.5	5.63(1)	−0.836(2)	33.3(2)	Cubic
1.5	5.31(3)	−0.799(4)	37.0(4)	Cooling
2.0	5.35(3)	−0.799(5)	37.0(5)	Cubic
2.5	5.34(3)	−0.795(5)	37.4(4)	Cubic
3.0	5.34(2)	−0.793(4)	37.6(4)	Cubic

Table 6.3: Average molecular elongations, $\langle L_m \rangle$, $\langle \cos\gamma' \rangle$, γ' and the simulation cell used for CRM+Ts with $\gamma = 20°$ along an isobar with $p^* = 4.0$. Digits in parentheses denote the statistical uncertainty in the last figure based on one standard deviation.

T^*	Q^2_{00}	Q^2_{22}	P
1.0	0.8795(1)	0.7743(1)	0.9294(2)
1.5	0.8333(2)	0.7543(1)	0.9143(1)
2.0	0.07(1)	0.02(1)	0.04(2)
2.5	0.08(1)	0.03(1)	0.03(2)
3.0	0.06(1)	0.02(1)	0.02(2)

Table 6.4: Uniaxial (Q^2_{00}), biaxial (Q^2_{22}) order parameters and bulk polarisation (P) for CRM+Ts with $\gamma = 40°$ along an isobar with $p^* = 4.0$. Digits in parentheses denote the statistical uncertainty in the last figure based on one standard deviation.

6.3.3 $\gamma = 40°$

Figure 6.31 shows the equation of state for CRM+Ts with $\gamma = 40°$ along an isobar with $p^* = 4.0$. Snapshots of a simulation configuration at a temperature of $T^* = 1.0$ are shown in Figs. 6.32(a) and (b). From this it can be seen that the molecules are tilted, with ϕ calculated to be $16.56°$ with respect to the layer normal. From the snapshots it can also be seen that the layers are distorted, with a large bend distortion. The addition of tails has disrupted the in-layer structure, compared to the corresponding system without flexible tails. The tails also form a 'lubricating' barrier between smectic layers. The radial distribution plot, shown in Fig. 6.33, exhibits some short range order suggestive of a smectic phase. The biaxial order parameter, Q^2_{22} and the bulk polarisation, shown in Table 6.4, persist at low temperatures. This would indicate that the layers remain correlated despite the increase in layer spacing, as a result of the tilt direction. Again the in-layer structure is ordered [Fig. 6.34(a)-(d)] with molecules in a hexagonal packing, yet the molecules remain aligned despite the deformed structure of the layers [Fig. 6.32(a)]. The steric dipoles (and hence tilt) of the molecules point towards the faces and the apex of a hexagonal net in hexatic phases, which will influence the radial distribution plots observed. With the high bulk polarisation observed, this is likely to be a ferroelectric polarisation state. As with the $\gamma = 20°$ system (Section 6.3.2) the slow evolution of the polarisation may be a result of the steric dipole. The low temperature systems presented here are ideal candidates for simulations where the simulation cell is allowed to tilt as per the Parrinello-Rahman method [44, 45] to allow equilibration of the layer tilt of these phases.

The single particle density plot, shown in Fig. 6.35, shows the interdigitation of the layers as observed with $\gamma = 0°$ and $20°$.

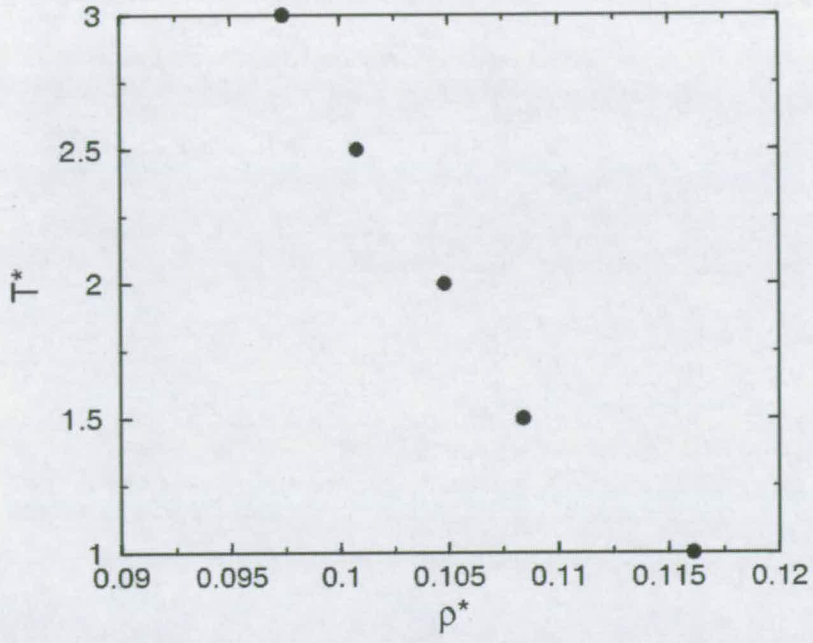

Figure 6.31: Equation of state for $\gamma = 40°$ with $p^* = 4.0$. Error bars are smaller than the symbol size.

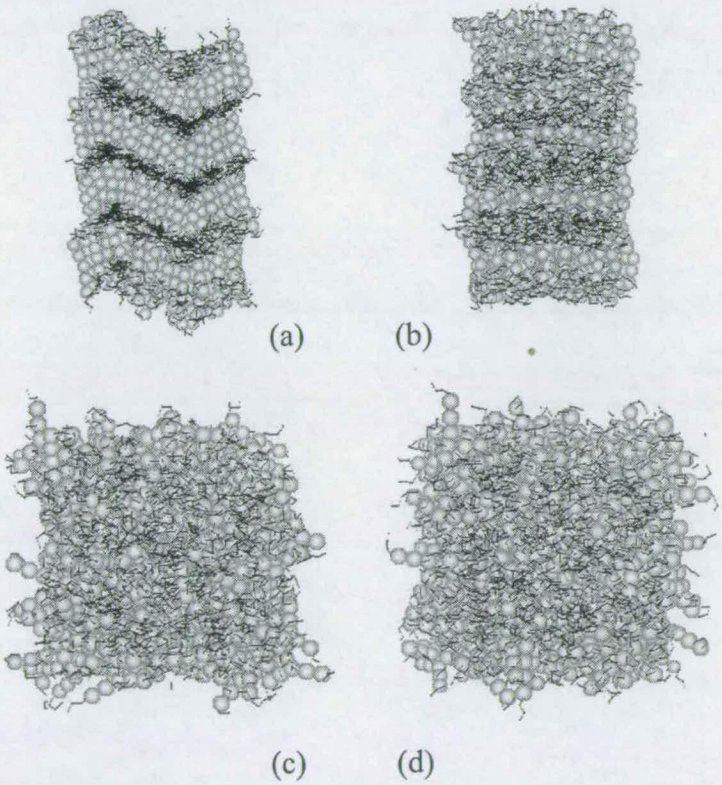

Figure 6.32: Snapshot representation for $\gamma = 40°$ with $p^* = 4.0$, (a) and (b) $T^* = 1.0$ and (c) and (d) $T^* = 3.0$.

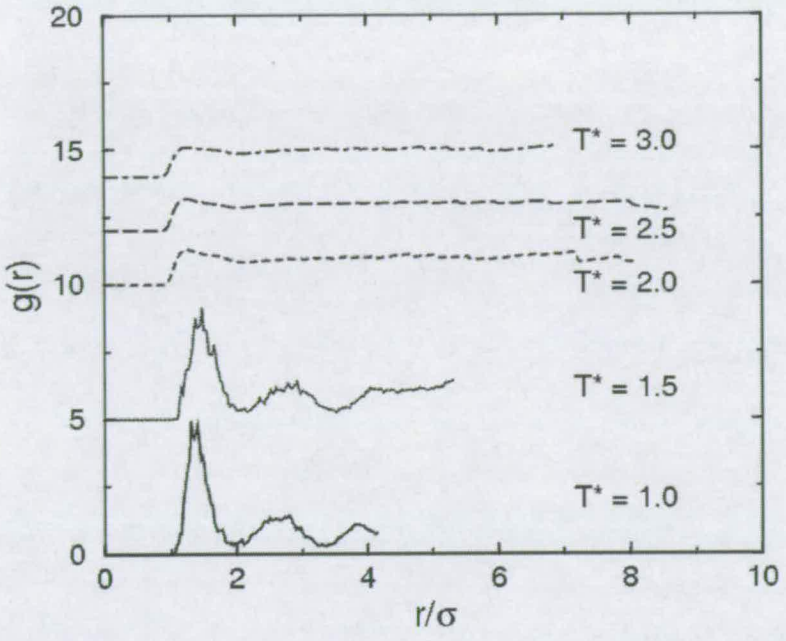

Figure 6.33: Radial distribution data for $T^* = 1.0 - 3.0$ for $\gamma = 40°$ with $p^* = 4.0$. Solid line - $T^* = 1.0$, dotted line - $T^* = 1.5$, dashed line - $T^* = 2.0$, long-dashed line - $T^* = 2.5$ and dot-dashed - $T^* = 3.0$. Plots have been displaced for clarity.

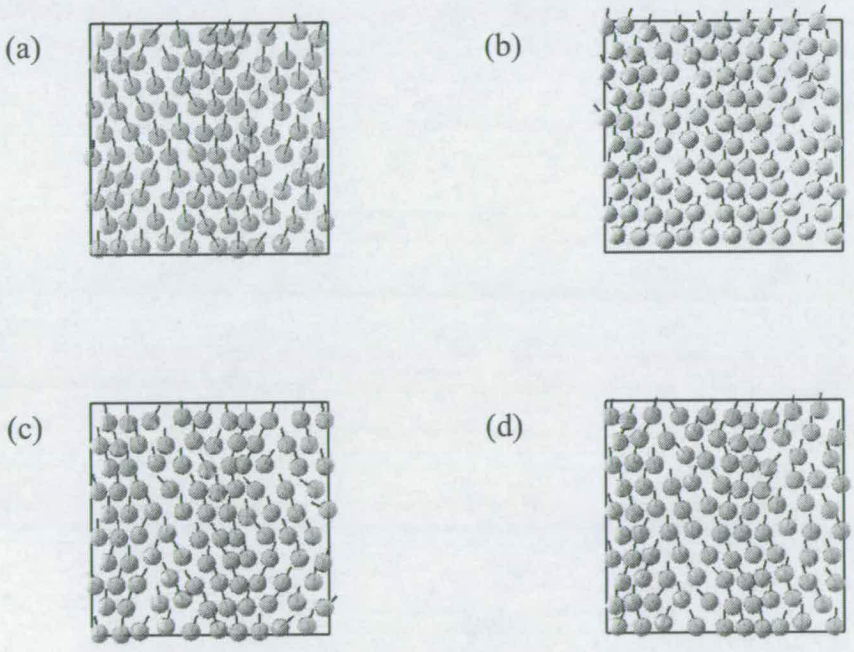

Figure 6.34: In-layer snapshot representations of CRM+Ts with $\gamma = 40°$, $p^* = 4.0$ and $T^* = 1.0$; (a) molecules $1-100$, (b) molecules $101-200$, (c) molecules $201-300$ and (d) molecules $301 - 400$. The black line indicates the direction of the steric dipole vector for each molecule and the layers are perpendicular to the Z-axis.

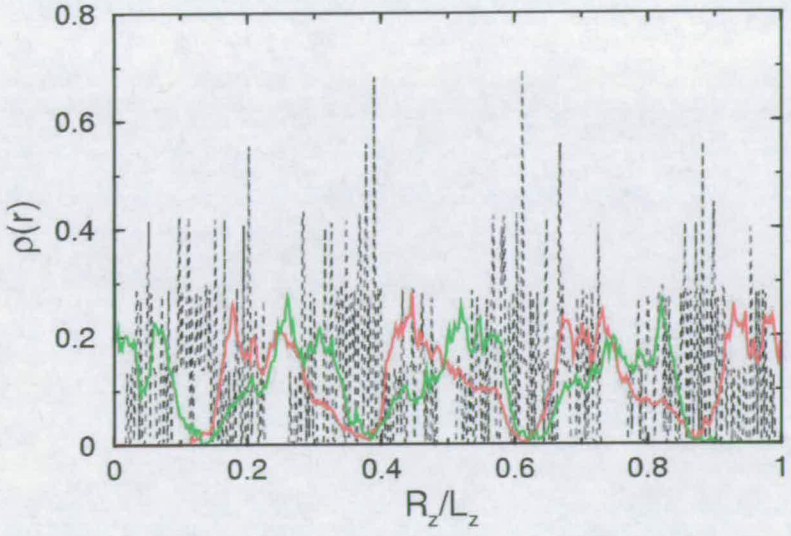

Figure 6.35: Single particle density function for $\gamma = 40°$ and $p^* = 4.0$ with $T^* = 1.0$. The red line corresponds to tail one and the green line tail two. The black dotted line represents the apical sphere single particle function.

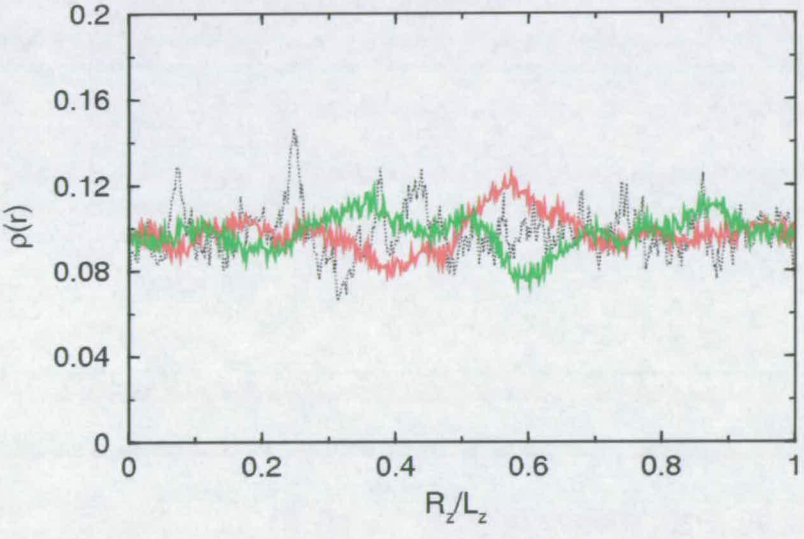

Figure 6.36: Single particle density function for $\gamma = 40°$ and $p^* = 4.0$ with $T^* = 3.0$. The red line corresponds to tail one and the green line tail two. The black dotted line represents the apical sphere single particle function.

Heating to a temperature of $T^* = 3.0$, the isotropic phase is observed, as shown in Figs. 6.32(c) and (d). At this high temperature the corresponding single particle density profile, shown in Fig. 6.36, is uniform, thus indicating a isotropic phase.

The variation of the uniaxial order parameter, Q^2_{00} as a function of temperature is shown in Table 6.4. The smectic-isotropic phase transition is signalled by a sharp drop in Q^2_{00} over the temperature range $1.5 \leq T^* \leq 2.0$.

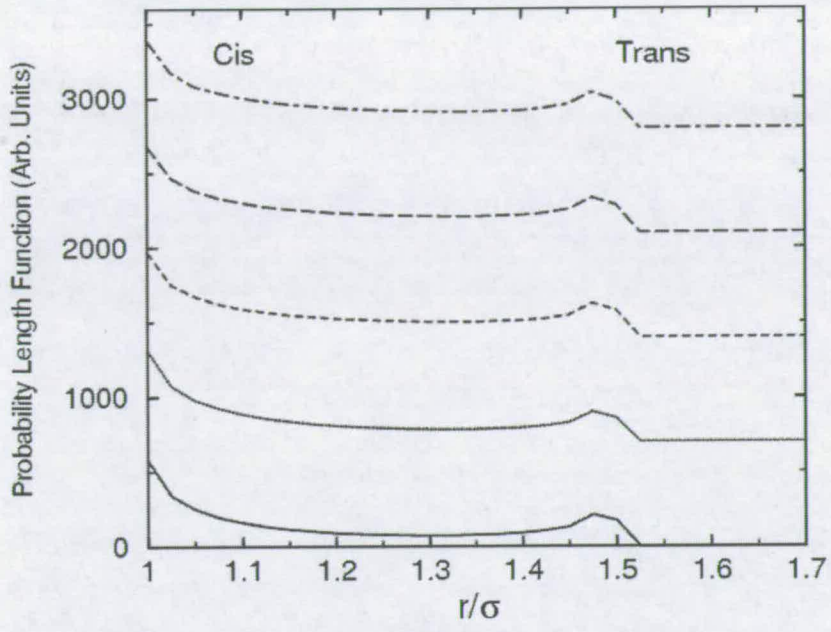

Figure 6.37: Probability length functions for $\gamma = 40°$ and $p^* = 4.0$ plotted as a function of temperature. Solid line, $T^* = 1.0$, dotted line, $T^* = 1.5$, dashed line, $T^* = 2.0$, long-dashed line, $T^* = 2.5$ and dot-dashed line, $T^* = 3.0$. Plots have been displaced for clarity.

Figure 6.37, shows the probability length functions. As with previous systems, these functions are independent of temperature and indicate *cis* and *trans* geometric forms. The tail order parameters remain show little variation and such disordered (Fig. 6.38).

A plot of $\langle L_m \rangle$ as a function of temperature as shown in Fig. 6.39. In contrast to the systems with $\gamma = 0, 20°$, $\langle L_m \rangle$ increases upon heating. Table 6.5 shows the molecular elongations as a result of the flexible tails and the effective bond angle γ'. At this bond the elongation of the rigid core is $4.76l/\sigma$. At low temperature $\gamma' \simeq 65°$ and in the isotropic phase, $\gamma' \simeq 50°$.

6.4 Conclusions

In this chapter we have presented results from constant pressure Monte Carlo simulations of model bent-core molecules constructed from 5 soft sphere arranged in a rigid 'v' shape with external bond angle γ and two 3 segment flexible tails. Here model molecule interactions are described by a simple repulsive potential and sphere-tail interactions calculated using Lorentz-Berthlot mixing

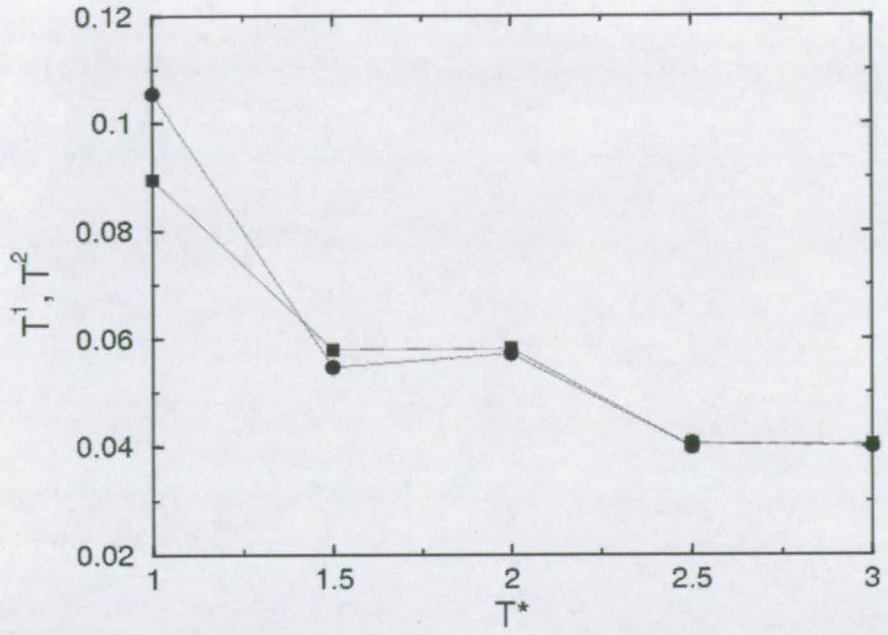

Figure 6.38: Tail order parameters for tail one (Circles) and tail two (Squares) for $\gamma = 40°$ and $p^* = 4.0$ plotted as a function of temperature. Error bars are smaller than the symbol size.

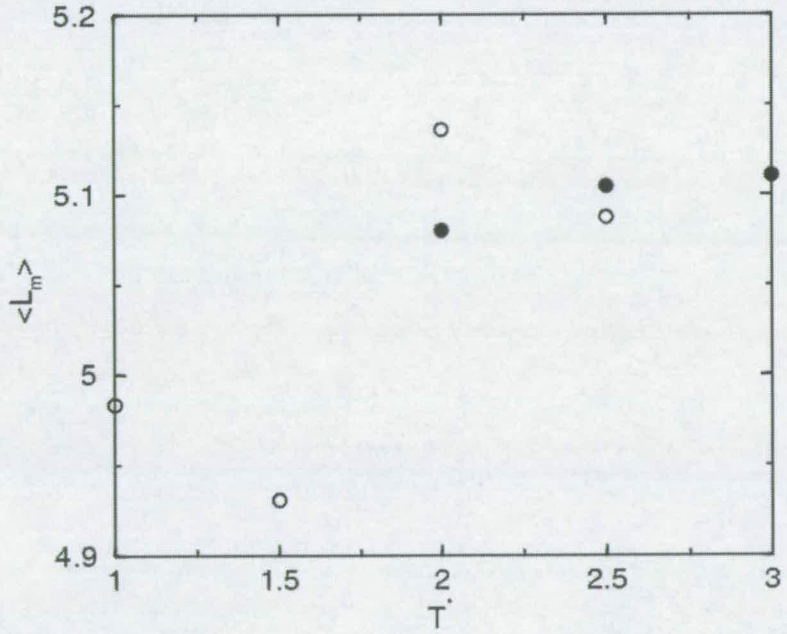

Figure 6.39: $(\langle L_m \rangle)$ plotted as a function of temperature for $\gamma = 40°$ and $p^* = 4.0$. Unfilled circles denote simulation results obtained with a cuboidal simulation cell and filled circles results utilising a cubic cell.

T^*	$\langle L_m \rangle$	$\langle \cos\gamma' \rangle$	$\gamma'/°$	Cell
1.0	4.98(1)	−0.420(6)	65.2(4)	Cuboidal
1.5	4.93(1)	−0.489(3)	60.7(2)	Cuboidal
2.0	5.14(1)	−0.612(4)	52.3(3)	Cuboidal
2.0	5.08(3)	−0.650(7)	49.5(5)	Cubic
2.5	5.09(3)	−0.64(1)	50.5(8)	Cuboidal
2.5	5.11(2)	−0.654(7)	49.2(6)	Cubic
3.0	5.11(2)	−0.650(7)	49.4(5)	Cubic

Table 6.5: Average molecular elongations, $\langle L_m \rangle$, $\langle \cos\gamma\prime \rangle$ and $\gamma\prime$ for CRM+Ts with $\gamma = 40°$ along an isobar with $p^* = 4.0$. Digits in parentheses denote the statistical uncertainty in the last figure based on one standard deviation.

rules. The flexible tails are regrown using the Configurational Bias technique. The phase behaviour of these molecules has been studied as a function of γ.

With linear molecules ($\gamma = 0°$) we find isotropic and tilted smectic phases. The low temperature smectic phase was tilted to $\simeq 14°$. The phase transition is not clearly defined as there is disparity between the simulation results obtained from heating and cooling. As a result the phase transition is likely to occur over the temperature range $1.0 \leq T^* \leq 2.0$. Absolute free energy calculations can be envisaged to locate the phase transition and assess the relative stabilities of the phases found over this temperature range. The phase transition in the corresponding 5 sphere CRM case occurs over the range $1.6 \leq T^* \leq 1.7$, in the low temperature phases the molecules are tilted to $> 50°$ with respect to the layer normal.

With $\gamma = 20°$, we find isotropic and tilted smectic ferroelectric phases. The low temperature phase was tilted to $\sim 18°$. The phase transition is not clearly defined and is thought to occur over the temperature range $1.0 \leq T^* \leq 2.0$. The phase transition for the corresponding 5 sphere core CRM system occurs over the temperature range $1.5 \leq T^* \leq 2.0$.

With $\gamma = 40°$, we find isotropic and tilted smectic ferroelectric phases. The low temperature phase was tilted to $\sim 17°$. The phase transition is not clearly defined and is thought to occur over the temperature range $1.0 \leq T^* \leq 2.0$. The phase transition for the corresponding 5 sphere core CRM system occurs over the temperature range $0.7 \leq T^* \leq 0.8$.

The addition of the flexible tails stabilises the layered phases, giving rise to unusual phase behaviour. The layers are distorted, with a large bend observed in

the $\gamma = 40°$ system. The molecules appear to pack hexagonally within layer, which merits further investigations. This phase behaviour would need to be investigated fully, perhaps utilising free energy calculations or performing simulations with a larger system size with Molecular Dynamics simulations to complement the Monte Carlo simulations performed here. Inclusion of the flexible tails reduces the molecular tilt found in the low temperature phases with $\phi \sim 14 - 18°$ as opposed to $> 50°$ for the 5 sphere CRM systems. The flexible tails appear to stabilise the ferroelectric phase, although this would need to be fully investigated with ferroelectric, antiferroelectric and superparaelectric polarisation states.

These simulations represent the first simulations of a multi-site model of bent-core molecules with flexible end groups. Already with this system we have reached the limit of what can be simulated on a desktop computer. The simulations require longer 'time' to reach a true equilibrium and we may not performed truly ergodic sampling. The next generation of simulations with this type of simple model would need to be performed on parallel computers. It would be interesting to investigate this simple model using molecular dynamics.

Ideally, the phase behaviour of the CRM+Ts would need to be fully investigated as a function of γ, interaction potential, alternative core sizes and various tail lengths. The configurational bias Monte Carlo technique is non-trivial and requires extensive computational processing power and would necessitate the use of supercomputers, such as the HPCx facility available in Edinburgh.

CHAPTER 7

Calculation of flexoelectric coefficients

The flexoelectric effect was first described by Meyer [1, 88]. This can be envisaged to be the liquid crystalline analogue of the piezoelectric effect in crystals. In the crystalline phase, piezoelectric polarisation is induced by application of strain (by applying an electric field the crystal will deform in a given direction as used in microscopic techniques such as atomic force microscopy). In the flexoelectric effect a net polarisation is induced by deformation of the director field in the nematic phase of molecules with steric asymmetry that carry a permanent dipole moment. Meyer [88] proposed two types of molecules that give rise to flexoelectricity. The first is a system of wedge-shaped molecules with a longitudinal dipole will exhibit a polarisation when a splay (book opening) deformation is applied to the director field, as shown in Fig. 7.1(a). The second is a system composed of banana-shaped molecules with a transverse dipole moment undergoing a bend deformation will also exhibit a polarisation, as shown in Fig.7.1(b). As such there will be two main contributions to the flexoelectric polarisation, $\vec{p}^f$, which is given by [1],

$$\vec{p}^f = e_1(\nabla \cdot \vec{n})\vec{n} + e_3(\nabla \times \vec{n}) \times \vec{n}, \tag{7.1}$$

where $\vec{n} = \vec{n}(\vec{r})$ denotes the director field, e_1 is the splay flexoelectric coefficient and e_3 is the bend flexoelectric coefficient. It must be noted that the flexoelectric effect is not only confined to nematic liquid cystals, but is also found in lipid membranes [89], which exhibit liquid crystalline order. The flexoelectricity observed in these membranes is a result of curvature-induced membrane polarisation [89].

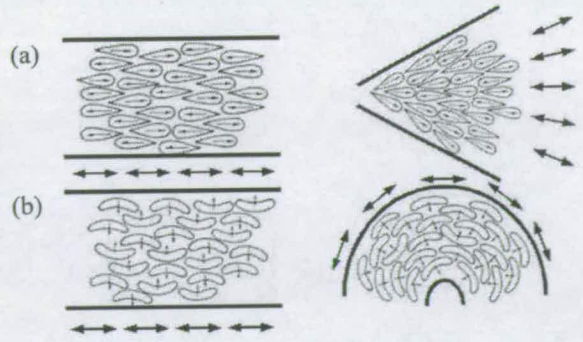

Figure 7.1: The effects of applying; (a) splay and (b) bend deformations to the director field of a nematic liquid crystal formed of wedge-shaped and banana-shaped molecules respectively. The black arrows denote the director field at the indicated locations.

There have been several experimental studies of the flexoelectric effect [90, 91]. The flexoelectric coefficients can be related to the optical response of a given system upon application of an electrical field to a nematic liquid crystal contained in hybrid aligned cell [90]. Upon application of an electric field, the molecular dipoles align, changing the molecular alignment and inducing optical anisotropy. It must noted that e_1 and e_3 are difficult to determine individually from experiment. In experiments, we measure $e_{\pm} = e_1 \pm e_3$ or the elastic coefficients, which will increase the error in the coefficients. This raises the importance of calculating the flexoelectric coefficients using theory and simulation methods [92, 93, 94] to examine the role of molecular structure upon the flexoelectric behaviour.

To date there have been four simulation studies devoted to the calculation of flexoelectric coefficients. Two of these studies utilised a simple model of a wedge-shaped molecule constructed from a Lennard-Jones sphere and Gay-Berne ellipsoid [95, 96]. In the former study by Stelzer *et al.* [95] the flexoelectric coefficients are evaluated from expressions derived from density functional theory. In this study the bend coefficients for molecules with two different steric dipoles were negligible in line with the predictions by Meyer based upon shape [88]. Increasing the ratio of the diameter of the LJ sphere and Gay-Berne ellipsoid, increases the splay coefficient at corresponding values of the nematic order parameter.

In the later study by Billeter and Pelcovits [96] the bend and splay coefficients were measured in the smectic and isotropic phases using fluctuational relations derived from linear response theory [97]. In this study increasing the reduced

steric dipole of the model molecules leads to an increase in magnitude and inversion of sign in the splay coefficient. With a larger wedge, the bend coefficient is smaller in magnitude. The statistical uncertainties reported for the flexoelectric coefficients are of the order of the coefficients themselves. As a general rule, the application of linear response fluctuation techniques require very long simulations and Billeter and Pelcovits only ran simulations of 500000 MC cycles, which was clearly not sufficient for statistically precise results.

In both of these studies there is some ambiguity in the sign of the splay coefficient. However, in both studies the splay coefficient decreases in magnitude upon heating. The negligible bend coefficients reported in the Stelzer study [95] are likely to be a result of the approximations used in the calculation of the direct correlation function in the density functional method, as Billeter and Pelcovits [96] report non-zero values of e_3. The bend flexoelectric coefficient should be zero with wedge-shaped molecules [88].

Zakharov and Vakulenko [98] studied the compound 5CB using a parametrised Gay-Berne model and Percus-Yevick closure of the Ornstein-Zernicke eqauation [94, 98]. As with the Stelzer *et al.* [95] study, Zakharov and Vakulenko utilised density functional theory and a direct correlation function. The calculated flexoelectric coefficients were in reasonable agreement with experimental measurements [98].

Latterly, Cheung *et al.* have calculated the flexoelectric coefficients of a nematic liquid crystal using atomic simulation methods [99]. They studied n-4-trans-4-n-pentylcyclohexyl benzonitrile (PCH5) using molecular dynamics coupled with a force field [22]. The coefficients have been calculated using linear response theory. It is suggested that both e_1 and e_3 both decrease linearly upon heating (hence deceasing nematic order parameter).

Calculation of the flexoelectric coefficients is beneficial for the design of future liquid crystalline materials. By careful tuning of molecular structure, desired electro-optical properties can be produced for optical transducers or display devices [100, 101].

In this chapter, we critically assess the reliability of the fluctuation scheme for the calculation of flexoelectric coefficients with our model system and compare the results to experimental results. Previous studies have focused on the splay

flexoelectric coefficients utilising wedge-shaped molecules. The simulation results presented presented in this chapter represents the first systematic attempt to calculate the flexoelectric coefficients for a series of bent-core molecules with bond angles in the range $0° - 30°$ with and without attractive interactions. It is unclear whether the splay coefficient should be zero with bent-core molecules.

7.1 Theory

To calculate the flexoelectric coefficients e_1 (splay) and e_3 (bend), we measure the fluctuations of the polarisation and orientational stress tensor. This approach was proposed by Nemstov and Osipov [97] and was subsequently used by Billeter and Pelcovits [96], Allen and Masters [102] and latterly by Cheung *et al.* [99, 103].

From the fluctuation-dissipation theorem, the response function can be determined from spontaneous fluctuations of the polarisation and orientational stress tensor. The polarisation of the system is given by,

$$\vec{P}_\alpha = E_{\alpha\beta\gamma}\gamma_{\beta\gamma}, \tag{7.2}$$

where we have used the summation convention over the Greek indices over the x, y and z directions, $E_{\alpha\beta\gamma}$ is the response function and $\gamma_{\beta\gamma}$ is the deformation tensor. This deformation tensor can be written as,

$$\gamma_{\alpha\beta} = \frac{\delta\theta_\alpha}{\delta r_\beta}, \tag{7.3}$$

where θ is the rotation angle of the director about the α-axis. For small discrete deformations this now becomes,

$$\gamma_{\alpha\beta} = \epsilon_{\alpha\mu\nu} n_\mu \partial_\beta n_\nu, \tag{7.4}$$

with $\delta_\beta n_\nu = \delta n_\nu / \delta r_\beta$, n_α is the α-component of the director $[\vec{n}(\vec{r})]$ and $\epsilon_{\alpha\beta\gamma}$ is the Levi-Citva tensor. The corresponding response function, $E_{\alpha\beta\gamma}$ is given by the correlation functions of the polarisation, P_α and orientational stress tensor, $\pi_{\beta\gamma}$.

$$E_{\alpha\beta\gamma} = -\frac{\beta}{V}\langle P_\alpha \pi_{\beta\gamma} \rangle, \tag{7.5}$$

where $\vec{P}_\alpha$ is the polarisation and

$$\pi_{\alpha\beta} = -\frac{1}{2}\sum_{i\neq j}\vec{r}_{ij}^{\alpha}\tau_{ij}^{\beta}, \tag{7.6}$$

in which $\vec{r}_{ij} = \vec{r}_j - \vec{r}_i$ is the intermolecular vector between molecule i and molecule j and τ_{ij} is the torque exerted on molecule i by molecule j.

We can then write the response function as,

$$E_{\alpha\beta\gamma} = E_1\epsilon_{\alpha\beta\gamma} + E_2\epsilon_{\mu\alpha\beta}n_\gamma n_\mu + E_3\epsilon_{\mu\gamma\beta}n_\alpha n_\mu + E_4\epsilon_{\mu\alpha\gamma}n_\beta n_\mu \tag{7.7}$$

Multiplying the first term of Eqn. 7.7 by the deformation tensor Eqn. 7.4, we obtain,

$$\begin{aligned} E_1\epsilon_{\alpha\beta\gamma}\epsilon_{\alpha\mu\nu}n_\mu\partial_\gamma n_\nu &= E_1(\delta_{\gamma\mu}\delta_{\alpha\nu} - \delta_{\gamma\nu}\delta_{\alpha\mu})n_\mu\partial_\gamma n_\mu \\ &= -E_1 n_\alpha\delta_\gamma n_\gamma + E_1 n_\gamma\delta_\gamma n_\alpha \end{aligned} \tag{7.8}$$

Similarly,

$$\begin{aligned} E_2\epsilon_{\lambda\alpha\beta}n_\gamma n_\lambda\epsilon_{\beta\mu\nu}n_\mu\partial_\gamma n_\nu &= E_2(\delta_{\lambda\mu}\delta_{\alpha\nu} - \delta_{\lambda\nu}\delta_{\alpha\mu})n_\gamma n_\lambda n_\mu\partial_\gamma n_\mu \\ &= E_2 n_\gamma\partial_\gamma n_\alpha - E_2 n_\lambda n_\gamma n_\alpha\partial_\gamma n_\lambda \\ &= E_2 n_\gamma\partial_\gamma n_\alpha \end{aligned} \tag{7.9}$$

$$\begin{aligned} E_3\epsilon_{\lambda\gamma\beta}n_\alpha n_\lambda\epsilon_{\beta\mu\nu}n_\mu\partial_\gamma n_\nu &= E_3(\delta_{\lambda\mu}\delta_{\gamma\nu} - \delta_{\lambda\nu}\delta_{\gamma\mu})n_\alpha n_\lambda n_\mu\partial_\gamma n_\nu \\ &= E_3 n_\alpha\partial_\gamma n_\gamma - E_3 n_\alpha n_\gamma n_\nu\partial_\gamma n_\nu \\ &= E_3 n_\alpha\partial_\gamma n_\gamma \end{aligned} \tag{7.10}$$

$$\begin{aligned} E_4\epsilon_{\lambda\alpha\gamma}n_\beta n_\lambda\epsilon_{\beta\mu\nu}n_\mu\partial_\gamma n_\nu &= E_4(\delta_{\lambda\beta}\delta_{\alpha\mu}\delta_{\gamma\nu} + \delta_{\lambda\mu}\delta_{\alpha\nu}\delta_{\gamma\lambda} \\ &+ \delta_{\lambda\nu}\delta_{\alpha\lambda}\delta_{\gamma\mu} - \delta_{\lambda\mu}\delta_{\alpha\beta}\delta_{\gamma\nu} - \delta_{\lambda\nu}\delta_{\alpha\mu}\delta_{\gamma\beta} \\ &- \delta_{\lambda\beta}\delta_{\alpha\nu}\delta_{\gamma\mu})n_\lambda n_\mu\partial_\gamma n_\nu \\ &= E_4 n_\alpha\partial_\gamma n_\gamma + E_4 n_\gamma\partial_\gamma n_\alpha \\ &+ E_4 n_\alpha n_\gamma n_\nu\partial_\gamma n_\nu - E_4 n_\alpha\partial_\gamma n_\gamma - E_4 n_\gamma\partial_\gamma n_\alpha \\ &- E_4 n_\alpha n_\gamma n_\nu\partial_\gamma n_\nu \\ &= 0 \end{aligned} \tag{7.11}$$

Thus,

$$E_{\alpha\beta\gamma}\gamma_{\beta\gamma} = (E_3 - E_1)n_\alpha\partial_\gamma n_\gamma + (E_1 + E_2)n_\gamma\partial_\gamma n_\alpha, \tag{7.12}$$

which is similar to the flexoelectric polarisation given in Eqn. 7.1. We can find expressions for e_1 and e_3 in terms of $E_{\alpha\beta\gamma}$ by multiplying Eqn. 7.7 by $\epsilon_{\mu\beta\gamma}\vec{n}_\mu\vec{n}_\alpha$ and $\epsilon_{\mu\alpha\beta}\vec{n}_\mu\vec{n}_\gamma$ for the splay and bend coefficients, respectively. This yields

$$e_1 = -\frac{1}{2}E_{\alpha\beta\gamma}\epsilon_{\mu\beta\gamma}n_\mu n_\alpha \tag{7.13}$$

$$e_3 = -\frac{1}{2}E_{\alpha\beta\gamma}\epsilon_{\mu\alpha\beta}n_\mu n_\gamma \tag{7.14}$$

For simulations it is convenient to translate this to the director-based frame of reference. With $\vec{n} = \vec{Z}$ the splay and bend coefficients become

$$e_1 = -\frac{1}{2}\left(E_{zxy} - E_{zyx}\right) \tag{7.15}$$

$$e_3 = -\frac{1}{2}\left(E_{xyz} - E_{yxz}\right) \tag{7.16}$$

The reduced flexoelectric coefficients are $e_1^* = e_1\sigma^2/\mu$ and $e_3^* = e_3\sigma^2/\mu$ for the splay and bend coefficients respectively assuming that the dipole-dipole interactions are negligible.

7.1.1 Simulation details

We performed constant volume, constant temperature Monte Carlo (NVT-MC) of N_m molecules in a cubic simulation cell with periodic boundary conditions applied [33, 34]. We are considering the CLJM and CRM systems as detailed in Chapters 3 and 4, respectively. The N_m molecules interacted via a simple repulsive pair potential (Eqn. 7.17) or the full $(12, 6)$ Lennard-Jones pair potential (Eqn. 7.18).

$$u = 4\epsilon\left(\frac{\sigma}{r_{ij}}\right)^{12}. \tag{7.17}$$

$$u = 4\epsilon\left[\left(\frac{\sigma}{r_{ij}}\right)^{12} - \left(\frac{\sigma}{r_{ij}}\right)^{6}\right], \tag{7.18}$$

We calculated the flexoelectric coefficients as shown in Eqns. 7.15 and 7.16, using the response function presented in Eqn. 7.5. The relevant polarisations, $\vec{P}_\alpha$, were

calculated using the function,

$$P_\alpha = \sum_{i=1}^{N_{mol}} \vec{P} \cdot \vec{n}_\alpha, \tag{7.19}$$

$$\tag{7.20}$$

where $\vec{r}_{ij}^{\alpha}$ is the α-component of the intermolecular vector between molecules i and j and n_α denotes the α-axis. The orientational stress tensor, $\pi_{\beta\gamma}$ was calculated via the function,

$$\tau_{ij}^{\beta} = \sum_{k=1}^{N_s} \vec{r}_k^{c} \times \vec{F}_{kj}, \tag{7.21}$$

where $\vec{r}_k^{c}$ is the intramolecular vector of the k^{th} sphere of the i^{th} molecule relative to the apical sphere of the i^{th} molecule and $\vec{F}_{kj}$ is the total force acting on the k^{th} sphere of molecule i from molecule j, ($\vec{F}_{kj} = \sum_l \vec{F}_{kl}$, where l denotes the sum over spheres on molecule j). The force, $\vec{F}_{kl}$ is the first derivative of the potentials used in the CRM (Eqn. 7.17) and CLJM (Eqn. 7.18) systems as shown in Eqns. 7.22 and 7.23, respectively.

$$\vec{F}_{kl} = \frac{24}{r}\epsilon\left(\frac{2}{r^{12}}\right)\vec{r}_{kl} \tag{7.22}$$

$$\vec{F}_{kl} = \frac{24}{r}\epsilon\left[\left(\frac{2}{r^{12}}\right) - \left(\frac{1}{r^{6}}\right)\right]\vec{r}_{kl}. \tag{7.23}$$

It must be noted that $\vec{r}_k^{c}$ and $\vec{F}_{kj}$ are both in the director frame. Eqns. 7.5, 7.15 and 7.16 are also similar to the expressions derived from the free energy by Allen and Masters [102].

The flexoelectric coefficients have been calculated in the nematic phase of apolar CRM and CLJM systems as a function of molecular bend angle, γ. For purposes of comparison the CRM and CLJM systems have been studied at fixed density and temperature for which the nematic phase is stable at several values of γ. For the two systems γ is the range $0° - 25°$ and $0° - 30°$ for the CRM and CLJM systems, respectively. These systems were allowed to equilibrate for a minimum of 4 million MC cycles (10000 simulation blocks) to ensure good statistics. These calculations were by no means trivial and a typical simulation block of 400 attempted translations/rotations per molecule required $\sim 600 - 1000$ seconds of computation time. The polarisation and the orientational stress tensor data was saved after every 20 MC sweeps (20 sets of data for each simulation block of 400 MC sweeps). These saved data was then used to evaluate the response function

presented in Eqn. 7.5 and hence the flexoelectric coefficient as per Eqns. 7.15 and 7.16

7.2 Results

7.2.1 Structural properties

A plot of the nematic order parameter, Q_{00}^2 as a function of external bond angle γ is shown in Fig. 7.2. From this data, we can predict the external bond angle at which the nematic phase is lost. We have fitted the data using a power law,

$$S(\gamma) = S(0)(1 - \gamma/\gamma_c)^{\alpha}, \tag{7.24}$$

where γ_c is the critical bend angle, above which the nematic phase is no longer stable, $S(0)$ is the Q_{00}^2 value for linear molecules and α is a specific exponent. The fitted values of γ_c, $S(0)$ and α for the CRM and CLJM systems are presented in Table 7.1.

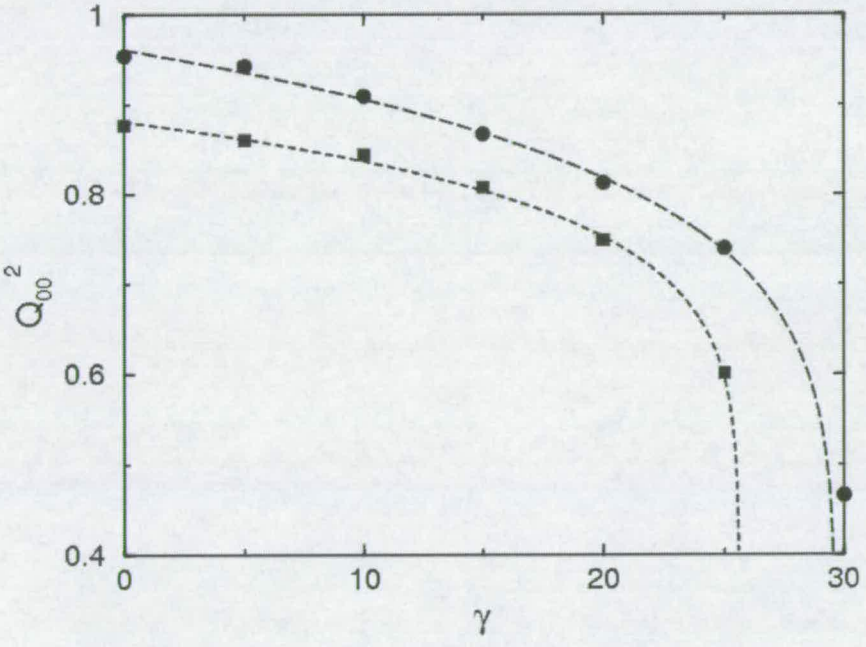

Figure 7.2: The nematic order parameter, Q_{00}^2 plotted as a function of temperature. The CRM system is denoted by black filled circles and the CLJM system by black filled squares. The curves indicate the respective fitted functions.

From the CRM data in Table 7.1 the critical angle is $25.53°$, above which the nematic phase is no longer stable. This was supported by simulations with $\gamma > 25°$,

	CRM	CLJM
γ_c	25.6(2)	29.6(1)
$S(0)$	0.881(4)	0.961(1)
α	0.104(7)	0.143(4)

Table 7.1: The fitted constants for both the CRM and CLJM systems. The figures in parentheses denote the statistical uncertainty in the last digit.

where $Q_{00}^2 \simeq 0$, within finite-size errors as discussed in Section 2.3.2. For the corresponding CLJM system the destabilisation of the nematic phase is predicted to occur at $\gamma > 30.25°$. We can also determine the critical exponent, β by plotting $\log_{10}(Q_{00}^2)$ as a function of $\log_{10}(\gamma_c - \gamma)$. This plot is shown in Fig. 7.3. The values of $\beta = 0.0927$ and 0.1508 for the CRM and CLJM systems respectively. The critical functions now become,

$$\log_{10}(Q_{00}^2) \propto \log_{10}(24.38 - \gamma)^{0.093} \tag{7.25}$$

$$\log_{10}(Q_{00}^2) \propto \log_{10}(30.25 - \gamma)^{0.151}. \tag{7.26}$$

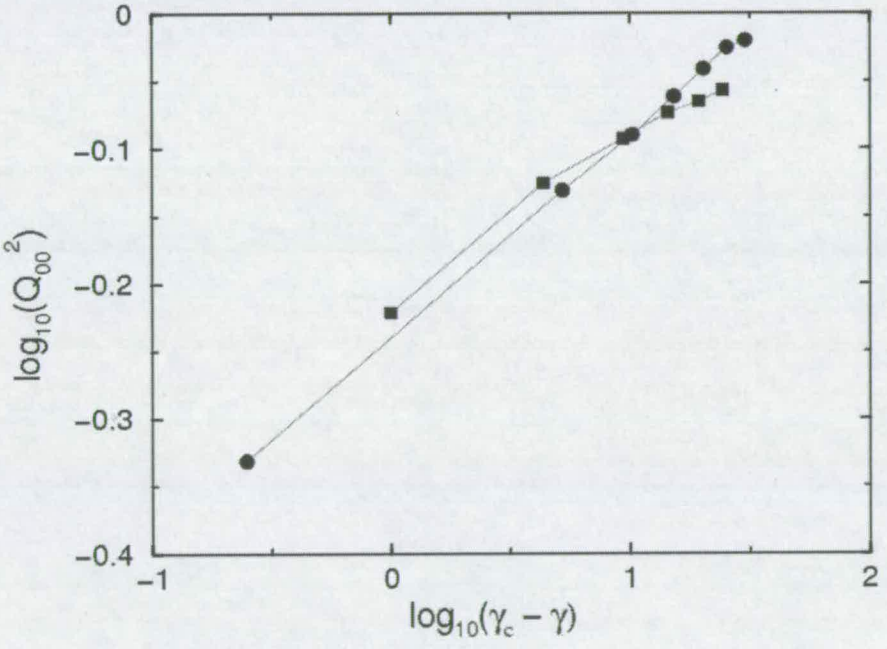

Figure 7.3: $\log_{10}(Q_{00}^2)$ plotted as a function of $\log_{10}(\gamma_c - \gamma)$, filled circles denote results from the CRM system and filled square from the corresponding CLJM system.

7.2.2 Flexoelectric coefficients

The splay and bend flexoelectric coefficients were calculated using Eqns. 7.15 and 7.16 and are plotted in Figs. 7.4 and 7.5, respectively. The flexoelectric coefficients have also been plotted as a function of Q_{00}^2, as suggested by Billeter and Pelcovits [96]. These plots are shown in Figs. 7.6 and 7.7 for the splay and bend coefficients, respectively. Experimental data for the two flexoelectric coefficients are often ambiguous [91]. There is also concern as to the correct sign of the coefficients.

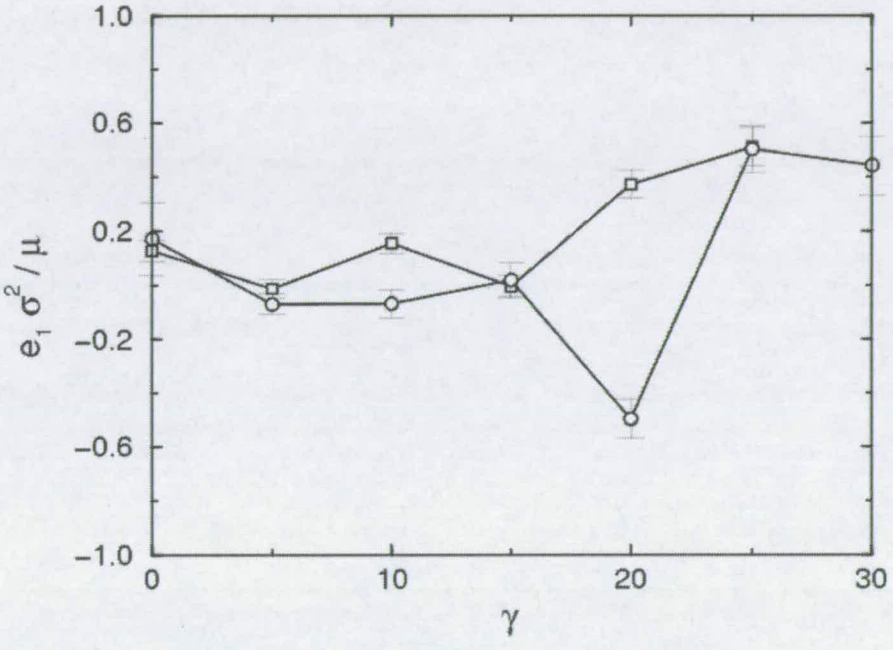

Figure 7.4: The splay flexoelectric coefficient (e_1) plotted as a function of γ. The unfilled squares denotes the data collected from the CRM system and the unfilled circles denote the data harvested from the CLJM simulation runs.

At low γ (high values of Q_{00}^2), it would be anticipated that for both the CRM and CLJM systems e_1 would be negligible as the molecules are not wedge-shaped. Indeed the splay coefficients for the CRM and CLJM systems fluctuate about zero for $Q_{00}^2 > 0.8$, as shown in Fig. 7.6. For the system with attractive interactions the values are larger in magnitude for the corresponding CRM state points. With $Q_{00}^2 = 0.95$ ($\gamma = 0°$) with attractive interactions $e_1^* \simeq 0.2$. This is possibly a result of large fluctuations in the polarisations in the x,y and z as shown in Fig. 7.8. The average polarisations are shown in Table 7.2 and are non-zero, even after long simulations. In the corresponding repulsive system the polarisation drifts (shown in Fig. 7.9), thus reinforcing the requirement for long simulation runs. At high values of γ the average polarisation in all three directions are large. This will have an impact on the flexoelectric coefficient for these bond angles. In order

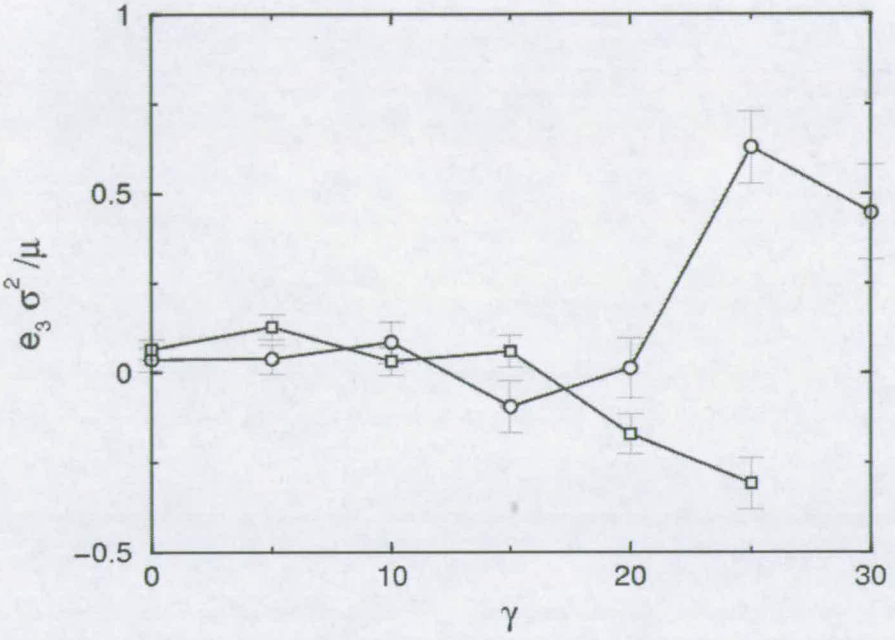

Figure 7.5: The bend flexoelectric coefficient (e_3) plotted as a function of γ. Unfilled squares denote data collected from the CRM system and the unfilled circles denote data harvested from the CLJM simulation runs.

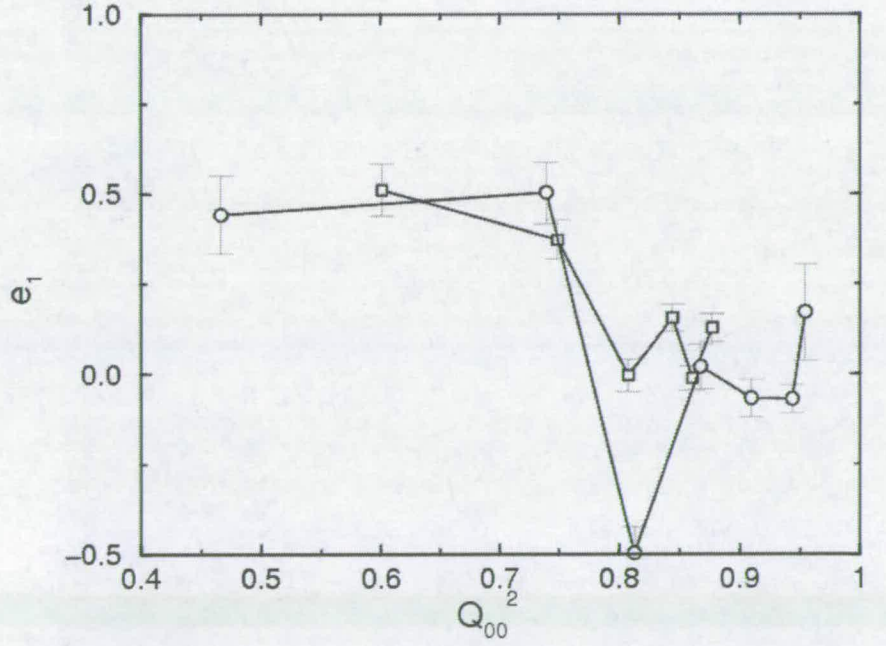

Figure 7.6: The splay flexoelectric coefficient (e_1) plotted as a function of Q_{00}^2. The unfilled squares denotes the data collected from the CRM system and the unfilled circles denote the data harvested from the CLJM simulation runs.

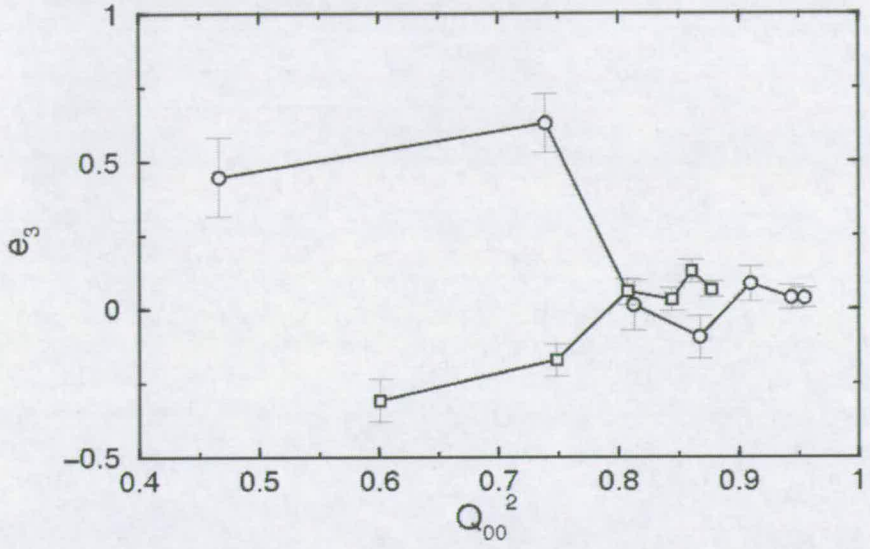

Figure 7.7: The bend flexoelectric coefficient (e_3) plotted as a function of Q_{00}^2. The unfilled squares denotes the data from the CRM simulations and the unfilled circles denote the data from CLJM simulation runs.

to assess the impact of the non-zero average polarisations would have on the flexoelectric coefficients, we calculated the co-variance of the response function, as per Eqn. 7.27,

$$E_{\alpha\beta\gamma} = \langle (P_\alpha - \overline{P_\alpha})(\pi_{\beta\gamma} - \overline{\pi_{\beta\gamma}}) \rangle. \tag{7.27}$$

The calculated co-variances (Table 7.3) did not result in any significant changes to our values of e_1 and e_3. As such, we take this as an indication that our simulation results are reliable.

At low values of Q_{00}^2, the molecules possess an small external bond angle and coupling this with a transverse dipole moment (longitudinal with respect to the wedge), the molecules, in effect act like large wedges. With this large wedge, the splay coefficients increase in magnitude, which can be seen in Fig. 7.6.

At low γ (high values of Q_{00}^2) both the bend coefficients are close to zero, within statistical error. This is in-line with the predictions by Meyer [88]. In general the bend coefficients for the purely repulsive system are < 0.25. Including attractive interactions increases the magnitude of the bend coefficient. The inclusion of the attractive interactions is likely increase the range over which the molecules interact giving rise to enhanced fluctuations present, it must also be noted that CLJM systems are at higher density and Q_{00}^2 than the corresponding CRM system. Above $\gamma = 20°$ the bend coefficients are larger in magnitude than those at low γ, suggesting that there is a critical angle at which the bend flexoelectric

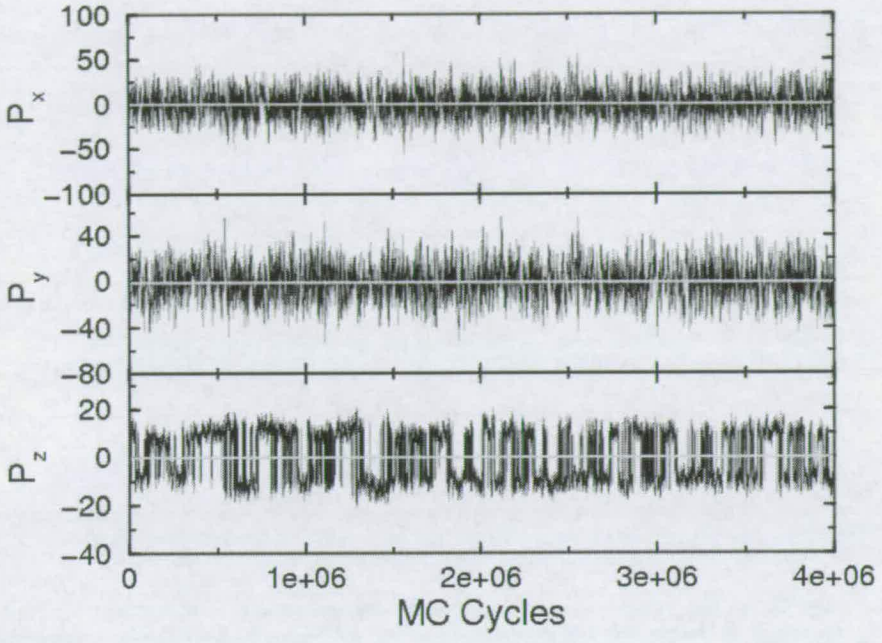

Figure 7.8: The polarisations in the x, y and z directions for CLJMs with $\gamma = 0°$. The grey line denotes the average polarisations in each case.

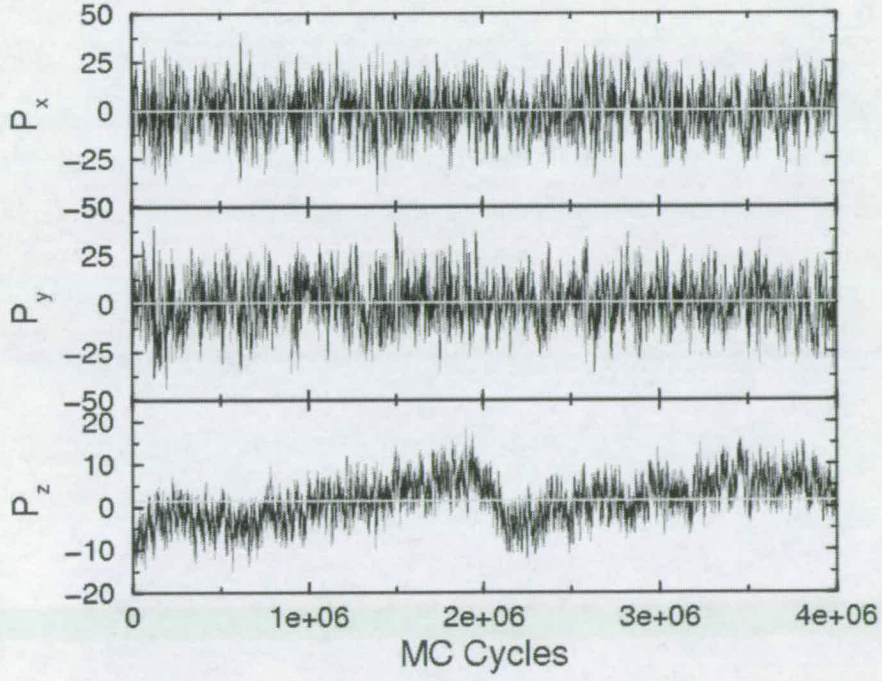

Figure 7.9: The polarisations in the x, y and z directions for CRMs with $\gamma = 0°$. The grey line denotes the average polarisations in each case.

γ°	$\langle p_x \rangle$	$\langle p_y \rangle$	$\langle p_z \rangle$
CRM, $T^* = 3.0$, $\rho = 0.0888$			
0	−0.21(2)	0.77(3)	1.43(1)
5	−0.31(3)	−0.38(3)	0.02(1)
10	0.27(3)	−0.38(3)	−0.10(1)
15	0.90(3)	−1.04(3)	0.56(1)
20	0.09(3)	−0.55(3)	0.67(2)
25	−1.10(3)	1.00(3)	−0.75(2)
CLJM, $T^* = 6.5$, $\rho = 0.1155$			
0	−0.13(3)	−0.78(3)	−0.13(2)
5	0.09(3)	−0.42(3)	0.126(6)
10	−0.29(3)	−0.17(3)	0.064(8)
15	−0.18(3)	−1.06(3)	0.10(1)
20	−2.03(3)	−0.04(3)	0.16(1)
25	2.41(3)	0.53(3)	−0.72(1)
30	−1.04(3)	2.93(3)	0.56(2)

Table 7.2: The average polarisations for the CRM and the CLJM systems. The figure in parentheses represents the uncertainty in the last digit.

γ°	e_1 calculated using $(\langle p_z \pi_{xy} \rangle$ - $\langle p_z \pi_{yx} \rangle)$	e_1 calculated using $[\langle (p_z - \overline{p}_z)(\pi_{xy} - \overline{\pi}_{xy}) \rangle$ - $\langle (p_z - \overline{p}_z)(\pi_{yx} - \overline{\pi}_{yx}) \rangle]$
CRM, $T^* = 3.0$, $\rho = 0.0888$		
0	0.13(4)	0.13(4)
5	−0.01(4)	−0.01(4)
10	0.16(4)	0.16(4)
15	−0.00(4)	−0.02(4)
20	0.37(5)	0.36(5)
25	0.51(7)	0.44(7)
CLJM, $T^* = 6.5$, $\rho = 0.1155$		
0	0.2(1)	0.2(1)
5	−0.07(4)	−0.07(4)
10	−0.07(5)	−0.07(6)
15	0.02(6)	0.02(6)
20	−0.50(7)	−0.48(7)
25	0.50(9)	0.51(9)
30	0.4(1)	0.5(1)

Table 7.3: The calculated splay flexoelectric coefficients and the calculated variances of the splay coefficients for $e_1 = [\langle (p_z - \overline{p}_z)(\pi_{xy} - \overline{\pi}_{xy}) \rangle - \langle (p_z - \overline{p}_z)(\pi_{yx} - \overline{\pi}_{yx}) \rangle$ for the CRM and CLJM systems, respectively. All values have been multiplied by a pre-factor of $-\beta/2V$. The figures in parentheses denote the uncertainty in the last digit.

γ°	e_3 calculated using $(\langle p_x \pi_{yz} \rangle$ - $\langle p_y \pi_{yxz} \rangle)$	e_3 calculated using $[\langle (p_x - \overline{p}_x)(\pi_{yz} - \overline{\pi}_{yz}) \rangle$ - $\langle (p_y - \overline{p}_y)(\pi_{xz} - \overline{\pi}_{xz}) \rangle]$
	CRM, $T^* = 3.0$, $\rho = 0.0888$	
0	0.07(3)	0.06(3)
5	0.13(4)	0.13(4)
10	0.03(4)	0.03(4)
15	0.06(5)	0.07(5)
20	−0.17(6)	−0.18(6)
25	−0.31(7)	−0.28(7)
	CLJM, $T^* = 6.5$, $\rho = 0.1155$	
0	0.04(3)	0.04(3)
5	0.04(4)	0.04(4)
10	0.09(6)	0.08(6)
15	−0.10(7)	−0.09(7)
20	0.01(8)	−0.02(8)
25	0.6(1)	0.6(1)
30	0.5(1)	0.5(1)

Table 7.4: The calculated bend flexoelectric coefficients and the calculated variance of the bend flexoelectric coefficient for $e_3 = [\langle (p_x - \overline{p}_x)(\pi_{yz} - \overline{\pi}_{yz}) \rangle$ - $\langle (p_y - \overline{p}_y)(\pi_{xz} - \overline{\pi}_{xz}) \rangle$ for the CRM and CLJM systems, respectively. All values have been multiplied by a pre-factor of $-\beta/2V$. The figure in parentheses denotes the uncertainty in the last digit

coefficient is significant. Unfortunately, increasing the bend angle also destabilises the nematic phase. The bend coefficients of the CRM and CLJM systems are opposite in sign. We have calculated the bend flexoelectric at $\gamma = 30°$, with values of $\sigma \simeq 0.5$ and $\mu \sim 1$ Debye, to be $\sim 7pcM^{-1}$. Experimentally $e_1 + e_3$ and $e_1 - e_3$ are quoted, for the CLJM system with $\gamma = 30°$, these are calculated to be $12pcM^{-1}$ and $-1.33pcM^{-1}$, respectively and are in good agreement with experimental results [90, 91]. There are slight differences between the calculated bend flexoelectric coefficients and their associated co-variances. This is likely to be a results of large net polarisations in the x and y directions at these bond angles.

7.3 Conclusions

In this chapter we have examined the phase behaviour of CRMs and CLJMs with bond angles in the range $0 - 30°$ at constant volume. As the bend angle is increased the nematic order parameter, Q_{00}^2 was seen to decrease at a given temperature. We propose critical angle functions as shown in Eqns. 7.25 and 7.26. With purely repulsive interactions, above $\gamma > 25°$, the nematic phase is absent,

with attractive interactions, the nematic phase is destabilised at $\gamma > 30°$. At these extreme bond angles the smectic phase is likely to represent the thermodynamically stable state.

We have also calculated the splay and bend flexoelectric coefficients for systems with and without attractive interactions. The calculated splay coefficients for molecules with γ in the range $0° - 30°$ do not exhibit any generic trends at low γ, which would be anticipated as the molecules are near-linear. However, at higher values of γ, the molecules behave like wide aspect wedges and give rise to increased e_1 values. The earlier simulation studies of flexoelectricity used a Lennard-Jones sphere and Gay-Berne ellipsoid as a wedged-shaped molecule, perhaps a model similar to that used by Barmes *et al.* [104] coupled with attractive interactions would be more suited to investigate the splay flexoelectric coefficient.

The bend flexoelectric coefficient for the CLJM system increases dramatically with $\gamma > 20°$, this would suggest that there is a critical value at which the bend flexoelectric coeffcients becomes increasingly important. Increasing the bend angle $> 30°$ destabilises the nematic phases so the range over which the bend flexoelectric effect is observed is restricted. The bend flexoelectric coefficient, e_3 for the CRM system is negative once $\gamma > 20°$. As such the attractive interactions are likely to play a crucial role in flexoelectricity and the inclusion of dipolar interactions may increase these coefficients.

The errors presented upon the flexoelectric coefficients are purely the statistical errors. It must be noted that the average polarisations and the average of the orientational stress tensor should be zero within statistical error. This is not the case, and this will lead to a large uncertainty in the calculated coefficients. Another factor to consider is the overestimation of the density at which the nematic phase is formed for a given bond angle (with CLJMs at $\gamma = 20°$ the true reduced density is 0.1049 not 0.1155). Ideally, the phase behaviour of CRM and CLJMs should be determined at each bond angle in the desired range and the flexoelectric coefficients calculated over a range of conditions, at which the nematic phase is stable. This is a mammoth undertaking given the size of systems and number of state points required and the long simulation runs required for the flexoelectric coefficients.

CHAPTER 8

Conclusions

In this thesis we have studied the phase behaviour of a series of site-site models of bent-core liquid crystals. The basic molecular model is constructed from seven soft spheres constrained to form a rigid 'v' shape, with external bond angle, γ. Neighbouring sites on a given molecule are separated by one unit sphere diameter. We have adopted a 'building block' approach to map out the phase behaviour of bent-core liquid crystals. We started from the basic model and the full Lennard-Jones potential, altering the interaction potential and culminating with model molecules with flexible tails grafted on to the ends of the molecules. All of these studies were performed using Monte Carlo (MC) computer simulations.

The first stage of this thesis was to investigate the phase behaviour of our simple site-site model with sphere-sphere interactions described by the full Lennard-Jones potential, $\{4\epsilon[(\sigma/r)^{12}-(\sigma/r)^{6}]\}$, where ϵ and σ are energy and range parameters respectively. These molecules are referred to as composite Lennard-Jones molecules (CLJMs). The external bend angle was in the range $0° - 60°$, which represents a range of bend angles for real bent-core molecules.

With linear molecules ($\gamma = 0°$), we find a isotropic, uniaxial nematic, untilted smectic A, tilted smectic B and crystalline phases. With $\gamma = 20°$ we find isotropic, uniaxial nematic and tilted smectic phases. The range over which the nematic phase persists is enhanced compared to linear molecules, albeit with the loss of the untilted smectic A phase. At a bend angle of $\gamma = 40°$ we only observe isotropic and tilted smectic phases, having lost the nematic phase. With an extreme bond angle of $\gamma = 60°$ we do not observe any orientationally ordered phases, with only the isotropic and crystalline phases observed. With the introduction of bend into the model molecules we raise the possibility of forming

chiral phases on account of the molecular tilt, as discussed in Chapter 1. Although the molecules were tilted to $\sim 30°$ with respect to the layer normal, we do not find any chiral phases, nor do we observe stable ferroelectric or antiferroelectric ordering. This molecular tilt is commensurate with tilt angles observed in experiments [43, 47]. This molecular tilt is not seen in simulations of hard spherocylinders [27] and is greatly reduced in simulations of Gay-Berne dimers [24, 25]. This degree of molecular tilt can be ascribed to the increased favourable interactions which result from the spheres on adjacent molecules hexagonally close packing. In order to achieve this, molecules have to tilt to $\sim 30°$.

The nematic phase is stable over a range of densities and temperatures with $\gamma = 0°$ and $\gamma = 20°$. Simulations at a fixed density of $\rho^* = 0.1155$ and at a temperature of $T^* = 6.5$ and γ in the range $0° - 40°$ showed that the nematic order parameter (S) varies like $S(\gamma) = S(0)(1 - \gamma/\gamma_c)^\alpha$, where $\gamma_c = 29.6(1)$, $S(0) = 0.961(4)$ and $\alpha = 0.143(4)$. Above γ_c the nematic phase is lost.

The bent-core molecules possess dipole moments which lie parallel to the C_2 rotation axis. We studied the phase behaviour of our basic model with the molecules interacting via a simple repulsive sphere-sphere interaction potential coupled with the dipole-dipole interaction. The dipolar interactions were calculated using the Ewald summation method. As with the CLJM system, we examined the phase behaviour with γ in the range $0° - 40°$ and reduced dipole strengths of $0, 1$ and 2.

With zero dipole moment, we observe phase behaviour similar to that found for the CLJM system, albeit with phase transitions occurring at lower temperatures and densities. At low temperature we find the herringbone phase, with molecules highly tilted ($\sim 60°$). CLJM systems at corresponding state points possessed higher nematic order parameters than with pure repulsive interactions.

The nematic phase is stable over a range of densities and temperatures with $\gamma = 0°$ and $\gamma = 20°$. Simulations at a fixed density of $\rho^* = 0.0888$ and at a temperature of $T^* = 3.0$ and γ in the range $0° - 40°$ showed that the nematic order parameter (S) varies like $S(\gamma) = S(0)(1 - \gamma/\gamma_c)^\alpha$, where $\gamma_c = 25.6(2)$, $S(0) = 0.881(4)$ and $\alpha = 0.104(7)$. Above γ_c the nematic phase is lost.

With linear molecules and a reduced dipole moment equal to one we find, isotropic, uniaxial nematic, untilted smectic A and tilted crystalline phases. At low temperature the dipolar interactions stabilise the tilted crystalline phases with a re-

duction in tilt from $\sim 60°$ found with zero dipole moment to $\sim 20°$. Doubling the dipole moment strength we observe isotropic, smectic B and tilted solid phases. The smectic phase is likely to represent the thermodynamically stable state, with dipoles aligning nose to tail. With this increase in dipole strength, the molecular tilt is further reduced to a value of $\sim 14°$. This reduction of tilt is likely to be a result of the strong dipole nose to tail interactions.

With bent-core molecules and dipole strength > 0, we observe unusual phase behaviour at low temperature. Under these conditions Monte Carlo simulations may be unsuitable as we observe vanishingly small displacement parameters. As such we may be unable to overcome kinetic barriers. We also may be sampling chiral conformational states which average to racemic conformations [105].

As with the CLJM systems we do not observe a stable ferroelectric or antiferroelectric phases. The molecular tilt observed decreases with increasing dipole strength. As such dipolar interactions are unlikely to be the source of chirality, although the phase behaviour of polar bent-core molecules with attractive interactions merits investigation. This is supported by Emelyaneko and Osipov [63], who investigated the influence of attractive dispersion interactions. The dipole strengths simulated in this thesis may be beyond those found experimentally. *Ab initio* calculations could be performed to determine appropriate dipole strengths and molecular conformational data.

We have also investigated the effect of reducing the elongation of the model molecules with simple repulsive and Lennard-Jones interaction potentials. With the repulsive interaction potential we only observe isotropic and herringbone phases. Molecules interacting via the Lennard-Jones potential yielded isotropic, tilted smectic and crystalline phases. We do not observe any intermediate orientationally ordered phases. As such, there is likely to be a critical number of constituent spheres for the onset of liquid crystalline behaviour. Indeed, with seven sphere CLJMs with $\gamma = 60°$ we may have reached this elongation limit for liquid crystallinity.

The bent-core molecules often possess flexible alkyl or alkoxy chains extending outward from the aromatic core of the molecules. As such we have investigated the effect of grafting 3-segment flexible tails on to a 5-sphere core. The reduced bond length between segments is 0.6. We employed the Configurational Bias Monte Carlo method to effectively sample the conformation and packing of molecules, with γ in the range $0° - 40°$. For most systems we observe

isotropic and tilted smectic phases. The inclusion of the flexible tails reduced the molecular tilt observed compared to the 5-sphere cores themselves. In the bent-core systems we observe a ferroelectric polarisation state, which may or may not be metastable and requires further simulation starting from an antiferroelectric phase to confirm this assertion. The structure within layers is highly distorted with the position of molecules undulating within the layer, with apparent hexagonal close packing of the apical spheres of the molecules. Interestingly, the majority of tails adopt a *cis* geometric form, although the *trans* form is also observed. We also observe a decrease in the effective total length of the molecules upon heating, as the tails contract towards the core of the molecule. It remains to be seen if this contraction will also be observed in true liquid crystalline simulations with attractive interactions. It would appear that the addition of flexible chains is unlikely to be the driving force for formation of chiral phases, but this requires further careful investigation.

We have also calculated and compared splay and bend flexoelectric coefficients utilising linear response theory for molecules with γ in the range $0° - 30°$ interacting via a simple repulsive or full Lennard-Jones potential. As would be anticipated the splay coefficients are zero within error at low γ. Above $\gamma = 20°$ the splay coefficients increase. Above a critical angle the molecules can behave as wide-aspect ratio wedges, hence the positive splay coefficients. At low values of γ the bend flexoelectric coefficients are negligible. The bend coefficients become significant above $\gamma = 20°$, which would suggest a critical value for the bend flexoelectric effect. Unfortunately, increasing the bend angle destabilises the nematic phase. The values for CLJM systems are typically greater in magnitude than the CRM systems. The values reported here are comparable to experimental values.

8.1 Future directions

Ideally, the phase behaviour of these bent-core molecules should be investigated as a function of γ, utilising a finer increment between systems. Free energy calculations, using umbrella sampling, whereby the uniaxial order parameter is maintained between critical values as per Lansac *et al.* [27], or the Frenkel-Ladd Einstein method can be envisaged to provide a useful indicator of the true thermodynamically stable states.

The effect of elongation of the molecules, whether the rigid core or rigid core and flexible tails needs full elucidation, with a view to determining the crucial elongation for the onset of liquid crystalline behaviour. The effect of the flexible tails is dramatic, with formation of grain boundaries. Larger-scale simulations are required to assess the fluctuations within smectic layers. Although algorithms exist for the optimisation [106] and to improve the efficiency of CB-MC [107], CB-MC is still computationally inefficient for a comprehensive study of the effect of tail elongation, as such Molecular Dynamics may prove more fruitful in this respect. Having reached a computational limit, we would have to utilise parallel computing techniques for larger scale simulations.

With current simulation methods the evolution of fluctuations, convergence and sampling are sluggish. Frenkel recently proposed a 'waste recycling' scheme [108], whereby rejected states are sampled, to reduce slowing down near critical points. This new scheme can be used to enhance the convergence and sampling of systems with dipolar interaction and those with flexible tails regrown utilising CB-MC. It is also possible to use this scheme when calculating the flexoelectric coefficients via enhanced fluctuations.

APPENDIX A

Equations for Ewald summation method

The total dipole-dipole interaction with conducting ('tin foil') boundary conditions ($\epsilon_s = \infty$) is given by,

$$
\begin{aligned}
U^{\mu\mu} &= \frac{1}{2}\sum_{i=1}^{N}\sum_{j=1}^{N}\left[\sum_{|n|}^{\infty}\left(\vec{\mu}_i\cdot\vec{\mu}_j\right)B\left(r\right)\left(\vec{r}_{ij}+\vec{n}\right)\right. \\
&- \left(\vec{\mu}_i\cdot\vec{r}_{ij}\right)\left(\vec{\mu}_j\cdot\vec{r}_{ij}\right)C\left(r\right)\left(\vec{r}_{ij}+\vec{n}\right) \qquad \text{(A.1)} \\
&+ \left.\sum_{\vec{k}\neq 0}\left(\frac{1}{\pi L^3}\right)\left(\vec{\mu}_i\cdot\vec{k}\right)\left(\vec{\mu}_j\cdot\vec{k}\right)\left(\frac{4\pi^2}{\kappa^2}\right)\exp\left(-\frac{\vec{k}^2}{4\kappa^2}\right)\cos\left(\vec{k}\cdot\vec{r}_{ij}\right)\right] \qquad \text{(A.2)} \\
&- \sum_{i=1}^{N}\frac{2\kappa^3\mu_i^2}{3\pi^{\frac{1}{2}}} \qquad \text{(A.3)} \\
B\left(r\right) &= \operatorname{erfc}\left(\kappa r\right)\frac{1}{r^3}+\left(\frac{2\kappa}{\pi^{\frac{1}{2}}}\right)\frac{\exp\left(-\kappa r^2\right)}{r^2} \qquad \text{(A.4)} \\
C\left(r\right) &= 3\operatorname{erfc}\left(\kappa r\right)\frac{1}{r^5}+\left(\frac{2\kappa}{\pi^{\frac{1}{2}}}\right)\left(2\kappa^2+\frac{3}{r^2}\right)\exp\frac{\left(-\kappa^2r^2\right)}{r^2}, \qquad \text{(A.5)}
\end{aligned}
$$

this can be split in to three parts; the real space sum, k (reciprocal) space and self potential terms.

A.1 Real space sum

We set $\mid n \mid = 0$ and as such the real space term (Eqn. A.1) now becomes,

$$
\frac{1}{2}\sum_{i=1}^{N}\sum_{j\neq i}^{N}\left(\vec{\mu}_i\cdot\vec{\mu}_j\right)B\left(r\right)\vec{r}_{ij}-\left(\vec{\mu}_i\cdot\vec{r}_{ij}\right)\left(\vec{\mu}_j\cdot\vec{r}_{ij}\right)C\left(r\right)\vec{r}_{ij} \qquad \text{(A.6)}
$$

Here the dipole direction is governed by the $\vec{b}$ vector, the magnitude of which is normalised, so we define $\vec{\mu}_i = \mu\vec{b}_i$. The real space sum becomes,

$$\begin{aligned}
&\frac{1}{2}\sum_{i=1}^{N}\sum_{j\neq i}^{N}\left(\vec{\mu}_i\cdot\vec{b}_i\right)\cdot\left(\vec{\mu}_j\cdot\vec{b}_j\right)B\left(r\right)\vec{r}_{ij} - \left[\left(\vec{\mu}_i\cdot\vec{b}_i\right)\cdot\vec{r}_{ij}\right]\left[\left(\vec{\mu}_j\cdot\vec{b}_j\right)\cdot\vec{r}_{ij}\right]C(r)\vec{r}_{ij} \\
= &\frac{1}{2}\sum_{i=1}^{N}\sum_{j\neq i}^{N}\left(\vec{\mu}_i\cdot\vec{\mu}_j\right)\left(\vec{b}_i\cdot\vec{b}_j\right)B\left(r\right)\vec{r}_{ij} - \left(\vec{\mu}_i\cdot\vec{\mu}_j\right)\left(\vec{b}_i\cdot\vec{r}_{ij}\right)\left(\vec{b}_j\cdot\vec{r}_{ij}\right)C\left(r\right)\vec{r}_{ij} \\
= &\frac{1}{2}\sum_{i=1}^{N}\sum_{j\neq i}^{N}\left(\vec{\mu}_i\cdot\vec{\mu}_j\right)\left[\left(\vec{b}_i\cdot\vec{b}_j\right)B\left(r\right)\vec{r}_{ij} - \left(\vec{b}_i\cdot\vec{r}_{ij}\right)\left(\vec{b}_j\cdot\vec{r}_{ij}\right)C\left(r\right)\vec{r}_{ij}\right] \\
= &\frac{1}{2}\mu^2\sum_{i=1}^{N}\sum_{j\neq i}^{N}\left(\vec{b}_i\cdot\vec{b}_j\right)B\left(r\right)\vec{r}_{ij} - \left(\vec{b}_i\cdot\vec{r}_{ij}\right)\left(\vec{b}_j\cdot\vec{r}_{ij}\right)C\left(r\right)\vec{r}_{ij} \qquad \text{(A.7)}
\end{aligned}$$

A.2 Reciprocal space sum

The reciprocal space sum can be written as,

$$\sum_{\vec{k}\neq 0}\left(\frac{1}{\pi L^3}\right)\left(\vec{\mu}_i\cdot\vec{k}\right)\left(\vec{\mu}_j\cdot\vec{k}\right)\left(\frac{4\pi^2}{k^2}\right)\exp\left(-\frac{\vec{k}^2}{4\kappa^2}\right)\cos\left(\vec{k}\cdot\vec{r}_{ij}\right). \qquad \text{(A.8)}$$

We can also write $f\left(\vec{k}\right) = \frac{1}{\pi L^3}\left[\left(\frac{4\pi^2}{k^2}\right)\exp\left(\frac{k^2}{4\kappa^2}\right)\right]$ and Eqn. A.8 becomes,

$$\begin{aligned}
&\frac{1}{2}\sum_{i=1}^{N}\sum_{j\neq i}^{N}\sum_{\vec{k}\neq 0} f\left(\vec{k}\right)\left(\vec{\mu}_i\cdot\vec{k}\right)\left(\vec{\mu}_j\cdot\vec{k}\right)\cos\left(\vec{k}\cdot\vec{r}_{ij}\right) \\
= &\frac{1}{2}\sum_{\vec{k}\neq 0} f\left(\vec{k}\right)\left[\sum_{i=1}^{N}\sum_{j\neq i}^{N}\left(\vec{\mu}_i\cdot\vec{k}\right)\left(\vec{\mu}_j\cdot\vec{k}\right)\cos\left(\vec{k}\cdot\vec{r}_{ij}\right)\right] \qquad \text{(A.9)}
\end{aligned}$$

The double sum can be split into two components using complex numbers. We write $\cos(\vec{k}\cdot\vec{r}_{ij}) = \frac{1}{2}\left[\exp\left(i\vec{k}\cdot\vec{r}_{ij}\right) + \exp\left(-i\vec{k}\cdot\vec{r}_{ij}\right)\right]$ and the reciprocal space becomes,

$$\frac{1}{2}\sum_{\vec{k}\neq 0} f\left(\vec{k}\right)\left[\sum_{i=1}^{N}\sum_{j\neq i}^{N}\left(\vec{\mu}_i\cdot\vec{k}\right)\left(\vec{\mu}_j\cdot\vec{k}\right)\frac{1}{2}\left[\exp\left(i\vec{k}\cdot\vec{r}_{ij}\right) + \exp\left(-i\vec{k}\cdot\vec{r}_{ij}\right)\right]\right], \qquad \text{(A.10)}$$

and resolving $\vec{r}_{ij}$ into its two components,

$$\begin{aligned}
&\frac{1}{2}\sum_{\vec{k}\neq 0} f\left(\vec{k}\right)\left[\frac{1}{2}\left(\vec{\mu}_i\cdot\vec{k}\right)\left(\vec{\mu}_j\cdot\vec{k}\right)\left[\exp\left(i\vec{k}\cdot\vec{r}_i\right)\exp\left(-i\vec{k}\cdot\vec{r}_j\right)\right]\right. \\
+ &\left.\frac{1}{2}\left(\vec{\mu}_i\cdot\vec{k}\right)\left(\vec{\mu}_j\cdot\vec{k}\right)\left[\exp\left(-i\vec{k}\cdot\vec{r}_i\right)\exp\left(i\vec{k}\cdot\vec{r}_j\right)\right]\right]
\end{aligned}$$

$$
\begin{aligned}
&= \frac{1}{2}\sum_{\vec{k}\neq 0} f\left(\vec{k}\right)\left[\sum_{i=1}^{N}\sum_{j\neq i}^{N}\left[\left(\vec{\mu}_i\cdot\vec{k}\right)\exp\left(i\vec{k}\cdot\vec{r}_i\right)\right]\left[\left(\vec{\mu}_j\cdot\vec{k}\right)\exp\left(-i\vec{k}\cdot\vec{r}_j\right)\right]\right.\\
&+ \left.\left[\left(\vec{\mu}_i\cdot\vec{k}\right)\exp\left(-i\vec{k}\cdot\vec{r}_i\right)\right]\left[\left(\vec{\mu}_j\cdot\vec{k}\right)\exp\left(i\vec{k}\cdot\vec{r}_j\right)\right]\right]\\
&= \frac{1}{2}\sum_{\vec{k}\neq 0} f\left(\vec{k}\right)\frac{1}{2}\left[\left[\sum_{i=1}^{N}\left(\vec{\mu}_i\cdot\vec{k}\right)\cos\left(\vec{k}\cdot\vec{r}_i\right)+i\left(\vec{\mu}_i\cdot\vec{k}\right)\sin\left(\vec{k}\cdot\vec{r}_i\right)\right]\right.\\
&\times \left.\left[\sum_{j=1}^{N}\left(\vec{\mu}_j\cdot\vec{k}\right)\cos\left(\vec{k}\cdot\vec{r}_j\right)-i\left(\vec{\mu}_j\cdot\vec{k}\right)\sin\left(\vec{k}\cdot\vec{r}_j\right)\right]\right]\\
&+ \frac{1}{2}\sum_{\vec{k}\neq 0} f\left(\vec{k}\right)\left[\frac{1}{2}\left[\sum_{i=1}^{N}\left(\vec{\mu}_i\cdot\vec{k}\right)\cos\left(\vec{k}\cdot\vec{r}_i\right)-i\left(\vec{\mu}_i\cdot\vec{k}\right)\sin\left(\vec{k}\cdot\vec{r}_i\right)\right]\right.\\
&\times \left.\left[\sum_{j=1}^{N}\left(\vec{\mu}_j\cdot\vec{k}\right)\cos\left(\vec{k}\cdot\vec{r}_j\right)+i\left(\vec{\mu}_j\cdot\vec{k}\right)\sin\left(\vec{k}\cdot\vec{r}_j\right)\right]\right]\\
&= \frac{1}{2}\sum_{\vec{k}\neq 0} f\left(\vec{k}\right)\left[\frac{1}{2}\left[\sum_{i=1}^{N}\left(\vec{\mu}_i\cdot\vec{k}\right)\cos\left(\vec{k}\cdot\vec{r}_i\right)\right]^2+\frac{1}{2}\left[\sum_{j=1}^{N}\left(\vec{\mu}_j\cdot\vec{k}\right)\sin\left(\vec{k}\cdot\vec{r}_j\right)\right]^2\right.\\
&+ \left.\frac{1}{2}\left[\sum_{i=1}^{N}\left(\vec{\mu}_j\cdot\vec{k}\right)\cos\left(\vec{k}\cdot\vec{r}_i\right)\right]^2+\frac{1}{2}\left[\sum_{j=1}^{N}\left(\vec{\mu}_j\cdot\vec{k}\right)\sin\left(\vec{k}\cdot\vec{r}_j\right)\right]^2\right]\\
&= \frac{1}{2}\sum_{\vec{k}\neq 0} f\left(\vec{k}\right)\left[\left[\sum_{i=1}^{N}(\vec{\mu}_i\cdot\vec{k})\cos\left(\vec{k}\cdot\vec{r}_i\right)\right]^2+\left[\sum_{j=1}^{N}(\vec{\mu}_j\cdot\vec{k})\sin\left(\vec{k}\cdot\vec{r}_j\right)\right]^2\right]
\end{aligned}
\tag{A.12}
$$

Thus the reciprocal space sum is calculated via cosine and sine sums.

APPENDIX B

Courses and conferences attended

B.1 Computing Courses

- 27/10/2001, Unix 1 - an introduction to unix, Edinburgh University Computing Services (EUCS)
- 12/11/2001 – 14/11/2001, Introduction to programming with Fortran 90, EUCS
- 15/11/2001, Unix 2 - Enhancing your unix skills, EUCS
- 23/09/2002, HTML and publishing on the WWW, EUCS
- 26/09/2002, Perl 5, EUCS
- 12/12/2002, Unix 3 - shell programming, EUCS
- 29/4/2003 – 1/05/2003, Scientific visualisation - a practical introduction, Edinburgh Parallel Computing Centre (EPCC)

B.2 Lecture courses

- 30/06/2002, 19th International liquid crystal conference tutorial day
- 6/07/2002 – 16/07/2002, CCP5 Summer school
- Microporous and mesoporous materials, 5 lectures, October 2002, School of Chemistry
- 24/08/2003, 9th International conference of Ferroelectric liquid crystals tutorial day
- Condensed matter physics, 18 lectures, October-December 2003, School of Physics
- Complex analysis, 18 lectures, October-December 2003, School of Physics
- Statistical mechanics, 18 lectures, January-March 2004, School of Physics

- Quantum Mechanics, 18 lectures, January-March 2004, School of Physics
- Computational biology and infomatics, 4 lectures, March 2004, School of Chemistry
- 4/04/2004, Condensed matter and materials physics tutorial day

B.3 General workshops

- 17/10/2001, Laboratory demonstrating course
- 17/06/2003, Career planning, Edinburgh University Careers Service
- 17/06/2003, Interview skills, Edinburgh University Careers Service
- 12/07/2003 – 17/07/2003, UK GRAD school
- 1/06/2004, Paper production, Edinburgh University Transferable Skills Program
- 4/06/2004, Thesis Workshop, Edinburgh University Transferable Skills Program
- 23/06/2004, Effective writing, Edinburgh University Transferable Skills Program

B.4 Conferences attended

- 1/07/2002 – 5/07/2002, 19^{th} International liquid crystal conference, poster title - 'Computer simulations of dipolar bent-core molecules'
- August 2002 – 2004, attended physical section reading group meeting, 2002 - Talk 'Computer simulations of liquid crystals' (10 minutes), 2003 - poster 'Computer simulations of a site-site model of bent-core molecules', 2004 talk - 'Computer simulations of "banana" liquid crystals' (45 minutes)
- 24/08/2003 – 29/08/2003, 9^{th} International conference of ferroelectric liquid crystals, poster title - 'Computer simulations of a site-site model of bent-core molecules'
- 15/03/2004, Science, engineering and technology, Houses of Parliment, poster title - 'Computer simulations of "banana" liquid crystals'
- 5/04/2004 – 7/04/2004, Condensed matter and materials physics, poster title - 'Computer simulations of a site-site model of bent-core molecules'

APPENDIX C

Papers published

1. Computer simulations of bent-core liquid crystals, Alastair Dewar and Philip J. Camp, Phys. Rev. E, **70**, 011704 (2004)
2. Dipolar interactions, molecular flexibility, and flexoelectricity in bent-core liquid crystals, Alastair Dewar and Philip J. Camp, *Submitted to Journal of Chemical Physics*, pre-print article available on condensed matter archive, arxiv.org/archive/cond-mat/0505162

These papers are bound at the back of this thesis.

References

[1] P. G. de Gennes and J. Prost. *The physics of liquid crystals.* Clarendon Press, Oxford, 1993.

[2] S. Singh. *Liquid Crystals Fundamentals.* World Scientific, Singapore, 2002.

[3] D. Wei and G.N. Patey. Orientational order in simple dipolar liquids: Computer simulation of a ferroelectric nematic phase. *Phys. Rev. Lett.*, 68:2043–2045, 1992.

[4] D.R. Link, G. Natale, R. Shao, J.E. Maclennan, N.A. Clark, E. Korblova, and D.M. Walba. Spontaneous Formation of Macroscopic Chiral Domains in a Fluid Smectic Phases of Achiral Molecules. *Science*, 278:1924–1926, 1997.

[5] C.T. Imrie. Relationship between molecular structure and transition temperatures for unconventional molecular structure. In D.A. Dunmur, A. Fukada, and G.R. Luckhurst, editors, *Physical properties of liquid crystals: nematics*, pages 36–54, London, 2001. Institute of electrical engineers.

[6] G.W. Gray and S.M. Kelly. Liquid crystals for twisted nematic display devices. *J. Mater. Chem.*, 9:2037–2050, 1999.

[7] D. Pauluth and K. Tarumi. Advanced liquid crystals for television. *J. Mater. Chem.*, 12:1219–1227, 2004.

[8] S.T. Lagerwald. Can liquids be macroscopically polar. *J. Phys.: Condens. Matter*, 8:9143–9166, 1996.

[9] T. Niori, T. Sekine, J. Watanabe, T. Furukawa, and H. Takezoe. Distinct ferroelectric smectic liquid crystals consisting of banana shaped achiral molecules. *J. Mater. Chem.*, 6:1231–1233, 1996.

[10] R Macdonald, F. Kentischer, P. Warnick, and G. Heppke. Antiferroelectricity and Chrial Order in New Liquid Crystals of Nonchiral Molecules Studied by Optical Second Harmonic Generation. *Phys. Rev. Lett.*, 81:4408–4411, 1998.

[11] A. Jakli, S. Rauch, D. Lotzsch, and G. Heppke. Uniform textures of smectic liquid-crystal phase formed by bent-core molecules. *Phys. Rev. E*, 57:6737–6740, 1998.

[12] J.P. Bedel, J.C. Rouillon, J.P Marcerou, M. Laguerre, H.T. Nguyen, and M.F. Achard. Influence of fluoro substituents on the mesophase behaviour of banana-shaped molecules. *J. Mater. Chem.*, 12:2214–2220, 2002.

[13] G. Pelzl, M.W. Schroder, U. Dunemann, S. Diele, W. Weissflog, C. Jones, D. Coleman, N.A. Clark, R. Stannarius, J. Li, B. Das, and S. Grande. The first bent-core mesogens exhibiting a diamorphism B_7-$S_m CPF_A$. *J. Mater. Chem*, 14:2492–2498, 2004.

[14] J.C. Rouillon, J.P Marceroiu, M. Laguerre, H.T. Nguyen, and M.F. Achard. New banana-shaped thiobenzoate liquid crystals with B6, B1 and B2 phases. *J. Mater. Chem.*, 11:2946–2950, 2001.

[15] G. Pelzl, A. Ermin, S. Diele, H. Kresse, and W. Weissflog. Spontaneous chiral ordering in the nematic phase of an achiral banana-shaped compound. *J. Mater. Chem*, 12:2592–2593, 2002.

[16] M. Kaspar, V. Hamplova, V. Novotna, M. Glogarova, and P. Vanek. New banana-type liquid crystal with a methoxy group substituted near the central ring. *J. Mater. Chem.*, 12:2221–2224, 2002.

[17] K. Fodo-Csorba, A. Vajda, A. Jakli, C. Slugove, G. Trimmel, D. Demus, E. Gacs-Baitz, S. Holly, and G. Galli. Ester type banana-shaped liquid crystalline monomers: synthesis and physical properties. *J. Mater. Chem*, 14:2499–2506, 2004.

[18] A. Jakli, G.G. Nair, C.K. Lee, R. Sun, and L.C. Chien. Macroscopic chirality of a liquid crystal from nonchiral molecules. *Phys. Rev. E*, 63:061710–1 – 061710–5, 2001.

[19] R. Car and M. Parrinello. Unified approach for molecular dynamics and density functional theory. *Phys. Rev. Lett.*, 55:2471–2474, 1985.

[20] S. Hauptmann, T. Mosell, S. Reiling, and J. Brickmann. Molecular dynamics simulations of the bulk phases of 4-cyano-4'-n-pentyloxybiphenyl. *Chem. Phys.*, 208:57–71, 1996.

[21] M.J. Cook and M.R. Wilson. The First Thousand-Molecule Simulation of a Mesogen at the Fully Atomistic Level. *Mol. Cryst. Liq. Cryst.*, 363:181, 2001.

[22] D.L. Cheung, S.J. Clark, and M.R. Wilson. Parametrisation and validation of a force field for liquid-crystal forming molecules. *Phys. Rev. E*, 65:051709, 2002.

[23] R. Memmer. Liquid crystal phases of achiral banana-shaped molecules a computer simulation study. *Liq. Crys.*, 29:483–496, 2001.

[24] S. J. Johnston, R. L. Low, and M. P. Neal. Computer simulation of apolar bent-core and rod-like molecules. *Phys. Rev. E*, 65:051706–1, 2002.

[25] S. J. Johnston, R. L. Low, and M. P. Neal. Computer simulation of polar bent-core. *Phys. Rev. E*, 66:061702, 2002.

[26] P. J. Camp, M. P. Allen, and A. J. Masters. Theory and computer simulation of bent-core molecules. *J. Chem. Phys.*, 111:9871–9881, 1999.

[27] Y. Lansac, P.K. Maiti, N.A. Clark, and M.A. Glaser. Phase behaviour of bent-core molecules. *Phys. Rev. E*, 67:011703, 2003.

[28] J. Xu, R. L. B. Selinger, J. V. Selinger, B. R. Ratna, and R. Shashidhar. Monte Carlo simulation of smectic liquid crystals and the electroclinic effect: The role of molecular shape. *Phys. Rev. E*, 60:5584–5590, 1999.

[29] J. Xu, R. L. B. Selinger, J. V. Selinger, and R. Shashidhar. Monte Carlo simulation of liquid-crystal alignment and chiral symmetry-breaking. *J. Chem. Phys.*, 115:4333–4338, 2001.

[30] G. V. Paolini, G. Ciccotti, and M. Ferrario. Simulation of site-site soft core liquid crystal models. *Mol. Phys.*, 80:279–312, 1993.

[31] J-P. Hansen and I. R. McDonald. *Theory of simple liquids*. Academic Press, London, 1986.

[32] N. Metropolis, A. W. Rosenbluth, M. N. Rosenbluth, A. H. Teller, and E. Teller. Equations of State Calculations by Fast Computing Machines. *J. Chem. Phys.*, 21:1087–1092, 1953.

[33] M. P. Allen and D. J. Tildesley. *Computer simulations of liquids*. Clarendon Press, Oxford, 1987.

[34] D. Frenkel and B. Smit. *Understanding molecular simulation*. Academic Press, London, 2002.

[35] C. Zannoni. Computer simulations. In G.R. Luckhurst and G.W. Gray, editors, *The molecular physics of liquid crystals*, pages 191–220, New York, 1979. Academic Press.

[36] C. Zannoni. Distribution functions and order parameters. In G.R. Luckhurst and G.W. Gray, editors, *The molecular physics of liquid crystals*, pages 51–83, New York, 1979. Academic Press.

[37] R. Eppenga and D. Frenkel. Monte Carlo study of the isotropic and nematic phases of infinitely thin platelets. *Mol. Phys*, 52:1303, 1984.

[38] I.M. Withers, C.M. Care, and D.J. Cleaver. A computer simulation study of tilted smectic mesophases. *J. Chem. Phys*, 113:5078–5090, 2000.

[39] D.C. Rapaport. *The art of Molecular Dynamics simulations*. Cambridge University Press, Cambridge, 1997.

[40] A. Dewar and P.J. Camp. Computer simulations of bent-core liquid crystals. *Phys. Rev. E*, 70:011704, 2004.

[41] D.C. Williamson and G. Jackson. Liquid crystalline phase behaviour in systems of hard sphere chains. *J. Chem. Phys*, 108:10294–10302, 1998.

[42] A. Galindo, C. Vega, E. Sanz, L.G. MacDowell, E. de Miguel, and F.J. Bias. Computer simulation study of the global phase behaviour of linear rigid Lennard-Jones chain molecules: Comparison with flexible models. *J. Chem. Phys.*, 120:3957–3968, 2003.

[43] H.F. Gleeson, Y. Wang, S. Watson, D. Sahagun-Sachez, J.W. Goodby, M. Hird, A. Petrenko, and M.A. Osipov. On the temperature dependence of the tilt and spontaneous polarisation in high tilt antiferroelectric liquid crystals. *J. Mater. Chem.*, 14:1480–1485, 2004.

[44] M. Parrinello and A. Rahman. Crystal structure and pair potential, a molecular dynamics study. *Phys. Rev. Lett.*, 45:1196–1199, 1980.

[45] A. Yashonath and C.N.R. Rao. A monte-carlo study of crystal structure transformation. *Mol. Phys.*, 54:245–251, 1985.

[46] I. Rodriguez-Ponce, J.M. Romero-Erique, E. Velasco, L. Mederos, and L.F. Rull. Anchoring and nematic-isotropic transitions in a confined nematic phase. *J. Phys. Condens. Matt.*, 12:A363–A367, 2000.

[47] M. Zennyoij, Y. Takanishi, K. Ishikawa, J. Thisayukta, J. Watanabe, and H. Takezoe. Partial mixing of opposite chirality in a bent-shaped liquid crystal molecular system. *J. Mat. Chem.*, 9:2775–2778, 1999.

[48] M.A. Glaser and N.A. Clark. Fluctuations and clinicity in tilted smectic liquid crystals. *Phys. Rev. E*, 66:021711, 2002.

[49] P.K. Maiti, Y. Lansac, M.A. Glaser, and N.A. Clark. Entropy-Stabilized Smectic C Phase in a System of Zigzag-Shaped Molecles. *Phys. Rev. Lett.*, 92:025501, 2004.

[50] S. C. McGrother, A. Gil-Villegas, and G. Jackson. The liquid-crystalline phase behaviour of hard spherocylinders with terminal point dipoles. *J. Phys.: Condsens. Matter*, 8:9649–9655, 1996.

[51] S. C. McGrother, A. Gil-Villegas, and G. Jackson. The effect of dipolar on the liquid crystalline phase transitions of hard spherocylinders with central longitudinal dipoles. *Mol. Phys.*, 95:657–673, 1998.

[52] A. Gil-Villegas, S. C. McGrother, and G. Jackson. Chain and ring structures in smectic phases of molecules with transverse dipoles. *Chem. Phys. Lett.*, 269:441–447, 1997.

[53] D. Levesque, J. J. Weis, and G. J. Zarragoicoechea. Monte Carlo simulation study of mesophase formation in dipolar spherocylinders. *Phys. Rev. E*, 47:496–505, 1993.

[54] K. Satoh, S. Mita, and S. Kondo. Monte Carlo simulations using the dipolar Gay-Berne model: effect of terminal dipole moment of mesophase formation. *Chem. Phys. Lett.*, 255:99–104, 1996.

[55] R. Berardi, S. Orlandi, and C. Zannoni. Antiphase structures in polar smectic liquid crystals and their molecular origin. *Chem. Phys. Lett.*, 261:357–362, 1996.

[56] M. Houssa, A. Oualid, and L.F. Rull. Reaction field and Ewald summation study of mesophase formation in dipolar Gay-Berne model. *Mol. Phys.*, 94:439–446, 1998.

[57] M. Houssa, L.F. Rull, and S.C. McGrother. Effect of dipolar interactions on the phase behaviour of the Gay-Berne liquid crystal model. *J. Chem. Phys.*, 109:9529–9542, 1998.

[58] M. Houssa, S. McGrother, and L.F. Rull. Reaction field and Ewald summation study of mesophase formation in dipolar Gay-Berne model. *Com. Phys. Comm.*, 121-122:259–261, 1999.

[59] E. Gwozdz, A. Brodka, and K. Pasterny. Molecular dynamics simulation study of a liquid crystal model: Gay-Berne particles with transverse dipole moments. *Chem. Phys. Lett.*, 267:557–562, 1997.

[60] R. Berardi, S. Orlandi, and C. Zannoni. Monte Carlo simulations of rod-like Gay-Berne mesogens with transverse dipoles. *Int. J. Mod. Phys.*, 10:477–484, 1998.

[61] P.D. Duncan and P.J. Camp. Structure and dynamics in a monolayer of dipolar spheres. *J. Chem. Phys.*, 121:11322–11331, 2004.

[62] J.J. Weis and D. Levesque. Chain Formation in Low Density Dipolar Hard Spheres: A Monte Carlo Study. *Phys. Rev. Lett.*, 71:2729–2732, 1993.

[63] A.V. Emelyanenko and M.A. Osipov. Origin of spontaneous polarisation, tilt, and chiral structure of smectic liquid-crystal phases composed of bent-core molecules: A molecular model. *Phys. Rev. E*, 70:021704, 2004.

[64] J.A.C. Veerman and D. Frenkel. Phase diagram of a system of hard spherocylinders by computer simulation. *Phys. Rev. A*, 41:3237–3244, 1990.

[65] S. C. McGrother, D.C. Williamson, and G. Jackson. A re-examination of the phase diagram of hard spherocylinders. *J. Chem. Phys*, 104:6755–6771, 1995.

[66] P. Bolhuis and D. Frenkel. Tracing the phase boundaries of hard spherocylinders. *J. Chem. Phys*, 106:666–687, 1997.

[67] C. Vega, C. McBride, and L.G. MacDowell. Liquid crystal phase formation for the linear tangent hard sphere model from Monte Carlo simulations. *J. Chem. Phys*, 115:4203–4211, 2001.

[68] E. De Miguel. Reexamining the phase diagram of the Gay-Berne fluid. *Mol. Phys.*, 100:2449–2459, 2002.

[69] E. De Miguel and C. Vega. The global phase of the Gay-Berne model. *J. Chem. Phys.*, 117:6313–6322, 2002.

[70] J.T. Brown, M.P. Allen, E.M del Rio, and E. de Miguel. Effects of elongation on the phase behaviour of the Gay-Berne fluid. *Phys. Rev. E*, 57:6685–6699, 1998.

[71] A. Perera and F. Sokolic. On the phase diagrams of fluids of linearily fused lennard-jones sites. *Mol. Phys.*, 88:543–557, 1996.

[72] G. Cinecchi, L. De Gaetani, and A. Tani. Numerical study of a calamitic liquid crystal model: Phase behaviour and structure. *Phys. Rev. E*, 71:031703, 2005.

[73] R. Dickman and C.K. Hall. Equation of state for chain molecules: Continuous-space analogue of Flory theory. *J. Chem. Phys.*, 85:4108–4115, 1986.

[74] J.K. Johnson, E.A. Muller, and K.E. Gubbins. Equation of state for Lennard-Jones chains. *J. Phys. Chem*, 98:6413–6419, 1994.

[75] J.M. Polson and D. Frenkel. Calculation of solid-fluid phase equilibria for systems of chain molecules. *J. Chem. Phys.*, 109:318–328, 1998.

[76] Introductory material for Configurational Bias Monte Carlo, http://www.cheme.buffalo.edu/courses/ce530/lectures/lecture22/index.htm.

[77] A.W. Rosenbluth and M.N. Rosenbluth. Monte-Carlo Calculation of the Average Extension of Molecular Chains. *J. Chem. Phys.*, 23:356–359, 1955.

[78] J. S. Van Duijneveldt and M. P. Allen. Computer simulation of a flexible-rigid-flexible model for liquid crystals. *Mol. Phys*, 92:855–, 1997.

[79] J. S. Van Duijneveldt, A. Gil-Villegas, G. Jackson, and M. P. Allen. Simulation study of the phase behaviour of a primitive model for thermotropic liquid crystal: Rodlike molecules with terminal dipoles and flexible tails. *J. Chem. Phys*, 112:9092–9104, 2000.

[80] C. McBride, C. Vega, and L.G. MacDowell. Isotropic-nematic phase transition: Influence of intramolecular flexibility using a fused hard sphere model. *Phys. Rev. e*, 64:011703, 2000.

[81] C. McBride and C. Vega. A Monte Carlo study of the influence of molecular flexibility on the phase diagram of a fused hard sphere model. *J. Chem. Phys*, 117:10370–10379, 2002.

[82] C. McBride and M.R. Wilson. Molecular dynamics simulations of a flexible liquid crystal. *Mol. Phys*, 97:511–522, 1999.

[83] H. Fukunaga, J-I. Takimoto, and M. Doi. Molecular dynamics simulation study on the phase behaviour of the Gay-Berne model with terminal dipole and a flexible tail. *J. Chem. Phys.*, 120:7792–7800, 2004.

[84] M.R. Wilson. Molecular dynamics simulations of flexible liquid crystal molecules using Gay-Berne/Lennard-Jones model. *J. Chem. Phys*, 107:8654–8663, 1997.

[85] F. Affouard, M. Kroger, and S. Hess. Molecular dynamics of model liquid crystals composed of semiflexible molecules. *Phys. Rev. E*, 54:5178–5186, 1996.

[86] J.I. Siepmann and D. Frenkel. Configurational-bias Monte Carlo: a new sampling scheme for flexible chains. *Mol. Phys*, 75:59–70, 1991.

[87] H. Goldstein. *Classical mechanics*. Addison-Wesley Press, Reading, Mass., 1950.

[88] R.B. Meyer. Piezoelectric effects in liquid crystals. *Phys. Rev. Lett.*, 22:918–921, 1969.

[89] A.G. Petrov. Flexoelectricity of model and living membranes. *Biochim. Biophys. Acta*, 85535:1–25, 2001.

[90] P.R. Maheswara Murthy, V.A. Raghunathan, and N.V. Madhusudana. Experimental determination of the flexoelectric coefficients of some nematic liquid crystals. *Liq. Cryst.*, 14:483–496, 1993.

[91] A.G. Petrov. Measurements and interpretation of flexoelectricity. In D.A. Dunmur, A. Fukada, and G.R. Luckhurst, editors, *Physical properties of liquid crystals: nematics*, pages 251–264, London, 2001. Institute of electrical engineers.

[92] J.P. Straley. Theory of piezoelectricity in nematic liquid crystals, and of the cholesteric ordering. *Phys. Rev. A*, 14:1835–1841, 1976.

[93] A. Ferrarini. Shape model for the molecular interpretation of the flexoelectric effect. *Phys. Rev. E*, 64:021710, 2001.

[94] A.V. Zakharov and R.Y. Dong. The flexoelectric effect in nematic liquid crystals: A statistical mechanics approach. *Eur. Phys. J. E*, 6:3–6, 2001.

[95] J. Stelzer, R. Berardi, and C. Zannoni. Flexoelectric effects in liquid crystals formed by pear-shaped molecules. A computer simulation study. *Chem. Phys. Lett.*, 299:9–16, 1998.

[96] J.L. Billeter and R.A. Pelcovits. Molecular shape and flexoelectricity. *Liq. Crys.*, 27:1151–1160, 2000.

[97] V.B. Nemetsov and M.A. Osipov. Statistical theory of flexoelectric effect in liquid crystals. *Sov. Phys. Crystallogr.*, 31:125–128, 1986.

[98] A.V. Zakharov and A.A. Vukulenko. Flexoelectric Effect and Statistical Properties in Polar Liquid Crystals. *Crystallography Reports*, 48:738–744, 2002.

[99] D.L. Cheung, S.J. Clark, and M.R. Wilson. Calculation of flexoelectric coefficients for a nematic liquid crystal by atomistic simulation. *J. Chem. Phys*, 121:9131–9139, 2004.

[100] C. Denniston and J.M. Yeomans. Flexoelectric Surface Switching of Bistable Nematic Devices. *Phys. Rev. Lett.*, 87:275505, 2001.

[101] A.J. Davidson and N.J. Motram. Flexoelectric switching in a bistable nematic device. *Phys. Rev. E*, 65:051710, 2002.

[102] M. P. Allen and A. J. Masters. Molecular simulation and theory of liquid crystals: chiral parameters, flexoelectric coefficients and elastic constants. *J. Mater. Chem.*, 11:2678–2689, 2001.

[103] D.L. Cheung. *Structure and properties of liquid crystals and related molecules from computer simulation*. PhD thesis, School of Chemistry, Durham Univeristy, 2002.

[104] F. Barmes, M. Ricci, C. Zannoni, and D.J. Cleaver. Computer simulations of hard pear-shaped particles. *Phys. Rev. E*, 68:021708, 2003.

[105] D.J. Earl, M.A. Osipov, H. Takezoe, Y. Takanishi, and M.R. Wilson. Induced and spontaneous deracemization in bent-core liquid crystal phases and in other phases doped with bent-core molecules. *Phys. Rev. E*, 71:021706, 2005.

[106] G.C.A.M. Mooij and D. Frenkel. A systematic optimization scheme for configurational bias monte carlo. *Mol. Sim.*, 17(1):41–55, 1996.

[107] T.J.H. Vlugt, M.G. Martin, B. Smit, J.I. Siepmann, and R. Krishna. Improving the efficiency of the configurational-bias Monte Carlo algorithm. *Mol. Phys.*, 94:727–733, 1998.

[108] D. Frenkel. Speed-up of Monte Carlo by sampling of rejected states. *PNAS*, 101:17571–17575, 2005.

Computer simulations of bent-core liquid crystals

Alastair Dewar and Philip J. Camp*
School of Chemistry, The University of Edinburgh, West Mains Road, Edinburgh EH9 3JJ, United Kingdom
(Received 29 December 2003; published 15 July 2004)

The phase behavior of model linear and bent-core molecules has been studied using isothermal-isobaric Monte Carlo computer simulations. The molecular model consists of seven Lennard-Jones spheres rigidly arranged in a "V" shape, with external bond angle, γ. With $\gamma=0°$ (linear molecules), we find isotropic, nematic, untilted smectic *A*, and two layered phases in which the molecules are tilted with respect to the layer normal. The latter two phases correspond to distinct branches in the equation of state, and possess different types of ordering within and between the layers; these phases are tentatively assigned as being smectic *B* and crystal. Apart from the possible existence of a tilted smectic *B*, the phase behavior of this system is broadly in line with earlier simulation studies on related linear molecular models. In the $\gamma=20°$ system, isotropic, nematic, and tilted smectic-*B* phases are observed. Interestingly, the range of stability of the nematic phase is enhanced compared to the $\gamma=0°$ system. In simulations of the $\gamma=40°$ system, nematic phases are absent, and only isotropic and tilted phases are in evidence. The in-layer structure of the tilted phases shows a very clear change from smectic-*B* to smectic-*A* ordering upon increasing the temperature. In all instances of a tilted phase, the degree of molecular tilt is in the region of $30\pm5°$, with respect to the smectic layer normal, which corresponds closely to typical experimental observations in real bent-core liquid crystals. In our model, the tilt provides efficient packing of the spheres and favorable attractive interactions between molecules. The relevance of the present simulation model to real bent-core liquid crystals is discussed critically.

DOI: 10.1103/PhysRevE.70.011704 PACS number(s): 61.30.Cz, 64.70.Md

I. INTRODUCTION

The emergence of a new class of liquid crystalline materials was signaled by the synthesis of achiral bent-core molecules that are able to form chiral ferroelectric or antiferroelectric smectic phases [1]. Typically, the molecules are of C_{2v} symmetry, and often possess a permanent electric dipole moment parallel to the principal molecular (C_2) symmetry axis. A typical example of a bent-core molecule is shown in Fig. 1. The substituents ("R" in Fig. 1) are usually either simple alkyl (C_nH_{2n+1}) [1] or alkoxy (OC_nH_{2n+1}) [2] groups.

In biaxial smectic phases, the dipoles are preferentially oriented perpendicular to the layer normal, largely as a result of the molecular biaxiality and the way in which the molecules pack. The formation of ferroelectric and antiferroelectric phases is also seen to be accompanied by the molecules being tilted with respect to the layer polarizations. Therefore, ferroelectric and antiferroelectric phases may exhibit chiral order if the molecules within each layer are tilted in the same sense with respect to the layer polarizations [1–3].

To date, several models of rigid bent-core molecules have been studied using Monte Carlo (MC) and molecular dynamics (MD) computer simulations. In the work summarized below, the molecules possess C_{2v} symmetry, with the "steric" or actual dipole parallel with the C_2 symmetry axis. In what follows, whether the molecules carry an electric dipole or not, the terms ferroelectric, antiferroelectric, superparaelectric, and paraelectric will be used to describe the ordering of the molecular C_2 axes and the layer polarizations in smectic and crystalline phases: ferroelectric means all C_2 axes and layer polarizations are aligned; antiferroelectric means that the polarizations of neighboring smectic layers are antiparallel; superparaelectric means that although the layers are polarized, there is a random distribution of polarization directions in the plane of the layers; and finally, paraelectric denotes a disordered distribution of the C_2 axes, i.e., the layers are not individually polarized. In addition, in tilted ferroelectric and antiferroelectric phases, synclinic ordering means that molecules in neighboring layers are tilted in the same direction with respect to the layer normal, whereas anticlinic ordering means that the molecules in neighboring layers are tilted in opposite directions.

The phase behavior of hard-spherocylinder dimers was studied in preliminary work by Camp *et al.* [4], and more thoroughly by Lansac *et al.* [5]. Referring to this latter work, isotropic, uniaxial nematic, paraelectric smectic-*A*, antiferroelectric smectic-*A*, columnar, paraelectric crystalline, and antiferroelectric crystalline phases were found. In neither of these studies were tilted phases in evidence. Lansac *et al.* also examined the relative thermodynamic stabilities of ferroelectric and antiferroelectric smectic-*A* phases [5]. For dimers with an external bond angle of $\gamma=60°$, and at a packing fraction of about 0.45, the antiferroelectric phase was calculated to be $(0.0035\pm0.0002)k_BT$ lower in Gibbs free energy than the ferroelectric phase. This can be rationalized using a "sawtooth model" in which the molecules in neighboring layers can partially interdigitate in the antiferroelectric phase, but not in the ferroelectric phase.

Continuous potentials studied to date include Gay-Berne dimers [6–8], and site-site molecular models made up of purely repulsive soft spheres [9]. Memmer carried out constant-pressure Monte Carlo (*NpT*-MC) simulations of Gay-Berne dimers with external bond angle $\gamma=40°$, in a

*Electronic address: philip.camp@ed.ac.uk

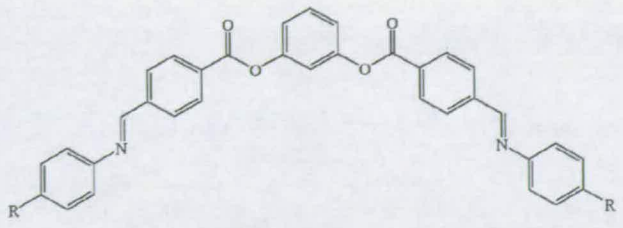

FIG. 1. A typical example of a bent-core molecule [1].

cuboidal simulation cell with independently varied box lengths [6]. These simulations showed nematic and untilted antiferroelectric smectic phases, and a chiral helical superstructure close to the nematic-smectic transition temperature. *NpT*-MD simulations of a similar Gay-Berne model with varying external bond angles in the range $0° \leqslant \gamma \leqslant 70°$ were carried out by Johnston *et al.* [7]. These simulations were performed in a cuboidal box with fixed aspect ratio 1:1:2. With $\gamma=0°$, isotropic, nematic, smectic-*A*, and smectic-*B* phases were found. With a modest amount of molecular bend ($\gamma=10°$), the nematic phase was seen to disappear, resulting in a direct isotropic-smectic transition. Upon increasing the bond angle further to $\gamma=20°$, the nematic phase was reinstated, and a tilted smectic-*B* phase was observed. An interesting twisted grain-boundary (TGB) phase was discovered in a system with $\gamma=40°$, while at a quite extreme molecular geometry ($\gamma=70°$), no ordered phases were observed. Johnston *et al.* have also carried out a simulation study of the same bent-core molecular model, but with a transverse dipole moment along the C_2 molecular axis [8]. It was seen that with moderate bond angles ($\gamma \leqslant 40°$) the additional dipole-dipole interactions destabilize the uniaxial nematic phase, and favor the formation of a synclinic antiferroelectric smectic phase.

A site-site bent-core model made up of seven soft spheres interacting via a Weeks-Chandler-Andersen repulsive potential was studied by Xu *et al.* [9]. Monte Carlo simulations of this model were carried out in the canonical (*NVT*) ensemble, using a cuboidal cell of variable shape containing four smectic layers. With an external bond angle $\gamma=40°$, a tilted paraelectric crystalline phase was found that undergoes a transition to a paraelectric smectic-*A* phase as the temperature is raised, or the density is lowered. The stability of the tilted phase was attributed to a favorable close packing of the spheres on neighboring molecules made possible by the molecular tilt.

From the work that has appeared to date, it should be clear that dipole-dipole interactions are not necessary in the formation of tilted smectic phases. On the other hand, it is obvious that dipolar forces would help stabilize antiferroelectric phases, since the lowest-energy configuration of neighboring layer polarizations is antiparallel; this has been demonstrated in the work on polar Gay-Berne molecules by Johnston *et al.* [8]. The formation of smectic phases of bent-core molecules with polarized layers is, therefore, driven largely by the molecular shape. With the exception of the composite soft-sphere model studied by Xu *et al.* [9], however, the models listed above are all dimer models. Although a great deal can be learned about the fundamental properties of condensed phases from such simple molecular models, it could be argued that a multisite model is more appropriate in the case of bent-core compounds. Attractive interactions might also be included in models of thermotropic liquid crystals; these are omitted from the model studied by Xu *et al.* [9].

With these comments in mind, we set out to study a family of model bent-core molecules that may provide a more faithful representation of the essential molecular characteristics of real compounds. The molecular model consists of seven Lennard-Jones (LJ) spheres arranged in a "V" formation with external bond angle γ, as illustrated in Fig. 2. We have investigated three bond angles, $\gamma=0°$, $\gamma=20°$, and $\gamma=40°$. Assuming that the relative locations of the aryl groups largely dictate the molecular geometry, the molecule as illustrated in Fig. 1 would have an external bond angle closer to $\gamma=60°$. It should be remembered, however, that there are intramolecular rotations that can reduce this figure considerably, and that in condensed phases, particular conformations may be thermodynamically favored if they lead to improved packing or energetic stabilization. Another factor is the orientation of the alkyl or alkoxy tail groups, which can influence the effective molecular elongation and degree of molecular nonlinearity. Experimental measurements indicate that γ is usually in the range 20°–40°, at least in condensed phases, and so the range of molecular bond angles studied in this work is physically relevant. We note that Paolini *et al.* have studied a similar model of linear molecules made up of 11 purely repulsive soft spheres [10]; they found isotropic, nematic, smectic-*A*, and crystalline chevron (tilted) phases. Galindo *et al.* have recently reported a simulation study of the vapor, isotropic liquid, and solid phases of linear molecules made up of three and five Lennard-Jones spheres [11]; however, no liquid-crystalline phases were observed in this work.

In the present model, the total configurational energy U of the system is given by a sum over all pairs of spheres on different molecules

$$U = \sum_{i=1}^{N_m} \sum_{j>i}^{N_m} \sum_{k=1}^{N_s} \sum_{l=1}^{N_s} u(|\mathbf{r}_{ik} - \mathbf{r}_{jl}|), \tag{1}$$

where N_m is the total number of molecules, $N_s=7$ is the number of spheres per molecule, and $\mathbf{r}_{ik}$ is the position vector of the kth sphere on the ith molecule. $u(r)$ is the sphere-sphere potential, which in this work we take to be the LJ (12,6) potential,

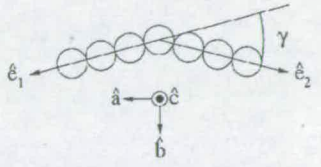

FIG. 2. The composite Lennard-Jones molecule (CLJM). $\hat{\mathbf{e}}_1$ and $\hat{\mathbf{e}}_2$ are unit vectors representing the orientations of the two "arms" of the molecule. The molecular frame is specified by the unit vectors $\hat{\mathbf{a}}$, $\hat{\mathbf{b}}$, and $\hat{\mathbf{c}}$ defined in Eqs. (4)–(6).

$$u(r)=\begin{cases}4\epsilon\left[\left(\frac{\sigma}{r}\right)^{12}-\left(\frac{\sigma}{r}\right)^{6}\right] & r\le r_{\text{cut}}\\ 0 & r>r_{\text{cut}}\end{cases}, \qquad (2)$$

where r is the pair separation, ϵ is the potential-well depth, σ is the LJ sphere diameter, and $r_{\text{cut}}=2.5\sigma$. Neighboring spheres on a given molecule are separated by a distance equal to 1σ. This part of the model represents the fairly rigid bent core of real molecules (cf. Fig. 1); for brevity we refer to these model molecules as composite LJ molecules (CLJMs).

In this paper we report the results of NpT-MC simulations of CLJMs carried out to explore the phase behavior. We will show that this molecular model is sufficient to simulate the formation of nematic and tilted smectic phases. Moreover, we confirm that the main driving force for the formation of tilted phases is the favorable interactions arising from the "close packing" of spheres on neighboring molecules. We argue that this scenario is physically relevant, bearing in mind that many real bent-core molecules are often made up of several aryl groups (see Fig. 1), and hence are quite "bumpy." In Sec. II we detail the simulation methods employed in this work. The results are presented in Sec. III, and Sec. IV concludes the paper.

II. SIMULATION DETAILS

We performed constant-pressure constant-temperature Monte Carlo (NpT-MC) simulations of N_m bent-core molecules in a cuboidal or a cubic simulation cell with periodic boundary conditions applied [12]. The cuboidal cell was constrained to have a square cross section, i.e., the box dimensions were $L_{xy}\times L_{xy}\times L_z$. To check that the cuboidal simulation cell did not artificially stabilize untilted solid or smectic phases, we computed the pressure tensor, Π, given by,

$$\prod=\left(\frac{N_m k_B T}{V}\right)\mathbf{I}+\frac{1}{V}\sum_{i=1}^{N_m}\sum_{j>i}^{N_m}\sum_{k=1}^{N_s}\sum_{l=1}^{N_s}(\mathbf{r}_{ik}-\mathbf{r}_{jl})\mathbf{f}_{ijkl}, \qquad (3)$$

where $\mathbf{I}$ is the second-rank unit tensor, $\mathbf{f}_{ijkl}$ is the force between the kth sphere on the ith molecule and the lth sphere on the jth molecule, and $(\mathbf{r}_{ik}-\mathbf{r}_{jl})$ is the corresponding sphere-sphere separation vector. In particular, we confirmed that the off-diagonal elements of the pressure tensor fluctuate about zero, indicating the absence of any significant stresses which might otherwise favor the development of a tilted simulation cell. We note that in almost all simulation studies of bent-core liquid crystals to date, untilted simulation cells have been employed without any reported pathological effects [4–9]. In the case of crystalline phases, however, the simulation cell should strictly be able to tilt—as in the Parrinello-Rahman method [13,14]—but these phases are not of primary concern in the current study.

The following reduced units are defined in terms of the LJ interaction parameters: the reduced pressure, $p^*=p\sigma^3/\epsilon$, the reduced temperature, $T^*=k_BT/\epsilon$, where k_B is Boltzmann's constant; the reduced molecular number density, $\rho^*=N_m\sigma^3/V$, where V is the volume of the simulation cell.

One MC sweep consisted of one trial translation or one trial rotation per molecule, and a single volume move. The rotational moves were effected by the Barker-Watts method [12]. Volume moves were carried out by sampling $\ln V$ [12]; in the cuboidal-cell simulations, the dimension to be scaled (L_{xy} or L_z) was chosen at random. All maximum displacement parameters were adjusted to give respective acceptance ratios of 50%. In general, we found that the equilibration of the simulations was sluggish, requiring $\sim 10^6$ MC sweeps; after equilibration we carried out production runs of comparable length.

Isotropic and nematic phases were simulated in a cubic simulation cell, whilst smectic phases were accommodated in a cuboidal simulation cell. In all simulations, the total number of molecules was $N_m=400$. In the simulations with a cuboidal cell, the molecules were distributed amongst four smectic layers of 100 each, with the layer normals aligned initially along the z direction. Although no constraints were applied to maintain the orientations of the smectic layer normals along the z direction, a visualization of simulation snapshots showed that they did not rotate significantly during the course of the simulations.

The global orientational ordering of the model molecules was assumed to involve preferential ordering of a set of molecular axes, defined as follows. The unit vectors $\hat{\mathbf{e}}_1$ and $\hat{\mathbf{e}}_2$ in Fig. 2 describe the orientations of the two "arms" of the molecule, with $\hat{\mathbf{e}}_1\cdot\hat{\mathbf{e}}_2=-\cos\gamma$. The molecular frame is defined by three orthonormal vectors given by

$$\hat{\mathbf{a}}=\frac{\hat{\mathbf{e}}_1-\hat{\mathbf{e}}_2}{|\hat{\mathbf{e}}_1-\hat{\mathbf{e}}_2|}, \qquad (4)$$

$$\hat{\mathbf{b}}=\frac{\hat{\mathbf{e}}_1+\hat{\mathbf{e}}_2}{|\hat{\mathbf{e}}_1+\hat{\mathbf{e}}_2|}, \qquad (5)$$

$$\hat{\mathbf{c}}=\hat{\mathbf{a}}\times\hat{\mathbf{b}}. \qquad (6)$$

Uniaxial and biaxial ordering of the molecules are described by the parameters Q^2_{00} and Q^2_{22} given by

$$Q^2_{00}=\frac{1}{2}(3\cos^2\theta-1), \qquad (7)$$

$$Q^2_{22}=\frac{1}{2}(1+\cos^2\theta)\cos 2\phi\cos 2\psi-\cos\theta\sin 2\phi\sin 2\psi, \qquad (8)$$

where (ϕ,θ,ψ) are the Euler angles in the rotation matrix mapping the molecular frame defined by Eqs. (4)–(6) to the laboratory frame [15]. To identify the laboratory frame, we take the director of the most aligned molecular axis to define the laboratory Z axis. The director of the second-most aligned molecular axis is taken to be the laboratory Y axis, and the X axis is orthogonal to Y and Z. With this convention, $Q^2_{00}=1$ and $Q^2_{22}=0$ denote a phase with perfect uniaxial orientational ordering, whilst $Q^2_{00}=1$ and $Q^2_{22}=1$ describe a phase with perfect biaxial orientational ordering. In the simulations, the directors and order parameters were obtained by diagonalizing the order tensors [16]

$$\mathbf{Q}_{aa} = \frac{1}{2N_m} \sum_{i=1}^{N_m} (3\hat{\mathbf{a}}_i \hat{\mathbf{a}}_i - \mathbf{I}), \tag{9}$$

where $\mathbf{I}$ is the second-rank unit tensor; corresponding definitions hold for $\mathbf{Q}_{bb}$ and $\mathbf{Q}_{cc}$. Diagonalization of each tensor in turn yields the eigenvalues $\lambda^+ \geqslant \lambda^0 \geqslant \lambda^-$, and the corresponding orthonormal eigenvectors, $\hat{\mathbf{n}}^+$, $\hat{\mathbf{n}}^0$, and $\hat{\mathbf{n}}^-$. The molecular axis with the largest λ^+ is identified as the z axis of the molecular frame, and the corresponding eigenvector (director) defines the laboratory Z axis ($\mathbf{Z}$). The molecular axis with the second-largest λ^+ is the y axis of the molecular frame, and the corresponding eigenvector (director) defines the laboratory Y axis ($\mathbf{Y}$). The molecular axis with the lowest λ^+ is taken to be the x axis of the molecular frame, and the laboratory X axis ($\mathbf{X}$) is orthogonal to $\mathbf{Y}$ and $\mathbf{Z}$. With these assignments, the order parameters in Eqs. (7) and (8) are equal to

$$Q_{00}^2 = \mathbf{Z} \cdot \mathbf{Q}_{zz} \cdot \mathbf{Z}, \tag{10}$$

$$Q_{22}^2 = \frac{1}{3}(\mathbf{X} \cdot \mathbf{Q}_{xx} \cdot \mathbf{X} + \mathbf{Y} \cdot \mathbf{Q}_{yy} \cdot \mathbf{Y} - \mathbf{X} \cdot \mathbf{Q}_{yy} \cdot \mathbf{X} - \mathbf{Y} \cdot \mathbf{Q}_{xx} \cdot \mathbf{Y}). \tag{11}$$

We note that finite-size errors are apparent in the order parameters calculated by diagonalizing order tensors; in the isotropic phase the errors are $\mathcal{O}(1/\sqrt{N_m})$, while in orientationally ordered phases, the errors are $\mathcal{O}(1/N_m)$ [17].

In all cases, the full radial distribution function, $g(r)$, was computed, but to help characterize smectic phases in a cuboidal simulation cell, the correlations between molecules in the same smectic layer were quantified by calculating the in-layer (two-dimensional) radial distribution function, $g_{xy}(r)$. This latter function is defined by

$$g_{xy}(r) = \left\langle \frac{L_{xy}^2}{2\pi r N_l^2} \sum_{i=1}^{N_l} \sum_{j \neq i}^{N_l} \delta(|\mathbf{r}_i - \mathbf{r}_j| - r) \right\rangle, \tag{12}$$

where $N_l = 100$ is the number of molecules within the layer, and $\mathbf{r}_i$ is the position vector of the apical sphere on the ith molecule.

The average tilt angle Φ between the molecular a axes and the smectic-layer normal was computed using

$$\cos \Phi = \frac{1}{N_m} \sum_{i=1}^{N_m} |\hat{\mathbf{a}}_i \cdot \hat{\mathbf{l}}|, \tag{13}$$

where $\hat{\mathbf{l}}$ is the layer normal, which we took to be the z axis of the simulation cell, since in simulation snapshots we could observe no significant rotation of $\hat{\mathbf{l}}$ during the course of the calculations.

For each system considered, we carried out sequences of simulations starting from *untilted* configurations on simple close-packed lattices in cuboidal simulation cells, with reduced densities of either $\rho^* = 0.14$ or $\rho^* = 0.15$. The reason for selecting untilted starting points was to ensure that molecular tilt developed spontaneously. After equilibration, we raised the temperature until we detected a transition to a homogeneous fluid phase (isotropic or nematic). We then switched over to a cubic simulation cell and carried out some cooling runs to confirm the existence of a transition, as well as performing some further heating runs to map out the high-temperature behavior. With $\gamma = 40°$, we carried out separate runs starting from perfectly ordered ferroelectric and antiferroelectric configurations, in order to detect any differences in the relative mechanical stabilities of the two polarization states. In most cases, (anti)ferroelectric ordering did not persist for the duration of the runs due to the smectic-layer polarizations reorienting in random directions.

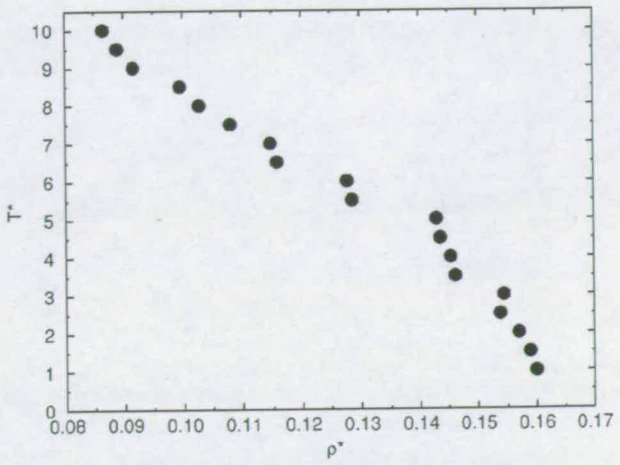

FIG. 3. The equation of state (temperature as a function of density) for CLJMs with external bond angle $\gamma = 0°$, along an isobar with $p^* = 4.0$.

III. RESULTS

A. $\gamma = 0°$

The equation of state of linear ($\gamma = 0°$) CLJMs along an isobar with $p^* = 4.0$ is shown in Fig. 3. Snapshots of the system at $T^* = 2.0$ shown in Figs. 4(a) and 4(b) clearly show crystalline ordering within the layers, and that the layers are tilted with respect to the layer normal. This kind of tilt has been demonstrated in simulations of solid-phase semiflexible chains made up of six spheres interacting via a truncated-and-shifted Lennard-Jones potential [18], in the calculations of Paolini *et al.* using a soft-sphere model [10], and in the simulations of three- and five-LJ-sphere linear molecules by Galindo *et al.* [11]. In our calculations, the average tilt angle of the molecules with respect to the layer normal—which develops spontaneously—is $\Phi \simeq 35°$, indicating the approximately close-packed interdigitation of the spheres within each layer. This tilt angle is comparable to the range of angles observed in experiments, this being between 25° and 35° [19,20], but in our simulations there is no global tilt direction. Our interest is not in the crystalline phases, but we note that a truly long-range ordered solid phase seems to be the thermodynamically stable state at temperatures $T^* \leqslant 3.0$. In these simulations carried out in the cuboidal simulation cell, the off-diagonal elements of the stress tensor fluctuated about zero, albeit sluggishly. Unsurprisingly, the worst

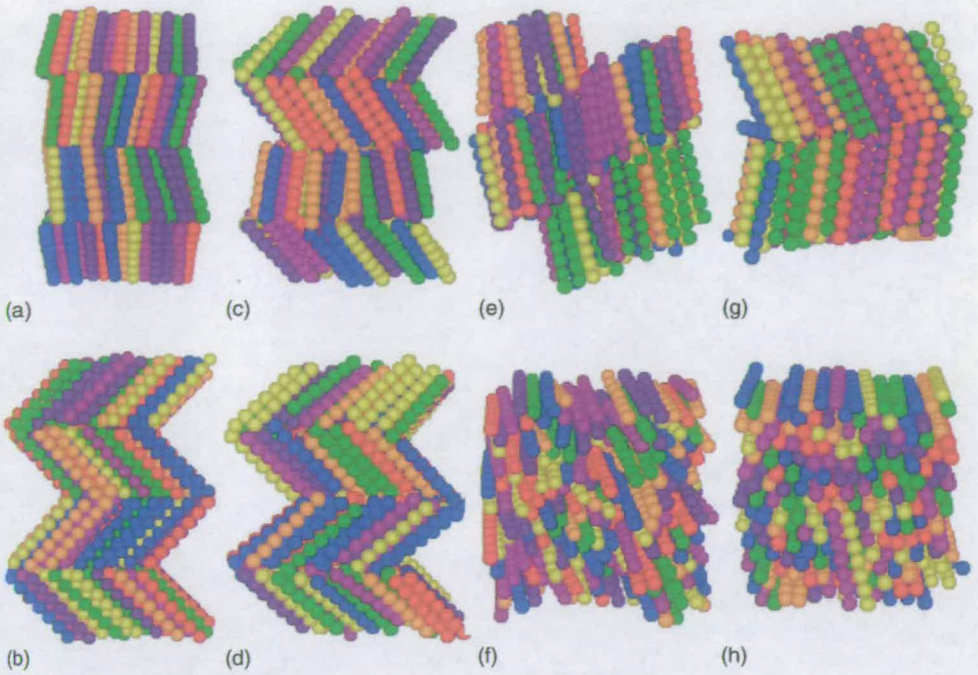

FIG. 4. (Color online) Snapshots from simulations of CLJMs with $\gamma=0°$, along an isobar with $p^*=4.0$: (a) and (b) crystalline phase at $T^*=2.0$ (cuboidal cell); (c) and (d) tilted smectic-B phase at $T^*=4.0$ (cuboidal cell); (e) and (f) untilted smectic A at $T^*=6.0$ (cubic cell); (g) and (h) tilted smectic-B phase at $T^*=4.0$ (cubic cell).

case was the low-temperature crystalline phase ($T^* \leqslant 3.0$) in which the root-mean-square fluctuations of Π_{xy}, Π_{xz}, and Π_{yz} were as high as $0.5\epsilon/\sigma^3$. We put this down to the fact that the simulation cell comprises only four tilted layers, leading to large statistical fluctuations. Our simulation results suggest that the uniformly tilted (synclinic) crystalline phase is not strongly favored over a phase with some disorder in the tilt directions. With regard to this question, we note that a similar situation holds in solid phases of hard dumbbell molecules [21], and in two-dimensional systems of hard-disk dimers [22]. It would be interesting to study further the possible crystalline phases of CLJMs, particularly in light of current research activity in polymorphism.

The low-temperature phase is stable up to a temperature $T^*=3.0$, above which it undergoes a crossover to a state which persists over the temperature range $3.5 \leqslant T^* \leqslant 5.0$, as evidenced by the distinct branch in the equation of state shown in Fig. 3; snapshots of this phase at $T^*=4.0$ obtained by heating from the crystalline phase are shown in Figs. 4(c) and 4(d). In an attempt to assess whether this state is metastable, a well-equilibrated untilted smectic-A phase at $p^*=4.0$ and $T^*=6.0$ ($\rho^*=0.128$) in a cubic simulation cell (see below) was cooled to $T^*=4.0$; snapshots of the untilted smectic-A phase at $T^*=6.0$ are shown in Figs. 4(e) and 4(f). Upon cooling, the final equilibrium density was $\rho^*=0.147$, which corresponds to the same branch of the equation of state obtained from the heating run; snapshots of this final state are shown in Figs. 4(g) and 4(h). Note that the tilt has been re-established spontaneously, and that the short-range ordering within the layer [shown in Fig. 4(h)] is hexagonal; there does not appear to be any crystalline long-range order. Without absolute free-energy calculations it is unclear whether these structures in the temperature range $3.5 \leqslant T^* \leqslant 5.0$ are representative of a true thermodynamically stable state. However, the distinct branch of the equation of state shows that this phase is at least mechanically stable, and on the basis of the structural properties indicated in Fig. 4, we tentatively assign this as a tilted smectic-B phase (since the in-layer short-range ordering is hexagonal).

Continuing along the isobar, we observe an *untilted* paraelectric smectic phase at temperatures of $T^*=5.5$ and 6.0, followed by a uniaxial nematic phase in the range $6.5 \leqslant T^* \leqslant 8.5$, and finally the isotropic phase at $T^* \geqslant 9.0$. The in-layer structure of the untilted smectic shown in Fig. 4(f) clearly exhibits only short-range ordering, and hence this is a smectic A.

In Fig. 5, the nematic order parameter Q_{00}^2 is shown as a function of temperature along the isobar with $p^*=4.0$. The crossover from tilted smectic and crystalline phases is clearly visible at $T^* \leqslant 5.0$. The tilted phases exhibit smaller values of Q_{00}^2 than does the nematic phase because the layers are not tilted in the same direction. The nematic-isotropic phase

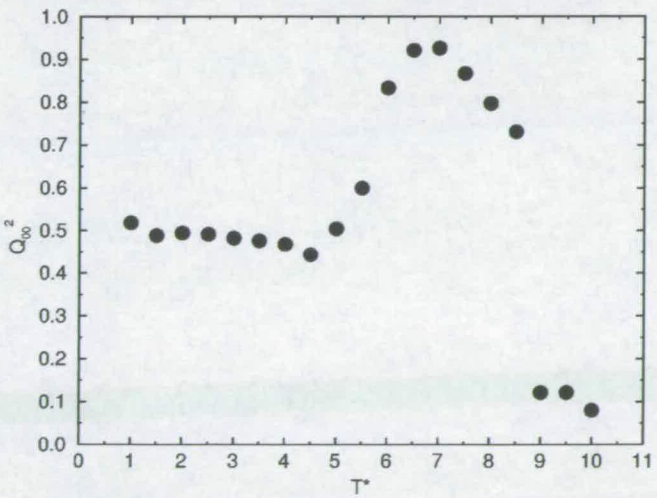

FIG. 5. The order parameter Q_{00}^2 as a function of temperature for CLJMs with external bond angle $\gamma=0°$, along an isobar with $p^*=4.0$.

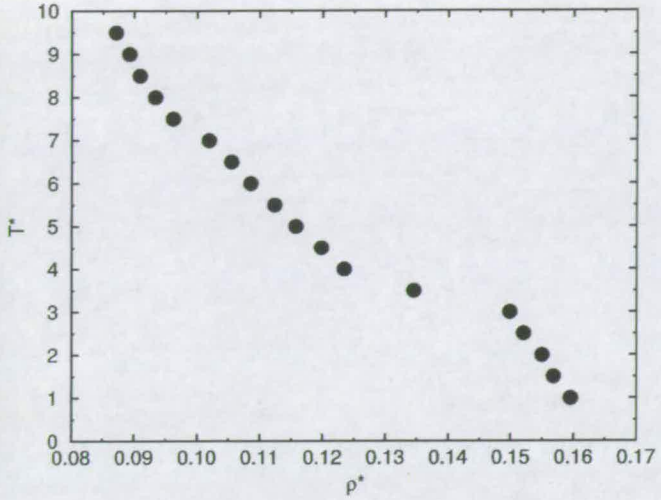

FIG. 6. Equation of state (temperature as a function of density) for CLJMs with external bond angle $\gamma=20°$, along an isobar with $p^*=4.0$.

transition is signaled by the drop in Q_{00}^2 between $T^*=8.5$ and 9.0.

With the exception of the tilted smectic-B phase ($3.5 \leqslant T^* \leqslant 5.0$), the phase behavior of CLJMs with $\gamma=0°$ is typical of cylindrically symmetric molecules with aspect ratios in the region of 10:1 [10].

B. $\gamma=20°$

The equation of state for CJLMs with $\gamma=20°$ along an isobar with $p^*=4.0$ is shown in Fig. 6. Three branches are apparent in the equation of state in the temperature ranges $T^* \leqslant 3.0$, $4.0 \leqslant T^* \leqslant 7.0$, and $T^* \geqslant 7.5$. The simulation at $T^*=3.5$ did not converge onto one of the main branches of the equation of state; the simulation configuration looks very much like the herring-bone structure shown in Figs. 4(c) and 4(d), and may represent a metastable state.

A snapshot from the simulation at $T^*=3.0$ is shown in Fig. 7(a). Clearly, the molecules are tilted within the layers; the average tilt angle with respect to the layer normal is $\Phi \simeq 35°$. In addition, the polarizations within the layer remain intact. The biaxial order parameter, Q_{22}^2, and the bulk polarization, $P \propto |\sum_{i=1}^{N_m} \hat{\mathbf{b}}_i \cdot \hat{\mathbf{n}}_b^+|$, where $\hat{\mathbf{n}}_b^+$ is the director of the molecular b axes, were seen to decay even during the lowest-temperature simulations, reflecting a low degree of correspondence between neighboring layers. Hence, this phase is superparaelectric, since it is the layer polarizations that are disordered, not the molecular orientations within the layer. From here on we will omit the descriptor "superparaelectric," since we have not found any stable ferroelectric or antiferroelectric smectic phases; the layer polarizations almost always rotated during the courses of the simulations to point in random directions. A detailed investigation of the in-layer structure at low temperatures suggests the existence of a smectic-B phase. Figure 8 shows the in-layer distribution function $g_{xy}(r)$ at two temperatures, $T^*=1.0$ and 3.0. At both temperatures, the second peak in $g_{xy}(r)$ is split, indicative of short-range hexagonal ordering. Neither of these functions is entirely consistent with long-range hexagonal (crystalline) ordering, however, and at the higher temperature, in-layer positional order is almost undetectable beyond $r/\sigma \simeq 4$. We therefore tentatively assign the low-temperature branch of the equation of state as corresponding to a tilted smectic-B phase. The alternatives are crystalline, or crystalline smectic; clearly the former is ruled out by a casual glance at Fig. 7(a). The differences between a smectic B and a "crystalline smectic" are subtle [23]. In a crystalline smectic, the layers possess long-range positional order, and obviously bond-orientational order, whereas neighboring layers are not in correspondence. In a smectic B, the layers

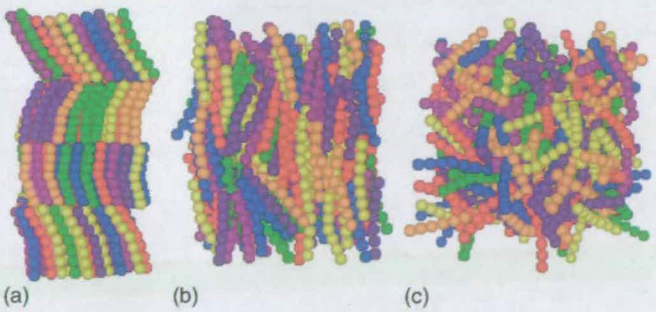

FIG. 7. (Color online) Snapshots from simulations of CLJMs with $\gamma=20°$, along an isobar with $p^*=4.0$: (a) tilted smectic-B phase at $T^*=3.0$ (cuboidal cell); (b) nematic phase at $T^*=5.0$ (cubic cell); (c) isotropic phase at $T^*=8.0$.

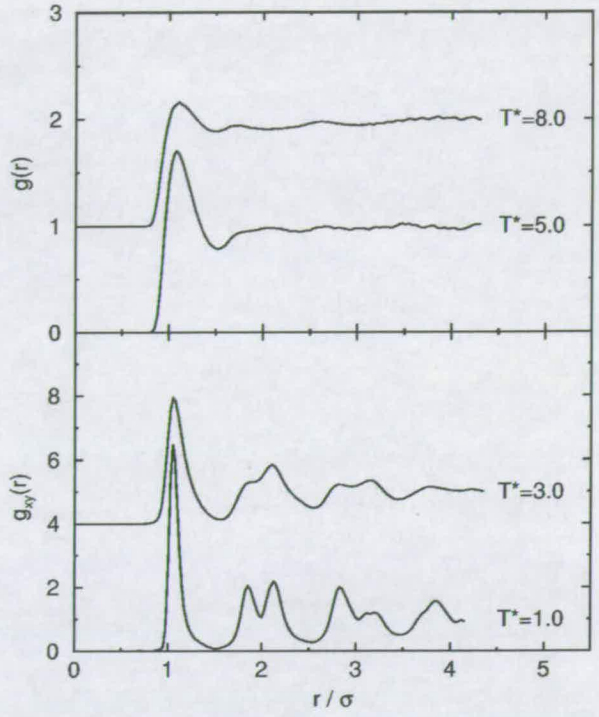

FIG. 8. Radial distribution functions for CLJMs with external bond angle $\gamma=20°$, along an isobar with $p^*=4.0$: (top) $g(r)$ in the isotropic phase at $T^*=8.0$ (upper), and in the uniaxial nematic phase at $T^*=5.0$ (lower) (functions are displaced by one unit for clarity); (bottom) in-layer radial distribution functions, $g_{xy}(r)$, in the tilted smectic-B phase at $T^*=3.0$ (upper) and 1.0 (lower) (functions are displaced by four units for clarity).

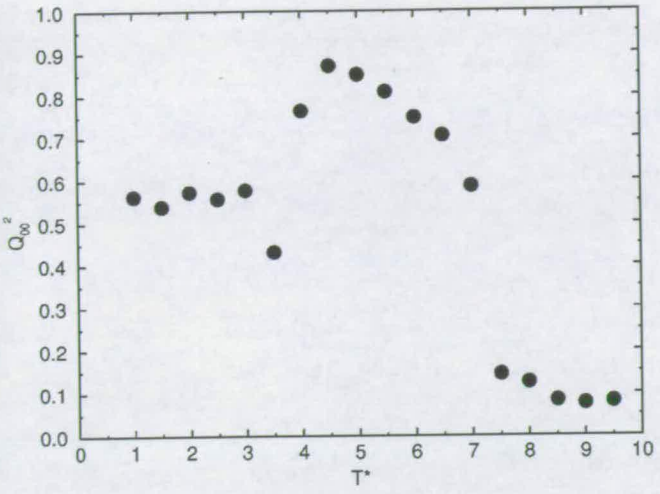

FIG. 9. The order parameter Q_{00}^2 as a function of temperature for CLJMs with external bond angle $\gamma=20°$, along an isobar with $p^*=4.0$.

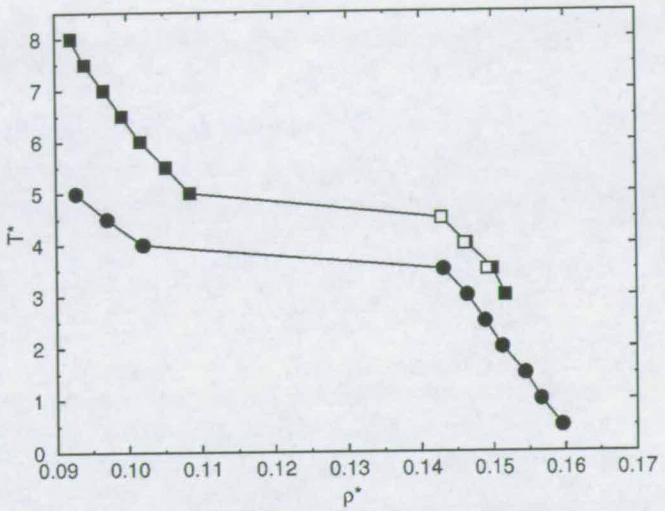

FIG. 10. The equation of state (temperature as a function of density) for CLJMs with external bond angle $\gamma=40°$, along isobars with $p^*=2.0$ (circles), and $p^*=4.0$ (squares). The filled and open symbols correspond to heating runs beginning from ferroelectric and antiferroelectric configurations, respectively (see text).

possess long-range bond-orientational order, but long-range crystalline order is destroyed by the presence of defects; typically, the positional order persists over a few hundred angstroms. Of course, in simulations with typical system sizes of $\sim 10^3$ molecules, it is almost impossible to make the distinction, because the long-range behavior of, say, $g_{xy}(r)$ is inaccessible. The snapshot in Fig. 7(a) is clearly not suggestive of a well-ordered crystalline phase, and hence we follow previous workers [7,8] and take the splitting of the second peak in $g_{xy}(r)$ as being indicative of a smectic-B phase.

The intermediate-temperature branch ($4.0 \leqslant T^* \leqslant 7.0$) in the equation of state corresponds to a uniaxial nematic phase. A snapshot from the simulation at $T^*=5.0$ is shown in Fig. 7(b). The radial distribution function, $g(r)$, for this same state point is shown in Fig. 8, which reflects the complete lack of any long-range positional ordering. The nematic-isotropic transition occurs at $T^*=7.0-7.5$; a snapshot of the isotropic phase at $T^*=8.0$ is shown in Fig. 7(c), and the corresponding $g(r)$ is shown in Fig. 8.

In Fig. 9 we plot the uniaxial order parameter, Q_{00}^2, as a function of temperature along an isobar with $p^*=4.0$. The nematic-isotropic phase transition, signaled by a sharp drop in Q_{00}^2, is very clear at $T^*=7.0-7.5$. The smectic phase at $T^* \leqslant 3.0$ exhibits smaller values of Q_{00}^2 due to the *random* tilt directions of the layers [see Fig. 7(a)]. Once again, the simulation at $T^*=3.5$ is anomalous, and likely reflects some sort of metastable state.

C. $\gamma=40°$

Equations of state for CLJMs with $\gamma=40°$ along isobars with $p^*=2.0$ and 4.0 are shown in Fig. 10. For the high-density, low-temperature branch of the $p^*=4.0$ isobar, two sets of results are presented; one sequence starting from an untilted ferroelectric configuration, and the other from a corresponding antiferroelectric configuration. On the basis of these two sets of results, the equation of state does not give a clear indication of whether one polarization state is any more (mechanically) stable than the other. Indeed, during the course of the simulations along the high-density branches, it was observed that the biaxial order parameter, Q_{22}^2, and the polarization, $P \propto |\Sigma_{i=1}^{N_m} \hat{\mathbf{b}}_i \cdot \hat{\mathbf{n}}_b^+|$, were seen to decay as the individual layer polarizations became uncorrelated. We are therefore led to the conclusion that there is no strong thermodynamic driving force for the formation of either a ferroelectric or an antiferroelectric phase, and hence the superparaelectric configuration of layer polarizations emerges; in what follows we do not distinguish between simulations started from different configurations, since they give almost identical results. The individual layers in the layered phases did show significant molecular tilt; along both isobars, the tilt angle remained at a value of $\Phi \simeq 27°$.

Surprisingly, we found no evidence of transitions to nematic phases along either of the isobars. Instead, we observed some rather subtle changes in the structural features of the tilted smectic phases—as indicated by $g_{xy}(r)$—before they eventually "melted" in to the isotropic phase. This is illustrated in Figs. 11 and 12 for the isobars with $p^*=2.0$ and 4.0, respectively. Starting with the lower-pressure isobar (Fig. 11), the in-layer distribution functions for $T^*=1.5$ and 3.0 retain a split second peak, which is indicative of a smectic-B phase; this persists up to the transition to the isotropic phase, which at $p^*=2.0$ is found to occur at $T^*=3.5-4.0$. The results for the isobar with $p^*=4.0$ are more interesting. The in-layer distribution functions indicate smectic-B ordering at $T^*=3.0$, but smectic-A ordering at $T^*=4.5$. By performing several independent runs at $T^*=3.0$, we confirmed that the smectic-A ordering was reproducible. We reiterate that molecular tilt within the layers persisted in all of the smectic phases.

In Fig. 13 we show the variation of the uniaxial order parameter, Q_{00}^2, as a function temperature along isobars with $p^*=2.0$ and 4.0. The smectic-isotropic transition is clearly signaled by a drop in Q_{00}^2 at $T^*=3.5-4.0$ for $p^*=2.0$, and at $T^*=4.5-5.0$ for $p^*=4.0$.

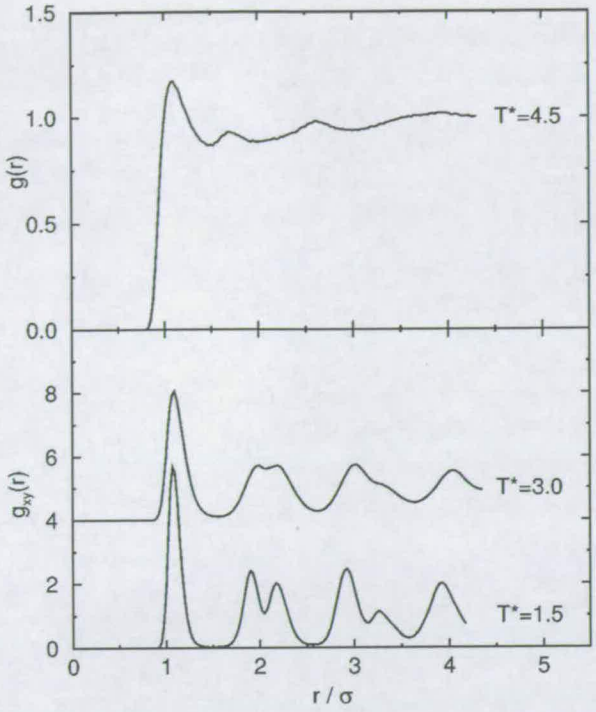

FIG. 11. Radial distribution functions for CLJMs with external bond angle $\gamma=40°$, along an isobar with $p^*=2.0$: (top) $g(r)$ in the isotropic phase at $T^*=4.5$; (bottom) in-layer radial distribution functions, $g_{xy}(r)$, in the tilted smectic-B phase at $T^*=3.0$ (upper) and $T^*=1.5$ (lower) (functions are displaced by four units for clarity).

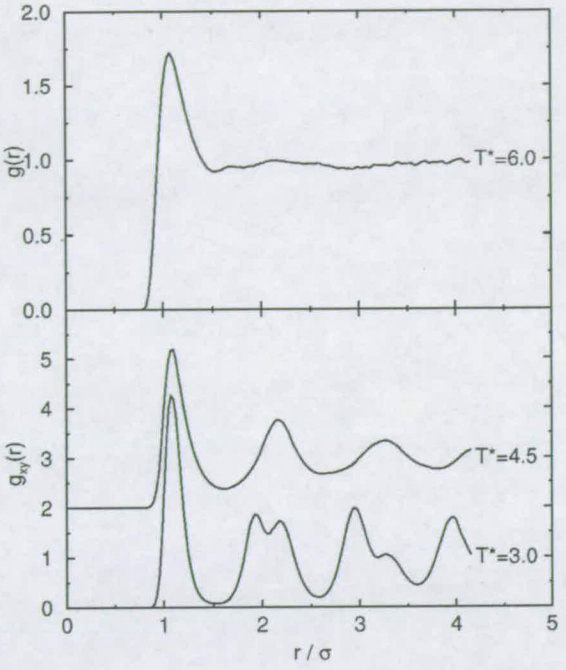

FIG. 12. Radial distribution functions for CLJMs with external bond angle $\gamma=40°$, along an isobar with $p^*=4.0$: (top) $g(r)$ in the isotropic phase at $T^*=6.0$; (bottom) in-layer radial distribution functions, $g_{xy}(r)$, in the tilted smectic-A phase at $T^*=4.5$ (upper), and in the tilted smectic-B phase at $T^*=3.0$ (bottom) (functions are displaced by two units for clarity).

IV. DISCUSSION

In this paper we have presented results from constant-pressure Monte Carlo computer simulations of model bent-core molecules (CLJMs) made up of seven Lennard-Jones spheres arranged to form a rigid "V"-shaped molecule with external bond angle γ. We have surveyed the phase behavior of CLJMs as a function of γ.

With $\gamma=0°$ (linear molecules), we find evidence for isotropic, nematic, untilted smectic-A, tilted smectic-B, and crystalline phases. The smectic-B and crystalline phases exhibit a molecular tilt of around 35° with respect to the layer normal, which confirms that, at least in this site-site model, tilted smectic phases are stabilized by a "close packing" of the spheres within a layer, as suggested by Xu *et al.* [9]. The observed phase behavior is in broad agreement with previously published work on linear molecules made up of 11 soft spheres (with repulsive interactions only) [10], with the exception of the tilted smectic-B phase. The existence of this phase demands further study, probably with the application of absolute free-energy calculations to confirm its thermodynamic (meta)stability. We note that the cuboidal simulation cells employed in this work may, in principle, artificially destabilize the synclinic crystalline phase, although no significant buildup of nonhydrostatic stresses was observed during the simulations.

For the system with $\gamma=20°$, we find isotropic, nematic, and tilted smectic-B phases. The range of stability of the uniaxial nematic phase is enhanced with respect to that in the $\gamma=0°$ system. In the smectic-B phase, the molecular tilt is in the region of 35° with respect to the layer normal.

With $\gamma=40°$, the nematic phase is no longer in evidence, the only phases we could find being isotropic and tilted smectic. At high pressure, the tilted smectic phase showed smectic-A ordering at high temperature, and smectic-B ordering at low temperature; the molecular tilt was around 27° with respect to the layer normal.

In none of these systems did we find evidence of truly chiral smectic phases, be they synclinic ferroelectric or anti-

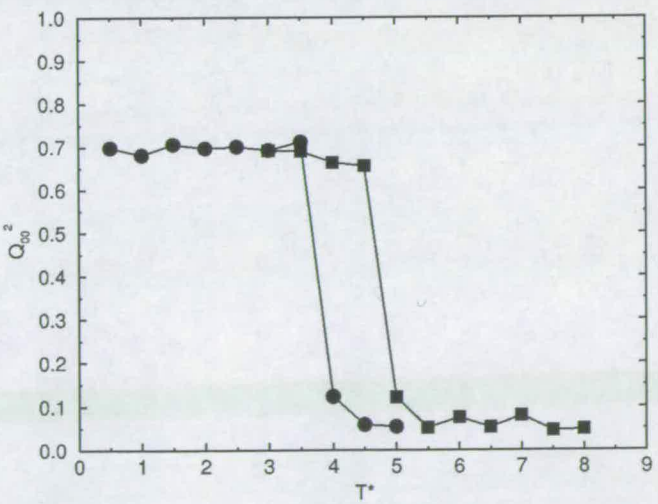

FIG. 13. Order parameter Q_{00}^2 as a function of temperature for CLJMs with external bond angle $\gamma=40°$, along isobars with $p^*=2.0$ (circles) and 4.0 (squares).

clinic antiferroelectric. In simulations of the $\gamma=40°$ system starting from untilted ferroelectric and antiferroelectric configurations, molecular tilt developed spontaneously, but global biaxiality did not persist for the duration of the runs. We note, however, that the range of values for the molecular tilt which developed spontaneously ($\Phi=27-35°$) compares favorably with typical experimental observations ($\Phi=25-35°$). Our molecular model is quite "bumpy," and it is interesting to speculate as to why tilt angles in the region of 30° are favored over more extreme angles. One possibility is that with a high degree of tilt, to take advantage of favorable attractive interactions, neighboring smectic layers would have to interdigitate to a greater extent; this would almost certainly reduce the configurational entropy of each molecule. It may therefore turn out that a tilt angle of ~30° represents an optimum balance of energy and entropy. To explore this issue, one could envisage carrying absolute free-energy calculations for systems with different proscribed tilt angles.

Of course, the most significant question is whether the present molecular model has any relevance to real bent-core molecules. On the one hand, the model is only a very crude representation of what are undoubtedly very complex molecules. On the other hand, it does possess the essential molecular characteristics of bend, interactions, and "bumpiness;" with regard to this latter point, it is worth remembering that the aryl groups in a typical bent-core molecule are very bulky.

With regard to further work, we are currently carrying out simulations of closely related molecular models that possess true dipole moments and flexible tails. Of course, the dipolar interaction is likely to stabilize antiferroelectric phases [8], but the specific role of flexible tails in stabilizing or destabilizing tilted smectics is, as yet, uncertain. Tail groups are a common element in bent-core molecules, and so this is likely to be a fruitful avenue of research. The results of these studies will appear in future papers.

ACKNOWLEDGMENTS

This research was supported by the Engineering and Physical Sciences Research Council (GR/45727/01), through the provision of computer hardware, and a studentship to A. D. We are grateful to Dr. Matthew Glaser for useful correspondence.

[1] T. Niori, T. Sekine, J. Watanabe, T. Furukawa, and H. Takezoe, J. Mater. Chem. **7**, 1231 (1996).
[2] A. Jákli, S. Rauch, D. Lötzsch, and G. Heppke, Phys. Rev. E **57**, 6737 (1998).
[3] R. Macdonald, F. Kentischer, P. Warnick, and G. Heppke, Phys. Rev. Lett. **81**, 4408 (1998).
[4] P. J. Camp, M. P. Allen, and A. J. Masters, J. Chem. Phys. **111**, 9871 (1999).
[5] Y. Lansac, P. K. Maiti, N. A. Clark, and M. A. Glaser, Phys. Rev. E **67**, 011703 (2003).
[6] R. Memmer, Mol. Phys. **29**, 483 (2000).
[7] S. J. Johnston, R. J. Low, and M. P. Neal, Phys. Rev. E **65**, 051706 (2002).
[8] S. J. Johnston, R. J. Low, and M. P. Neal, Phys. Rev. E **66**, 061702 (2002).
[9] J. Xu, R. L. B. Selinger, J. V. Selinger, and R. Shashidhar, J. Chem. Phys. **115**, 4333 (2001).
[10] G. V. Paolini, G. Ciccotti, and M. Ferrario, Mol. Phys. **80**, 297 (1993).
[11] A. Galindo, C. Vega, E. Sanz, L. G. MacDowell, E. de Miguel, and F. J. Blas, J. Chem. Phys. **120**, 3957 (2003).
[12] M. P. Allen and D. J. Tildesley, *Computer Simulation of Liquids* (Clarendon, Oxford, 1987).
[13] M. Parrinello and A. Rahman, Phys. Rev. Lett. **45**, 1196 (1980).
[14] S. Yashonath and C. N. R. Rao, Mol. Phys. **54**, 245 (1985).
[15] H. Goldstein, *Classical Mechanics*, 2nd ed. (Addison-Wesley, London, 1980).
[16] *The Molecular Physics of Liquid Crystals*, edited by G. R. Luckhurst and G. W. Gray (Academic, New York, 1979).
[17] R. Eppenga and D. Frenkel, Mol. Phys. **52**, 1303 (1984).
[18] J. M. Polson and D. Frenkel, J. Chem. Phys. **109**, 318 (1998).
[19] S. Diele, S. Grande, H. Kruth, C. H. Lischka, G. Pelzl, W. Weissflog, and I. Wirth, Ferroelectrics **212**, 169 (1998).
[20] J. P. Bedel, J. C. Rouillon, J. P. Marcerou, M. Laguerre, M. F. Achard, and H. T. Nguyen, Liq. Cryst. **27**, 103 (2000).
[21] L. Vega, E. de Miguel, L. F. Rull, G. Jackson, and I. A. McLure, J. Chem. Phys. **96**, 2296 (1992).
[22] K. W. Wojciechowski, D. Frenkel, and A. C. Branka, Phys. Rev. Lett. **66**, 3168 (1993).
[23] P. G. de Gennes and J. Prost, *The Physics of Liquid Crystals*, 2nd ed. (Clarendon, Oxford, 1993).

Dipolar interactions, molecular flexibility, and flexoelectricity in bent-core liquid crystals

Alastair Dewar and Philip J. Camp*
School of Chemistry, The University of Edinburgh,
West Mains Road, Edinburgh EH9 3JJ, United Kingdom
(Dated: May 6, 2005)

The effects of dipolar interactions and molecular flexibility on the structure and phase behavior of bent-core molecular fluids are studied using Monte Carlo computer simulations. Some calculations of flexoelectric coefficients are also reported. The rigid cores of the model molecules consist of either five or seven soft spheres arranged in a 'V' shape with external bend angle γ. With purely repulsive sphere-sphere interactions and $\gamma = 0°$ (linear molecules) the seven-sphere model exhibits isotropic, uniaxial nematic, smectic-A, and tilted phases. With $\gamma \geq 20°$ the smectic-A phase disappears, while the system with $\gamma \geq 40°$ shows a direct tilted smectic–isotropic fluid transition. The addition of electrostatic interactions between transverse dipole moments on the apical spheres is generally seen to reduce the degree of tilt in the smectic and solid phases, destabilize the nematic and smectic-A phases of linear molecules, and destabilize the tilted smectic-B phase of bent-core molecules. The effects of adding three-segment flexible tails to the ends of five-sphere bent-core molecules are examined using configurational-bias Monte Carlo simulations. Only isotropic and smectic phases are observed. On the one hand, molecular flexibility gives rise to pronounced fluctuations in the smectic-layer structure, bringing the simulated system in better correspondence with real materials; on the other hand, the smectic phase shows almost no tilt. Lastly, the flexoelectric coefficients of various nematic phases – with and without attractive sphere-sphere interactions – are presented. The results are encouraging, but the computational effort required is a drawback associated with the use of fluctuation relations.

I. INTRODUCTION

There has been a surging interest in bent-core liquid crystals since their discovery in 1996[1]. Typically, these materials consist of molecules comprising rigid, banana-shaped cores made up of a conjugated system of linked aryl groups, and flexible alkyl or alkoxy tails attached to each end. The molecules are usually achiral and possess electric dipole moments parallel with the molecular C_2 axes. One of the most intriguing properties of these compounds is that, in some cases, chiral ferroelectric or antiferroelectric smectic phases can be observed[1,2,3]. The chirality arises because the molecules tilt within the smectic layers; in chiral (anti)ferroelectric phases all of the molecules tilt in the same sense with respect to the layer polarization vector. It is not yet clear what is responsible for this spontaneous symmetry-breaking process, although a variety of explanations has been proposed. One popular explanation involves the long-range dipole-dipole interaction[4], while recent theoretical work has identified a central role for dispersion interactions[5]. Other possible explanations include entropic 'free-volume' mechanisms[6] in which an antiferroelectric ordering of the smectic-layer polarizations affords more room for layer fluctuations, and mechanisms in which the molecules themselves spontaneously select chiral molecular conformations[7].

There is a growing simulation literature on bent-core liquid crystals. One of the most simple bent-core molecular models is a dimer made up of two hard spherocylinders[6,8]. This system exhibits isotropic, nematic, smectic, and crystalline phases, but no tilted phases. The Gay-Berne dimer model has been studied extensively, with and without molecular dipoles. In the works by Memmer[9] and Johnston *et al.*[10,11], isotropic, nematic, tilted smectic, and helical phases were found, depending on the molecular bend angle[9,10] and the magnitude of the dipole moment[11]. Xu *et al.* studied composite molecules made up of repulsive soft spheres, and found isotropic and tilted crystalline phases[12]. More recently, we have studied composite molecules made up of Lennard-Jones spheres – so called 'composite Lennard-Jones molecules' (CLJMs) – which exhibit isotropic, nematic, tilted smectic, and tilted crystalline phases[13].

In this work the effects of molecular dipole moments and molecular flexibility on the phase behavior of model bent-core molecules are studied using computer simulations. The model (to be detailed in Section II) consists of a rigid 'V'-shaped core of soft spheres with a point dipole moment oriented along the C_2 axis. Molecular flexibility is included by the addition of short flexible tails to either end. There is a substantial literature on the effects of these molecular characteristics on linear molecules. In hard-spherocylinder fluids, the addition of longitudinal molecular dipoles is seen to destabilize the nematic phase, and can even destabilize smectic phases if the dipoles are displaced toward the ends of the molecules[14,15]; transverse dipoles also destabilize the nematic phase with respect to the smectic A[16]. Gay-Berne ellipsoids with longitudinal point dipoles show a stabilization of the nematic phase with respect to the isotropic phase as the dipoles are moved from the centers of the molecules to the ends[17], and can exhibit antiferroelectric smectic phases with striped structures[18]. Tilted polar smectic phases have been reported in fluids of Gay-Berne molecules with transverse dipole moments[19]. As far as

molecular flexibility is concerned, the general consensus is that the introduction of flexible tail groups destabilizes the nematic phases of hard spherocylinders[20], fused hard-sphere chains[21,22], Gay-Berne[23], and soft-sphere chains[24]. Interestingly, the simultaneous presence of flexible tails and molecular dipole moments can lead to a stabilization of the nematic phase[25,26]. With regard to bent-core molecules, Johnston *et al.* have shown that the presence of transverse molecular dipoles on Gay-Berne dimers stabilizes the smectic phases at the expense of nematic phases, increases the tilt angle in tilted smectic phases, and can induce long-range polar ordering[11]. In the current work we will show that for the bent-core soft-sphere models considered, the additions of dipolar interactions and flexible tails both destabilize the nematic phase, and that the dipolar interactions reduce the degree of molecular tilt in smectic phases.

This paper also reports our attempts to measure the flexoelectric coefficients[27,28] of model bent-core molecules. There are relatively few accounts of such measurements in the literature. Experimentally, the determination of these quantities is highly non-trivial[29,30], mainly due to the fact that the flexoelectric coefficients are not measured directly, but rather in linear combinations or as ratios involving elastic constants. In simulations, the flexoelectric coefficients of pear-shaped Gay-Berne ellipsoid/Lennard-Jones sphere molecules have been measured directly using expressions involving the direct correlation function[31]. The coefficients for a similar model were studied in simulations using fluctuation expressions[32]. The compound 5CB has been studied using a parameterized dipolar Gay-Berne model and the Percus-Yevick closure of the Ornstein-Zernike equation[33,34]. The flexoelectric coefficients were computed using the direct correlation function route, and the results compared moderately well with experiment[29]. A very recent simulation study of PCH5 – using a fully atomistic molecular model – employed fluctuation formulae which yielded results in good agreement with experiment[35]. In the present work we critically assess the reliability of the fluctuation route in the context of our model systems, and show that the bend flexoelectric coefficients for non-polar molecules can be comparable to those measured in experiments, reflecting the significant role of molecular packing in dense liquids.

This paper is organized as follows. In Section II the molecular model to be studied is fully defined, and the required simulation methods are described. Simulation results for rigid linear molecules are presented in Section III A, and those for rigid bent-core molecules in Sections III B and III C. The effects of molecular flexibility are considered in Section III D, and flexoelectricity is discussed in Section III E. Section IV concludes the paper.

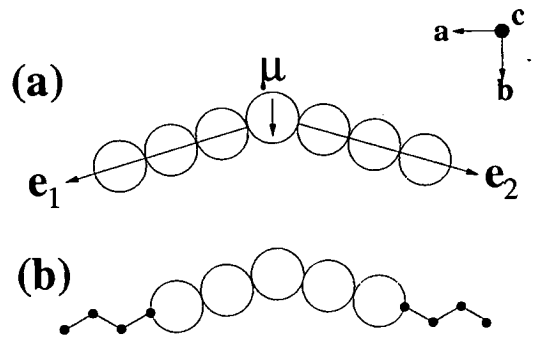

FIG. 1: The molecular models studied in this work: (a) the CSSM model; (b) the CSSMT model. Also shown are the molecular axes, **a**, **b**, and **c**.

II. MOLECULAR MODEL AND SIMULATION METHODS

The molecular models considered in this work are shown schematically in Fig. 1. The most basic model [Fig. 1(a)] consists of a rigid core of seven soft spheres arranged in a 'V' shape with external bond angle γ defined such that $\mathbf{e}_1 \cdot \mathbf{e}_2 = \cos(180° - \gamma)$, where $\mathbf{e}_1$ and $\mathbf{e}_2$ are unit vectors pointing along the two 'arms' of the molecule. The sphere-sphere interaction potential is taken to be the repulsive part of the Lennard-Jones (12,6), i.e.,

$$u_{ss}(r) = 4\epsilon \left(\frac{\sigma}{r}\right)^{12}, \qquad (1)$$

where r is the sphere-sphere separation, ϵ is an energy parameter, and σ is the sphere 'diameter'. In this work the intramolecular sphere-sphere bond length is set equal to 1σ. To identify the molecular axes that will be aligned in orientationally ordered phases, we define three unit vectors associated with the rigid cores of the molecules, as illustrated in Fig. 1. These vectors are given by $\mathbf{a} = (\mathbf{e}_1 - \mathbf{e}_2)/|\mathbf{e}_1 - \mathbf{e}_2|$, $\mathbf{b} = (\mathbf{e}_1 + \mathbf{e}_2)/|\mathbf{e}_1 + \mathbf{e}_2|$ and $\mathbf{c} = \mathbf{a} \wedge \mathbf{b}$.

Many real bent-core molecules possess a transverse electric dipole moment aligned along the C_2 molecular symmetry axis. To represent dipole-dipole interactions we have considered the model represented in Fig. 1(a), where a point dipole moment is placed at the center of the apical sphere along the C_2 symmetry axis (**b**). The dipole-dipole interaction is,

$$u_{dd}(\mathbf{r}, \boldsymbol{\mu}_1, \boldsymbol{\mu}_2) = \frac{\boldsymbol{\mu}_1 \cdot \boldsymbol{\mu}_2}{r^3} - \frac{3(\boldsymbol{\mu}_1 \cdot \mathbf{r})(\boldsymbol{\mu}_2 \cdot \mathbf{r})}{r^5}, \qquad (2)$$

where $\mathbf{r}$ is the pair separation vector, $r = |\mathbf{r}|$, and $\boldsymbol{\mu}_i = \mu \mathbf{b}_i$ is the dipole vector on particle i. For brevity, we shall refer to these molecules as 'composite soft-sphere molecules' (CSSMs).

Common additional features of real bent-core molecules include alkyl or alkoxy chains (typically 3-12 carbons in length) attached to both ends of each

molecule. To represent these tails we consider the addition of four extra spheres at each end of the model molecules, as represented in Fig. 1(b). The resulting tail segments are allowed to pivot under the following constraints: the tail bond length is equal to 0.6σ, which corresponds to the ratio of the carbon-carbon bond length to the diameter of the aromatic ring in real bent-core liquid crystals; each tail segment is oriented at the tetrahedral angle, $\cos^{-1}(-\frac{1}{3}) = 109.47°$, with respect to its neighboring segments, mimicking the bond angles in a simple hydrocarbon tail. Clearly this extension will cause a considerable increase in the number of interactions to be evaluated, so to make the simulations tractable we have made the following simplifications. Firstly, we have reduced the size of the rigid bent-core to five spheres. (With the addition of the tail segments, this actually makes the effective elongations for all of the models considered more comparable.) Secondly, we neglect interactions between tails on different molecules. Within the Lorentz-Berthelot mixing rules[36], this corresponds to setting the tail-sphere diameter to zero. Denoting the core and tail spheres by 'c' and 't', respectively, the interaction potential is,

$$u_{ss}^{ij}(r) = 4\epsilon\left(\frac{\sigma_{ij}}{r}\right)^{12}, \qquad (3)$$

with i,j = c or t, $\sigma_{cc} = \sigma$, $\sigma_{tt} = 0$, $\sigma_{ct} = \frac{1}{2}(\sigma_{cc} + \sigma_{tt}) = \frac{1}{2}\sigma$, and for simplicity the energy parameter ϵ is the same for all pairs. This is clearly a very crude representation of molecular flexibility, but it has proven to be an appropriate means of extending the range of applicability of simple liquid-crystal models[20,25]. Even though this is a simple model, configurational-bias MC techniques are required to simulate the system efficiently; these are summarized in Section II A. For brevity, we shall refer to these molecules as 'composite soft-sphere molecules with tails' (CSSMTs).

Reduced units for these systems are defined as follows: reduced molecular density, $\rho^* = N_m\sigma^3/V$, where N_m is the number of molecules and V is the system volume; reduced temperature, $T^* = k_BT/\epsilon$; reduced pressure, $p^* = p\sigma^3/\epsilon$; reduced dipole moment, $\mu^* = \sqrt{\mu^2/\epsilon\sigma^3}$.

A. Monte Carlo

The phase behavior of the model systems was investigated using constant-pressure (NPT) and constant-volume (NVT) Metropolis MC simulations[36]. In all of the simulations reported in this work, the number of molecules was $N_m = 400$, with initial high-density crystalline configurations consisting of four layers of 100 molecules. The general approach was to equilibrate the system at low temperature ($T^* \sim 1$) and high density ($\rho^* \sim 0.14$) using NVT simulations in a cuboidal simulation cell with dimensions $L_x = L_y \neq L_z$ and volume $V = L_xL_yL_z$, and then switching over to NPT simulations at a fixed pressure of $p^* = 4$; earlier work indicated that all of the expected liquid-crystalline phases could be stabilized in a CLJM system at this pressure[13]. Simulations along the isobar were carried out at progressively higher temperatures in order to locate phase transitions between solid, smectic, nematic and isotropic phases; transitions were identified by measuring the equation of state (density as a function of temperature) and relevant order parameters (detailed below). Cooling runs were carried out using cuboidal and/or cubic simulation cells to confirm the existence and nature of the transitions. As explained in Ref. 13, spot checks on the stress tensor showed that the cuboidal/cubic cells did not mechanically destabilize liquid-crystalline phases.

For the CSSM system, straightforward simulation techniques were employed as detailed in earlier work[13]; single-particle translation and rotation moves, and volume moves (in $\ln V$), were generated with respective maximum displacement parameters to achieve $\sim 50\%$ acceptance rates. The long-range dipolar interactions were handled using Ewald summations with conducting ('tin-foil') boundary conditions[36].

For the CSSMT system the CBMC technique was implemented and optimized as described in Refs. 37,38. Tail conformations were sampled by generating 5 trial orientations per segment per MC move. Translational and rotational displacement parameters were adjusted to give an acceptance ratio of 10%; in NPT simulations the volume moves were adjusted to give a 50% acceptance ratio. The computational effort required to simulate this system was considerable. To carry out a MC sweep consisting of one attempted translation and rotation per molecule, and one volume move, took approximately 4 seconds on a 2.2 GHz Intel Xeon processor; to achieve equilibration at each state point required at least 10^5 MC sweeps

To monitor orientational order, the order tensors $\mathbf{Q}_{\alpha\alpha} = \frac{1}{2}\sum_{i=1}^{N}(3\alpha\alpha - 1)$ for each of the molecular axes $\boldsymbol{\alpha} = \mathbf{a}$, $\mathbf{b}$, and $\mathbf{c}$ were diagonalized yielding the eigenvalues $\lambda_\alpha^- < \lambda_\alpha^0 < \lambda_\alpha^+$, and the corresponding orthonormal eigenvectors, $\mathbf{n}_\alpha^-$, $\mathbf{n}_\alpha^0$, and $\mathbf{n}_\alpha^+$[39]. The molecular x, y, and z axes were then assigned in order of increasing λ_α^+, and the laboratory axes, $\mathbf{X}$, $\mathbf{Y}$, and $\mathbf{Z}$, were identified with the corresponding directors. In practice this almost invariably meant that the molecular z axis was the 'long' axis $\mathbf{a}$ and the x and y axes were $\mathbf{b}$ and $\mathbf{c}$, and that the laboratory z axis was $\mathbf{n}_a^+$. The usual nematic and biaxial order parameters – S and Q_{22}^2 - are then given by,

$$S = \mathbf{Z}\cdot\mathbf{Q}_{zz}\cdot\mathbf{Z}, \qquad (4)$$

$$Q_{22}^2 = \tfrac{1}{3}(\mathbf{X}\cdot\mathbf{Q}_{xx}\cdot\mathbf{X} + \mathbf{Y}\cdot\mathbf{Q}_{yy}\cdot\mathbf{Y} - \mathbf{X}\cdot\mathbf{Q}_{yy}\cdot\mathbf{X} - \mathbf{Y}\cdot\mathbf{Q}_{xx}\cdot\mathbf{Y}). \qquad (5)$$

In a perfect uniaxial nematic phase, $S = 1$ and $Q_{22}^2 = 0$, whereas in a perfect biaxial phase, $S = 1$ and $Q_{22}^2 = 1$. In practice no biaxial ordering was detected in any of the simulations, and so we will not report the numerical values of Q_{22}^2 (which are less than ~ 0.1). Some additional measured observables include the polarization, $\mathbf{P} = \mu\sum_i \mathbf{b}_i$, and the intermolecular torque-density tensor, $\mathbf{\Pi}$. In particular, these quantities are required for

the calculation of flexoelectric coefficients, full details of which will be given in Section III E.

III. RESULTS

A. CSSMs with $\gamma = 0°$

The equation of state and order parameters for apolar ($\mu^* = 0$) linear CSSMs along an isobar with $p^* = 4$ are shown in Figs. 2(a) and 2(b), respectively. In order of increasing temperature we find a high-density tilted phase ($0.5 \leq T^* \leq 1.5$), a smectic A ($2.0 \leq T^* \leq 2.5$), a uniaxial nematic ($2.75 \leq T^* \leq 4$), and ultimately the isotropic phase ($T^* \geq 4.5$). Simulation snapshots are shown in Fig. 3. In the tilted phase, the molecules are arranged in layers tilted by about 60° with respect to each other, as shown in Fig. 3(a). This 'herringbone' structure clearly allows close-packing of the constituent spheres. It is difficult to resolve the molecules in to layers unambiguously, but it is quite clear from examining simulation snapshots that there is no long-range crystalline order. In the absence of such order we therefore classify this phase as tilted smectic B, if only to indicate that it is not crystalline[28]. We found no stable crystalline phase at $T^* \geq 0.5$. Referring to Fig. 2(b), the jump in nematic order parameter in the temperature range $1.5 < T^* < 2.0$ is due to the transition from the tilted smectic-B phase to the untilted smectic-A phase; the drop in the range $4 < T^* < 4.5$ signals the smectic A-nematic transition. In all, the results for this system are in good qualitative correspondence with those for a whole host of similar (linear) molecular models, including soft-sphere chains[40], and Lennard-Jones chains[41]. The results are also comparable to those presented in Ref. 13 for seven-sphere CLJM fluids in which the sphere-sphere interaction is given by $4\epsilon[(\sigma/r)^{12} - (\sigma/r)^6]$. Qualitatively, the CSSM and CLJM systems are very similar, but in the latter case the phase transitions are shifted to higher temperatures due to the attractive component of the interaction potential.

With the addition of a small molecular dipole ($\mu^* = 1$) we see little qualitative difference in the equation of state at $p^* = 4$, as shown in Fig. 2(c). Despite the small change in the equation of state, the gross structure of the tilted smectic-B phase is quite different from that in the apolar system. The low-temperature smectic-B phase is not so strongly tilted as in the apolar system, exhibiting a tilt angle with respect to the layer normal of $\sim 20°$. This is most likely to allow dipoles on neighboring molecules to attain the low-energy 'nose-to-tail' conformation within the plane of the layer. The nematic order parameter – shown in Fig. 2(d) – is relatively high at temperatures $T^* \leq 1.5$ due to the reduced degree of tilt. The tilted smectic B-smectic A and smectic A-nematic transitions are signaled by changes in S at $1.5 < T^* < 2$ and $4 < T^* < 4.5$, respectively.

With a large dipole moment ($\mu^* = 2$) and $p^* = 4$ we see some dramatic differences in the phase behavior: the

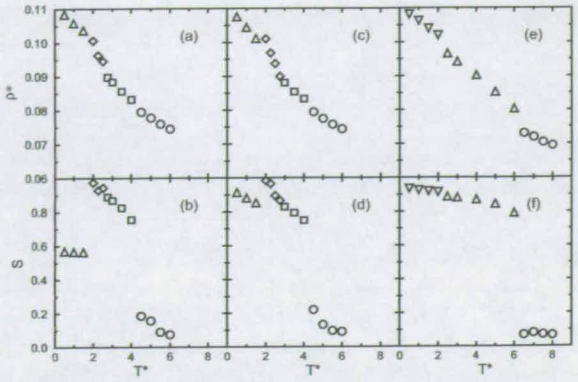

FIG. 2: Equations of state [(a),(c),(e)] and order parameters [(b),(d),(f)] for CSSM systems with $\gamma = 0°$ along an isobar with $p^* = 4$: (a),(b) $\mu^* = 0$; (c),(d) $\mu^* = 1$; (e)m(f) $\mu^* = 2$. The symbols denote different phases: solid (down triangles); tilted smectic B (up triangles); smectic A (diamonds); nematic (squares); isotropic (circles).

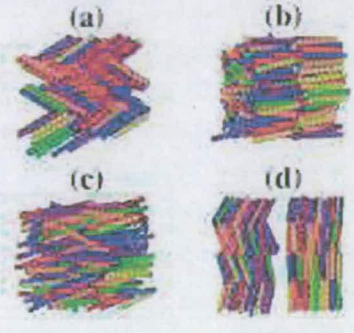

FIG. 3: Simulation snapshots of the CSSM system with $\gamma = 0°$ (linear molecules) along an isobar with $p^* = 4$: (a) tilted smectic-B ($\mu^* = 0$, $T^* = 2$); (b) smectic-A ($\mu^* = 0$, $T^* = 2.5$); (c) nematic ($\mu^* = 0$, $T^* = 4$); (d) tilted smectic-B ($\mu^* = 1$, $T^* = 2$).

nematic and smectic-A phases are completely absent, and there is instead a distinct transition between two high-density layered phases in the range $2 \leq T^* \leq 2.5$. Simulation snapshots at temperatures of $T^* = 2$ and $T^* = 4$ are shown in Fig. 4. Examination of the layers [Fig. 4(c) and 4(d)] shows that at $T^* \leq 2$ the system is in a crystalline phase, with apparently long-range positional order within the layers. At $T^* = 4$ the in-layer ordering is qualitatively different, showing short-range positional correlations and defects that destroy long-range positional order. The equation of state and nematic order parameter are shown in Figs. 2(e) and 2(f). We assign the branches in the equation of state as corresponding to crystalline ($0.5 \leq T^* \leq 2.0$), tilted smectic-B ($2.5 \leq T^* \leq 6.0$), and isotropic ($T^* \geq 6.5$) phases.

To summarize, the addition of dipolar interactions to linear seven-sphere molecules leads to a reduction in the degree of tilt in the low-temperature smectic-B phase. With high dipole moments, the smectic-A and nematic phases disappear, and a solid-smectic B transition is

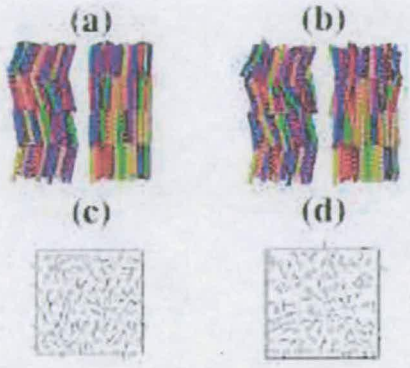

FIG. 4: Simulation snapshots of the CSSM system with $\gamma = 0°$ and $\mu^* = 2$: (a) crystalline phase ($T^* = 2$); (b) tilted smectic-B phase ($T^* = 4$); (c) a typical layer in the crystalline phase ($T^* = 2$); a typical layer in the tilted smectic-B phase ($T^* = 4$). In (c) and (d) the short black lines indicate the orientations of the molecular dipole moments.

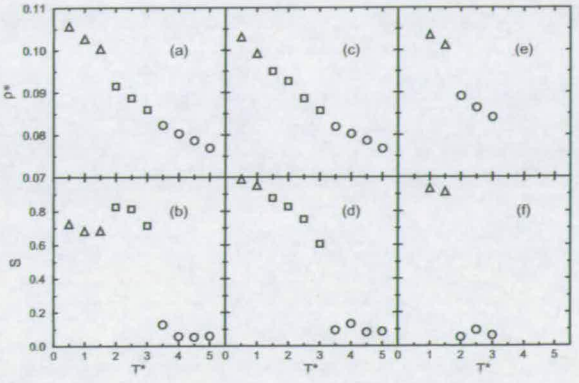

FIG. 5: Equations of state [(a),(c),(e)] and order parameters [(b),(d),(f)] for CSSM systems with $\gamma = 20°$ and $\gamma = 40°$ along an isobar with $p^* = 4$: (a),(b) $\gamma = 20°$ and $\mu^* = 0$; (c),(d) $\gamma = 20°$ and $\mu^* = 1$; (e),(f) $\gamma = 40°$ and $\mu^* = 0$. The symbols denote different phases: tilted smectic B (up triangles); nematic (squares); isotropic (circles).

shifted in to the range of temperatures considered in this work.

B. CSSMs with $\gamma = 20°$

The equations of state and nematic order parameters for CSSM systems with $\gamma = 20°$ along an isobar with $p^* = 4$ are shown in Fig. 5. Results are shown for two dipole moments, $\mu^* = 0$ [Figs. 5(a) and 5(b)] and $\mu^* = 1$ [Figs. 5(c) and 5(d)]. Both the apolar and polar systems exhibit tilted smectic-B, nematic, and isotropic phases; examples of the smectic and nematic phases in the $\mu^* = 0$ system are illustrated in Fig. 6. In the smectic-B phases it was observed that the degree of molecular tilt with respect to the layer normal is far greater in the apolar case ($\sim 53°$) than in the polar case ($< 20°$). The smectic B-nematic phase transition appears to be more pronounced in the apolar system than in the polar system, as evidenced by the associated features in the equations of state and in the variations of the nematic order parameters. Some simulations were attempted with $\mu^* = 2$ but these suffered from convergence problems; simulations with different initial configurations failed to converge on to the same branch of the equation of state. It is possible that this was due to the combination of the steric dipole (molecular bend) and the 'electric' dipole resulting in strong anisotropic interactions and prohibitively slow convergence.

A comparison of Figs. 2 and 5 shows that the presence of a modest molecular bend leads to the smectic-A phase being destabilized. This same trend was observed in simulations of the CLJM system[13]. The introduction of dipolar interactions to the bent-core model then seems to stabilize the nematic phase slightly in favor of the smectic B. The smectic-B phases themselves are tilted, but the degree of tilt is reduced significantly upon the addition of dipolar interactions. This perhaps provides

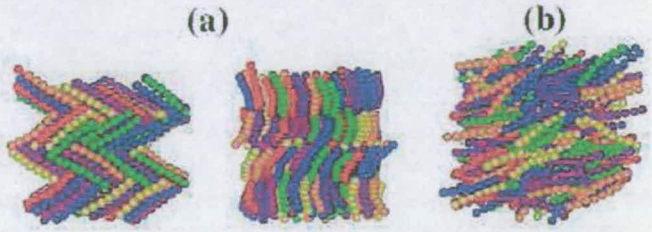

FIG. 6: Simulation snapshots of the CSSM system with $\gamma = 20°$ along an isobar with $p^* = 4$: (a) two views of the tilted smectic B phase at $T^* = 1$; (b) nematic phase at $T^* = 3$.

a clue as to why dipolar interactions apparently disfavor the smectic B; the bent-cores want to form a tilted phase, but the dipolar interactions want an untilted phase as explained in Section III A.

C. CSSMs with $\gamma = 40°$

The convergence problems encountered with the $\gamma = 20°$ system were exacerbated by an increase of the bend angle to $\gamma = 40°$. In this case it was only possible to achieve reliable results for the apolar system. Results at $\mu^* = 0$ and $p^* = 4$ are shown in Fig. 5(e) and 5(f). The equation of state and order parameters show only two branches, which correspond to tilted smectic-B and isotropic phases. This is very similar to the situation in the CLJM system with the same bend angle[13], albeit with the CSSM system undergoing a phase transition at lower temperature.

D. CSSMTs

We performed NPT simulations of CSSMT systems with bend angles of $\gamma = 0°$, $20°$, and $40°$ along an iso-

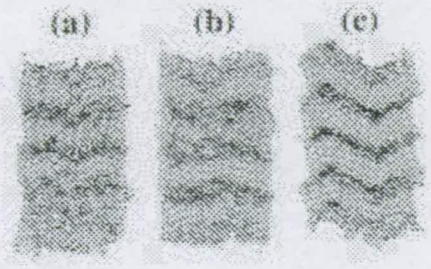

FIG. 7: Simulation snapshots of CSSMT systems at $T^* = 1$ and $p^* = 4$: (a) $\gamma = 0°$; (b) $\gamma = 20°$; (c) $\gamma = 40°$.

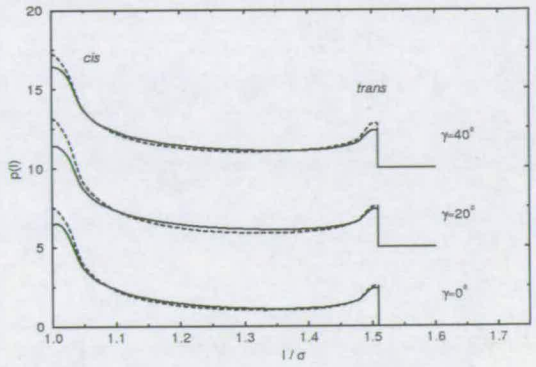

FIG. 8: Tail-length distribution functions for the terminal four-center tails in CSSMT systems along an isobar with $p^* = 1.0$: (bottom) $\gamma = 0°$; (middle) $\gamma = 20°$; (top) $\gamma = 40°$. The curves for each bond angle are displaced by 10 units along the ordinate for clarity. In each case the solid lines correspond to $T^* = 1$ and the dashed lines to $T^* = 3$. With bond lengths of 0.6σ the pure *cis* conformation corresponds to $l = (5/3) \times 0.6\sigma = \sigma$, and the pure *trans* conformation to $l = \sqrt{19/3} \times 0.6\sigma \simeq 1.51\sigma$.

bar with $p^* = 4$. Due to the computational effort required for these simulations we were not able to map out equations of state as comprehensive as those for the CSSM systems. The simulation results are presented in Table I. The only phases observed in our simulations were smectic and isotropic. In all cases the smectics were stable at $T^* \leq 1.5$, and the smectic-isotropic transition occurred in the range $1.5 \leq T^* \leq 2$. Some simulation snapshots of the smectic phases are shown in Fig. 7. In all cases the translational ordering within the layers was of the smectic-B type, i.e., local hexagonal coordination. The systems with $\gamma = 0°$ and $\gamma = 20°$ showed no appreciable molecular tilt within the smectic layers, while the $\gamma = 40°$ system showed an unusual 'grain-boundary' structure between clearly demarcated domains of untilted smectic. Larger-scale simulations will be required to determine whether this is a signal of a long-wavelength modulated structure. It is particularly striking that the smectic-layer fluctuations are much larger than those in the CSSM (and CLJM[13]) systems. Indeed, one criticism of the latter models – and other rigid-rod models – is that the smectics are too well ordered. Unsurprisingly, the introduction of molecular flexibility has improved the correspondence between simulated smectic structures, and those inferred from light-scattering experiments on common (flexible or semiflexible) mesogens[28].

The conformations of the flexible tail groups were investigated using some simple measures. The extension of each tail was identified with the distance, l, between the first and fourth joint (the black spheres in Fig. 1). The probability density function, $p(l)$, is shown in Fig. 8 for all of the CSSMT systems at $T^* = 1$ (smectic B) and $T^* = 3$ (isotropic). Each function shows peaks at $l/\sigma = 1$ and $l/\sigma \simeq 1.5$. For a perfect *cis* conformation the tail extension is (5/3) times the bond length, while for the *trans* conformation it is $\sqrt{19/3}$ times the bond length. With the bond length being 0.6σ, these distances correspond to $l/\sigma = 1$ and $l/\sigma \simeq 1.51$, respectively. Firstly, the *cis* conformation is clearly the more favorable, presumably because the molecules strive to attain the shortest effective elongation to minimize excluded-volume interactions. Interestingly, for each system the *cis* conformation appears slightly more favorable in the isotropic phase than in the smectic phase. This may be due to the opportunity for interdigitation of the tails with the cores in neighboring smectic layers, which would explain the accompanying increase in the occurrence of the *trans* conformation.

The effective molecular bend angle was determined by calculating the dot product of the two unit vectors linking the apical sphere to the terminal tail units, $\mathbf{u}_1$ and $\mathbf{u}_2$; the required angle is then $\gamma_{\text{eff}} = \cos^{-1}(-\mathbf{u}_1 \cdot \mathbf{u}_2)$. Values of γ_{eff} are reported in Table I. For each system $\gamma_{\text{eff}} > \gamma$ which shows that the tails must curl up in such a way as to make the molecule more banana shaped. In the smectic phases this can be observed directly in Fig. 7, where the tails prefer to be oriented in the plane of the smectic layers, rather than pointing straight down toward the neighboring layers. This idea is confirmed by the fact that the effective molecular bend is more pronounced in the smectic phase than in the isotropic phase.

In summary, the addition of molecular flexibility results in the disappearance of the nematic phase, and in the case of the linear molecules, the smectic-A phase as well. This is in good qualitative agreement with the trends observed in a variety of other liquid-crystal models[20,21,22,23,24,26]. The smectic-layer structures of the flexible model systems correspond more closely to those in real smectic liquid crystals.

E. Flexoelectric coefficients

In 1969 Meyer predicted the existence of what is now known as the *flexoelectric effect* in nematic liquid crystals, in which long-wavelength distortions of the local molecular alignment (director field, $\mathbf{n}$) give rise to a bulk polarization, $\mathbf{P}$[27]. The textbook explanation of the effect is that if the director field possesses curvature then an

TABLE I: Results from NPT simulations of the CSSMT system along an isobar with $p^* = 4$. Digits in brackets denote the estimated statistical uncertainty in the last figure.

γ / degrees	T^*	ρ^*	S	l/σ	$\gamma_{\rm eff}$ / degrees
0	1.0	0.1098(4)	0.918	5.48(1)	48.0(3)
0	1.5	0.1018(4)	0.725	5.82(1)	29.6(2)
0	2.0	0.1067(7)	0.091	5.40(3)	31.8(3)
0	2.5	0.1019(7)	0.097	5.45(3)	32.3(3)
0	3.0	0.0981(7)	0.063	5.44(2)	32.5(3)
20	1.0	0.1128(2)	0.865	5.41(1)	50.9(4)
20	1.5	0.1101(2)	0.787	5.51(1)	43.3(2)
20	2.0	0.1057(7)	0.200	5.35(3)	37.0(5)
20	2.5	0.1010(3)	0.062	5.34(3)	37.4(4)
20	3.0	0.0976(7)	0.054	5.34(2)	37.6(4)
40	1.0	0.1161(3)	0.879	4.98(1)	65.2(4)
40	1.5	0.1084(1)	0.833	4.93(1)	60.7(2)
40	2.0	0.1048(6)	0.067	5.08(3)	49.5(3)
40	2.5	0.1008(6)	0.081	5.10(2)	49.2(6)
40	3.0	0.0974(7)	0.057	5.11(2)	49.4(5)

asymmetric molecular shape can dictate a favorable local packing arrangement which, in the presence of molecular dipoles, may give rise to a polarization[28]. With a splay deformation ($\nabla \cdot \mathbf{n} \neq 0$) wedge-shaped molecules with longitudinal dipole moments pack most efficiently when the dipoles are aligned. With a bend deformation ($|\nabla \wedge \mathbf{n}| \neq 0$) banana-shaped molecules with transverse dipole moments are arranged preferentially to give a net polarization. General symmetry arguments lead to the following relationship between the polarization density, $\mathbf{p} = V^{-1}\mathbf{P}$ (units C m^{-2}), and the lowest order deformations of the director field,

$$\mathbf{p} = e_1(\nabla \cdot \mathbf{n})\mathbf{n} + e_3(\nabla \wedge \mathbf{n}) \wedge \mathbf{n}. \qquad (6)$$

where e_1 and e_3 are the splay and bend flexoelectric coefficients, respectively, with units of C m^{-1}. Historically there is some ambiguity in the sign of e_3; to be clear, throughout this work we employ the convention used by Meyer in his original study[27], Nemtsov and Osipov in their analysis of flexoelectricity in the context of linear-response theory[42], and de Gennes and Prost in their canonical text[28]. Allen and Masters have supplied a comprehensive account of various simulation methods for measuring the flexoelectric coefficients[43]. Following the sign conventions in Ref. 43 we have calculated e_1 and e_3 using the relationships,

$$e_1 = \tfrac{1}{2}\beta V^{-1}\left(\langle P_z\Pi_{xy}\rangle - \langle P_z\Pi_{yx}\rangle\right), \qquad (7)$$

$$e_3 = \tfrac{1}{2}\beta V^{-1}\left(\langle P_y\Pi_{zx}\rangle - \langle P_x\Pi_{zy}\rangle\right). \qquad (8)$$

where $\mathbf{\Pi} = -\sum_{i<j}\mathbf{r}_{ij}\boldsymbol{\tau}_{ij}$ is the orientational stress density tensor, $\mathbf{r}_{ij} = \mathbf{r}_i - \mathbf{r}_j$ is the intermolecular separation vector, and $\boldsymbol{\tau}_{ij}$ is the torque on molecule i due to molecule j. $\boldsymbol{\tau}_{ij}$ was calculated as a sum of moments of the sphere-sphere interactions about the apical sphere, and all vectors and tensors were calculated in a frame in which the laboratory z axis coincides with the nematic director, $\mathbf{n}_a^+$. It is easy to show that the combinations $(P_z\Pi_{xy} - P_z\Pi_{yx})$ and $(P_y\Pi_{zx} - P_x\Pi_{zy})$ are invariant with respect to a rotation of the x and y axes about $\mathbf{n}$, and so the assignments of the x and y axes are arbitrary. It should be noted that we have only calculated the flexoelectric coefficients for non-polar systems. The 'steric dipole' is still parallel to $\mathbf{b}$ in Fig. 1, but there are no *electrostatic* dipole-dipole interactions. The polarization is given by $\mathbf{P} = \mu\sum_{i=1}^{N_m}\mathbf{b}_i$, and carries the trivial factor of μ by virtue of there being no electrostatic interactions.

The flexoelectric coefficients have been calculated in the nematic phases of non-polar CSSM and CLJM[13] systems as a function of the molecular bend angle, γ. For the purposes of comparison, the CSSM system has been studied at a fixed density and temperature for which the nematic phase is stable at several values of γ. An examination of Figs. 2(a) and 5(a) shows that in the range $0° \leq \gamma \leq 20°$, the nematic phase is stable at temperatures and densities in the regions of $T^* \sim 3$ and $\rho^* \sim 0.085$, respectively. A particular state point from the $\gamma = 0°$ system was selected arbitrarily for all of the simulations, this being $T^* = 3$ and $\rho^* = 0.0888$. Canonical (NVT) simulations were used to equilibrate nematic phases for systems with bend angles in the range $0° \leq \gamma \leq 25°$. The nematic order parameter, S, is shown as a function of γ in Fig. 9(a). We found that S could be fitted with a power law,

$$S(\gamma) = S(0)\left(1 - \frac{\gamma}{\gamma_c}\right)^{\alpha}, \qquad (9)$$

where $S(0)$ is the order parameter for linear molecules, γ_c is a critical bend angle above which the nematic phase is no longer thermodynamically stable, and α is a specific exponent. The fit is shown in Fig. 9(a); the fit parameters were $S(0) = 0.881(4)$, $\gamma_c = 25.6(2)°$, and $\alpha = 0.104(7)$. A similar procedure was carried out for the CLJM system studied in Ref. 13. Nematic phases were simulated at

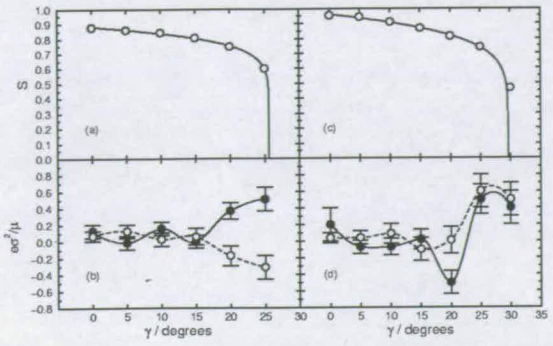

FIG. 9: Nematic order parameters [(a) and (c)] and flexoelectric coefficients [(b) and (d)] for the CSSM system at $\rho^* = 0.0888$ and $T^* = 3$ [(a) and (b)] and the CLJM system at $\rho^* = 0.1155$ and $T^* = 6.5$ [(c) and (d)]. In (b) and (d) the flexoelectric coefficients are those corresponding to splay deformations (filled symbols) and bend deformations (open symbols). The lines are spline fits to guide the eye.

$T^* = 6.5$ and $\rho^* = 0.1155$ for systems with $0° \leq \gamma \leq 30°$. The nematic order parameter is shown as a function of γ in Fig. 9(c). A power-law fit yielded the parameters $S(0) = 0.961(4)$, $\gamma_c = 29.6(1)°$, and $\alpha = 0.143(4)$; the fit is shown in Fig. 9(c).

Equations (7) and (8) were evaluated using results from immense NVT-MC simulations. In general we carried out runs consisting of $\sim 4 \times 10^6$ attempted MC translations and rotations per molecule. In all cases the components of $\mathbf{P}$ fluctuated about zero, but long runs were required to ensure that the average polarization, $\langle \mathbf{P} \rangle$, was almost zero. Results for the reduced flexoelectric coefficients $e_1^* = e_1\sigma^2/\mu$ and $e_3^* = e_3\sigma^2/\mu$ in the CSSM and CLJM systems are presented in Table II and Fig. 9. Also included in Table II are the components of the average polarization, $\mathbf{P}$, and estimated uncertainties. In both the CSSM and CLJM systems, the measured flexoelectric coefficients are small when the molecular bend angles are less than about 20°. For more pronounced bend angles, both the splay and the bend coefficients deviate significantly from zero. The results for e_3^* are encouraging, but there is some concern over the measured values of e_1^*; naively we would expect that the splay coefficients should be small for banana-shaped molecules with transverse dipoles. Table II yields a valuable clue; the measured flexoelectric coefficients deviate significantly from zero in those simulations where there is a more pronounced average polarization. Therefore, it may be that the simulations are still not long enough to ensure a reliable evaluation of the fluctuation formulae. It is perhaps worth pointing out that during the course of the atomistic simulations performed by Cheung *et al.* there was a 'small net polarization'[35]: the magnitudes of the average polarizations ($P \sim 10^{-28}$ C m^{-1}) and the average molecular dipole moments ($\mu \sim 10^{-29}$ C m^{-1}) give reduced polarizations $P/\mu \sim 10$, which are large compared to the average polarizations reported in Table II. It is possible that neither the estimates of Cheung *et al.* nor the current estimates are particularly reliable. We attempted to make *ad hoc* corrections to the fluctuation formulae in Eqns. (7) and (8) by evaluating terms like $\langle (P_\alpha - \langle P_\alpha \rangle)(\Pi_{\beta\gamma} - \langle \Pi_{\beta\gamma} \rangle) \rangle$, but these resulted in insignificant changes to the values of e_1 and e_3.

Notwithstanding the potential problems highlighted above, we can attempt to make some useful comments on the measured values of e_3. At the highest bend angles, $\gamma = 20°$-$30°$, the magnitude of the reduced bend flexoelectric coefficient is in the region of 0.5. With typical values of $\sigma \sim 0.5$ nm and $\mu \sim 1$ Debye, this reduced value corresponds to a real bend flexoelectric coefficient of $e_3 \sim 7$ pC m^{-1}. This is in good agreement with typical values of $e_3 \sim 10$ pC m^{-1} measured in experiments[29,30]. It is therefore reasonable to suggest that the steric or packing contributions to the flexoelectric effect are significant. The roles of dipolar and quadrupolar electrostatic interactions must surely be at least as significant, and these should be studied in a systematic fashion. For now, though, we conclude that short-range interactions between bent-core molecules are as important in giving rise to flexoelectricity as they are in dictating the short-range structure of dense atomic liquids[44]. In drawing this analogy perhaps we should not be too surprised by the current observations. The reduced densities of spheres in the CSSM and CLJM systems are equal to $7\rho^* \sim 0.7$ at which packing effects and short-range correlations are particularly pronounced (recall that the triple-point density for the Lennard-Jones system is in the region of 0.85).

IV. CONCLUSIONS

In this work the structure, phase behavior, and flexoelectricity of model bent-core molecules have been studied using MC computer simulations. The molecular bent core consists of a 'V' shaped rigid array of soft spheres, with a transverse point dipole moment aligned along the C_2 symmetry axis.

In a linear seven-sphere non-polar model, isotropic, nematic, smectic-A, and tilted smectic-B (herringbone) phases are observed. With an opening angle of 160° the smectic A is absent, while an opening angle of 140° gives rise to a direct tilted smectic B – isotropic transition. The effects of dipolar interactions were seen to depend on the opening angle. In the linear-molecule systems these interactions appeared to destabilize the nematic and smectic-A phases. In the bent-core systems, dipolar interactions reduced the degree of molecular tilt in the tilted smectic phases; this is a significant observation, particularly since dipolar interactions have often been cited as the cause of spontaneous chiral symmetry breaking in some bent-core liquid crystals[4]. Chirality arises in this case from the correlation between molecular tilt within smectic layers and the long-range ordering of smectic-layer polarizations. Although spontaneous (anti)ferroelectric order will be favored by long-range dipolar interactions, the

TABLE II: Results from NVT simulations of CSSM and CLJM systems in the nematic phase at reduced density ρ^* and reduced temperature T^*. γ is the molecular bend angle, S is the nematic order parameter, $e_1^* = e_1\sigma^2/\mu$ and $e_3^* = \sigma^2/\mu$ are the reduced splay and bend flexoelectric coefficients, respectively, and P_α is the average of the α component of the system polarization. Digits in brackets denote the estimated statistical uncertainty in the last figure based on two standard deviations.

γ / degrees	S	e_1^*	e_3^*	P_x/μ	P_y/μ	P_z/μ
CSSM, $T^* = 3$, $\rho^* = 0.0888$						
0	0.877	0.13(4)	0.07(3)	−0.21(4)	0.77(6)	1.43(2)
5	0.861	−0.01(4)	0.13(4)	−0.31(6)	−0.38(6)	0.02(2)
10	0.844	0.16(4)	0.03(4)	0.27(6)	−0.38(6)	−0.10(2)
15	0.807	−0.00(4)	0.06(5)	0.90(6)	−1.04(6)	0.56(2)
20	0.749	0.37(5)	−0.17(6)	0.09(6)	−0.55(6)	0.67(4)
25	0.601	0.51(7)	−0.31(7)	−1.10(6)	1.00(6)	−0.75(4)
CLJM, $T^* = 6.5$, $\rho^* = 0.1155$						
0	0.954	0.2(1)	0.04(3)	−0.13(6)	−0.78(6)	−0.13(4)
5	0.943	−0.07(4)	0.04(4)	0.09(6)	−0.42(6)	0.13(2)
10	0.909	−0.07(5)	0.09(6)	−0.29(6)	−0.17(6)	0.06(2)
15	0.867	0.02(6)	−0.10(7)	−0.18(6)	−1.06(6)	0.10(2)
20	0.813	−0.50(7)	0.01(8)	−2.03(6)	−0.04(6)	0.16(2)
25	0.739	0.50(9)	0.6(1)	2.41(6)	0.53(6)	−0.72(2)
30	0.466	0.40(1)	0.5(1)	−1.04(6)	2.93(6)	0.56(4)

observation that these same interactions reduce molecular tilt seems to suggest that there may be another explanation for chirality in banana liquid crystals[5,6,7].

Real bent-core liquid crystals often possess flexible tail groups at the ends of the rigid bent core, and so CBMC simulations of a flexible-rigid-flexible model were performed. Each molecule consisted of a five-sphere rigid bent core, and a three-segment flexible tail attached to each end. We could only find smectic and isotropic phases, but significantly the smectic phases showed no spontaneous tilt. This is probably due to the tails providing a lubricating barrier between the smectic layers that serves to decorrelate the order within neighboring layers. Hence, the addition of molecular flexibility is likely to mitigate against the type of entropic 'sawtooth' mechanisms that have been found to stabilize antiferroelectric ordering in hard-particle bent-core models[6]. The addition of the flexible tails was also seen to give rise to significant spatial fluctuations in the smectic layers. It is worth pointing out that the smectic phases of rigid model molecules are often far more ordered than real smectics (as evidenced by scattering experiments[28]). The introduction of molecular flexibility therefore brings the model systems in to better correspondence with experiment.

Finally, the flexoelectric properties of non-polar seven-sphere bent-core molecules - with and without attractive interactions - have been studied by calculating the splay and bend coefficients in the nematic phase using fluctuation relations derived from linear-response theory[42,43]. An immense investment of computational effort was required to obtain reasonable results via this route, which serves to highlight how careful one must be in evaluating the required formulae. Nonetheless, our results show that a significant flexoelectric response can be measured for opening angles below about 150°. With typical molecular dimensions and dipole moments, the measured flexoelectric coefficients are in the region of 10 pC m^{-1} which is in excellent agreement with experiment. The flexoelectric response of real bent-core liquid crystals is often attributed largely to dipolar and quadrupolar interactions, but our results show that the molecular shape is also significant. This shouldn't be too much of a surprise, since most thermotropic nematics are, after all, dense molecular liquids, and it is well known that the structure and dynamics in such systems are dictated by short-range repulsive interactions. We are in no way suggesting that electrostatic interactions are insignificant, and we have not studied flexoelectricity in dipolar or quadrupolar systems because of the computational effort which will probably be required to obtain reliable results. A systematic study of this point is required, and will hopefully be the subject of future papers.

Acknowledgments

The provision of a studentship for AD and computing hardware by the Engineering and Physical Sciences Research Council (UK) (GR/R45727/01) is gratefully acknowledged. We are grateful to Professor M. P. Allen (Warwick) for helpful comments.

* Electronic address: philip.camp@ed.ac.uk

[1] T. Niori, T. Sekine, J. Watanabe, T. Furukawa, and

H. Takezoe, J. Mater. Chem. **7**, 1231 (1996).
[2] R. Macdonald, F. Kentischer, P. Warnick, and G. Heppke, Phys. Rev. Lett. **81**, 4408 (1998).
[3] A. Jákli, S. Rauch, D. Lötzsch, and G. Heppke, Phys. Rev. E **57**, 6737 (1998).
[4] N. V. Madhusudana, Mol. Cryst. Liq. Cryst. **409**, 371 (2004).
[5] A. V. Emelyanenko and M. A. Osipov, Phys. Rev. E **70**, 021704 (2004).
[6] Y. Lansac, P. K. Maiti, N. A. Clark, and M. A. Glaser, Phys. Rev. E **67**, 011703 (2003).
[7] D. J. Earl, M. A. Osiopov, H. Takezoe, Y. Takanishi, and M. R. Wilson, Phys. Rev. E **71**, 021706 (2005).
[8] P. J. Camp, M. P. Allen, and A. J. Masters, J. Chem. Phys. **111**, 9871 (1999).
[9] R. Memmer, Molec. Phys. **29**, 483 (2000).
[10] S. J. Johnston, R. J. Low, and M. P. Neal, Phys. Rev. E **65**, 051706 (2002).
[11] S. J. Johnston, R. J. Low, and M. P. Neal, Phys. Rev. E **66**, 061702 (2002).
[12] J. Xu, R. L. B. Selinger, J. V. Selinger, and R. Shashidhar, J. Chem. Phys. **115**, 4333 (2001).
[13] A. Dewar and P. J. Camp, Phys. Rev. E **70**, 070407 (2004).
[14] S. C. McGrother, A. Gil-Villegas, and G. Jackson, J. Phys.: Condens. Matter **8**, 9649 (1996).
[15] S. C. McGrother, A. Gil-Villegas, and G. Jackson, Mol. Phys. **95**, 657 (1998).
[16] A. Gil-Villegas, S. C. McGrother, and G. Jackson, Chem. Phys. Lett. **269**, 441 (1997).
[17] K. Satoh, S. Mita, and S. Kondo, Chem. Phys. Lett. **255**, 99 (1996).
[18] R. Berardi, S. Orlandi, and C. Zannoni, Chem. Phys. Lett. **261**, 357 (1996).
[19] E. Gwozdz, A. Brodka, and K. Pasterny, Chem. Phys. Lett. **267**, 557 (1997).
[20] J. S. van Duijneveldt and M. P. Allen, Mol. Phys. **92**, 855 (1997).
[21] C. McBride, C. Vega, and L. G. MacDowell, Phys. Rev. E **64**, 011703 (2001).
[22] C. McBride and C. Vega, J. Chem. Phys. **117**, 10370 (2002).
[23] M. R. Wilson, J. Chem. Phys. **107**, 8654 (1997).
[24] F. Affrouard, M. Kroger, and S. Hess, Phys. Rev. E **54**, 5178 (1996).
[25] J. S. van Duijneveldt, A. Gil-Villegas, G. Jackson, and M. P. Allen, J. Chem. Phys. **112**, 9092 (2000).
[26] H. Fukunaga, J.-I. Takimoto, and M. Doi, J. Chem. Phys. **120**, 7792 (2004).
[27] R. B. Meyer, Phys. Rev. Lett. **22**, 918 (1969).
[28] P. G. de Gennes and J. Prost, *The physics of liquid crystals* (Clarendon Press, Oxford, 1993), 2nd ed.
[29] P. R. M. Murthy, V. A. Raghunathan, and N. V. Madhusudana, Liq. Cryst. **14**, 483 (1993).
[30] A. G. Petrov, in *Physical Properties of Liquid Crystals: Nematics*, edited by D. A. Dunmur, A. Fukuda, and G. R. Luckhurst (The Institute of Electrical Engineers, London, 2001), p. 251.
[31] J. Stelzer, R. Berardi, and C. Zannoni, Chem. Phys. Lett. **299**, 9 (1998).
[32] J. L. Billeter and R. A. Pelcovits, Liq. Cryst. **27**, 1151 (2000).
[33] A. V. Zakharov and R. Y. Dong, Eur. Phys. J. E **6**, 3 (2001).
[34] A. V. Zakharov and A. A. Vukulenko, Crystallography Reports **48**, 738 (2002).
[35] D. L. Cheung, S. J. Clark, and M. R. Wilson, J. Chem. Phys. **121**, 9131 (2004).
[36] M. P. Allen and D. J. Tildesley, *Computer simulation of liquids* (Clarendon Press, Oxford, 1987).
[37] J. I. Siepmann and D. Frenkel, Mol. Phys. **75**, 59 (1991).
[38] D. Frenkel and B. Smit, *Understanding molecular simulation* (Academic Press, London, 2002), 2nd ed.
[39] C. Zannoni, in *The molecular physics of liquid crystals*, edited by G. R. Luckhurst and G. W. Gray (Academic Press, New York, 1979), pp. 191–220.
[40] G. V. Paolini, G. Ciccotti, and M. Ferrario, Molec. Phys. **80**, 297 (1993).
[41] A. Galindo, C. Vega, E. Sanz, L. G. MacDowell, E. de Miguel, and F. J. Blas, J. Chem. Phys. **120**, 3957 (2003).
[42] V. B. Nemtsov and M. A. Osipov, Sov. Phys. Crystallogr. **31**, 125 (1986).
[43] M. P. Allen and A. J. Masters, J. Mat. Chem. **11**, 2678 (2001).
[44] J.-P. Hansen and I. R. McDonald, *Theory of simple liquids* (Academic Press, London, 1986).